Templated Carbon and Graphene Based Hydrogen Storage Materials

Thesis
submitted in partial fulfillment of the requirements for the degree of

Doctor of Philosophy

by

Sohan Bir Singh

(Roll No. 146107026)

Department of Chemical Engineering

Indian Institute of Technology Guwahati

September 2019

Dedicated to my parents and family

You are the reason I have become what I am today……..

Department of Chemical Engineering
Indian Institute of Technology Guwahati
Guwahati – 781039, India

CERTIFICATE

This is to certify that the work contained in the thesis entitled **"Templated Carbon and Graphene Based Hydrogen Storage Materials"** submitted by ***Sohan Bir Singh*** for award of the degree of Doctor of Philosophy, has been carried out under my supervision and this work has not been submitted elsewhere for award of any degree.

.....

(Mahuya De)
Professor
Department of Chemical Engineering,
Indian Institute of Technology Guwahati
Guwahati – 781039, India.

Acknowledgement

It's a pleasure to finally express my appreciation to all those who made it possible for my successful completion of thesis. First and foremost, I would like to express my gratitude to my thesis supervisor Dr. Mahuya De, for her invaluable support and encouragement throughout the research work. I appreciate her moral support and guidance since the early stage of my research study, to develop an understanding in this area. It has been an amazing experience working with her; especially I enjoyed her style of mentoring students from which I have been benefited greatly in my professional and personal growth.

My heartiest gratitude goes to all doctoral committee members Prof. G. Pugazhenthi, Prof. Chandan Das and Dr. S Senthilkumar for their valuable advices and suggestions throughout my research work. I must also thanks to the faculty members of the Department of Chemical Engineering for their kind inspiration and suggestions during my entire research period.

My sincere thanks goes to all the staff members of Chemical Engineering department of IITG especially Mr. Harsaraj Biswanath, Mr. Jayanta Mout, Mr. Kaustavmoni Deka, Dr. Lukumoni Borah, Mr. Deep Jyoti, Mr. Ariful and Mr. Bhagya Boro for their help and support in different aspects of my work.

I would like to acknowledge the Central Instruments Facility of IIT Guwahati for allowing me to carry out SEM, FESEM, EDX, TEM and high pressure adsorption analysis of my samples and in this regard my sincere thanks goes to Mr. Madhurjya Borah.

My special thanks goes to my friends Ms. Madhuri Sarkar, Dr. Ruhit Jyoti, Dr. Rupak Kishor and Mr. Shailesh Varade for their moral support, encouragements and kind help in different aspects.

Moreover, I am lucky enough to work with Dr. N. Vinothkumar, Ms. Priyanka Hajare, Mr. Yashwant, Mr. Rishabh Saxena, Mr. Saptrashi Gupta, Ms. Shweta Kumbhar, Mr. Nilesh Khalse, Mr. Rahul Kumar, Mr. Ramanuj Pandey, Ms. Ankita Pandey, Ms. Shiva Sukla, Dr. Richa Sharma, Mr. Prakram Sehgal, Mr. Paran Sharma, Mr. Syam, Mr. Atanu Kumar, Dr. Mood Mohan and many more as lab–mate and would like to acknowledge their help and encouragement throughout this research period.

Most of all, I would like to express my deepest sense of gratitude to all my family members and

my parents. Their love, care, sacrifices and encouragement have made it possible for me to come so far. I appreciate the courage, understanding and dedicated support shown by all of them despite many testing times at their end. My sincere apology goes to all of those to whom I forget to mention but helped me at any part of the research work.

…….

(Sohan Bir Singh)

Abstract

Hydrogen has been explored as an alternative source of energy due to its various advantages, such as higher energy density, non–polluting characteristics and renewable nature. The main concern regarding using hydrogen as fuel is its storage. Researchers have reported various porous carbon materials for hydrogen storage application. Majority of the reported hydrogen storage materials are microporous having high surface area. The commercially reported templates such as zeolites or silica gel are also expensive. The mesoporous carbons (2–20 nm) of high surface area and high pore volume are also reported recently as adsorbents. Incorporation of nonmetals and metals in the carbon matrix has been reported to affect the hydrogen uptake property. Among structured carbons, graphene has also high potential for hydrogen storage because of the unique layered structure and presence of heteroatoms in form of functional groups.

The objective of this study was to develop low cost mesoporous templated carbons and explores the scope of different graphene based materials for hydrogen storage. In this study, the low cost alumina based mesoporous templates were developed and the efficiency of corresponding templated carbons for hydrogen storage was explored and compared with that of templated carbons prepared using commercially available microporous zeolite and mesoporous silica gel templates. The effects of non-metal (nitrogen) and metal (platinum, palladium or nickel) doping on templated carbons were investigated. For investigation on graphene based materials, graphene oxide was treated by chemical and thermal methods and physicochemical properties and hydrogen uptakes of the final graphene like products were studied and compared. The effects of preparation conditions and incorporation of metals (platinum, palladium or nickel) were also investigated. The hydrogen uptake capacities of prepared samples were determined at different temperatures and pressures using volumetric adsorption analysis. The heat of adsorption, reversibility and cycle stability of samples were also determined.

Alumina and sodium dodecyl sulfate (SDS) surfactant modified alumina templates were prepared in the laboratory by precipitation method. The templated carbons were prepared by chemical vapour deposition using cyclohexane or acetonitrile as a source of carbon and/or nitrogen. The graphene based materials were prepared from graphite oxide by chemical reduction and thermal exfoliation. The effects of exfoliation temperatures (200–500 °C) and carrier gases (hydrogen, argon, or air) were studied. The metals like platinum, palladium and

nickel were incorporated in carbon matrix by impregnation to see the effects of dopants on hydrogen storage.

The physicochemical properties of the samples were determined by various characterization techniques including TGA, XRD, XPS, FTIR, UV–Vis, Raman spectroscopy, CO–chemisorption, AFM, EDX, FESEM, TEM and surface area and pore analyzer. The hydrogen storage properties of the prepared samples were determined at –196 °C at 25 or 30 bar.

The alumina based templated carbons were mesoporous (2–10 nm) having agglomerated tubular/noodle like structures. The surface area was in the range of 1050–1221 m^2/g. The nitrogen doping did not affect the pore structure of templated carbons significantly but the surface area was enhanced. At –196 °C and 25 bar, the hydrogen uptake capacity for alumina–SDS templated carbon was 3.9 wt.%. On co–doping 3 wt.% platinum with nitrogen, the surface area and pore volume decreased for all the templated carbons. However, the drop for mesoporous surfactant modified alumina templated carbon was least. This may be associated with the highest dispersion of the Pt metal within the mesoporous matrix of surfactant modified alumina templated carbon. The hydrogen uptake increased to 4.1 wt.% for nitrogen and platinum co–doped surfactant modified alumina templated carbon at –196 °C and 25 bar. The mesoporous surfactant modified alumina templated carbon was further co–doped with nitrogen and nickel or palladium. The highest dispersion of metal was observed for palladium and nitrogen co–doped carbon, which also showed noodle or tubular structure in contrast to the aggregated structure of nitrogen–doped carbon. The palladium and nitrogen co–doped carbon with 2 wt.% palladium showed the highest hydrogen uptake of 5.0 wt.% at –196 °C and 25 bar. This may be attributed to its highest number of active sites corresponding to the highest metal dispersion and amount of nitrogen present. Also, the highest heat of adsorption of 22.9 kJ/mol was obtained for the same sample.

The graphene based hydrogen storage materials were prepared from GO by thermal exfoliation and chemical hydrazine treatment and compared for physicochemical properties and hydrogen uptake. The exfoliation temperature was observed to have a significant effect on the surface and structural properties of the samples. The exfoliated graphene oxide samples showed fluffy layered structure. The oxygen content decreased with increasing exfoliation temperature. Exfoliation temperature of 300 ^oC was observed to be optimum. It showed surface area of 248 m^2/g and total pore volume of 1.64 cm^3/g. The corresponding hydrogen uptake was 3.12 wt.% at –196 ^oC and 30 bar. A part of the synthesized graphene oxide (GO) was subjected to

hydrazine treatment and the remaining part was thermally treated in different gaseous (H_2, Ar or Air) environments. Structurally hydrazine reduced graphene oxide (RGO) was similar to parent graphene oxide having wrinkled layered structure but oxygen to carbon (O/C) ratio value was significantly lower than that of exfoliated graphene oxide samples suggesting more retainment of residual oxygen–containing functional groups in the latter. The BET surface area was highest for RGO (461 m^2/g) while, O/C value was highest for EGO (Air). The maximum hydrogen uptake of 3.34 wt.% was obtained for EGO (Air) at –196 °C and 30 bar followed by that of RGO. The hydrogen uptake capacity was observed to increase with O/C ratio as the presence of highly electronegative oxygen may have facilitated the interaction with incoming highly electropositive hydrogen. On addition of palladium metal to RGO and EGO, the hydrogen uptake capacity was enhanced from 2.50 to 3.22 wt.% and 3.34 to 3.52 wt.% respectively.

Surfactant modified alumina was observed to be an effective and economic template for synthesis of mesoporous templated carbons. Significant surface area, pore volume, relatively narrow pore size distribution, and tubular structure gave unique physicochemical characteristics to surfactant modified alumina based templated carbon. Its mesoporous structure facilitated higher metal dispersion. For templated carbons, the hydrogen uptake capacity was observed to be dependent not only on the surface area but also on pore volume. For doped templated carbon amount of dopant and dispersion of metal was observed to be an important criteria for hydrogen uptake; higher nitrogen content and higher metal dispersion resulted in higher hydrogen uptake. For graphene based materials, the considerable hydrogen uptake may be the combined effect of high pore volume, mesoporous fluffy layered structure, and significant content of surface oxygen heteroatom. The higher oxygen content usually favored hydrogen uptake. All the templated carbon and graphene based adsorbents showed good reversibility and cyclic stability for hydrogen storage at –196 °C.

List of Publications

Publication from thesis

1. Sohan Bir Singh, Mahuya De, Alumina based doped templated carbons: A comparative study with zeolite and silica gel templates, ***Microporous and Mesoporous Materials***, 257 (2018) 241–252.

2. Sohan Bir Singh and Mahuya De, Scope of doped mesoporous (< 10 nm) surfactant modified alumina templated carbons for hydrogen storage applications, ***International Journal of Energy Research*** 43 (2019) 4264–4280.

3. Sohan Bir Singh and Mahuya De, Thermally exfoliated graphene oxide for hydrogen storage: Study on structural effect, ***Materials Chemistry and Physics*** 239 (2020) 122102.

4. Sohan Bir Singh and Mahuya De, Chemically and thermally treated graphene oxides for hydrogen storage application: Comparative study on role of physical and chemical properties (Under Review).

5. Sohan Bir Singh and Mahuya De, Role of metal on physicochemical and hydrogen uptake properties of reduced and exfoliated graphene oxide (To be submitted).

6. Sohan Bir Singh and Mahuya De, Effect of metal and templates towards hydrogen adsorption for Pt–doped templated carbons, (Under preparation).

International conference

1. Sohan Bir Singh, Ruhit Jyoti, Priyanka Hajare and Mahuya De, ‘‘Effect of different templates on platinum modified carbons for hydrogen storage’’, International Conference on Materials Science and Technology (ICMTech–2016), 1–4 March 2016 at University of Delhi, Delhi, India.

2. Sohan Bir Singh and Mahuya De, ‘‘Mesoporous templated carbons’’, International conference on Sophisticated Instruments in Modern Research (ICSIMR–2017), 30 June –1 July 2017 at Indian Institute of Technology Guwahati, India.

3. Sohan Bir Singh and Mahuya De, ‘‘Platinum–doped templated carbon and reduced graphene oxide for hydrogen storage’’, International Conference on Chemical, Agriculture, Environment and Natural Sciences (CAENS–2017), 20–21 November 2017 at Kuala Lumpur, Malaysia.

4. Sohan Bir Singh and Mahuya De, ‘‘Thermally exfoliated graphite oxide for hydrogen storage application’’, Materials & Technologies for Energy Conversion and Storage (M–TECS 2018), 26–29 September 2018 at BARC, Mumbai, India.

CONTENTS

LIST OF FIGURES

LIST OF TABLES

APPENDICES

Chapter 1
Introduction

1. Introduction

1.1 Hydrogen as alternative fuel

Today the world is increasingly facing energy and environmental crisis. The demand for energy is increasing at a rapid rate, along with increase in the world population. The International Energy Agency (IEA) has projected the consumption of energy to be more than 400 Mton by 2035 as shown in Figure 1.1. After China, India is projected as the second largest consumer of energy. At present, most of the required energy is produced from fossil fuel based sources such as petroleum, natural gas, coal, etc. (Capuano et al. 2016). The rapid consumption and depleting condition of fossil fuels have driven the need to explore alternative and renewable sources of energy (Zhao et al. 2019). Renewable energy is considered to be the long–term solution to the world's future energy demands (Jiang et al. 2014). Another major problem associated with these fossil fuels is the release of significant quantity of carbon oxide gases and carbon particulates into the atmosphere that causes environmental pollution (Dincer et al. 2000). The main available renewable energy sources include solar, ocean, wind, geothermal, biomass, etc. (Jacobson et al. 2011). The carbon neutral characteristics of these sources result in zero contribution towards environmental pollution (Resch et al. 2008). At present, the contribution of renewable energy sources is limited. In 2012, only 22% of the total world energy generation was supplied by renewable energy sources (Owusu et al. 2016).

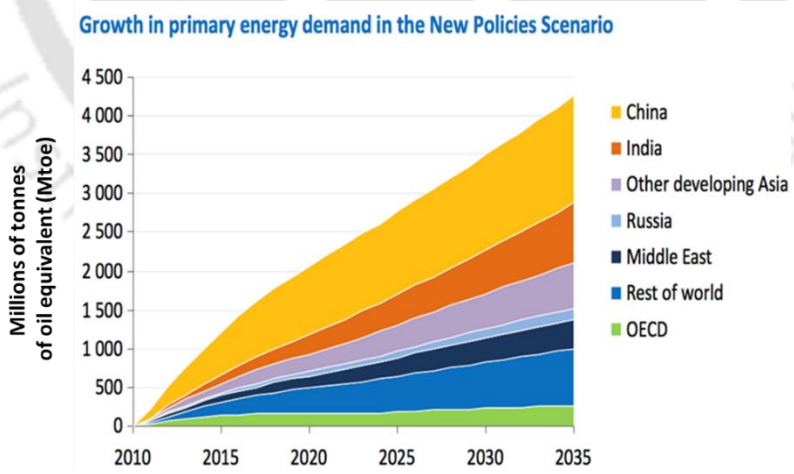

Figure 1.1: Projection of global energy consumption for various countries and region by International Energy Agency, IEA (Valero et al. 2018).

Another source of energy that is being pursued rigorously is hydrogen (Nicoletti et al. 2015). Hydrogen has been explored as an alternative source of energy due to its various advantages,

such as higher energy density (142 MJ/Kg), non–polluting characteristics and renewable nature (Jiang et al. 2014). Hydrogen is one of the most abundant elements on earth and its oxidation product is water. Hydrogen is thus a clean, safe, convenient and sustainable source (Geng et al. 2015). Hydrogen has more specific energy compared to any conventional energy source, as shown in Figure 1.2. Specific energy of hydrogen is 7, 3 and 2.5 times higher compared to that of coal, diesel/gasoline and methane respectively.

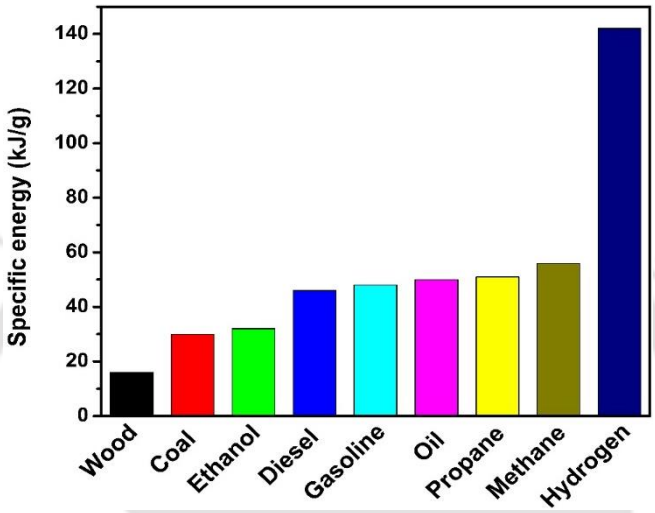

Figure 1.2: Specific energy of hydrogen in comparison with different fuels (http://greencon.net/).

Hydrogen can be used in both mobile and stationary fuel cell applications. Mobile application involves use as fuel in cars, trucks, buses or airplanes. Stationary fuel cells can be utilized in power plants, businesses, homes and even cell phones or laptop.

1.2 Hydrogen production

At present, hydrogen is mainly produced from fossil fuels such as natural gas, coal and naptha via steam reforming, gasification and partial oxidation processes. The hydrogen is also produced from renewable energy sources such as electrolysis of water, solar photo catalytic decomposition of water and direct thermochemical decomposition of water (Oriňáková et al. 2011). However, the contribution of these renewable sources to total hydrogen production at present is quite low (Ni et al. 2008).

1.3 Hydrogen Storage

For hydrogen to be used as source of energy, its efficient storage near point of application has become a very determining factor and considered as main hurdle towards the establishment of

the hydrogen based economy. Various challenging issues are associated with storage of hydrogen in a safe, efficient and economical way, particularly for mobile application. There are different methods to store hydrogen and each method has its own advantages and disadvantages (Jiang et al. 2014; Züttel et al. 2004). Hydrogen is conventionally stored in compressed gaseous or liquid form.

1.3.1 Compressed hydrogen gas

Compressed hydrogen gas is the most common technology for hydrogen storage and is being used in prototype hydrogen powered vehicles. In this method, the hydrogen gas is stored by compressing at a high pressure in the range of 200 to 700 bar. The storage tank is usually made by carbon fiber–reinforced composite which can sustain pressure up to 700 bar. At 700 bar, the gravimetric and volumetric hydrogen storage capacity is about 4.5 wt.% and 0.025 kg per liter, respectively (Takeichi et al. 2003). Generally, hydrogen based vehicles drive at a storage pressure of 350 bar. City buses run by hydrogen were launched in Germany, Japan, and the UK using pressurized hydrogen gas tank. The main issues regarding the mobile application of compressed hydrogen storage are space and weight. For long driving time higher quantity of compressed hydrogen gas will be required which involve larger storage tank. This in turn will increase the cost and weight of the vehicle and decrease the space for passengers and goods within vehicle. Further the use of very high pressure storage on board is potentially unsafe for vehicular application in spite of various development.

1.3.2 Liquid hydrogen storage

This is also a commercially available technology for hydrogen storage. In this technology, liquid hydrogen is stored in cryogenic tanks at –253 °C and atmospheric pressure or stored by simultaneous application of cryogenic condition and high pressure (240 bar) (Ahluwalia et al. 2010). The liquefied hydrogen has higher density compared to that of compressed hydrogen. However, the technology is highly energy intensive and expensive. Another disadvantage of this method is continuous ‘boil–off’ during hydrogen storage. The cryogenic hydrogen storage is not desirable for automotive applications due to safety related issues. The refueling process of hydrogen is very very difficult under cryogenic conditions.

Based on the above discussion, the conventional compressed and liquefied storage technologies have not been able to satisfy all the technical requirements for transportation applications and also have safety–related issues. Hence, there is a need to develop alternative storage

technologies for hydrogen and solid–state hydrogen storage is one of the best options. In this method, hydrogen is stored in the form of hydride or adsorbed within porous materials.

1.3.3 Solid–state hydrogen storage

The U.S. Department of Energy (DOE) has recommended the desirable properties for solid state hydrogen storage systems which are accepted globally (Anton et al. 2013). Table 1.1 summarizes the targets of a hydrogen storage system for mobile application (light–duty vehicles). None of the developed solid storage systems till date have been able to satisfy all the conditions.

Table 1.1: Targets for solid state hydrogen storage systems as proposed by U.S. Department of Energy (DOE).

Storage parameters	Target (2015)	Target (2017)
Gravimetric capacity (kWh/kg)	1.5	1.8
H_2 (wt.%)	5.5	5.5
Volumetric capacity (kWh/kg)	0.9	1.3
Cycle life	1500	1500
Operating temperature (^oC)	– 30 to 50 °C	– 40 to 60 °C
Min/max delivery temperature (°C)	– 40 to 85 °C	– 40 to 85 °C
System fill time for 5 kg H_2 (min)	4.2	3.3

The solid materials should have greater storage capacity both in terms of volume and weight percent. The kinetics of hydrogen uptake and release require to be very fast. Solid state materials also need to be lightweight and economic. At present, all these aspects are yet to be attained at desired values. The refills of the storage materials is also an issue. The major advantage of solid material based hydrogen storage method is its safe nature. However, it needs further improvement to be a commercial sources. The various methods for solid state hydrogen storage have been discussed below.

1.3.3.1 Hydrides materials

The hydrides are intermetallic compounds that are formed on exposure to hydrogen gas at moderate temperature and pressure. Hydrides have higher volumetric density and safety advantages compared to that of cryogenic or compressed storage (Sakintuna et al. 2007). The hydrogen atoms are chemically bounded in hydrides materials. The hydrides are categorized as metal hydrides, complex hydrides and related compounds (Durbin et al. 2013). The most commonly used hydrides for hydrogen storage are $NaAlH_4$, MgH_2, $LiBH_4$, $TiFeH_2$ and $Mg(BH_4)_2$ (Züttel et al. 2010). The hydrogen storage capacity of 3.7 wt.% was reported for

sodium alanate ($NaAlH_4$) at ambient temperature and pressure by Zaluska et al. (2000), but the maximum theoretical storage capacity is 5.5 wt.%. The theoretical hydrogen storage capacity of magnesium hydrides and lithium borohydride are up to 7.6 and 18.0 wt.% respectively which do satisfy the target capacity of DOE (Sakintuna et al. 2007; Züttel et al. 2003). However, major drawback of these systems is slow kinetics and requirement of high temperature (up to 300 °C) to release the hydrogen (Sakintuna et al. 2007). Numerous studies have been reported on metal hydrides in the last decade in direction to reduce release temperature and improve the kinetics. The stability of these hydrides has also been studied and Dehouche et al. (2000) reported that the MgH_2 hydride is stable up to 1000 cycles of hydrogen intake and release.

1.3.3.2 Porous materials

The porous materials contribute the other group that is being studied extensively towards solid state hydrogen storage application. These porous materials mainly store hydrogen by adsorption mechanism, while hydrogen is released by desorption. The fast adsorption–desorption kinetics is advantage of these materials (Thomas 2007). Various type of porous materials is reported in literature for hydrogen storage application, including carbon based materials, metal–organic frameworks (MOFs), zeolite, silica gel, etc. (Gangu et al. 2019; Li et al. 2018; Thomas et al. 2007). For porous materials, the hydrogen uptake generally depends on the surface area and pore volume (Wang et al. 2016). The porous materials are characterized based on the pore size range; materials with pores less than 2 nm are known as microporous. When the pores are between 2–50 nm, they are known as mesoporous (Wang et al. 2016). The pores greater than 50 nm constitute the materials known as called as macroporous. Most of the hydrogen storage studies have been done for microporous materials (Mohan et al. 2019; Nishihara et al. 2018; Xia et al. 2013; Suh et al. 2011; Chen et al. 1999).

1.3.3.3 Carbon based hydrogen storage materials

There is a wide range of carbon based materials that have been reported for hydrogen storage application such as activated carbons, carbon fibers, carbon nanotubes, etc. (Bénard et al. 2007; Kojima et al. 2006; Tibbetts et al. 2001; Chen et al. 1999; Dillon et al. 1997). In recent years more structured carbons such as templated carbon or graphene have generated interests (Gadipelli et al. 2015; Xia et al. 2013; Chen et al. 2007; Gadiou et al. 2005). Carbon materials are attractive candidates for hydrogen storage because of high surface area, high pore volume, better chemical and thermal stability, faster adsorption–desorption kinetics, excellent recyclability, lightweight, ease of availability, etc. (Xia et al. 2013). Generally, the porous

carbons are synthesized from either synthetic carbon precursors or naturally available carbon precursors (wood, coal, agricultural by–product and biomass) using various preparation routes (Ioannidou et al. 2007). However, the main drawback of carbon materials, as any porous materials, is lower hydrogen uptake capacity, particularly at ambient conditions. More details are discussed in the second chapter of 'Literature Review'.

1.4 Mechanism of hydrogen storage

For porous material, the hydrogen uptake occurs through physical adsorption or physisorption. In physisorption, the gas molecules interact with the surface of the adsorbent through van der Waals forces forming a layer of adsorbate on the surface (Rouquerol et al. 2013). The monolayer thus form on the surface, interacts with more incoming adsorbate molecules resulting in the formation of multilayers of adsorbate on the surface (Figure 1.3). These adsorbed layers are easily desorbed, making adsorption–desorption kinetics fast. Usually, the physical adsorption is associated with molecular adsorption.

When the surface of the adsorbent contains stronger active sites such as non–metal or metal heteroatoms, stronger interaction can take place (Darkrim et al. 2002). Depending on the nature of metal, the hydrogen molecules can interact to form chemisorbed state either in associated or dissociated form (Rouquerol et al. 2013). The potential energy curves for physical and chemical adsorption of hydrogen are shown in Figure 1.4 (Thomas et al. 2014).

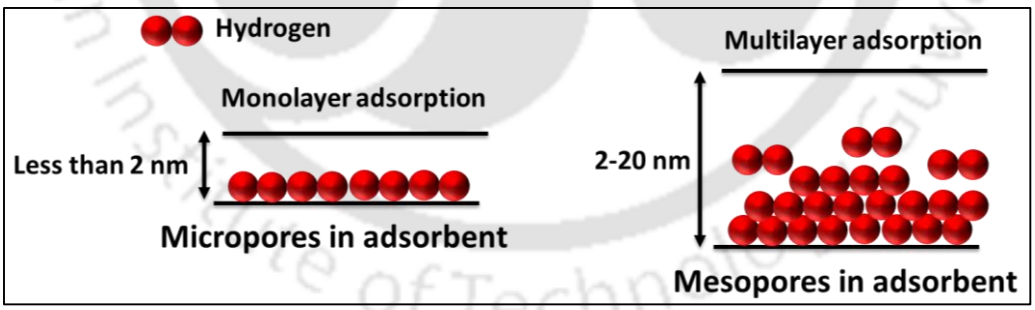

Figure 1.3: Schematic representation of monolayer and multilayer adsorption in microporous and mesoporous materials.

The hydrogen adsorption capacity has been reported to be enhanced by doping of small amount of non–metals and metals on the porous materials. These metals mainly contribute to hydrogen storage by facilitating chemisorption on these sites. Nonmetals are reported to activated carbon matrix promoting hydrogen adsorption. The metals are believed to provide additional active sites for hydrogen adsorption to enhance hydrogen uptake capacity (Zacharia et al. 2005). Also,

spillover mechanism involving metal sites are reported to contribute to the increased hydrogen storage capacity (Lachawiec et al. 2008). The hydrogen spillover involves dissociation of hydrogen molecules on metal site with subsequent migration of hydrogen atoms on adjacent support surface sites through surface diffusion. The schematic representing the spillover mechanism over any metal is given in Figure 1.5.

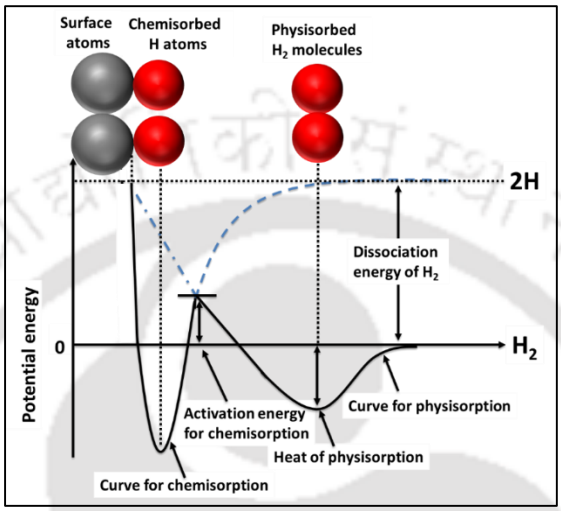

Figure 1.4: Potential energy curves for physical and chemical adsorption of hydrogen (Thomas et al. 2014).

The microporous materials, pore less than 2 nm, are extensively used for hydrogen storage application because of their high surface area (Nishihara et al. 2018). Surface area as high as 4000 m^2/g has been reported (Gaslain et al. 2006). Zeolites have been extensively studied as microporous material for hydrogen storage application. The narrow pore size is expected to create a very effective force field for adsorption of hydrogen. One of the drawback of the microporous carbons is low pore volume, less than 1 cm^3/g. Lately, mesoporous material with high surface areas are also investigated for hydrogen storage. Surface area more than 2000 m^2/g has been reported (Inagaki et al. 2016). The mesoporous materials are associated with large pore volumes (more than 2 cm^3/g). The pore size distribution of the mesoporous carbon can be controlled in the range of 2–20 nm (Cai et al. 2015). Silica based materials are mainly investigated as mesoporous material for hydrogen storage application. The mesoporous adsorbent with larger average pore size is expected to be better suited compared to microporous materials for the incorporation larger heteroatoms, such as metals, within the adsorbent matrix, resulting in higher dispersion of metals.

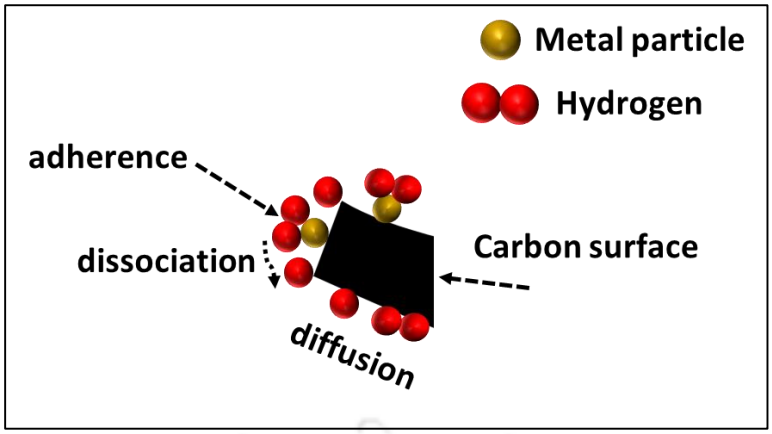

Figure 1.5: Spillover mechanism of hydrogen adsorption over any metal (Lachawiec et al. 2008).

The thesis has been organized in the following sections:

Introduction, Literature review, Objectives, Experimental, Result and Discussion, Conclusion and Future work.

Chapter 2
Literature Review

2. Literature Review

The carbon based porous materials are highly suitable for adsorption of small gaseous molecules such as hydrogen. High surface area, optimum pore size and high pore volume are the determining factors in their role as highly adsorptive material. Among porous carbon materials activated carbons and carbon nanotubes (CNTs) are widely reported in the literature. The templated carbon and graphene based adsorbents have attracted attention in the recent years for hydrogen storage application.

Activated carbon is one of the most reported forms of porous carbon for adsorption process (Xia et al. 2013; Yürüm et al. 2009). Activated carbons are generally prepared by carbonization method from organic precursors, which are subjected to activation by chemical or physical treatment in the mild oxidative atmosphere (Mohan et al. 2019; Marsh et al. 2006). Numerous studies have been reported for hydrogen storage using activated carbon. The physical properties and hydrogen uptake capacity of activated carbons based material are summarised in Table 2.1. The surface area of physically activated carbon was reported in the range of 700–1800 m^2/g. For activated carbons with KOH activation, very high surface areas was reported in the range of 2000–4000 m^2/g. Mostly were microporous in nature. The corresponded hydrogen uptake was reported in the range of 1.4 to 8 wt.% at –196 °C up to adsorption pressure of 70 bar. At room temperature and lower pressure, the hydrogen uptake was reduced drastically.

Carbon nanotubes (CNT) were first discovered in 1952 in Russia (Radushkevich et al. 1952; Iijima, 1991). The CNTs can be synthesized by different methods such as laser ablation, chemical vapor deposition and electric arc (Mohan et al. 2019; Mehra et al. 2014). The hydrogen uptake capacity depended on structure, pretreatments, geometry, structural defects, operating temperature and pressure (Poirier et al. 2004). Both single wall and multiwall nanotubes have been reported for hydrogen storage application (Panella et al. 2005; Lee et al. 2002). Most of the CNTs are microporous in nature. Lower surface areas have been reported for CNTs (200–800 m^2/g) compared to that of activated carbons (Table 2.2). The hydrogen uptake varied in the range of 1–8 wt.%, depending on adsorption temperature, pressure and surface area. As observed from Table 2.2, that in spite of using very high pressure up to 120 bar, the hydrogen uptake was on the lower side.

The study on the effect of incorporation of non–metals on hydrogen storage properties is limited for activated carbons and carbon nanotubes. The non–metals that have been studied for hydrogen storage application includes boron, oxygen and nitrogen.

Table 2.1: Reported physical properties and hydrogen uptake capacities of undoped and metal doped activated carbons at –196 °C.

Adsorbent materials	BET Surface area (m^2/g)	Pressure (bar)	Hydrogen uptake (wt.%)	References
AC	860	1	1.4	(Wang et al. 2011c)
AC	1585	20	3.8	(Wang et al. 2009)
AC	1394	20	4.5	(Hirscher et al. 2005)
AC–KOH	2451	30	4.8	(Zhao et al. 2012)
AC–KOH	4310	30	8.3	(Blankenship et al. 2017)
AC–B–KOH	2704	1	3.7	(Kopac et al. 2017)
AC–N–KOH	2919	20	6.7	(Xia et al. 2009)
AC–B	780	30	3.2	(Chung et al. 2008)
AC–N	2919	20	6.7	(Wang et al. 2016)
Ni/AC	976	1	1.8	(Wang et al. 2011c)
Pd/AC	2880	40	5.5	(Zhao et al. 2012)

AC : Activated carbon (physically activated)

The hydrogen storage capacity was observed to enhance by addition of the heteroatoms to activated carbons or CNTs (Xia et al. 2009; Sankaran et al. 2007). The hydrogen uptake and physical properties of the non–metal doped activated carbon and carbon nanotubes are included in Table 2.1 & 2.2, respectively. The theoretical studies showed that the presence of non–metals in the carbon matrix could activate the hydrogen in carbon network (Sankaran et al. 2006; Viswanathan et al. 2003). Chung et al. (2008) and Wang et al. (2016) reported boron and nitrogen doped activated carbons respectively, having hydrogen uptake in the range of 3.2–6.7 wt.% at –196 °C. They observed hydrogen uptake capacity enhanced with the incorporation of boron and nitrogen into activated carbon. About 50% and 18% enhancement in hydrogen uptake was observed on incorporating boron and nitrogen in activated carbon, respectively.

Table 2.2: Reported physical properties and hydrogen uptake capacities of undoped and metal doped carbon nanotubes (CNTs) at –196 °C.

Adsorbent materials	BET Surface area (m^2/g)	Pressure (bar)	Hydrogen uptake (wt.%)	References
SWCNT	285	70	8.0	(Mohan et al. 2019)
SWCNT	854	70	2.4	(Panella et al. 2005)
SWCNT	229	120	1.7	(Liu et al. 2010)
SWCNT	–	100	1.73	(Zhao et al. 2017a)
MWCNT	238	90	2.6	(Muthu et al. 2016)
MWCNT	840	100	6.46	(Gao et al. 2003)
SWCNT–B	523	1	1.1	(Sankaran et al. 2007)
SWCNT–N	552	1	1.0	(Anson et al. 2004)
Pt/MWCNT	–	90	3.7	(Reddy et al. 2007)

SWCNT: Single Walled Carbon Nanotube; MWCNT: Multi Walled Carbon Nanotube

Xia et al. (2009) have observed the role of nitrogen in the KOH activated carbon for enhancement of hydrogen storage capacity. The boron and nitrogen doped CNTs were reported for hydrogen uptake study by Sankaran et al. (2007) and Anson et al. (2004) respectively. The hydrogen uptake capacities of boron and nitrogen doped CNTs were obtained between 1.0–1.1 wt.% at –196 °C and 0.01–2.0 wt.% at 25 °C.

Very few studies have been reported on metal modified activated carbons or carbon nanotubes for hydrogen storage. The hydrogen uptake capacity was also reported to be enhanced by doping of small amount of metals in carbon matrix. These metals mainly contributed by providing additional adsorption sites. The interaction of hydrogen with these sites is believed to be chemisorption in nature. Also, the molecular hydrogen may undergo dissociation at metal sites and subsequently spillover to surface, contributing to hydrogen storage (Han et al. 2017; Zieliński et al. 2007). Zhao et al. (2012), Lee et al. (2011) and Zieliński et al. (2007) have reported the spillover effect for Pt, Ni and Pd respectively which enhanced the hydrogen uptake capacity of activated carbon at room temperature. Zhao et al. (2012) reported hydrogen uptake slightly increase from 0.28 to 0.32 wt.% at 20 bar on Pd doping on activated carbon. Lee et al. (2011) reported enhancement in hydrogen uptake on Pt doped activated carbon at vary high pressure of 100 bar. The hydrogen uptake increased from 0.4 to 0.7 wt.%. The positive effect of Ni doping on hydrogen uptake capacity for activated carbon was observed by Zieliński et al. (2007) at 30 bar; the uptake was enhanced from 0.15 to 0.53 wt.%. For carbon nanotubes, the spillover effect was reported for Ni and Pt doped CNTs by Han et al. (2017) and Reddy et al. (2007) respectively. The hydrogen uptake capacity and surface area of doped carbons are reported in Table 2.1 & 2.2. At –196 °C and different pressure, the hydrogen uptake capacity was reported in the range of 1.0–5.5 wt.% for metal doped activated carbons.

2.1 Templated carbon

A non–conventional carbon matrix that has been investigated in recent years is templated carbon. First reported ordered templated carbon with the high surface area was by Kyotani et al. (1997) and co–worker. After that, various research groups have explored the potentials of templated carbons in several applications including hydrogen storage. The porous templated carbon have been synthesized by chemical vapor deposition (CVD) and carbonization of carbon precursors using ordered mesoporous silica and microporous zeolite as templates (Yang et al. 2007; Chen et al. 2007; Gadiou et al. 2005; Kyotani et al. 1997).

CVD is a well established technique for the deposition of precursor molecules on or inside the substrate (Kyotani et al. 1997). The wide range of precursor can be deposited by CVD process with very high purity. The carbon precursor infiltrates through the porous structure of the inorganic template and undergoes thermal decomposition at high temperature, developing a template–carbon composite. The removal of inorganic template from the template–carbon composite is usually done by the hydrofluoric (HF) acid treatment.

Different types of carbon precursor are used in CVD process for the preparation of templated carbons such as sucrose, furfuryl alcohol, pyrene, vinyl acetate, propylene, acetonitrile, cyclohexane, etc. (Xia et al. 2011; Jiang et al. 2010; Konwar and De 2015; Meyers et al. 2001; Armandi et al. 2008; Nishihara et al. 2009). The nature of the precursor is one of the essential parameters that can be controlled to enhance the properties of the templated carbons (Attia et al. 2013). The properties of templated carbons depend on the interaction of the precursor with the templates. The efficiency of filling of template pores by precursor controls the surface area and pore volume of the resultant templated carbons. Better filling reported to enhance the surface area as well as pore volumes (Bohme et al. 2005; Konwar et al. 2015). The selection of precursor also determined the nature of deposition within the templated carbons. For example, acetonitrile was used as precursor for deposition of both carbon and nitrogen on the template surface, whereas hydrocarbons including propylene or butylenes have been used for deposition of only carbon (Alam et al. 2011; Giraudet et al. 2010; Ma et al. 2002).

The role of templates is important for the synthesis of templated carbons (Attia et al. 2013) as it determines the porous structure of the templated carbons. Properties such as microporous or mesoporous nature, surface area, pore–volume, etc. depend on the selection of template (Xia et al. 2011). The microporous zeolite template has been used extensively for the preparation of microporous templated carbon (Nishihara et al. 2018; Masika et al. 2014; Stadie et al. 2012;

Yang et al. 2007), whereas different forms of silica have been reported as templates for preparation of mesoporous templated carbons (Carraro et al. 2019; Inagaki et al. 2016; Oh et al. 2013; Zheng et al. 2010).

Table 2.3: Reported physical properties and hydrogen uptake capacities of undoped and metal doped templated carbons.

Adsorbent materials	BET Surface area (m^2/g)	Pressure (bar)	Hydrogen uptake (wt.%)	References
ZTC	1307	20	2.9	(Yang et al. 2006)
ZTC	2136	50	3.1	(Guan et al. 2009)
ZTC	3041	20	7.0	(Masika et al. 2014)
ZTC	3591	20	6.4	(Stadie et al. 2012)
ZTC	3021	20	6.6	(Balahmar et al. 2016)
N/ZTC	1833	20	3.9	(Alam et al. 2011b)
N/ZTC	3150	20	6.9	(Yang et al. 2007)
N/ZTC	3360	20	6.0	(Xia et al. 2011)
N/ZTC	1825	20	4.5	(Yang et al. 2006)
Pt–N/ZTC	2314	20	4.8	(Alam et al. 2011a)
Pd–N/ZTC	1858	20	5.3	(Masika et al. 2013)
MTC	877	20	2.2	(Oh et al. 2013)
MTC	749	19	1.6	(Attia et al. 2013)
N/MTC	1173	20	3.4	(Xia et al. 2007)
N/MTC	942	30	2.8	(Giraudet et al. 2011)
N/MTC	334	20	1.5	(Zheng et al. 2010)
N/MTC	1335	30	2.8	(Giraudet et al. 2010)
Pt/MTC	882	20	2.2	(Oh et al. 2013)
Ni/MTC	948	10	1.8	(Carraro et al. 2019)
Ni/C–aerogel	968	40	2.3	(Kabbour et al. 2006)
Pd/MTC	712	18	1.1	(Campesi et al. 2008)
Pd/C–aerogel	617	10	1.1	(Zhong et al. 2015)
Ni/MTC	910	10	1.2	(Carraro et al. 2014)
Ni–N/MTC	984	30	2.8	(Giraudet et al. 2011)

ZTC: Zeolite Templated Carbon; N: Nitrogen; MTC: Mesoporous Templated Carbon

For microporous zeolite templated carbon, the surface area has been reported in the range of 1307–3591 m^2/g and pore volume in the range of 0.7–1.9 cm^3/g (Balahmar et al. 2016; Masika et al. 2014; Stadie et al. 2012; Yang et al. 2006; Kyotani et al. 2003). The pore size range has been below 2 nm rendering the templated carbon microporous. The corresponding hydrogen uptake capacities are reported in the range of 2.9–7.0 wt.% (Balahmar et al. 2016; Masika et al. 2014; Stadie et al. 2012; Yang et al. 2007; Yang et al. 2006)

Kyotani et al. (2003) reported microporous zeolite templated carbons with surface area in the range of 1040–2470 m^2/g synthesized by CVD process. Recently, the templated carbon with very high surface area and high pore volume of 3341 m^2/g and 1.72 cm^3/g respectively, was reported by Musyoka et al. (2018) synthesized from zeolite 13X template. They reported hydrogen uptake capacity of this sample as 2.5 wt.% at liquid nitrogen temperature and pressure of 1 bar. Guan et al. (2009) and Yang et al. (2006) reported hydrogen uptake capacity of 2.9 and 3.1 wt.% respectively for zeolite templated carbons at pressure of 20 bar having respective surface area of 1317 and 2136 m^2/g. A linear relationship between hydrogen uptake capacity and surface area of carbons was experimentally demonstrated by Poirier et al. 2001. At room temperature, hydrogen storage capacity of 1.9 wt.% at 100 bar was reported by Stadie et al. (2012) for the surface area of 3400 m^2/g. Lachawiec et al. (2008) reported 5.1 wt.% hydrogen uptake capacity for the surface area of 3591 m^2/g at very high pressure of 300 bar for zeolite templated carbons. The hydrogen storage on zeolite templated microporous carbons have been summarized in Table 2.3.

Silica based mesoporous templates were used to synthesize the mesoporous templated carbons having pores in the range of 2–20 nm (Giraudet et al. 2011; Zheng et al. 2010; Xia et al. 2007). Pang et al. (2004) reported the surface area in the range of 886–2314 m^2/g for mesoporous templated carbons prepared by CVD. The two most reported silica based templates are well–ordered MCM–48 and SBA–15 (Jun et al. 2000; Ryoo et al. 1999). Wu et al. (1994) first reported the synthesis of mesoporous templated carbon using MCM–41 as the template. The mesoporous materials are also reported with moderately high surface area, narrow pore size distribution and faster adsorption–desorption kinetics (Inagaki et al. 2016). The major feature of mesoporous carbon is large pore volume which is believed to enhance storage capacity for any (Inagaki et al. 2016). The surface area of mesoporous templated carbons is reported in the range 400–1900 m^2/g with pore volume up to 2.4 cm^3/g. Attia et al. (2013) reported hydrogen uptake capacity of 1.61 wt.% at −196 °C and 19 bar for silica based mesoporous templated carbons. The hydrogen uptake capacity of 2.2 wt.% at 20 bar was reported by Oh et al. (2013) for mesoporous templated carbon prepared using silica template. Studies related to hydrogen storage on mesoporous templated carbon are tabulated in Table 2.2.

2.2 Doped templated carbons

Studies on hydrogen storage over the templated carbons modified with different non–metals and metals heteroatoms are discussed below.

2.2.1 Non–metal doped templated carbon

Studies have established that the hydrogen uptake capacity is enhanced by adding non–metals such as N, B, S, P to templated carbons (Alam et al. 2011). The nitrogen doped templated carbons have distinctive properties such as unique electronic, mechanical and adsorption properties among various non–metal modified carbons (Wang et al. 2009). Nitrogen has been reported to modify electron density of carbon matrix enhancing interaction with hydrogen (Giraudet et al. 2010). Also, the presence of nitrogen in carbon matrix is reported to activate dissociation of hydrogen favoring hydrogen uptake (Xia et al. 2011). Vinayan et al. (2013) reported the changes in the electron charge density of the carbon support with heteroatom doping. Recently, nitrogen doping has also been reported to result in an enhanced surface chemical activity in terms of polarity and basicity (Chetty et al. 2009). Generally, nitrogen doped templated carbons were prepared by chemical vapor deposition process using acetonitrile as both carbon and nitrogen precursor (Wang et al. 2016; Xia et al. 2011; Giraudet et al. 2011; Yang et al. 2007). A wide surface area range of 408–3360 m^2/g are reported in the literature with nitrogen loadings of 3.7–13 wt.% for both microporous and mesoporous templated carbons. The hydrogen uptake capacity and physical properties of nitrogen doped microporous templated carbons at –196 °C are summarized in Table 2.3. Most of the microporous templated carbons were prepared using different types of zeolites such as zeolite–Y, zeolite EMC–2, zeolite 13X & many more. Alam et al. (2011) reported 3.9 wt.% hydrogen uptake at −196 °C and 20 bar for microporous nitrogen doped templated carbon synthesized from zeolite Y template. Xia et al. (2011) later on reported the synthesis of nitrogen doped templated carbons using zeolite EMC–2 by vapor phase deposition from acetonitrile precursor. They reported the surface area and nitrogen loading in the range of 565–3360 m^2/g and 3.65–7.66 wt.% respectively at different vapor deposition temperatures. However, they reported hydrogen uptake capacity in the range of 1–6 wt.% at –196 °C and 20 bar. Yang et al. (2007) reported the synthesis of nitrogen doped zeolite templated carbons using acetonitrile precursor and very high BET surface area of 3150 m^2/g. The hydrogen uptake was obtained to be about 6.9 wt.% at adsorption temperature of –196 °C and 20 bar. Yang et al. (2006) observed the positive effect of the nitrogen doping on the physical properties and hydrogen uptake for microporous zeolite templated carbons. The surface area and pore volume were enhanced from 1022 to 1764 m^2/g and 0.67 to 0.97 cm^3/g, respectively when nitrogen was doped on microporous templated carbon. Also, the hydrogen uptake was observed to increase more than double when it is enhanced from 2.0 to 4.3 wt.% at –196 °C and 20 bar. Xia et al. (2011)

reported the nitrogen content in the range of 3.65–7.66 wt.% but the properties and hydrogen uptake of microporous templated carbon were not affected by nitrogen doping. The surface area and pore volume were lowest for highest nitrogen content in the templated carbon and maximum hydrogen uptake capacity was obtained for microporous templated carbon having nitrogen content of 4.70 wt.%.

The mesoporous nitrogen doped templated carbons were mostly prepared using silica templates. The hydrogen uptake capacity and physical properties of samples are mentioned in Table 2.3. Ordered mesoporous nitrogen doped templated carbons, synthesized using acetonitrile from SBA–15 template with surface area of 1335 m^2/g, was reported by Giraudet et al. (2010). Kruk et al. (2000) reported the surface area of 1380 m^2/g for templated carbons synthesized from MCM–41 template. For the nitrogen doped mesoporous templated carbons synthesized using SBA–15 template, the hydrogen uptake was reported in the range of 1.49–3.4 wt.% at pressure of 20–30 bar. The corresponding surface area was in the range of 334–1335 m^2/g. Jiang et al. (2010) prepared hollow nitrogen–containing carbon spheres using SBA–15 template with surface area in the range of 408–872 m^2/g. The highest hydrogen uptake capacity of 0.96 wt.% at –196 °C and 1 bar, was observed by Jiang et al. (2010) for sample with nitrogen loading of 2.3 wt.%. However, Xia and Mokaya (2007) reported hydrogen adsorption of 3.4 wt.% (20 bar) for SBA–15 templated nitrogen doped carbon having surface area of 1173 m^2/g. Cai et al. (2015) reported the synthesis of 13 wt.% of nitrogen doped mesoporous templated carbon for hydrogen storage application with a surface area of 1123 m^2/g. They stored hydrogen was 3.1 wt.% at –196 °C and 36 bar. Recently, the hydrogen uptake capacity of the mesoporous templated carbons synthesized from MCM–41 and SBA–15 templates was reported in the range of 1.5–2.3 wt.% at –196 °C and 10 bar (Carraro et al. 2018; Juárez et al. 2017). The more study on hydrogen uptake capacity of nitrogen doped microporous templated carbons are summarized in Table 2.3. Giraudet et al. (2011) observed the enhancement in surface area and hydrogen uptake capacity for nitrogen doped on mesoporors templated carbon. The surface area and hydrogen uptake were increased from 825 to 942 m^2/g and 2.3 to 2.8 wt.% respectively. Kabbour et al. (2006) reported slight increase in hydrogen uptake from 2.0 to 2.3 wt.% (at 40 bar) for approximately 9 wt.% Ni doped mesoporous carbon aerogel.

2.2.2 Metal doped templated carbons

The various types of metals including Pt, Pd, Ni, Co, Cu, Zn and Ru, have been reported for hydrogen storage application. The incorporation of metals in the templated carbon matrix has been reported to affect the hydrogen uptake property (Cai et al. 2015; Masika et al. 2013; Alam et al. 2011; Reyhani et al. 2011; Campesi et al. 2008; Wang et al. 2008). The dopant metals provided the additional active sites for hydrogen adsorption (Berube et al. 2007). The studies available for hydrogen storage at –196 °C on metal doped microporous and mesoporous templated carbons are included in Table 2.3. Only two studies have been reported on microporous templated carbon with the doping of Pt and Pd metals for hydrogen storage application at –196 °C. Alam et al. (2011) have shown that Pt doped microporous zeolite templated carbon can store hydrogen up to 4.8 wt.% at 20 bar. The reported higher surface areas were in the range of 1400–2200 m^2/g with highest isosteric heat of adsorption (9 kJ/mol). At same pressure, Masika et al. (2013) reported hydrogen uptake capacity of 5.3 wt.% for Pd doped microporous zeolite templated carbon, having maximum surface area of 1858 m^2/g. The effect of Pd loading variation (0.2–2 wt.%) on hydrogen uptake was studied by Masika et al. (2013). The initially hydrogen uptake capacity was reported to increase when palladium loading was increased from 0.2 to 0.4 wt.%, thereafter hydrogen uptake reduced further palladium loading increased from 0.4 to 2.0 wt.%

At –196 °C more studies have been reported for metal doped mesoporous templated carbons compared to that of metal doped microporous templated carbons. A major advantage of mesoporous carbons compared with that of microporous carbons is that the former can facilitate incorporation of larger dopants in carbon matrix, resulting in their higher dispersion and better performance in applications. The diffusion limitation is reported to be higher in microporous carbon (Barsukov et al. 2006). Oh et al. (2013) observed hydrogen storage of 2.2 wt.% for Pt doped mesoporous silica templated carbon with surface area of 882 m^2/g at −196 °C and 20 bar. Oh et al. (2013) reported the slight enhancement in surface area and pore volume on addition of Pt to mesoporous templated carbon. It is usually reported in literature that surface area and pore volumes decreased due to metal particle deposited inside the pores of carbon matrix. The hydrogen uptake capacity was not affected with addition of Pt metal, it was same of 2.2 wt.% for both undoped and Pt doped carbons at −196 °C and 20 bar. Carraro et al. (2014) improved the hydrogen uptake capacity from 0.76 to 1.16 wt.% for 1 wt.% Ni on mesoporous MCM-41 templated carbon at 10 bar. However, for 15 wt.% Ni, they noticed decrease in hydrogen uptake from 0.76 to 0.45 wt.% at similar conditions. The surface area and pore

volume were reduced on both loadings of Ni (1 & 15 wt.%). Zhong et al. (2015) reported a solution–phase synthesis method to prepare Pd doped mesoporous carbon aerogels with different loading. The reported hydrogen uptake capacity 1.1 wt.% at –196 °C and 10 bar with surface area of 617 m^2/g.

2.2.3 Non–metal and metal co–doped templated carbons

The limited studies have been reported on the co–doped templated carbons for hydrogen storage. Generally, the co–doped templated carbons were prepared by a CVD process. The non–metal and metal were doped on templated carbons. The Ni and N co–doped mesoporous templated carbon prepared from SBA–15 templates reported by Giraudet et al. (2011) and the hydrogen uptake of 2.8 wt.% was observed at –196 °C and 30 bar.

2.3 Graphene

Graphene is an sp^2 bonded carbon sheet which is arranged in a hexagonal honeycomb lattice. The length of the carbon–carbon bond is in graphene about 0.142 nm. The layers in graphene interact weakly through van der Waals forces. The graphene based materials can be prepared using different way. These methods consist of chemical, thermal and electrochemical treatment of graphene oxide (GO) (Zhou et al. 2016; Çiplak et al. 2015; Abdelkader et al. 2015; Botas et al. 2013; Parambhath et al. 2011; Moon et al. 2010). In the chemical method, GO was reduced with hydrazine and methanol (Wei et al. 2016; Çiplak et al. 2015; Moon et al. 2010). For the thermal method, GO is treated at high temperature under different gaseous environments (hydrogen, argon, vacuum, hydrogen/argon) resulting in exfoliation of graphene layers (Zhou et al. 2016; Botas et al. 2013; Parambhath et al. 2011). The exfoliation temperature of GO is reported in the range of 127–2400 °C. The exfoliation temperature plays a crucial role in the separation of graphene layers. In case of electrochemical technique, the desired potential was applied between the GO anode and metal cathode which facilitated the production of electrons in anode resulting in the breaking of GO layers to form bulk reduced graphene oxide (Abdelkader et al. 2015; Khanra et al. 2014). The graphene, having extraordinary electrical, thermal and mechanical properties, has been reported widely for many applications including supercapacitor, sensor, fuel cell, electrodes, heat mirror etc. (Vaqueiro–Contreras et al. 2018; Selvakumar et al. 2018; Gadipelli et al. 2015; Hu et al. 2015; Ismail et al. 2015). In recent years, graphene has also been reported for gas storage application including hydrogen storage (Jung et al. 2016; Gadipelli et al. 2015; Divya et al. 2014). The unique layered structure of graphene results in its significant surface area and pore volume, which are useful for gas

storage. The physical properties and hydrogen uptake capacity of graphene are included in Table 2.4.

Reduced graphene oxides prepared by hydrazine treatment reported to have surface area between 466–754 m^2/g (Gadipelli et al. 2015; Kuila et al. 2013; Srinivas et al. 2011; Srinivas et al. 2010). Graphene synthesized by the thermal method in hydrogen and argon environment reported a surface area between 156–751 m^2/g (Zhou et al. 2016; Chowdhury et al. 2016; Gadipelli et al. 2015; Divya et al. 2014; Zheng et al. 2013; Wu et al. 2009).

The range of hydrogen storage reported for graphene materials at –196 °C is quite broad depending on the material and pressure used. Srinivas et al. (2010) reported hydrogen uptake capacity about 1.17 wt.% at 10 bar for reduced graphene oxide having surface area of 640 m^2/g. Ismail et al. (2015) reported 2.0 wt.% hydrogen storage capacity at 20 bar for reduced graphene oxide but did not report the surface area. Zheng et al. (2013) obtained hydrogen uptake capacity of 1.75 wt.% for exfoliated graphene at 54 bar having the surface area of 300 m^2/g. Hudson et al. (2014) reported 2.07 wt.% hydrogen storage capacity with surface area of 375 m^2/g for exfoliated graphene. The reported maximum uptake capacity of 3.0 wt.% was by Subrahmanyam et al. (2008) for exfoliated graphene oxide. They reported surface area of 925 m^2/g. At room temperature using moderate pressures, the hydrogen uptake varied in the range of 0.1 to 0.7 wt.% and the corresponding surface areas were in the range of 156–470 m^2/g.

Table 2.4: Reported physical properties and hydrogen uptake capacities of undoped and metal doped graphene.

Adsorbent materials	BET Surface area (m^2/g)	Pressure (bar)	Hydrogen uptake (wt.%)	References
RGO	640	10	1.17	(Srinivas et al. 2010)
RGO	–	20	2.0	(Ismail et al. 2015)
RGO	470	10	1.2	(Srinivas et al. 2011)
EGO	300	54	1.75	(Zheng et al. 2013)
EGO	375	50	2.07	(Hudson et al. 2014)
EGO	925	100	3.0	(Subrahmanyam et al. 2008)
Expanded graphite	555	20	1.20	(Lueking et al. 2005)
Ni/RGO	–	20	2.70	(Ismail et al. 2015)
Pd/RGO	–	20	2.80	(Ismail et al. 2015)
Fe/EGO	190	50	2.16	(Hudson et al. 2014)

RGO: Hydrazine Reduced Graphene Oxide; EGO: Exfoliated Graphene Oxide

2.4 Doped graphene

Compared to doped templated carbon, less studies are reported for doped graphene based materials for hydrogen storage. The variety of methods are reported for the doping of heteroatoms on graphene including CVD, impregnation, thermal annealing of graphene oxides (GO) with heteroatom precursors, plasma and arc–discharge approaches (Cui et al. 2017; Chen et al. 2015; Liu et al. 2014; Tang et al. 2014). For graphene, doping with nitrogen or boron elements is reported to influence the interaction between the hydrogen and graphene layers as observed by Wang et al. (2011). Parambhath et al. (2012) and Vinayan et al. (2013) reported that the nitrogen doping could help dispersion and high coverage on graphene material, as well as hydrogen uptake capacity. The hydrogen uptake capacity was reported in between 1–1.5 wt.% at 25 °C and 40 bar. Vinayan et al. (2013) reported the hydrogen uptake increase from 0.68 to 1.06 wt.% after nitrogen doped on exfoliated graphene. Theoretical calculations showed a high hydrogen storage capacity (8.38 wt.%) of Ca–decorated B doped graphene that was reported by Beheshti et al. (2011). Hydrogen uptake study at liquid nitrogen temperature for non–metal doped graphene was not reported. The different metal (Ni, Pt, Fe, Ti or Pd) doped graphenes are reported to enhance the interactions between molecular hydrogen and graphene (Wang et al. 2009; Ataca et al. 2008). The maximum study has been reported at room temperature on metal doped graphene, whereas only few studies have been reported at liquid nitrogen temperature. The enhancement in hydrogen uptake generally reported by spillover mechanism at room temperature. Ismail et al. (2015) reported the 5 and 10 wt.% of Ni and Pd doped graphene for hydrogen storage. They observed that hydrogen uptake increased for both 5 and 10 wt.% loading of Ni and Pd doped on reduced graphene oxide (RGO). The hydrogen uptake was obtained in the range of 2.7–2.8 wt.% at –196 °C and pressure of 20 bar. Hudson et al. (2014) reported a hydrogen uptake in the range of 2.16 wt.% by iron doped exfoliated graphene oxide at –196 °C and 50 bar. With addition of iron to exfoliated graphene oxide, the surface area was reduced from 375 to 190 m^2/g but the hydrogen uptake was slightly enhanced from 2.07 to 2.16 wt.%. At room temperature, hydrogen uptake capacity was reported in the range of 0.07–5 wt.% for Ni, Pt and Pd doped graphene samples at pressure range of 30–100 bar (Gadipelli et al. 2015; Parambhath et al. 2011). Very few studies on the co–doped graphene for hydrogen storage was reported. Wang et al. (2011b) reported hydrogen uptake capacity of 2.81 wt.% for Ni–B co–doped two–dimensional graphene, whereas around 4.4 wt.% hydrogen uptake capacity was obtained by Wang et al. (2011a) for Ni–B co–doped three–dimensional

graphene at –196 °C and 1 bar. The hydrogen uptake capacity of Pd–N co–doped graphene was reported in the range of 1.5–4.4 wt.% at 25 °C and 40 bar (Parambhath et al. 2012).

2.5 Knowledge gap and motivation

The detail study of literature available on carbon based hydrogen storage materials suggests that the properties of the developed materials are still unable to fulfill the required specifications of hydrogen storage materials. Mostly microporous templated carbons were reported. The zeolite and silica gel templates, mostly used in the reported studies, are relatively costly. Hence development of a low cost template will be useful towards commercialization of templated carbon. The alumina which has extensive porous network have high potential to be used as templates. The alumina can be prepared easily in the laboratory from low cost precursors. The pore structure of alumina can also be modified easily using surfactant during preparation. Use of alumina based templates are not reported for the synthesis of templated carbons for hydrogen storage. So, the present study will develop this low cost mesoporous alumina based templates. The properties of corresponding templated carbons will be compared to that of zeolite and silica gel templated carbons. Further mesoporous templates of high surface area and high pore volume may be more desirable for hydrogen storage than microporous template having high surface area but very low pore volume. High surface area and higher average pore size of mesoporous carbon will further help to accommodate and disperse the incorporated heteroatoms more efficiently which is expected to positively contribute towards hydrogen uptake. Hence mesoporous carbons with high surface area and pore volume prepared from a low cost template will have high potential towards hydrogen storage application.

Unique layered structure of graphene with presence of surface heteroatom in form of functional groups is expected to play a positive role in hydrogen uptake. However, few studies have been reported in this area. The study on effect of physical structure of graphene based materials on hydrogen uptake is very limited. Metal doped graphene oxide may also be worthwhile to explore. Study on effect of the preparation methods on structure of graphene oxide will also help to understand its role in hydrogen storage application. Based on above observation, following objectives have been formulated.

2.6 Objectives of the thesis

The objective of this study was to develop carbon based hydrogen storage materials. Mesoporous templated carbon and graphene based structures were investigated. More specific objectives are described below:

- Development of mesoporous low cost alumina based templated carbons and comparison with templated carbons prepared using commercially available microporous zeolite and mesoporous silica gel as templates.
- Study the effects of doping of templated carbon with non–metal (nitrogen) and metals (Platinum, Palladium, or Nickel). Determination of the effect of metal loading. The effects of preparation conditions and incorporation of metal to be investigated.
- Preparation and comparison of graphene based materials by chemical and thermal treatments. Study the effect of variation in preparation conditions and incorporation of metal.
- Hydrogen uptake capacities of prepared samples to be tested at liquid nitrogen temperature and moderate pressure using volumetric adsorption analysis. For selected adsorbents hydrogen uptake at room temperature will be determined. The heat of adsorption, reversibility and the cycle stability of samples will be investigated.

Chapter 3
Experimental

3. Experimental

3.1 Templated carbon based materials

3.1.1 Chemicals

Alumina based templates were prepared from aluminium nitrate nonahydrate (Merck, $Al(NO_3)_3 \cdot 9H_2O$) precursor using ammonia solution (Merck, NH_4OH, 30%) as the precipitating agent. Sodium dodecyl sulfate (Merck, SDS, 90%) was used as the additive for the preparation of surfactant modified alumina. The NH_4Y–zeolite (Product No. 334413, Sigma–Aldrich) and silica gel (Sigma–Aldrich, High Purity Merck Grade 10180) were used as templates in as received condition without any further pre–treatment. Cyclohexane (Merck, C_6H_{12}, 99.9%) was used as a carbon precursor. Acetonitrile (Merck, CH_3CN, 99.9%) was used as precursor for carbon as well as nitrogen. The chloroplatinic acid hexahydrate (Sigma–Aldrich, $H_2Cl_6Pt \cdot 6H_2O$, 37.50%), palladium chloride (Sigma–Aldrich, $Pd\ Cl_2$, 99 %) and nickel acetate tetrahydrate (Sigma–Aldrich, $Ni(OCOCH_3)_2 \cdot 4H_2O$, 98 %) were used as sources of metals. Hydrofluoric acid (Merck, HF, 48%) was used to remove the template from the carbon–template composite. Hydrazine hydrate (Merck, $N_2H_4 \cdot H_2O$, 99%) was used as a reducing agent.

3.1.2 Preparation of alumina based templates

Alumina based templates were prepared by precipitation method, with and without using surfactant. The preparation steps are shown in Figure 3.1. To prepare 3 g of alumina, the required amount of aluminium nitrate (22 g) was dissolved in 250 ml of deionized water. The solution was stirred for 15 min at room temperature and then precipitation was carried out by the addition of 30 % ammonia solution. The pH was maintained at 10.5. After completion of precipitation, the mixture was stirred for 60 min at room temperature followed by aging under reflux at 75 °C for 6 h. After aging, the mixture was cooled to room temperature. The precipitate was filtered and washed repeatedly to deionized water. The final washed precipitate was dried at 120 °C for 12 h in a hot air oven followed by calcination at 550 °C for 4 h in static air. The preparation procedure was based on the optimum conditions reported by Patel et al. (2015).

For the preparation of the surfactant modified alumina, sodium dodecyl sulfate solution was added to aluminium nitrate solution. The preparation steps was described earlier in Figure 3.1. The sodium dodecyl sulfate solution was prepared by dissolving of 4.23 g surfactant in 100 ml of deionized water and aluminium nitrate solution was prepared by dissolving of 22 g aluminium nitrate precursor in 250 ml of deionized water.

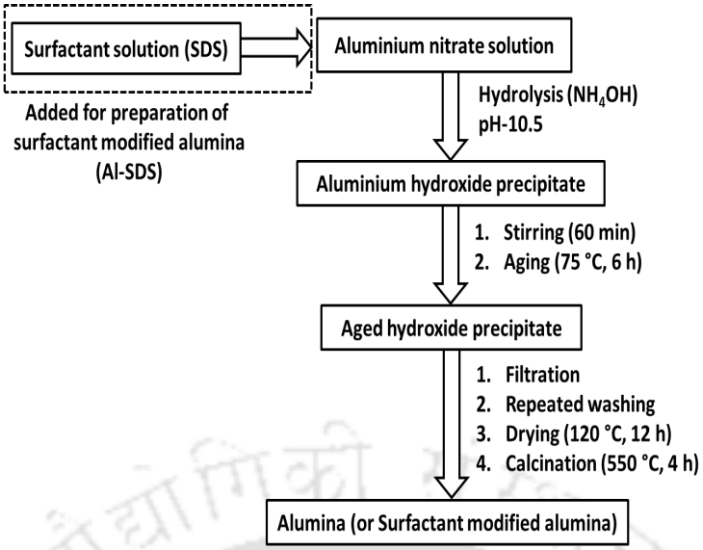

Figure 3.1: Preparation scheme for alumina and surfactant modified alumina templates.

The molar concentration of both the aluminium nitrate and surfactant solutions was maintained at 0.1 M each. Thereafter precipitation was carried out by addition of NH_4OH to the solution containing metal precursor as well as the surfactant. The subsequent steps were same as described earlier (Figure 3.1). The final product sample was surfactant modified alumina. The surfactant was removed from final product during calcination step at 550 °C. The removal of surfactant was confirmed by TGA analysis. The final alumina and surfactant modified alumina were described as alumina (Al) and alumina–SDS (AlS) respectively in text.

3.1.3 Preparation of templated carbons

The templated carbons were synthesized by chemical vapor deposition (CVD) on different templates using a carbon precursor. A schematic diagram of the experimental setup of CVD is shown in Figure 3.2. In this method, the required amount of template was placed in a quartz boat in the horizontal furnace. The carrier gas flow was split in two; a fraction of gas flowed directly to the reactor and remaining gas passed through the flask containing the carbon precursor or carbon and nitrogen precursor. The three–neck flask containing the precursor was maintained at the desired temperature and the carrier gas flowing through it carried the precursor vapor to the template which was maintained at deposition temperature. The carrier gas flow rate and temperature of carbon precursor controlled the vapor phase concentration of precursor. For this study, the precursor containing flask (unit 7 in Figure 3.2) was maintained at 30 °C. The total flow rate of carrier gas was 50 ml/min and the flow through the flask was maintained at 30 ml/min. Under these conditions, the final concentration of cyclohexane in vapor phase inside the reactor was 65 ppm and for acetonitrile, it was 70 ppm. The

concentration was measured by Gas Chromatograph (NUCON–5765).

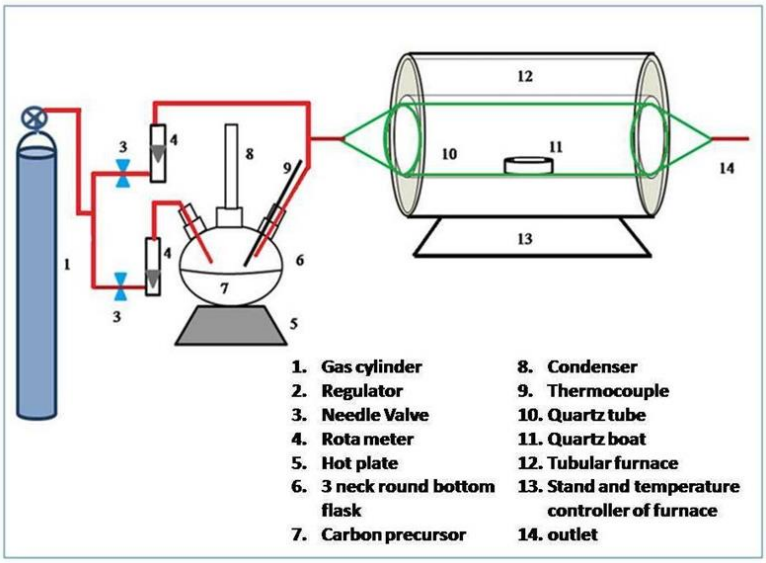

Figure 3.2: Schematic of experimental set up for carrying out chemical vapor deposition.

The templates were heated to the desired deposition temperature of 750 °C in the flow of the argon at heating rate of 10 °C/min. As template reached the target deposition temperature, the flow of gas carrying the precursor vapor was started and continued for specific deposition time of 3 h. The cyclohexane was used as the carbon precursor for this study. During entire deposition time, constant deposition temperature was maintained for template. The deposition condition was selected based on earlier studies reported by Konwar et al. (2014). After completion of the deposition time, the carbon–template composite was further treated for 2 h in the inert carrier gas at 800 °C. Thereafter the carbon–template composite was cooled down to the room temperature in the same flow of argon. The carbon–template composite was collected from the furnace and treated with 40 ml of 48% aqueous HF solution at room temperature for 24 h to remove the template. The template got dissolved in hydrofluoric acid and thereby separated from the carbon by etching process. To ensure complete removal of the dissolved template, the residual carbon was washed several times with deionized water and filtered. The filtered carbon was finally dried overnight at 150 °C in the air oven. In text, the templated carbon samples are denoted as Al–C, AlS–C, SG–C and Z–C prepared using alumina, alumina–SDS, silica gel and zeolite respectively as templates.

The nitrogen doped templated carbons were prepared in similar way as described above. Only difference is that cyclohexane precursor was replaced by acetonitrile which acted as precursor for both carbon and nitrogen deposition. The synthesized nitrogen doped templated carbons are

denoted in text as Al–N, AlS–N, SG–N and Z–N derived from alumina, alumina–SDS, silica gel and zeolite respectively.

For the preparation of metal doped templated carbons, the metal was first introduced in the templates by impregnation method. The metal–template composite was then subjected to CVD process. The platinum was used as the metal and cyclohexane was used as the carbon precursor. The preparation steps for the metal doped templated carbon are shown in Figure 3.3. The dry impregnation method was carried out for platinum incorporation into templates. In dry impregnation, the platinum precursor was dissolved in deionized water. The deionized water was taken as per the pore volume of alumina. Metal precursor amount corresponded to 0.0045 mg metal/g of the template. The metal precursor solution was added drop wise to the template and properly mixed. This wet metal–template composite was dried at 120 °C for 12 h. Then, the dry metal–template composite was subjected to CVD process to obtain the metal–template–carbon composite. The template was removed by HF treatment to obtain the metal doped templated carbon. The platinum doped samples are represented as Pt/Al–C, Pt/AlS–C, Pt/SG–C and Pt/Z–C derived from alumina, alumina–SDS, silica gel and zeolite templates respectively.

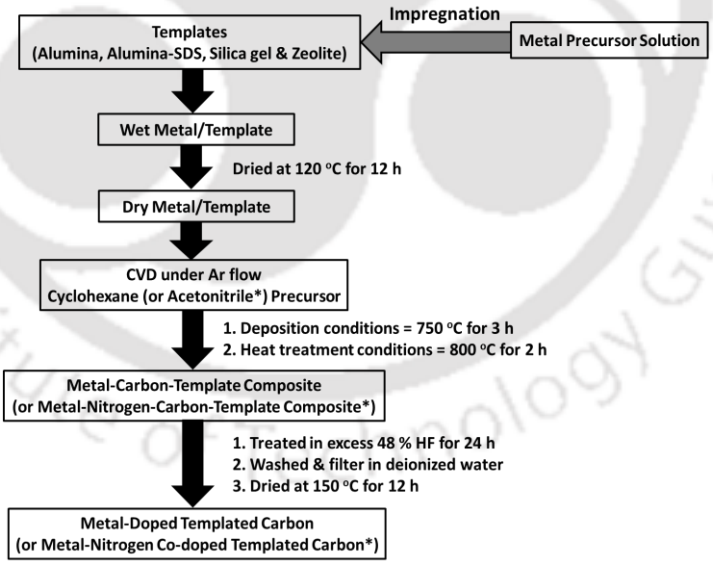

Figure 3.3: Preparation steps for platinum doped and platinum and nitrogen co–doped templated carbons using cyclohexane and acetonitrile precursor, respectively.

For the preparation of metal and nitrogen co–doped templated carbons, same procedure as that for metal–doped templated carbon was carried out. The metal was first incorporated into the template by impregnation procedure as described above. Thereafter the CVD was carried out over the metal–template composite using acetonitrile as the precursor. The preparation steps

for the metal–nitrogen co–doped templated carbons are shown in Figure 3.3. Platinum and nitrogen co–doped templated carbons are represented as Pt/Al–N, Pt/AlS–N, Pt/SG–N and Pt/Z–N respectively for alumina, alumina–SDS, silica gel and zeolite templates.

To see the effect of nature of metal in co–doped carbons, nickel and palladium were also used as the metal source. These metal and nitrogen co–doped templated carbons were prepared using only alumina–SDS template and referred as Ni/AlS–N and Pd/AlS–N.

The effect of metal loading was studied by varying the palladium content as 0.6, 1, 2 and 3 wt.% in the palladium and nitrogen co–doped templated carbons prepared using alumina–SDS template. The samples were denoted as $Pd_{0.6}$/AlS–N, Pd_1/AlS–N, Pd_2/AlS–N and Pd_3/AlS–N. The suffix represented weight percent of metal loaded.

The effect of sequence of addition of metal in co–doped carbon was explored by incorporation of palladium metal in the nitrogen doped carbon prepared by CVD process. At first, the nitrogen doped carbon using the surfactant modified alumina template was prepared followed by incorporation of metal into it by impregnation. The wet palladium and nitrogen co–doped templated carbon was dried at 100 °C for 12 h. Finally, the dried sample was calcined at 400 °C for 4 h. This palladium and nitrogen co–doped sample was denoted as Pd/AlS–N_ IMPA. IMPA indicated palladium impregnation after CVD process. The palladium and nitrogen co–doped alumina–SDS templated carbons were also prepared by the electroless deposition method. The steps involved are shown in Figure 3.4(a) and (b). The electroless deposition method was carried out in two ways as shown in Figure 3.4(a) and (b).

In first method (Figure 3.4a), the required amount of palladium precursor was dissolved in distilled water under stirring condition. The pH of the precursor solution was maintained at 2 using 37 % HCl solution. The molar ratio of N_2H_4 to palladium was maintained at molar ratio of 1:1 so that the reducing agent was in 50 % excess to the palladium precursor. Hydrazine reacts with palladium chloride on the alumina–SDS and templated carbon surface in the following reaction: $N_2H_4 + 2PdCl_2 \rightarrow 2Pd^0 + N_2 + 4HCl$

At first 20 ml, hydrazine solution was passed through the support followed by 20 ml of the precursor solution. About 10 min of interaction time was maintained for each passage. Above two steps represented one cycle and the cycle was repeated for four times to get the desired deposition of palladium on alumina–SDS. The wet sample was dried at 100 °C for 12 h in hot air oven to get the palladium–template composite. Then CVD process was carried out for synthesis of palladium and nitrogen co–doped alumina–SDS templated carbon using acetonitrile precursor as explained above. This sample was denoted as Pd/AlS–N_EDB.

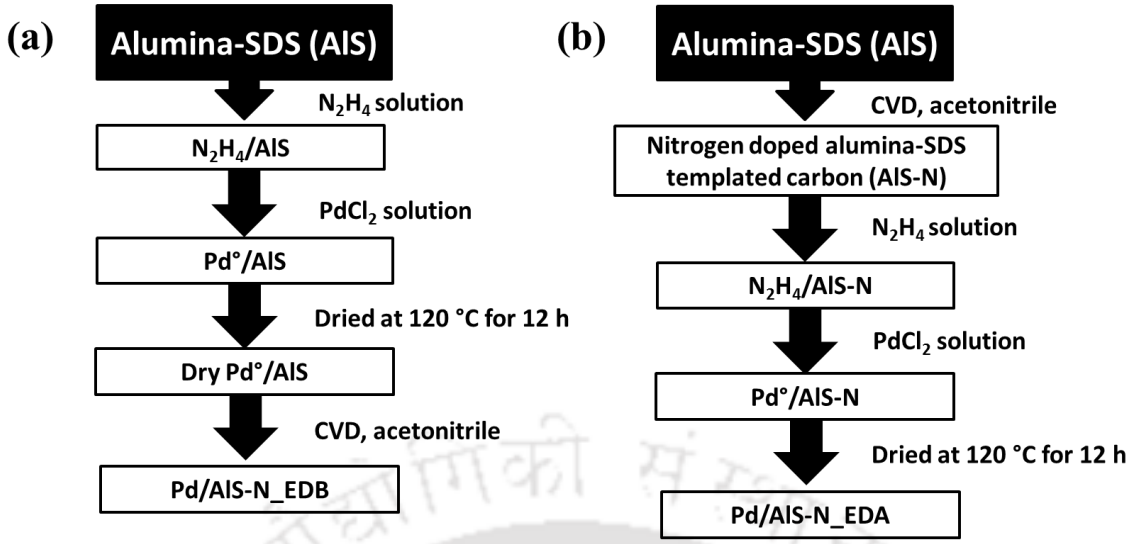

Figure 3.4: Steps preparation of palladium and nitrogen co–doped alumina–SDS templated carbons (Pd/AlS–N_ED) by electroless deposition method (a) before and (b) after CVD.

In a second pathway (Figure 3.4b), the nitrogen doped templated carbon, previously prepared by CVD process, was used as the substrate in the electroless deposition method. Same steps were repeated as described above. Then the sample was dried at 100 °C for 12 h and calcined at 400 °C for 4 h. This sample was named as Pd/AlS–N_EDA.

3.2 Graphene based materials

3.2.1 Chemicals

Commercial graphite (Sigma–Aldrich, 3–20 µm) powder was used as raw material for the synthesis of graphene oxide (GO) by modified Hummer's method. Other chemicals used in this method were sodium nitrate (Merck, $NaNO_3$), sulphuric acid (Merck, H_2SO_4, 98%), potassium permanganate (Merck, $KMnO_4$, 98.5%), hydrogen peroxide (Merck, H_2O_2, 30 %), hydrochloric acid (Merck, HCl, 37 %) and deionized water. Hydrazine hydrate (Merck, $N_2H_4{\cdot}H_2O$, 99%) was used for the reduction of GO. Hydrogen, argon and air were used as carrier gases for thermal exfoliation of GO. The chloroplatinic acid hexahydrate (Sigma–Aldrich, $H_2Cl_6Pt{\cdot}6H_2O$, 37.5%), palladium chloride (Sigma–Aldrich, $PdCl_2$, 99%) and nickel acetate tetrahydrate (Sigma–Aldrich, $Ni(OCOCH_3)_2{\cdot}4H_2O$, 98%) were used as precursors for the metals.

3.2.2 Preparation of graphene oxide (GO)

The GO was prepared by oxidizing graphite powder based on the modified Hummers method. The steps are described in Figure 3.5. One g of pure graphite was taken in a beaker and $NaNO_3$ (0.5 g) and H_2SO_4 (25 ml) were added. The mixture was stirred for 1 h in an ice bath, maintaining a temperature less than 10 °C. The $KMnO_4$ was added slowly to the mixture and stirred for another 1 h under the same condition. The mixture was thereafter removed from the ice bath and allowed to attain the room temperature under stirring condition. It was further stirred for 1 h at room temperature (35 °C). About 100 ml of deionized water was added at a rate of 10 ml/min to this mixture. After complete addition of water, the mixture was heated up to 90 °C using hot plate and stirred at room temperature for 1 h. The colour of the mixture appeared dark brown. The mixture was then cooled to room temperature followed by addition of 100 ml of deionized water and 10 ml of H_2O_2. The entire mixture was stirred for 1 h at room temperature and the colour of the mixture changed from dark brown to yellowish. The mixture was filtered and the solid sample was washed with acidic water ($HCl:H_2O::1:9$) followed by repeated washing with deionized water until the pH was neutralized. Finally, the obtained solid GO was dried in an air oven at 60 °C for 12 h. Nearly ~0.50 g weight of GO was obtained after drying, resulting in 50 % yield.

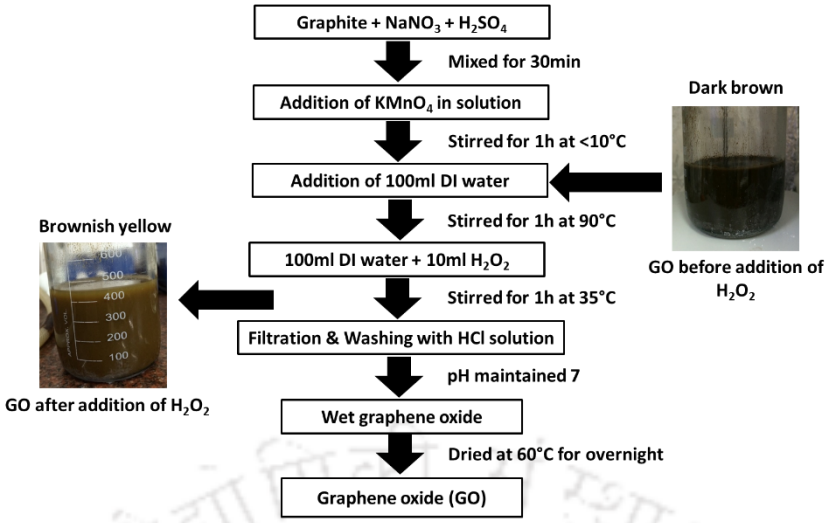

Figure 3.5: Preparation steps of graphene oxide (GO).

3.2.3 Preparation of reduced graphene oxide (RGO) using hydrazine

Preparation steps of reduced graphene oxide (RGO) from graphene oxide (GO) are shown in Figure 3.6. The aqueous suspension of GO containing 3 mg/ml was prepared. The suspension was stirred for 4 h at room temperature and thereafter sonicated for 2 h. The mixture was heated to 90 °C and about 0.4 ml of hydrazine hydrate was added to it. The mixture was further stirred for 6 h, maintaining the temperature at 90 °C. Thereafter, the mixture was cooled to room temperature. Finally, the suspension was filtered. The separated solid was washed several times with deionized water and dried at 60 °C. The obtained black powder was the reduced graphene oxide and named as RGO(hyd).

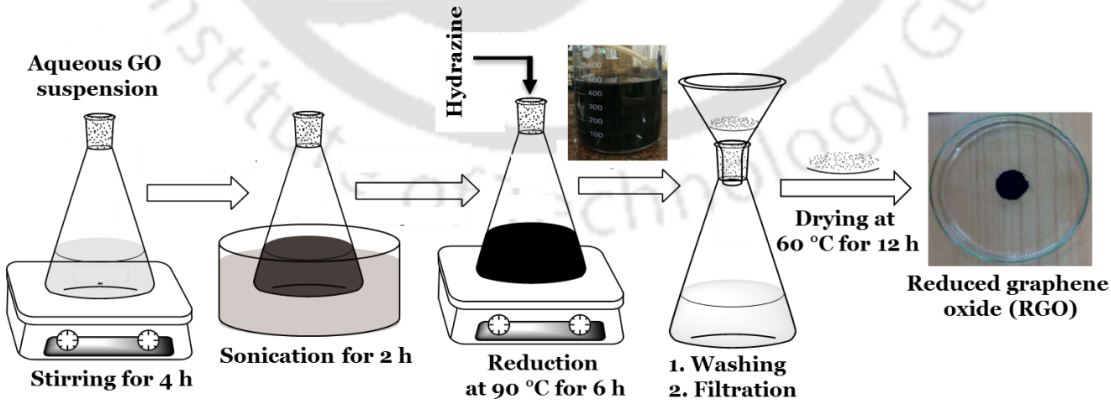

Figure 3.6: Preparation sequence of reduced graphene oxide (RGO) from graphene oxide (GO).

3.2.4 Preparation of exfoliated graphene oxide (EGO)

Exfoliation of graphene oxide was done for separation of the layers. During exfoliation the removal of oxygen–rich functional groups in form of CO, CO_2 and/or H_2O vapor from the surface (Botas et al. 2013) are expected to contribute towards separation of layers producing graphene of few layers. Figure 3.7 shows the preparation procedure of exfoliated graphene oxide (EGO) from graphene oxide (GO) in the flow of carrier gas. About 1 g of the prepared GO was taken into a quartz boat and placed at the center of the horizontal quartz reactor. Initially, nitrogen gas was flowed through the quartz reactor for 20 min to create an inert environment. The temperature was increased at a rate of 10 °C/min from room temperature to the desired exfoliation temperature in flow of nitrogen.

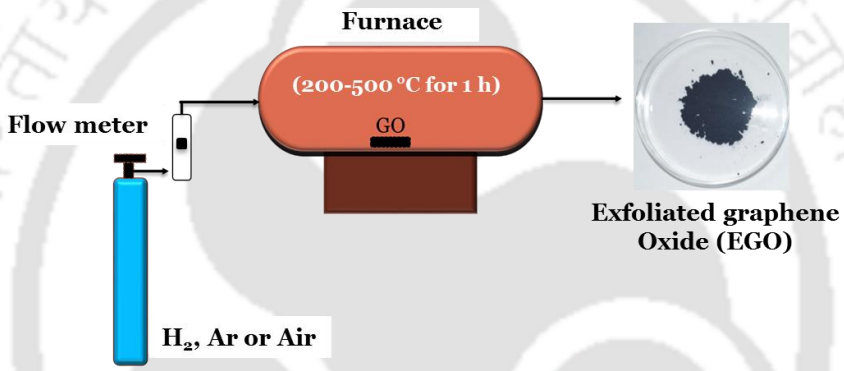

Figure 3.7: Preparation sequence of exfoliated graphene oxide (EGO) from graphene oxide (GO).

As the sample attained the desired exfoliation temperature, the flow of nitrogen gas was switched to the selected carrier gas. To study the effect of exfoliation temperature, it was varied as 200, 300, 400 and 500 °C. For this study, exfoliation was carried out for 1 h in flow of hydrogen. The synthesized exfoliated GO samples are denoted as EGO–X in text, where X is 200, 300, 400, 500 , the respective exfoliation temperature.

The effect of exfoliation environment was studied using different carrier gas such as hydrogen, argon or air. The exfoliation was carried out at 300 °C for 1 h for this study. The exfoliated GO samples prepared using different carrier gases were referred as EGO(H_2), EGO(Ar) and EGO(Air).

3.2.5 Preparation of metal doped graphene oxide

For the preparation of metal doped RGO and EGO samples, first GO was prepared by modified Hammer's method as discussed in section 3.2.2. Figure 3.8 shows the preparation schematic of metal doped samples. The desired metal (Ni, Pt or Pd) was impregnated on the graphene oxide (GO). The dry metal doped GO sample was divided into two parts. One part was reduced by

hydrazine to obtain the metal doped RGO and the remaining part was exfoliated to obtain the metal doped EGO sample. The details are discussed below.

The impregnation of GO was carried out by dissolving required amount of metal (Pt/Ni/Pd) precursor in deionized water and adding the aqueous solution drop wise to 1 g of GO. The resultant metal–GO mixture was thoroughly mixed to form a homogeneous sample. This wet metal–GO composite sample was dried at 60 °C for 12 h. For the preparation of metal doped reduce graphene oxide (M/RGO), about 1 g of the dry metal–GO composite sample was dispersed in 300 ml of deionized water under stirring condition. Thereafter, similar procedure was followed as preparation of reduced graphene oxide (RGO) sample. That is the suspension of metal–GO composite was stirred and sonicated at room temperature followed by addition of hydrazine at 90 °C. The final sample after drying gave metal doped RGO denoted as Pt/RGO, Ni/RGO or Pd/RGO.

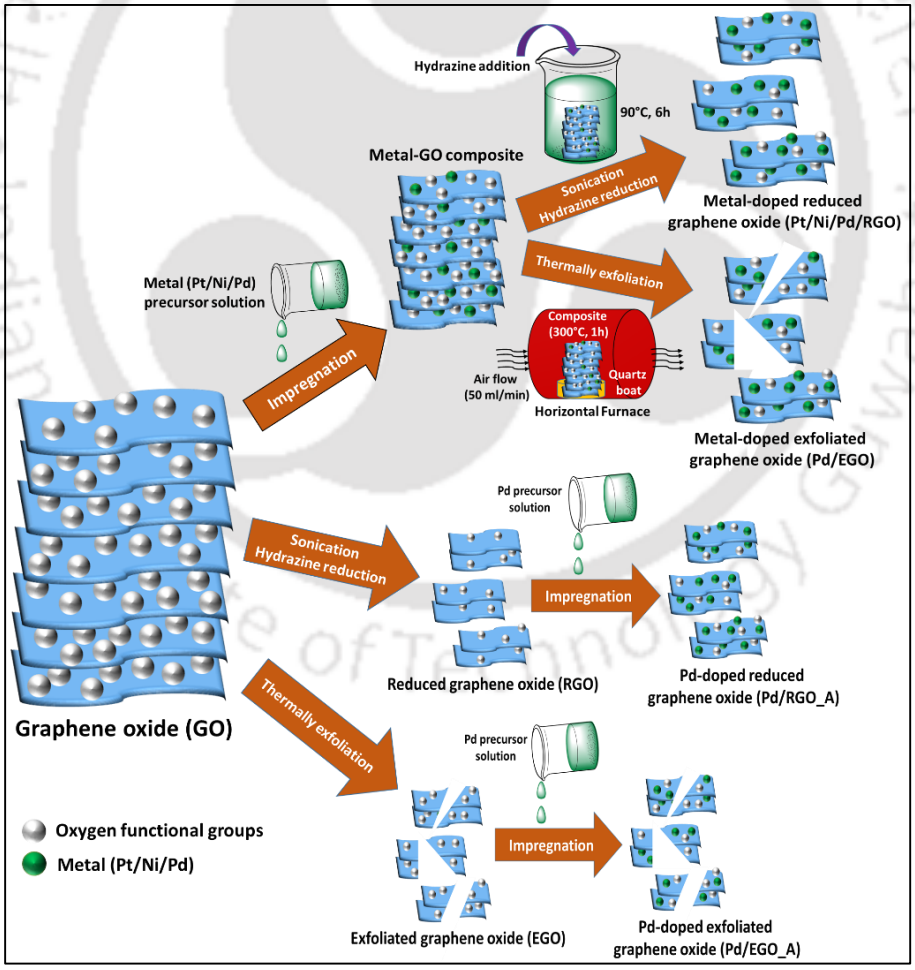

Figure 3.8: Preparation sequence of metal doped reduced and exfoliated graphene oxide.

The metal doped exfoliated graphene oxide (M/EGO) was prepared using palladium. Around 1 g of dried palladium–GO composite sample was taken into a quartz boat and placed in the horizontal furnace. Air was used as the carrier gas for this study. Thereafter, the temperature of the furnace was increased from room temperature to 300 °C under air flow. The sample was maintained at exfoliation temperature of 300 °C further for 1 h in same flow of air. The furnace was cooled down to room temperature in flow of same carrier gas air. The obtained sample was palladium doped EGO and named as Pd/EGO.

To study the effect of the sequence of doping another two samples were prepared by the direct impregnation of palladium on prepared RGO and EGO. In this case, the RGO and EGO samples were first prepared as described in section 3.2.3 and 3.2.4. Thereafter these samples were impregnated using palladium chloride solution as described above in this section 3.2.5. The final palladium–RGO and palladium–EGO composites was dried at 100 °C for 12 h and thereafter calcined at 300 °C for 4 h to obtain the final doped samples. For impregnation of palladium on EGO sample, 30 % aqueous ethylene glycol was used as the solvent for the dispersion of EGO. These prepared samples were named as Pd/RGO_A and Pd/EGO_A. A denoted 'after'.

3.3 Characterization of materials

The physicochemical properties of the different templates, templated carbons and graphene based materials were investigated using TGA, UV–Vis, FTIR, XPS surface area and pore analysis, XRD, Raman Spectroscopy, AFM, EDX, FESEM, TEM and CO–pulse chemisorption.

3.3.1 Thermogravimetric analysis (TGA)

The thermal stability of samples was determined using TGA (TG, Netzsch) instrument in nitrogen atmosphere with a constant heating rate of 10 °C/min. To establish the complete removal of templates from the templated carbons and to determine the combustion temperature properties of templated carbons, the TGA was performed in an air atmosphere.

3.3.2 Ultra–violet visible spectroscopy (UV–Vis)

The UV–Vis profiles of samples were recorded with a Shimadzu spectrophotometer (UV–1601 PC) in the range of 200–800 nm. Before UV–Vis analysis, the samples were dispersed in water with the help of sonication at room temperature.

3.3.3 Fourier transform infrared spectroscopy (FTIR)

The oxygen–containing functional groups of the graphene oxide (GO) and graphene samples were investigated by FTIR spectroscopy. This was investigated by PerkinElmer–Frontier instrument and spectra were recorded in the wave number from 400 cm^{-1} to 4000 cm^{-1} with maximum resolution of 4 cm^{-1}. The sample was prepared using KBr pellet method.

3.3.4 X–ray photoelectron spectroscopy (XPS)

The X–ray photoelectron spectroscopy (XPS) spectra were performed using a Thermo Fisher Scientific (ESCALAB) instrument under the high vacuum of 10^{-10} mbar. The Al Kα was used as the excitation source. The fitting of peaks was performed in Origin software by Gaussian method.

3.3.5 Surface area and pore analysis

The surface area and pore analysis of the samples was done using Quantachrome Autosorb iQ at −196 °C. Before analysis, the samples were oven dried at 200 °C for 2 h and degassed at 200 °C for 3 h in a helium atmosphere. The BET surface area was determined over the relative pressure range (P_s/P_o) 0.05–0.30 and pore volume up to 0.99. The micropore area was calculated from t–plot analysis. Pore size distributions of samples were determined by Barrett–Joyner–Halenda (BJH) and density functional theory (DFT) methods. The dV(d) represents differential pore volume with respect to pore diameter.

3.3.6 X–ray diffraction (XRD)

The powder X–ray diffraction profiles of the samples were recorded between 5–70° using Bucker D8 advance diffractometer. The diffractometer was operated at 40 kV and 40 mA with Cu K_α radiation. The average crystallite size was calculated using Scherer's formula:–

$$D_c = \frac{K\lambda}{\beta \cos\theta} \qquad (1)$$

Where, D_c is the average crystal size, a value of 0.9 was used for K, the constant associated with the crystallite shape factor. λ (nm) is the X–ray wavelength. The term β represented the broadness of the peak at half maximum.

The approximate number of graphene layers was determined by equation 2 (Botas et al. 2013):

$$N_L = \frac{D_c}{d_{(002)}} + 1 \qquad (2)$$

Where, N_L and $d_{(002)}$ represent number of layers and spacing between the layers respectively. D_c, the average crystal size of the graphitic zone.

3.3.7 Raman Spectroscopy

The degree of graphitization of the materials was characterized by Raman spectroscopy. Raman spectra were obtained by Jobin–Yvon T6400 laser micro–Raman system with the 514 nm line of Ar^+ ions laser as the excitation source. For Raman analysis, the samples were manually placed at the probe tip near the desired point of the sample on a glass slide at room temperature.

3.3.8 Atomic force microscopy (AFM)

The AFM images of samples were recorded in Agilent, 5500 series instrument. The height profile graph and average thickness were determined with the help of WSxM 5.0 Develop 8.2–Image browser software. Two unit areas of 10×10 µm and 2×2 µm were scanned for the analysis of the sample.

3.3.9 Field emission scanning electron microscopy (FESEM)

The surface morphology of synthesized templated carbons was studied by FESEM (Model: Zeiss 1430VP) at different magnifications. For FESEM analysis, the samples are dispersed in an appropriate solvent and then deposited on an aluminium foil before mounting on the sample holder for gold coating.

3.3.10 Energy dispersive X–ray spectroscopy (EDX)

The elemental composition and spectra of the materials were measured by EDX analysis. This EDX facility was connected with FESEM.

3.3.11 Transmission electron microscopy (TEM)

The TEM images of the samples were recorded using JEM 2100 (Make: JEOL) at 200 kV. The sample preparation was done by first dispersing the sample in a solvent using ultra sonication

followed by deposition on a copper grid. The average metal cluster size was calculated by Image J software from TEM images. The calculation of average metal cluster was done using 100 number of particles.

3.3.12 CO–pulse chemisorption

The metal dispersion was calculated from CO–pulse chemisorption carried out in Chemisorb 2720 (Micromeritics) instrument under He flow of 30 ml/min at 27 °C. Before analysis, the required amount of sample was taken in U–shape quartz tube and degassed at 150 °C for 1 h in the flow of He gas. The samples were reduced for 1 h at 600 °C in flow of hydrogen–argon mixture. The reduced sample was flushed with He at 200 °C for 1 h to remove any adsorbed hydrogen and then were cooled down to room temperature (27 °C). Then the pulses of CO–He mixture (0.1 ml each) were injected repeatedly until the sample was saturated. The percentage of metal dispersion was calculated by the following equation:

$$d_m\,(\%) = SF \times \frac{VA}{V_{CO}} \times \frac{M_{MW}}{\%M_P} \times 100 \times 100 \qquad (3)$$

Where, d_m *:* dispersion of metal, *VA :* volume adsorbed, V_{CO} *:* molar volume of CO (STP), M_{MW} *:* metal molecular weight, $\%M_P$ *:* percent of metal. For both the metals, the stoichiometry factor (*SF*) of adsorption was considered 1.

3.4 Hydrogen uptake measurement

The hydrogen adsorption–desorption isotherms were recorded using a volumetric device iSorb–HP1–XKRLSPN100 (Make: Quantachrome). About 100 mg of sample was used for each analysis. Initially, the sample was degassed at 200 ^{o}C for 3 h in ultra–vacuum to remove the unwanted adsorbed gas and moisture on the surface. The sample was cooled to 30 °C to start the analysis. The hydrogen adsorption–desorption isotherms were analyzed using high–purity hydrogen (99.999%). The hydrogen uptake capacity was evaluated at different temperatures 25, 0, –10 & –196 °C up to 25 and 30 bar. The temperature was maintained during analysis by an external circulator bath and isothermal liquid nitrogen bath.

The Clausius–Clapeyron equation was used to determine the isosteric heat of adsorption (ΔH_{ads}) by hydrogen uptake data. The ΔH_{ads} of the samples was calculated using isotherm data of three different temperatures (25, 0 & –10 °C). To check the cyclic stability of best samples, the adsorption–desorption cycle was repeated up to 10 times under the same temperature of –196 ^{o}C.

In this study, the hydrogen storage is expressed in terms of weight percent (wt.%). The wt.% storage capacity is defined as the mass of hydrogen adsorbed over the total mass of carbon and adsorbed hydrogen, i.e.: $$wt.\% = \frac{m_{H_2}}{m_{H_2} + m_S} \times 100$$

Where m_{H_2} is the mass of adsorbed hydrogen and m_s is the mass of the sample.

Chapter 4
Results and Discussions

भारतीय प्रौद्योगिकी संस्थान गुवाहाटी
Indian Institute of Technology Guwahati

4. Results and Discussions

4.1 Templated carbon based materials

4.1.1 Templates

Alumina based templates were prepared in the laboratory, using low cost precursors and compared with commercially available zeolite and silica gel templates. All the templates were used for preparation of templated carbons. The physical properties of the templates were characterized by surface area and pore analysis, XRD, FESEM and TEM analysis. The stability of the templates was determined using TGA analysis.

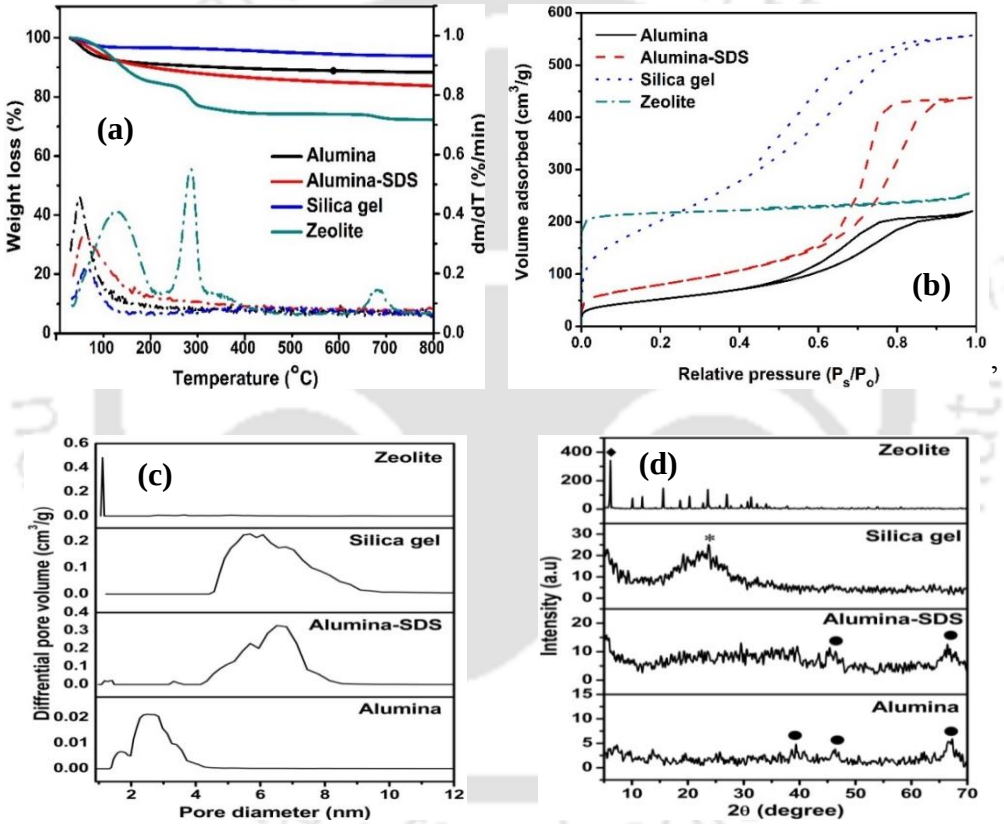

Figure 4.1: Physical properties of the templates (a) TGA curves (b) N_2 adsorption–desorption isotherms (c) Pore size distributions (d) XRD profiles.

During preparation of surfactant modified alumina, the surfactant was added to alumina precursor solution in micelle form by keeping the concentration of surfactant solution well above the critical micelle concentration (CMC) value. On addition of surfactant micelles to aluminum nitrate solution, the Al^{3+} positive ions with higher charge density assembled around negative polar head groups of micelles by replacing of Na^{+} ions as shown in Appendix Figure A1. After addition of NH_4OH solution to mixture, the hydrolysis and condensation reactions

resulted in the formation of $Al(OH)_3$ matrix with surfactant micelles embedded within. On calcination at higher temperature, the surfactant micelles were removed from the hydroxide matrix producing the mesoporous structure.

The TGA analysis was carried out in a nitrogen atmosphere and the profiles are shown in Figure 4.1(a). Weight loss was observed in the temperature range of 30–150 °C for alumina, alumina–SDS and silica gel templates which may be attributed to evaporation of adsorbed moisture present in the template. Thereafter, no further significant weight loss was observed up to 800 °C. Presence of no peak in the range of 550–650 °C suggested that all the incorporated SDS surfactant molecules were removed from the template during calcination at 550 °C. The sulfate group of SDS has been reported to be removed from the alumina matrix in the temperature range of 550–650 °C (Patel et al. 2015). For zeolite template three distinct peaks were observed at 120, 290 and 675 °C which may be assigned respectively to the removal of the absorbed moisture, decomposition of ammonium ions and loss of constitutive water by dehydration of zeolite structure (Su et al. 2005). The weight losses were 16, 9 and 4 % respectively at 120, 290 and 675 °C. The analysis suggested that all the templates had reasonable stability up to 800 °C and can be used as templates for the CVD process.

The nitrogen adsorption–desorption isotherms of the templates are shown in Figure 4.1(b). The presence of significant hysteresis loop for silica gel and surfactant modified alumina–SDS suggested both the materials to be highly mesoporous. The isotherms were of type IV with H2 hysteresis loops for silica gel, alumina and alumina–SDS templates. The H2 type loop is usually attributed to ink–bottle pores having strong interconnectivity. For zeolite, the isotherm was of type I corresponding to a microporous material.

Table 4.1: Physical properties of the templates.

Templates	BET surface area (m^2/g)	Micropore area (m^2/g)	Total pore volume (cm^3/g)	Average pore size (nm)
Alumina (Al)	190	0	0.34	5.7
Alumina–SDS (AlS)	288	16	0.68	7.9
Silica gel (SG)	740	0	0.65	6.3
Zeolite (Z)	697	624	0.37	1.1

Based on the isotherms, the BET surface area, pore volume and average pore size of the templates were calculated and are tabulated in Table 4.1. The surface areas of alumina based templates were low at 190 and 288 m^2/g compared to that of silica gel or zeolite having 740

and 697 m^2/g respectively. For zeolite, 90 % of the total area was micropore area while the remaining three templates were mesoporous.

Figure 4.1(c) shows the pore size distributions of all the templates. The zeolite template showed a very narrow micropore distribution in the range of 1–1.2 nm while the other three templates had broader pore distribution. The alumina template showed pore distribution in the size range of 1.5–4.5 nm. For surfactant modified alumina and commercial silica gel, the mesopores existed between 4–10 nm. The total pore volume and average pore size were highest for surfactant modified alumina template (Table 4.1).

The XRD profiles of the templates are shown in Figure 4.1(d). The alumina and surfactant modified alumina templates had mainly amorphous nature as suggested by the absence of any prominent peaks. The very low intensity peaks observed at 38.6°, 45.7° and 66.8° may be assigned to γ–alumina, while surfactant modified alumina showed peak at 45.7° and 66.8° (Patel et al. 2015). The silica gel also showed amorphous nature with a broad peak at 25° corresponding to its amorphous framework (JCPDF file no.00–029–0085). The zeolite showed several sharp peaks corresponding to its crystalline nature. The highest intensity peak at 6.31° corresponded to (111) planes (Su et al. 2004).

The FESEM images of the different templates are shown in Figure 4.2. Particle morphology was observed for zeolite, while amorphous morphology for other templates. The TEM images of different templates are shown in Figure 4.3. The TEM images also reflected agglomerated nature for all the templates except zeolite for which particle morphology was observed. The silica gel showed a denser structure compared to that of alumina based templates. The morphology of surfactant modified alumina appeared to be more porous than alumina.

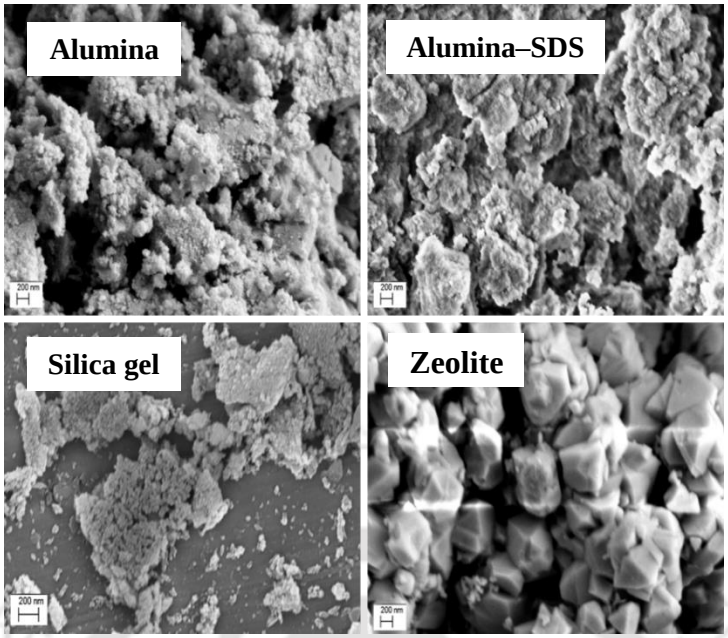

Figure 4.2: FESEM images of the templates.

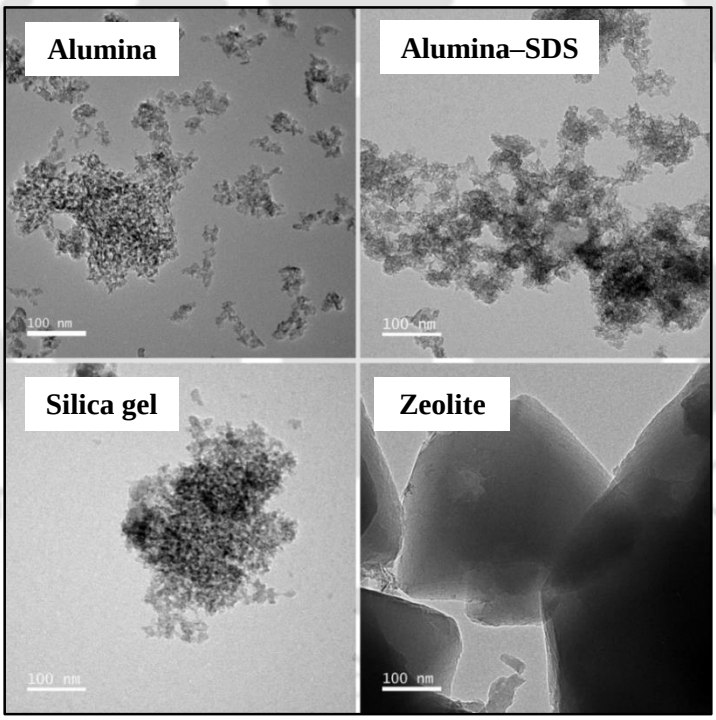

Figure 4.3: TEM images of the templates.

4.1.2 Templated carbons

In this section, the physicochemical and hydrogen storage properties of alumina and surfactant modified alumina templated carbons are discussed and compared with templated carbons prepared from commercially available zeolite and silica gel templates. The hydrogen uptake capacity was measured at –196 °C up to 25 bar for all the samples. The alumina and surfactant modified alumina templated carbons are represented as Al–C and AlS–C, respectively. The zeolite and silica gel templated carbons are represented as Z–C and SG–C, respectively.

The yield of carbon depended on the proper infiltration of carbon precursor into pores of the template. A complete infiltration is expected to give higher carbon yield. The higher average pore size of templates tends to facilitate the infiltration process and results in higher carbon yield. The Table 4.1 shows that the surfactant modified alumina template having highest average pore size (7.9 nm) resulted in the highest yield of templated carbon; this happened in spite of lower surface area of surfactant modified alumina compared to mesoporous silica gel or microporous zeolite. The TGA analysis of template–carbon composite was carried out in the air to estimate the carbon deposited within the template pores.

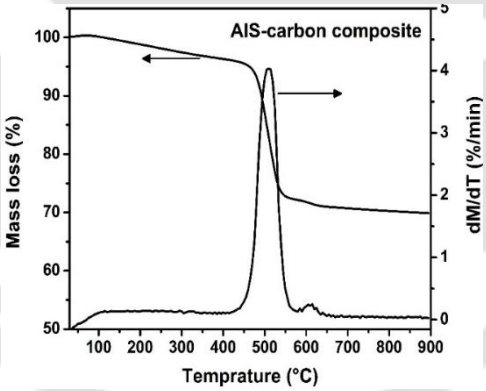

Figure 4.4: TGA profile of surfactant modified alumina template and carbon composite.

From Figure 4.4, about 28.2 % weight loss was observed within a temperature range of 300–900°C for surfactant modified alumina template and carbon composite, which may be attributed to the partial oxidation of carbon. Thus it can be suggested that the 28.2 wt. % carbon was present in the template–carbon composite. This result agreed with the actual carbon yield for surfactant modified alumina template which was about 30 wt.%. This was the highest yield among various templated carbons. The yield of carbon was calculated from the following equation.

$$Carbon\ Yield\ (\%) = \frac{Templated\ Carbon\ Produced\ (\mathrm{wt.})}{Initial\ Template\ Used\ (\mathrm{wt.})} \times 100$$

The surface area and pore properties of the templated carbons were determined using nitrogen adsorption–desorption isotherms measured at –196 °C and shown in Figure 4.5(a). The isotherms of alumina, alumina–SDS and silica gel templated carbons followed the same trend as observed for respective templates.

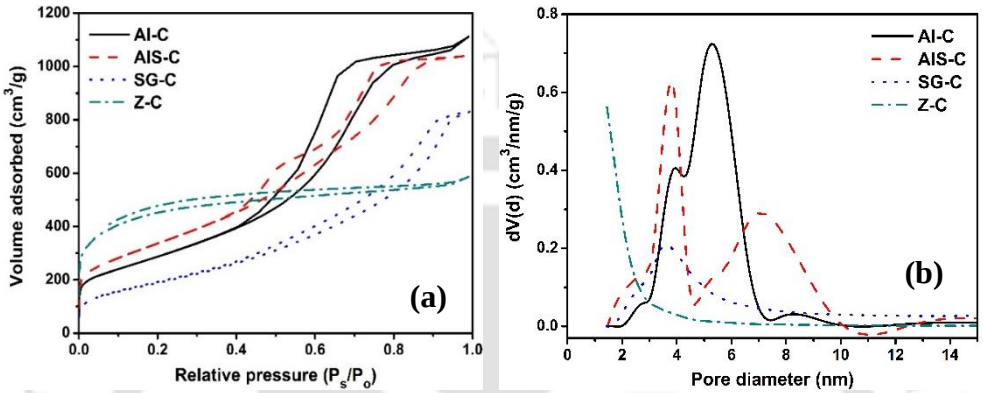

Figure 4.5: (a) N_2 adsorption–desorption isotherms (b) Pore size distributions of the templated carbons.

The isotherm of type IV with H2 type hysteresis loops corresponding to interconnected pores was observed for alumina, alumina–SDS and silica gel templated carbons. Whereas in the case of zeolite templated carbon, it was type I with a hysteresis loop of H4 type corresponding to the presence of narrow slit–shaped pores.

Table 4.2: Physical properties of the templated carbons.

Sample ID	BET surface area (m^2/g)	Micropore area (m^2/g)	Total pore volume (cm^3/g)	Average pore size (nm)	I_D/I_G ratio	Carbon yield (%)
Al–C	1050	77	1.72	4.9	1.02	26
AlS–C	1221	49	1.61	5.4	0.97	30
SG–C	736	0	1.51	4.2	0.93	25
Z–C	1462	525	0.91	1.4	1.01	20

The BET surface area, micropore area, total pore volume and pore size for the templated carbons were calculated from the respective isotherms and are summarized in Table 4.2. The BET surface area of alumina, alumina–SDS, silica gel and zeolite templates were 190, 288, 740, 697 m^2/g, respectively (Table 4.1). Except for silica gel templated carbon, the BET surface area of templated carbons was higher compared to their respective templates. The total pore volume was higher for all the templated carbons with respect to their corresponding templates.

For alumina and alumina–SDS templated carbons, the surface area was significantly enhanced by 81% and 76% compared to their respective templates. The significantly enhanced surface area of mesoporous alumina and alumina–SDS templated carbons suggested that the larger pore size of the templates facilitated incorporation of carbon precursor within the templates pore framework. For zeolite templated carbon, the BET surface area was enhanced only by 52 % with respect to template. The maximum surface area of 1221 m^2/g was obtained for mesoporous alumina–SDS templated carbon and highest pore volume of 1.72 cm^3/g was obtained for alumina templated carbon. The microporous zeolite templated carbon had the surface area and total pore volume of 1462 m^2/g and 0.91 cm^3/g, respectively. The maximum micropore area of 525 m^2/g was observed for zeolite templated carbon. However, for silica gel templated carbon, there was no significant difference between surface area values of the template and derived carbon, suggesting less effective development of the porous carbon structure within template.

The pore size distribution of all the templated carbons is shown in Figure 4.5(b). The pores were observed in the range of 2–10 nm for all the samples except zeolite templated carbon. For zeolite templated carbon, the pore size was observed to be in the range of 1.1–4.5 nm. The alumina and alumina–SDS templated carbons showed trimodal and bimodal pore size distributions, respectively whereas, zeolite and silica gel templated carbons had unimodal pore size distribution. The average pore size order (in nm) was AlS–C (5.4) > Al–C (4.9) > SG–C (4.2) > Z–C (1.4) (Table 4.2).

Figure 4.6(a) depicts the XRD patterns of the templated carbons. The broad diffraction peak at 25° was observed for all the samples. This peak corresponded to the presence of the graphitic plane (002) (Chen et al. 2012). The higher peak intensity was observed for silica gel templated carbon compared to other templated carbons which suggested the formation of higher amount of graphitic carbon zone in the former. The absence of any peaks of template in XRD profiles confirmed complete removal of the templates by HF acid treatment. The complete removal of template was also confirmed by EDX analysis.

The quality and degree of graphitization of templated carbons were determined by Raman spectroscopy and the corresponding spectra are shown in Figure 4.6(b). Two peaks attributed to D–band and G–band, were observed for all the samples. The peak for D–band was observed in between 1340 to 1345 cm^{-1} and that for G–band in between 1590 to 1596 cm^{-1}. The D–band represents the defects or disorder produced in the graphitic structure, whereas G–band appears

due to the in–plane vibration of the graphitic structure (Oh et al. 2013).

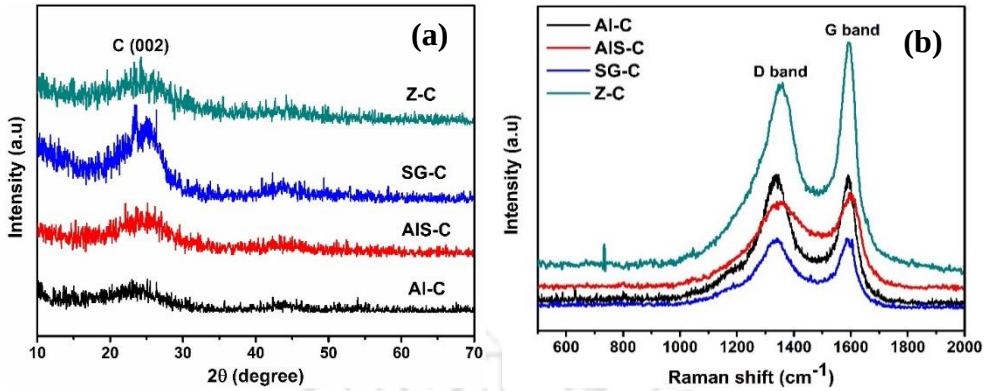

Figure 4.6: (a) XRD profiles (b) Raman spectra of the templated carbons.

The intensity ratios of D and G–band (I_D/I_G), shown in Table 4.2, can be used to represent the degree of graphitization ordering. Lower the value of I_D/I_G ratio, higher is the degree of graphitization (Oh et al. 2013). The lowest intensity ratio (I_D/I_G) of silica gel templated carbon suggested the presence of highest degree of graphitization. The comparison of I_D/I_G ratio of the samples suggested that the mesoporous structure of alumina–SDS and silica gel templated carbons promoted higher extent of graphitization. The results of Raman analysis agreed with the XRD results.

The FESEM images of the templated carbons are shown in Figure 4.7. The morphology of the templated carbons depended on type of template used. The zeolite templated carbon showed regular uniform particle structure similar to the original template, with an average particle size of 422 nm. Alumina and alumina–SDS templated carbons predominantly showed agglomerated tubular/noodle like structure. The average diameter of the tubular/noodle structure of alumina and alumina–SDS templated carbons were 52 and 86 nm, respectively. A dense spherical agglomerate structure appeared for silica gel templated carbon.

The TEM images of the samples are shown in Figure 4.8. Alumina based templated carbons showed tubular/noodle like structure, while silica gel templated carbon showed agglomerated form as was also observed from their FESEM images. For zeolite templated carbon, particle like structure was observed.

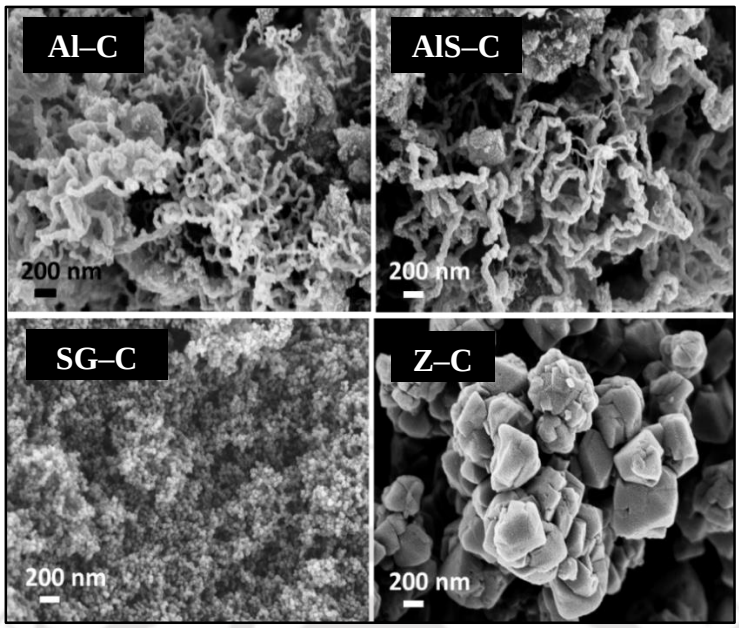

Figure 4.7: FESEM images of the templated carbons.

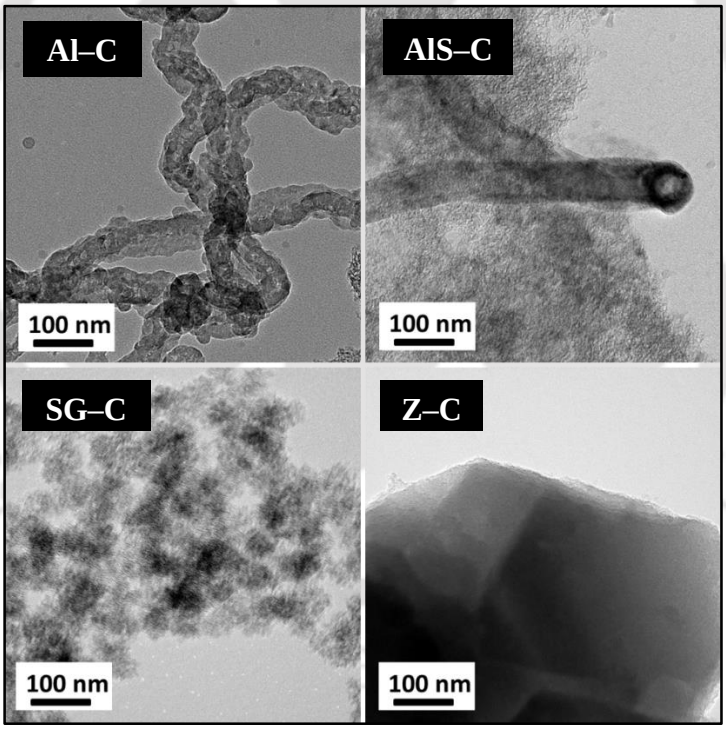

Figure 4.8: TEM images of the templated carbons.

The thermal stability of the templated carbons was investigated in flow of air by TGA. The TGA and DTG profiles of the templated carbons are shown in Figure 4.9(a) and (b), respectively. All the samples displayed around 1–5 % weight loss below 100 °C, which corresponded to the removal of moisture present in the samples. At the temperature range of 460–710 °C, the samples underwent combustion due to oxidative atmosphere. The combustion

temperature varied with the type of templated carbons as can be observed from Figure 4.9(b). The broad peaks were observed at 560, 610, 627 and 630 °C for zeolite, alumina–SDS, alumina and silica gel templated carbons respectively. The higher degree of graphitization for silica gel templated carbon, as confirmed by XRD and Raman analysis, may be the reason for its higher combustion temperature (Lee et al. 2006). Its dense agglomerated structure, as was observed from the microscopic image, may have also contributed to its higher combustion temperature by providing higher diffusional resistance. The comparatively dense tubular morphology of alumina templated carbon might be the reason for its second highest combustion temperature. The lowest combustion temperature and sharper peak in case of the zeolite may have resulted from lower diffusional resistance as it had particle morphology.

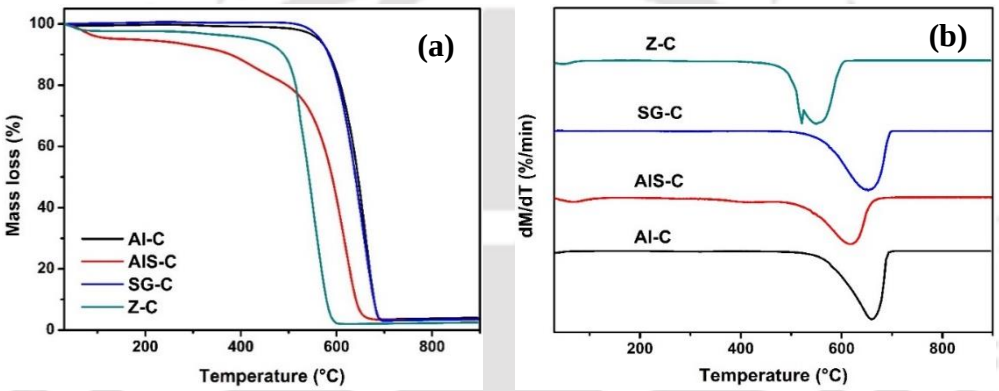

Figure 4.9: Thermal analysis of the templated carbons in flow of air (a) TGA profiles (b) DTG profiles.

The zeolite templated carbons showed a shoulder at 520 °C to the main peak at 560 °C. The presence of two peaks suggested the presence of at least two structural arrangements of slight variation in the zeolite templated carbon. The smaller or agglomerated carbon structures are expected to oxidize more easily compared to more definite and larger particles, and therefore oxidize at lower temperature. Comparison of the areas under the two combustion peaks, suggested higher content of the latter structures. The residue for all the samples was about 1–4 % which also suggested that the carbons were mostly free from the starting templates.

Hydrogen uptake

Hydrogen uptake capacity of templated carbons was measured at –196 °C and 25 bar and the corresponding uptake isotherms are shown in Figure 4.10(a). The hydrogen uptake capacity and density of templated carbons are summarized in Table 4.3. The increasing order of hydrogen uptake capacity, in wt.% , was as follows: SG–C (2.4) < Z–C (2.9) < Al–C (3.46) <

AlS–C (4.3). Except for zeolite templated carbon, the hydrogen uptake capacity increased linearly with increase in the surface area of the templated carbons (Figure 4.10c).

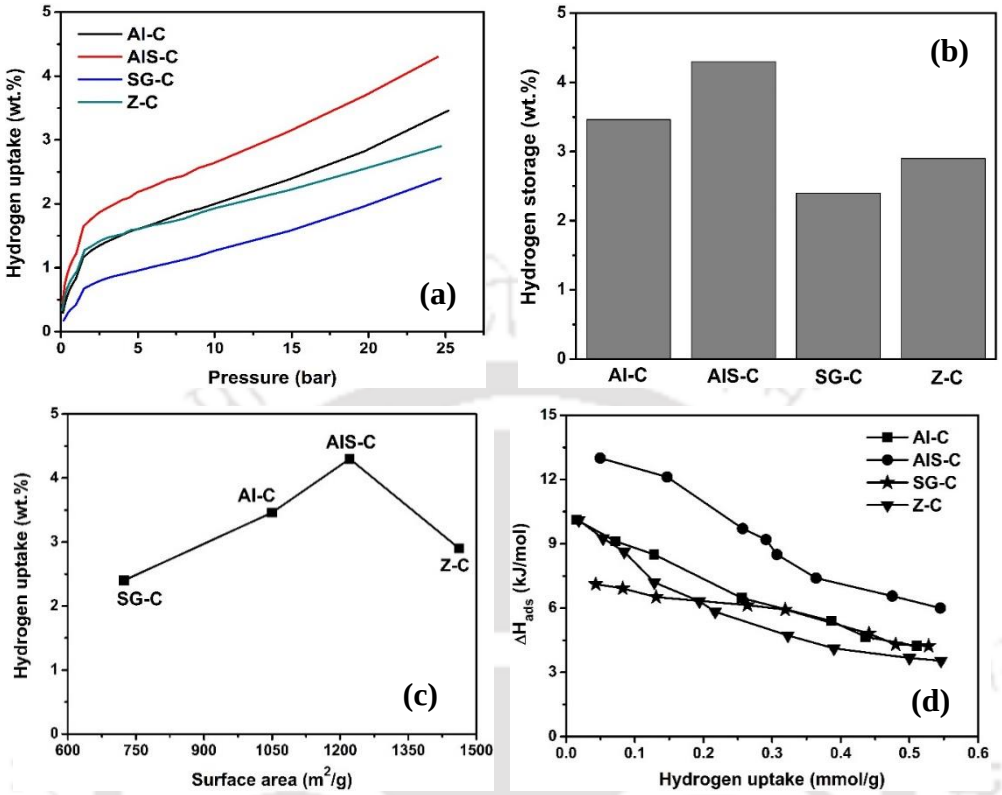

Figure 4.10: For templated carbons (a) Hydrogen uptake isotherms at –196 °C up to 25 bar (b) Hydrogen uptake capacity at –196 °C and 25 bar (c) Relation between hydrogen uptake capacity and surface area of samples (d) Isosteric heats of adsorption as a function of the amount of H_2 adsorbed on samples.

Among mesoporous templated carbons, the higher surface area and pore volume of surfactant modified alumina templated carbon along with higher average pore size may have contributed to its highest hydrogen uptake. The alumina–SDS templated carbon gave the highest hydrogen uptake capacity of 4.3 wt.% at 25 bar in spite of having lower surface area compared to that of zeolite templated carbon.

Table 4.3: Hydrogen uptake capacity and density of the templated carbons at –196 °C.

Sample ID	Hydrogen uptake at 25 bar	
	wt.%	density (μmol/m^2)
Al–C	3.46	19
AlS–C	4.30	21
SG–C	2.40	20
Z–C	2.90	12

In general surface area has been accepted as the major determining factor in hydrogen uptake. Higher the surface area, higher is the hydrogen uptake (Yang et al. 2007). Chahine's rule reported about 1 wt.% hydrogen uptake per 500 m^2/g surface area (Poirier et al. 2001). From the hydrogen uptake values of the samples, it can be observed that all the mesoporous samples showed much higher hydrogen uptake capacity than that predicted by Chahine's rule. Only microporous zeolite templated carbon showed a hydrogen uptake that agreed with the value predicted by Chahine's rule. This higher uptake of the mesoporous templated carbons suggested that apart from surface area other additional factors are also responsible for the hydrogen uptake for these samples. For alumina based templated carbons, the higher pore volume and pore size of the mesoporous structure may have accommodated multilayer adsorption. The tubular structure of alumina based templated carbons may also have contributed to additional hydrogen uptake. Both the outer and inner walls of these tubular structures may have contributed to hydrogen adsorption (Poirier et al. 2004) and thereby enhancing the uptake. The combined effect of all these factors may have contributed to excess hydrogen uptakes for alumina based templated carbons than that predicted by Chahine's rule. For silica gel templated carbon, the structure was mainly agglomerated. No tubular structure was observed. These may have resulted in lowest surface area and hydrogen uptake for silica gel templated carbon. Table 4.3 shows the density of hydrogen uptake, that is hydrogen uptake per unit surface area ($\mu mol/m^2$), was higher and similar for all mesoporous templated carbons (19–21 $\mu mol/m^2$) compared to that observed for microporous zeolite templated carbon (12 $\mu mol/m^2$). The higher pore volume and average pore size of the mesoporous carbon may have contributed to multilayer adsorption and thereby higher uptake per unit area.

The hydrogen uptake studies at –196 °C reported in the literature for different microporous zeolite templated carbon and mesoporous silica gel templated carbons are compared with the results of the present study (Table 4.4). The hydrogen uptake capacity was reported in the range of 3.1–7.0 wt.% for microporous templated carbons, having surface area in between 1833–3591 m^2/g. In this study, microporous zeolite templated carbon showed hydrogen uptake of 2.9 wt.% which is similar to that reported by Guan et al. (2009). They reported 2.9 wt.% hydrogen uptake for microporous templated carbon at pressure of 25 bar having surface area of 2136 m^2/g. Almost similar hydrogen uptake of 2.9 wt.% at 20 bar was also reported by Yang et al. (2006) for zeolite templated carbon with similar surface area of 1307 m^2/g. For higher surface area, higher hydrogen uptake was reported. For mesoporous templated carbons, the hydrogen uptake capacity was reported in the range of 2.2–4.2 wt.%. They have reported surface area in

the range of 749–1995 m^2/g. Compared to these reported results, the mesoporous alumina–SDS templated carbon showed better hydrogen uptake capacity. The silica gel templated carbon showed lower or comparable hydrogen uptake capacity with respect to the reported values.

Table 4.4: Comparison of physical properties and hydrogen uptake capacities for microporous and mesoporous templated carbons of present study with that reported in the literature at –196 °C.

Template	Nature of templated carbon	Surface area (m^2/g)	Pressure (bar)	Hydrogen uptake (wt.%)	References
Zeolite–Y	Microporous	2136	25	2.9	(Guan et al. 2009)
Zeolite–Y	Microporous	1307	20	2.9	(Yang et al. 2006)
Zeolite EMC–2	Microporous	3041	20	7.0	(Masika et al. 2014)
Zeolite–Y	Microporous	3591	20	6.4	(Stadie et al. 2012)
Zeolite–Y	**Microporous**	**1462**	**25**	**2.9**	**Present study**
Silica	Mesoporous	877	20	2.2	(Oh et al. 2013)
Silica	Mesoporous	1995	50	4.2	(Hu et al. 2008)
Silica	Mesoporous	749	73	2.4	(Attia et al. 2013)
Silica gel	**Mesoporous**	**736**	**25**	**2.4**	**Present study**
Alumina–SDS	**Mesoporous**	**1221**	**25**	**4.3**	**Present study**

Isosteric heat of adsorption (ΔH_{ads}) was determined as a function of hydrogen uptake using the Clausius–Clapeyron equation. The calculated ΔH_{ads} for the templated carbons is shown in Figure 4.10(d). It can be seen that the heat of adsorption decreased with increase in hydrogen uptake for all the samples. At lower hydrogen uptake, the heat of adsorption was ~13 kJ/mol for alumina–SDS, ~10.1 kJ/mol for alumina, ~7.1 kJ/mol for silica gel and ~10 kJ/mol for zeolite templated carbons. The ΔH_{ads} decreased to 3.5–6 kJ/mol at higher hydrogen uptake. At the beginning of the adsorption, stronger sites of the heterogeneous surface interacted with the incoming hydrogen molecules resulting in stronger interaction and hence higher heat of adsorption. As surface coverage increased, the stronger sites were gradually consumed by the adsorption process. Hence incoming hydrogen molecules interacted more and more with the available weaker sites resulting in gradual lowering of heat of adsorption with increasing surface coverage. The heat of adsorption values for hydrogen adsorbed on carbons are reported between 3–10 kJ/mol at lower uptake (Alam et al. 2010).

Summary

In this section, hydrogen uptake studies were done on developed mesoporous alumina based templated carbons and compared with that of templated carbons prepared using commercially available microporous zeolite and mesoporous silica gel as templates. Alumina based templates were prepared in the laboratory by precipitation method. The sodium dodecyl sulfate surfactant was used to prepare surfactant modified alumina template. Use of surfactant increased the surface area, pore volume and average pore size of the template. The alumina templated carbon was mainly mesoporous with pores in the range of 2–7 nm with average pore size of 4.9 nm. The surface area was 1050 m^2/g. For surfactant modified alumina, the surface area increased to 1221 m^2/g and average pore size increased to 5.4 nm which agreed with more voidage observed within its agglomerated tubular structure. In comparison, the mesoporous silica gel (736 m^2/g) and microporous zeolite templated carbon (1462 m^2/g) showed spherical agglomerates and particle structure, respectively. The surfactant modified alumina templated carbon gave the highest hydrogen uptake capacity of 4.3 wt.%, in spite of lower surface area than zeolite templated carbon. Higher hydrogen uptake capacity of surfactant modified alumina templated carbon may be attributed to its higher pore volume, highest average pore size and presence of tubular structures. The isosteric heat of adsorption was highest for this templated carbon; 13 kJ/mol at lower hydrogen uptake.

4.1.4 Nitrogen doped templated carbons

In this section, the effect of nitrogen doping on physicochemical properties and hydrogen uptake capacity of alumina based templated carbons were investigated and also compared with that of zeolite and silica gel nitrogen doped templated carbons. The hydrogen uptake capacity of the samples was investigated at –196 °C and 25 bar. The alumina and surfactant modified alumina templated nitrogen doped carbons are represented as Al–N and AlS–N respectively. Z–N and SG–N were used for zeolite and silica gel templated nitrogen doped carbons respectively.

Table 4.5: Elemental analysis of nitrogen doped templated carbons using EDX.

Sample ID	Elements (wt.%)		
	C	N	O
Al–N	79.5	7.2	13.3
AlS–N	77.8	8.1	14.1
SG–N	85.7	6.4	7.9
Z–N	79.9	9.1	11.0

The elemental analysis of nitrogen doped templated carbons was done using EDX (Table 4.5). The nitrogen content in the range of 6.4–9.1 wt.% was obtained. The variation in nitrogen content may also be attributed to different extent of cracking of acetonitrile precursor, which acted as source of both carbon and nitrogen. The Al–N and SG–N approximately showed carbon yield of 26 wt.%, whereas, AlS–N showed 20 wt.% of the corresponding template (Table 4.6). Least yield was shown by microporous zeolite templated carbon, 14 wt.%. The larger pore size and pore volume of mesoporous templated carbons might have resulted in higher yield of carbon by facilitating better infiltration of carbon precursor into template pores during the CVD process.

Figure 4.11(a) shows nitrogen adsorption–desorption isotherms of all the nitrogen doped templated carbons. The isotherms were observed to follow the same pattern as the corresponding templates (Figure 4.1b). For alumina and silica gel based templated carbons, type IV with H2 type hysteresis loops were observed similar to the corresponding templates. The volume of nitrogen adsorption for alumina–SDS templated carbon was significantly higher compared to that of the other carbon samples. For zeolite templated carbon, though the isotherm was of type I but a narrow hysteresis loop tending to H4 type was observed for the carbon. This type of loop corresponds to the presence of narrow slit shape pores. The presence of the hysteresis loop over a wide pressure range for the zeolite templated carbon suggested the

presence of both micropores and mesopores, which is also reflected in pore size distribution (Figure 4.11b). Though for the zeolite template, the pore size distribution was very sharp and narrow, it was broader with multi–nodal nature for corresponding nitrogen doped templated carbon. The presence of mesopores in zeolite templated carbon is probably due to the partial collapse of carbon frameworks during the CVD process.

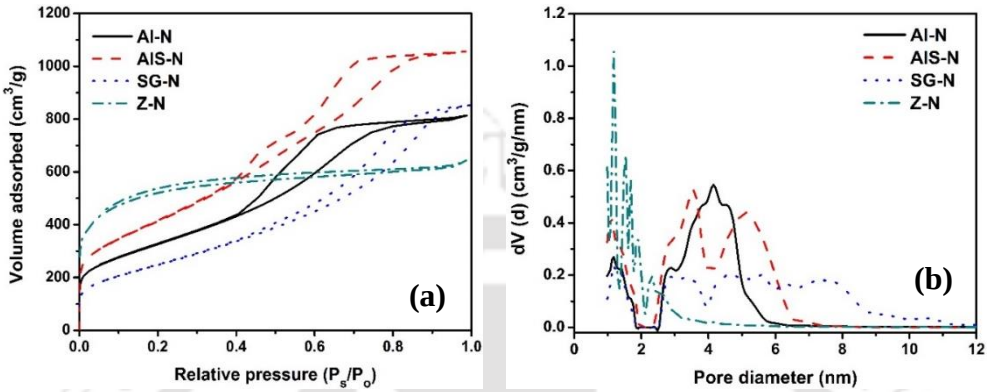

Figure 4.11: (a) N_2 adsorption–desorption isotherms (b) Pore size distributions of nitrogen doped templated carbons.

The BET surface area, pore volume, average pore size and carbon yield of the nitrogen doped templated carbons are shown in Table 4.6. The surface area and total pore volume of nitrogen doped templated carbons was higher with respect to corresponding templates and the enhancement varied with the type of template as was also observed for undoped templated carbons.

Table 4.6: Physical properties of nitrogen doped templated carbons.

Sample ID	BET surface area (m^2/g)	Micropore area (m^2/g)	Total pore volume (cm^3/g)	Average pore size (nm)	I_D/I_G ratio	Carbon yield (%)
Al–N	1171	71	1.26	4.1	0.94	20
AlS–N	1508	49	1.64	3.5	0.99	26
SG–N	908	0	1.32	5.2	0.91	22
Z–N	1664	597	1.00	1.3	1.03	26

For alumina, it was increased by more than 6 times, while it was 5 times increase for surfactant modified alumina template. The amorphous morphology and large pore volume of the alumina based templates may have contributed to the higher yield and porosity of templated carbons by facilitating incorporation of the carbon precursor within the template porous structure. The BET surface area of carbon increased from 1171 to 1508 m^2/g and pore volume from 1.2 to 1.6 cm^3/g when the surfactant modified alumina template was used instead of the only alumina.

Though commercial silica gel was amorphous with higher surface area compared to that of modified alumina based templates, still increase in surface area of corresponding carbon was only 1.2 times that of the template. The denser morphology of silica gel template compared to that of alumina based templates, as observed from TEM images, may have generated more resistance toward incorporation of carbon precursor resulting in generation of less porous carbon. Slightly higher average pore size of the modified alumina template compared to that of silica gel may also have facilitated incorporation of the precursor in the former. For zeolite template, the surface area of corresponding carbon was increased by only 2.4 times compared to that of the template. The crystalline nature, particle morphology, lower pore size and pore volume of the zeolite template may have restricted incorporation of precursor resulting in the observed result. The maximum BET surface area of 1664 m^2/g was achieved for zeolite templated carbon, whereas the highest total pore volume of 1.6 cm^3/g was obtained for alumina–SDS templated carbon. The higher surface area of the zeolite template may have contributed to highest surface area of the corresponding templated carbon. The higher pore volume of surfactant modified alumina templated carbon may have resulted from the mesoporous structure of the corresponding template.

The pore size distribution of the nitrogen doped templated carbons are shown in Figure 4.11(b). They had pore size distribution in the same range as their corresponding templates, with slight shifts depending on the template type. For microporous zeolite templated nitrogen doped carbon, the size distribution shifted to higher size (1–4 nm) compared to less than 2nm sizes for zeolite template. For mesoporous alumina–SDS and silica gel templated carbons, the shift was to slightly lower value (4–9 nm) compared to that of corresponding templates (4–10 nm). The alumina templated carbon had pore size distribution in the same range as the template itself that is less than 4 nm. The total pore volume was enhanced significantly for all nitrogen doped templated carbons as can be compared from Table 4.1 and 4.6. All the synthesized nitrogen doped templated carbons had prominent multinodal pore size distributions particularly that derived from the zeolite.

Compared to undoped templated carbons, the surface area of all the corresponding nitrogen doped templated carbons was higher. However, the pore volume and average pore size were either similar or slightly reduced for nitrogen doped templated carbons. The micropore area of zeolite templated carbons also increased from 525 m^2/g for undoped to 597 m^2/g for nitrogen doped templated carbon. The isotherms and hysteresis loop nature were similar for both unhoped and nitrogen doped templated carbons.

Figure 4.12(a) shows the XRD profiles of different nitrogen doped templated carbons. All the samples exhibited a broad peak at 26° which may be attributed to the diffraction by (002) graphitic plane (Chen et al. 2012). The broad peak of low intensity suggested that the nitrogen doped templated carbons were highly amorphous with small graphitic domains. The higher peak intensity was observed for silica gel templated carbon as compared to that of other carbons, implying a slightly higher degree of graphitization for the former. The absence of any peak of templates suggested complete removal of the templates by HF treatment. The EDX analysis also confirmed complete removal of the templates from the prepared carbons.

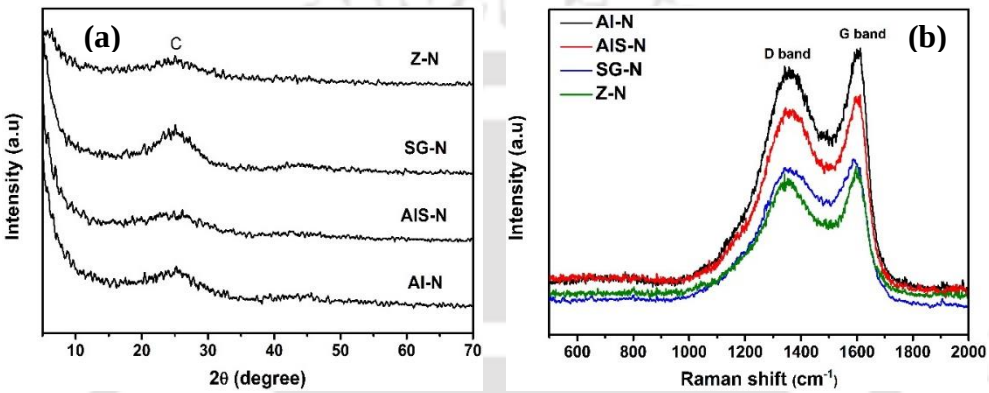

Figure 4.12: (a) XRD profiles (b) Raman spectra of nitrogen doped templated carbons.

Raman spectroscopy was used to evaluate the degree of graphitization and quality of the synthesized nitrogen doped templated carbons. The spectra of the samples are shown in Figure 4.12(b). Two peaks were observed in the range of 500–2000 cm^{-1} for all the doped templated carbons. One peak was located in between 1341–1346 cm^{-1}, which was attributed to the D band. The other peak was observed in the range of 1590–1600 cm^{-1}, corresponding to the G band. The peaks can be related to the disorder in the carbon textures and sp^2–hybridized carbon atoms respectively (Oh et al. 2013). The intensity ratios of D to G band (I_D/I_G) of different templated carbon are shown in Table 4.6. The intensity ratio (I_D/I_G) of all samples was obtained between the range of 0.91 to 1.03. The lowest intensity ratio (I_D/I_G) of 0.91 was observed for silica gel templated carbon, indicating highest degree of graphitization compared to other nitrogen doped templated carbons. These results agreed with the XRD results shown in Figure 4.12(a). The comparison of XRD and Raman spectra of undoped and nitrogen doped templated carbons suggested that the extent of graphitization was enhanced for nitrogen doped carbons. This was observed for the doped carbons prepared from all the templates.

The FESEM images of nitrogen doped templated carbons are shown in Figure 4.13. The morphology of alumina based and silica gel templates was distinctly different from that of the

zeolite template as discussed earlier in section 4.1.1 (Figure 4.2 & 4.3). This difference in morphological nature of templates was also reflected in the corresponding nitrogen doped templated carbons. The nitrogen doped zeolite templated carbon had particle morphology whereas others were mostly agglomerated; type of agglomeration was template dependent. Compared to respective template the morphological change was significant for silica gel and surfactant modified alumina templated carbons compared to that observed for zeolite and alumina templated carbons. The silica gel and surfactant modified alumina templated nitrogen doped carbons appeared to be denser having spherical agglomerates. Silica gel templated carbon appeared to be denser than modified alumina template based carbon which may explain the higher pore volume of the latter. For zeolite templated carbon, the particles were of more uniform hexagonal shape, in size range of 200–600 nm with average particle size of 374 nm.

The morphology of nitrogen doped templated carbons appeared to be different from that of undoped templated carbons when derived from alumina based templates. As discussed earlier in section 4.1.3 (Figure 4.7), the undoped templated carbon had mostly agglomerated tubular structure while nitrogen doped templated carbon was observed to have agglomerated spherical morphology. For silica gel and zeolite templated carbons, the basic morphology of templated carbons was retained on nitrogen doping. The average particle size of zeolite templated nitrogen doped carbon decreased on nitrogen doping.

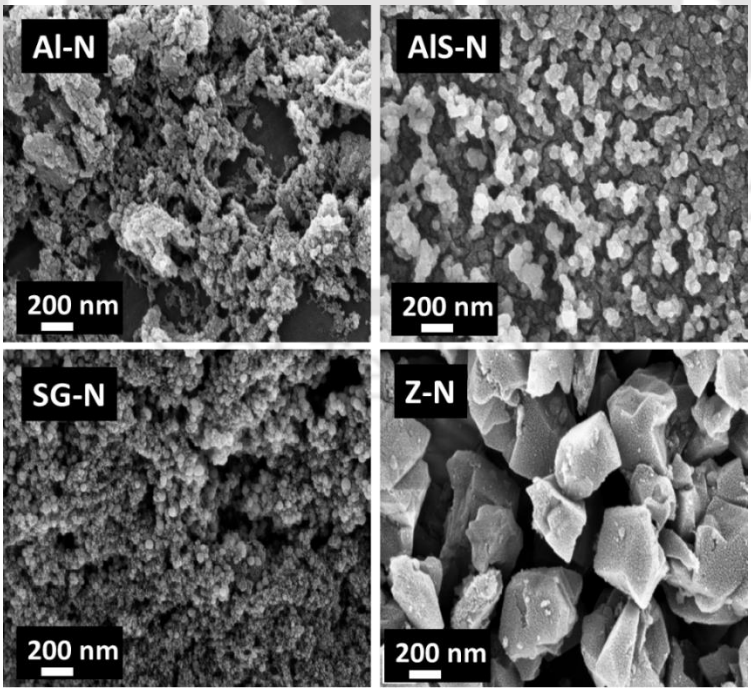

Figure 4.13: FESEM images of nitrogen doped templated carbons.

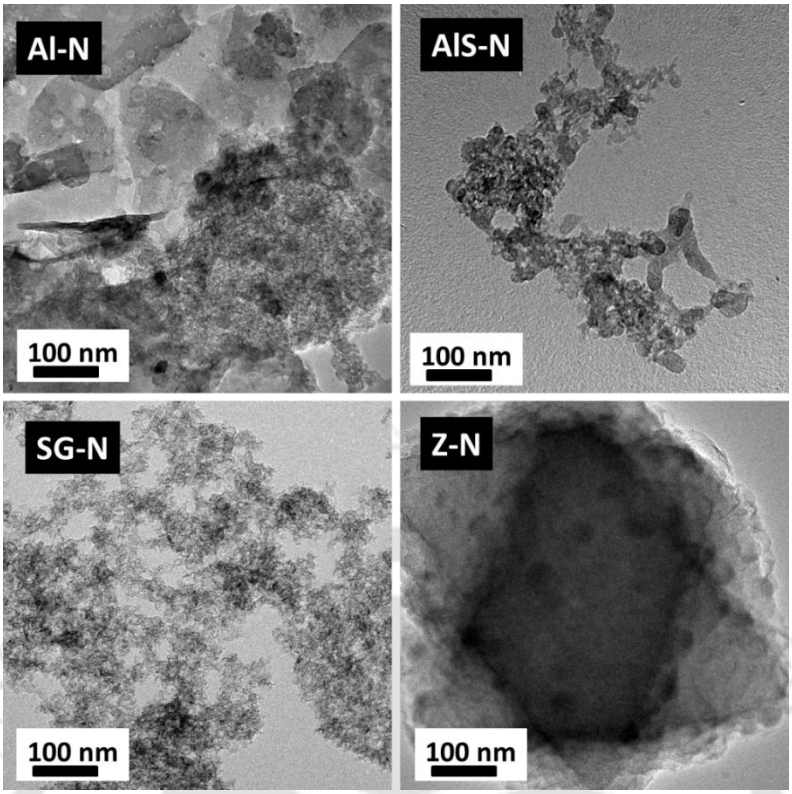

Figure 4.14: TEM images of nitrogen doped templated carbons.

Figure 4.14 shows the TEM images of nitrogen doped templated carbons prepared using different templates. The morphology of the nitrogen doped samples was similar to that observed from FESEM images. Tubular structure was not observed for nitrogen doped alumina based templated carbons (Al–N & AlS–N). This was in contrast to tubular structure obtained corresponding undoped templated carbons (Al–C & AlS–C) (Figure 4.8 and 4.14). The TEM images of silica gel and zeolite templated carbons were also similar for undoped and nitrogen doped templated carbons (Figure 4.8 and 4.14).

Figure 4.15 shows the TGA curves and corresponding differential DTG profiles for the nitrogen doped templated carbons. All the nitrogen doped carbons showed similar profiles with residual weight of about 1–5 %, confirming that the carbons were mostly template free. A small mass loss at ~100 ^{o}C was observed for all samples corresponding to the loss of absorbed moisture. All the mesoporous templated carbons showed weight loss between 470–700 ^{o}C corresponding to the combustion of carbon. The zeolite templated carbon exhibited carbon combustion in the lower temperature range of 415 to 600 °C. The peaks were broader in nature with peak maxima at 540, 600, 605 and 620 ^{o}C for zeolite, surfactant modified alumina, alumina and silica gel nitrogen doped templated carbons respectively. The order of the peaks was similar to that observed for undoped templated carbons (Figure 4.9). For zeolite templated

nitrogen doped carbon, a shoulder at lower temperature appeared with the main peak, same as that observed for the corresponding undoped one.

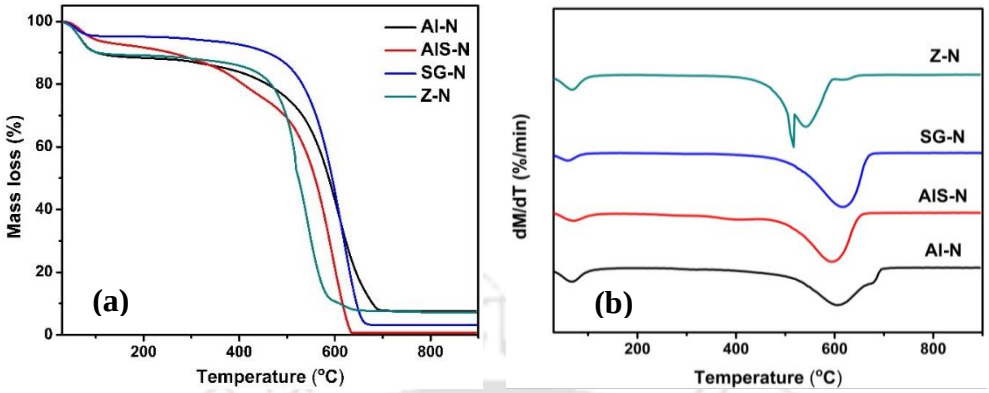

Figure 4.15: Thermal analysis of nitrogen doped templated carbons (a) TGA profiles (b) DTG profiles.

The presence of nitrogen reduced the combustion temperature for all the templated carbons compared to the undoped ones. The presence of nitrogen enhanced the porosity of the templated carbons as observed from increased surface area for all the samples. The enhanced porosity of nitrogen doped samples along with some catalytic effect of nitrogen may have been responsible for lowering the combustion temperature (Kichambare et al. 2011). For the mesoporous carbons with more porosity, the lowering of combustion temperature was relatively less. The degree of graphitization was higher for silica gel templated carbon, as already observed from XRD and Raman analysis, and may be responsible for its highest combustion temperature. Saimilar higher level of graphitization was also observed for undoped silica gel templated carbon. For zeolite templated nitrogen doped carbon again two peaks were observed as in case of corresponding undoped one and the intensity of first peak was higher and sharper than the second peak. As suggested earlier, the lower temperature peak may be associated with the combustion of agglomerated or smaller particles. The high intensity of this low temperature peak suggested relatively higher amount of smaller particles in zeolite templated nitrogen doped carbon. This was established from TEM results. The average particle size of undoped zeolite templated carbon was 422 nm which decreased to 374 nm on nitrogen doping.

Hydrogen uptake

Hydrogen adsorption isotherms of nitrogen doped templated carbons were measured at –196 °C up to 25 bar pressure and are shown in Figure 4.16(a). The corresponding hydrogen uptake capacity and density are summarized in Table 4.7. At 25 bar and –196 °C, the hydrogen uptake

capacity varied between 3.4 to 4.0 wt.% and decreased in the order of Z–N (4.0) > AlS–N (3.9) > Al–N (3.6) > SG–N (3.4).

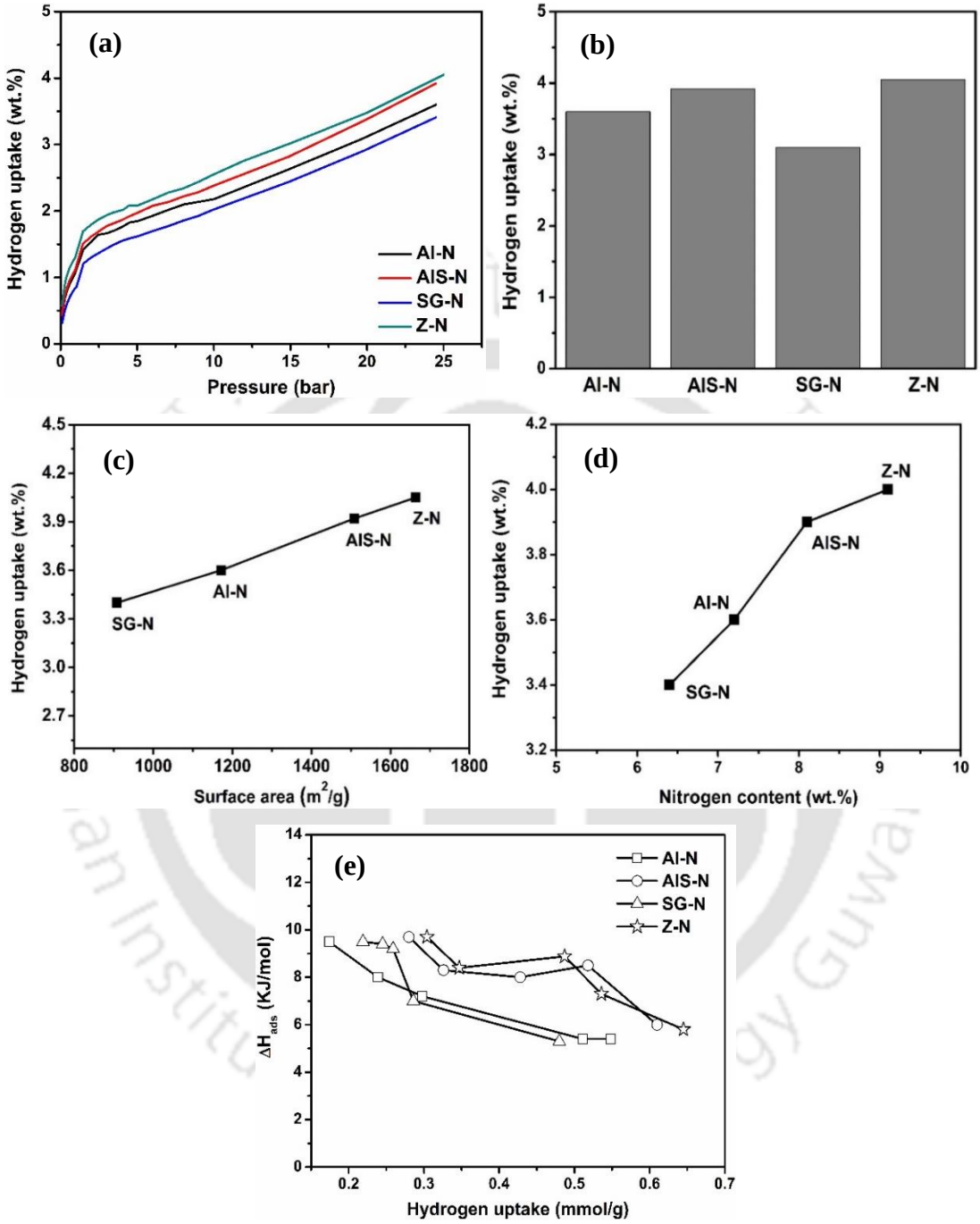

Figure 4.16: For nitrogen doped templated carbons (a) Hydrogen adsorption isotherms at –196 °C up to 25 bar (b) Hydrogen uptake capacity at –196 °C and 25 bar (c) Relation between hydrogen uptake capacity and surface area of samples (d) Hydrogen uptake capacity as function of nitrogen content of samples (e) Isosteric heats of adsorption as a function of amount of adsorbed H_2 on samples.

The hydrogen uptake capacity of the nitrogen doped carbons almost increased linearly with increase in the surface area (Figure 4.16c), which agrees with many studies that reported the

linear relationship of hydrogen uptake with surface area (Sangchoom et al. 2015; Adeniran et al. 2015; Stadie et al. 2012). Hydrogen storage capacity is also related to the pore structure (Xia et al. 2011). For micropores, hydrogen is reported to experience higher force field resulting in stronger interaction and higher uptake. Hence an increase in the fraction of micropore area will further enhance hydrogen uptake. In case of the zeolite templated carbon, the highest surface area and the largest fraction of micropore area may have facilitated hydrogen uptake resulting in the best performance. The silica gel templated carbon showed the lowest hydrogen uptake capacity, which may be due to the lowest surface area. For alumina–SDS templated carbon, second highest hydrogen uptake capacity may be attributed mainly to the pores residing in the range of 2–4 nm. Though the average pore size of alumina–SDS templated carbon (3.5 nm) was higher as compared to that of 1.3 nm for zeolite templated carbon, the larger pore volume of former (1.6 cm^3/g compared to the value of 1.0 cm^3/g for zeolite) may have played a significant role in the hydrogen uptake capacity. The mesoporous structure of alumina–SDS templated carbon may have facilitated multilayer adsorption, thereby enhancing the hydrogen uptake.

The mesoporous carbon materials were observed to have higher uptake density as compared to that of microporous zeolite templated carbon (Table 4.7). This may be correlated with multilayer adsorption in mesoporous carbons as discussed earlier. Higher uptake density was also observed for mesoporous undoped templated carbons.

Table 4.7: Hydrogen uptake capacity of nitrogen doped templated carbons at –196 °C.

Sample ID	Hydrogen uptake at 25 bar	
	wt.%	density (μmol/m^2)
Al–N	3.6	15
AlS–N	3.9	13
SG–N	3.4	18
Z–N	4.0	12

The results of the present study are encouraging in comparison with other reported results of nitrogen doped microporous and mesoporous templated carbon materials at –196 °C (Table 4.8). Alam et al. (2011) reported 3.9 wt.% hydrogen uptake at –196 °C and 20 bar for nitrogen doped microporous templated carbon synthesized from zeolite–Y. Under similar condition, Xia et al. (2007) reported 3.4 wt.% hydrogen uptake for silica based nitrogen doped mesoporous templated carbons.

Table 4.8: Comparison of physical properties and hydrogen uptake capacities at –196 °C for nitrogen doped templated carbons of present study with that reported in the literature.

Template	Nature of templated carbon	Surface area (m^2/g)	Pressure (bar)	Hydrogen uptake (wt.%)	References
Zeolite–Y	Microporous	1825	20	4.5	(Yang et al. 2006)
Zeolite–Y	Microporous	1833	20	3.9	(Alam et al. 2011)
Zeolite–EMC 2	Microporous	3360	20	6.0	(Xia et al. 2011)
Zeolite–Y	**Microporous**	**1664**	**25**	**4.0**	**Present study**
Silica	Mesoporous	942	30	2.8	(Giraudet et al. 2011)
Silica	Mesoporous	1335	30	2.8	(Giraudet et al. 2010)
Silica	Mesoporous	1173	20	3.4	(Xia et al. 2007)
Alumina–SDS	**Mesoporous**	**1508**	**25**	**3.9**	**Present study**

The results of the present study are better or comparable to reported hydrogen uptake values for nitrogen doped microporous and mesoporous templated carbons at –196 °C, as can be observed from Table 4.8. The hydrogen uptake of nitrogen doped mesoporous carbon prepared in this study is much higher than that of the reported ones at similar adsorption conditions. The higher value may be attributed to higher surface area and pore volume.

The positive effect of nitrogen doping on hydrogen uptake can be observed in Figure 4.16(d). The hydrogen uptake of samples increased with increase in nitrogen content. The presence of nitrogen in the carbon matrix is reported to activate dissociation of hydrogen favoring its uptake (Xia et al. 2011). The higher amount of nitrogen in the carbon framework strongly activates the absorbent surface towards hydrogen promoting its adsorption. Any element with higher reduction potential is expected to have more reactivity towards hydrogen and thereby sites containing these elements are expected to contribute positively towards hydrogen storage. The higher reduction potential of nitrogen (0.057 V) compared to that of carbon (–0.132 V) may have facilitated activation of hydrogen molecules on the nitrogen doped surface resulting in higher uptake (Konwar et al. 2016; Viswanathan et al. 2003). The higher value of hydrogen uptake for all the nitrogen doped samples with respect to Chahine's rule can be attributed to the presence of nitrogen on the surface facilitating hydrogen uptake as discussed above.

With respect to undoped templated carbons, the surface area of respective nitrogen doped samples was enhanced. Increased surface area, porosity and presence of nitrogen enhanced the hydrogen uptake of all the nitrogen doped carbons with respect to undoped ones except that of surfactant modified alumina templated carbon. The slight decrease in the hydrogen uptake

values from 4.3 to 3.9 wt.% on nitrogen doping for the surfactant modified alumina templated carbon may be attributed to significant modification of the morphology for alumina based templated carbon from agglomerated tubular to agglomerated spherical structure. The extensive tubular structure may have contributed to slightly higher hydrogen uptake for the undoped surfactant modified alumina templated carbon.

The isosteric heat of H_2 adsorption for nitrogen doped templated carbons are shown in Figure 4.16(e). The heats of adsorption of the samples were determined using the Clausius–Clapeyron equation. The isosteric heats of adsorption at lower H_2 uptake on the nitrogen doped carbons were between 9.5–9.7 kJ/mol; thereafter decreased at higher adsorption to ~5 kJ/mol. As coverage increased, adsorption occurred on comparatively weaker sites on carbon surface and consequently, the heat of adsorption decreased. In literature, the heats of adsorption for hydrogen molecules on carbons are reported between 3–10 kJ/mol (Alam et al. 2010).

Summary

Alumina and surfactant modified alumina were used as templates for preparation of nitrogen doped templated carbons using the CVD process and acetonitrile as the precursor. The properties and hydrogen uptake capacities were compared with that of silica gel and zeolite templated nitrogen doped carbons. For alumina based doped templated carbons, 5 to 6 times higher surface area was obtained compared to the corresponding templates while that for zeolite and silica gel templated doped carbons, it was only 1–2 times higher. The use of nitrogen dopant increased the surface area for all the nitrogen doped carbon compared to respective undoped one. With respect to undoped templated carbons the hydrogen uptake of all the nitrogen doped carbons was enhanced except that of surfactant modified alumina templated carbon. The slight decrease for the latter may be attributed to significant modification of its morphology in presence of nitrogen. The surfactant modified alumina templated doped carbon had pores in the same range as that of silica gel templated carbon (4–9 nm) while alumina templated carbon had pores less than 4 nm similar to that of zeolite. The highest degree of graphitization was observed for silica gel templated carbon from XRD as well as Raman analysis. The FESEM analysis showed particle morphology for zeolite templated nitrogen doped with average particle size of 374 nm. The silica gel and both the alumina based nitrogen doped templated carbons showed spherical agglomerates. At 25 bar and –196 °C, the hydrogen uptake capacity varied between 3.4 to 4.0 wt.% and decreased in the order of Z–N (4.0) > AlS–N (3.9) > Al–N (3.6) > SG–N (3.4). The surface area of nitrogen doped templated carbons were

in the range of 908–1664 m^2/g and hydrogen uptake capacity almost increased linearly with increase in the surface area. The hydrogen uptake also increased with increasing nitrogen content of the sample. The maximum hydrogen uptake capacity of 4.0 wt.% was obtained for microporous zeolite templated carbon having both the highest surface area and nitrogen content. For mesoporous templated carbons, the alumina–SDS templated carbon had the highest hydrogen uptake capacity of 3.9 wt.% having the highest surface area and nitrogen content among the mesoporous carbons.

4.1.5 Platinum doped templated carbons

In this section platinum doped templated carbons, prepared from different templates (alumina, alumina–SDS, silica gel & zeolite) by CVD process using cyclohexane as precursor, are discussed. The platinum was incorporated in all the templates in equal amount before subjecting them to CVD process. The physicochemical and hydrogen uptake properties of alumina based platinum doped templated carbons (Pt/Al–C, Pt/AlS–C) were compared with that of silica gel and zeolite templated platinum doped carbons (Pt/SG–C, Pt/Z–C).

The elemental composition of platinum doped templated carbons determined by EDX analysis is summarized in Table 4.9. The platinum content was found to be in the range of 1.8 to 2.1 wt.%, in spite of the fact that equal amount of platinum (0.0045 mg Pt/g of the template) was impregnated into all the templates before carrying out the vapor deposition. The corresponding EDX spectra are added in Appendix Figure B1. The slight variation in the platinum loading was caused by difference in the final yield of the carbons. The yield varied in the range of 28 to 32 wt.%. The higher carbon yield of 32 wt.% for Pt/Al–C and Pt/SG–C samples resulted in lower values of 1.8 wt.% Pt loading as can be observed from the comparison of values of yield (Table 4.10) and platinum wt.% loading (Table 4.9). The variation in carbon yield may be attributed to different extent of cracking of precursor depending on the template type. Higher extent of cracking of precursor is expected to result in higher carbon yield. Presence of 3–6 wt.% oxygen was observed in all the samples.

Table 4.9: Elemental analysis of platinum doped templated carbons using EDX.

Sample ID	Elements (wt.%)		
	Pt	C	O
Pt/Al–C	1.8	92.8	5.4
Pt/AlS–C	2.1	94.9	3.0
Pt/SG–C	1.8	92.2	6.0
Pt/Z–C	2.0	95.0	3.0

The adsorption–desorption isotherms of the platinum doped templated carbons are shown in Figure 4.17(a). The nature of isotherm and hysteresis loop of platinum doped templated carbons were similar to that of corresponding undoped ones. The volume of adsorbed nitrogen was observed to decrease on platinum doping. The reduction of volume depended on the type of template. The maximum reduction in the volume of nitrogen adsorbed was observed for platinum doped silica gel templated carbon.

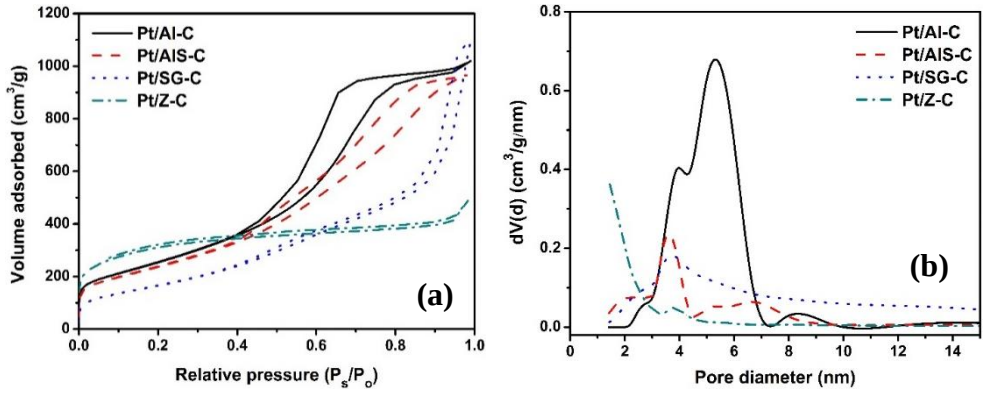

Figure 4.17: (a) N_2 adsorption–desorption isotherms (b) Pore size distributions of platinum doped templated carbons synthesized using different templates.

The BET surface area, micropore area, total pore volume, average pore size and the carbon yield of platinum doped templated carbons are tabulated in Table 4.10. All the samples showed decrease in surface area and pore volume on platinum doping and the extent of reduction depended on the type of template. The highest reduction in surface area was observed for zeolite templated platinum doped carbon compared to that of the other doped samples. The surface area decreased from 1462 to 1023 m^2/g. For platinum doped mesoporous silica, alumina and alumina–SDS templated carbons, the surface areas were decreased to 620, 935 and 870 m^2/g from 736, 1050 and 1221 m^2/g of respective undoped carbons. The maximum decrease in pore volume (15 %) was also observed for zeolite templated platinum doped carbon. The reduction in surface area and pore volume may have been caused by the partial blockage of pores by platinum clusters. As was also observed for undoped templated carbons, the zeolite templated platinum doped carbon showed the highest micropore area. However, the micropore area dropped significantly from 525 m^2/g for undoped carbon to 301 m^2/g for platinum doped carbon.

The pore size distribution of platinum doped templated carbons is shown in Figure 4.17(b). Pores were exhibited in the range of 1.2–10 nm except for silica gel templated platinum doped templated carbon which showed a broader pore size distribution between 1.2–15 nm. The silica gel and zeolite templated platinum doped carbons showed bimodal pore size distributions. Whereas, alumina based platinum doped templated carbons showed multimodal pore size distributions. The platinum doping resulted in decrease in the pore volumes compared to corresponding undoped carbons as can be observed from Table 4.2 and 4.10. As explained earlier, the decrease in pore volume may be attributed to partial blockages of carbons

framework by platinum clusters. The average pore size of the platinum doped samples was obtained in the range of 1.5–5.3 nm.

Table 4.10: Physical properties of platinum doped templated carbons.

Sample ID	BET surface area (m^2/g)	Micropore area (m^2/g)	Total pore volume (cm^3/g)	Average pore size (nm)	I_D/I_G ratio	Carbon Yield (%)
Pt/Al–C	935	55	1.58	5.3	0.97	32
Pt/AlS–C	870	47	1.50	4.0	0.96	28
Pt/SG–C	620	0	1.42	3.7	0.92	32
Pt/Z–C	1023	301	0.77	1.5	0.99	30

Figure 4.18(a) shows the XRD profiles of the platinum doped templated carbons. The graphitic carbon peak (002) was observed in the range of 24.6°–25.75° for the samples. The graphitic nature of the templated carbons was affected with addition of platinum as compared to that of undoped templated carbons. The increase in graphitic nature was observed for all the samples. Tang et al. (2013) also reported increase of the graphitic nature of mesoporous carbons with doping of platinum. The peak intensity of silica gel templated platinum doped carbon was slightly higher than that of other samples, corresponding to the higher order of graphitic carbon present in the sample. Higher graphitic nature was also observed for silica gel templated undoped and nitrogen doped carbons. Three peaks of platinum were observed at 39.9°, 46.3° and 67.6° in alumina, alumina–SDS and silica gel carbons corresponding to lattice planes of Pt (111), Pt (200) and Pt (220) respectively (Oh et al. 2013). The zeolite templated carbon showed only two platinum peaks at 39.9° and 46.3°. Sharper and higher intensity peak at 39.9° of platinum was observed for alumina–SDS templated platinum doped carbon compared to that of other doped samples. The average crystallite size of the platinum was estimated by the Debye–Scherrer formula using the platinum peak at 39.9°. It was 9, 10, 25, 27 nm for zeolite, silica gel, alumina and alumina–SDS templated platinum doped carbons respectively. The value of average platinum crystal size was almost equal for zeolite and silica templated platinum doped carbons.

Figure 4.18(b) shows the Raman spectra of platinum doped templated carbons. The peaks were observed at 1341–1350 cm^{-1} for D–band and 1590–1600 cm^{-1} for G–band. The calculated intensity ratio (I_D/I_G) were 0.97, 0.96, 0.92 and 0.99 for alumina, alumina–SDS, silica gel and zeolite platinum doped templated carbons respectively. As was observed for undoped and nitrogen doped carbons, the silica gel templated carbon had the lowest I_D/I_G ratio value

corresponding to highest degree of graphitization. This result was in good agreement with the observation from XRD profiles.

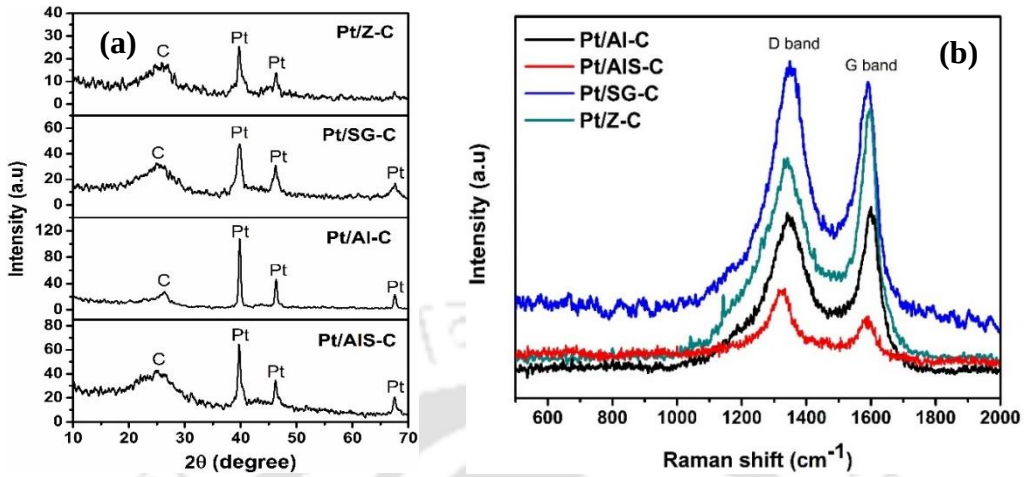

Figure 4.18: (a) XRD profiles (b) Raman spectra of platinum doped templated carbons.

TGA and DTG profiles of platinum doped templated carbons recorded in flow of air are shown in Figure 4.19(a) and (b), respectively. The samples were mostly oxidized as the temperature reached 700 °C. The residual weight of about 1–4 % was observed which may be accommodated by the presence of platinum as well as residual templates, if any. In comparison to the undoped templated carbons, the combustion peaks of platinum doped templated carbons were shifted to lower temperature range. The peak was shifted to the range of 400–675 °C for platinum doped carbons from 460–710 °C for undoped ones. This shift may be attributed to the presence of platinum which may have catalytic effect on the oxidation of the carbon matrix. Similar observation have been also reported by Su et al. (2009).

Maxima of the peak was observed at 440, 545, 550 and 615 °C for alumina, surfactant modified alumina, zeolite and silica gel templated platinum doped carbons respectively. However, the alumina templated platinum doped carbon showed a sharper peak at lower combustion temperature range of 400–580 °C compared to that of other doped samples. The silica gel templated platinum doped carbon showed the highest combustion temperature range of 490–615 °C. The higher level of graphitization for silica gel templated platinum doped carbon might be the reason for its higher combustion temperature. Multiple peaks were observed for all the samples, except silica gel templated platinum doped carbon, suggesting the presence of different structured entity of carbon matrix that were oxidized at slightly different temperatures.

Presence of at least two types of structures can be predicted corresponding to the two main peaks of the profiles.

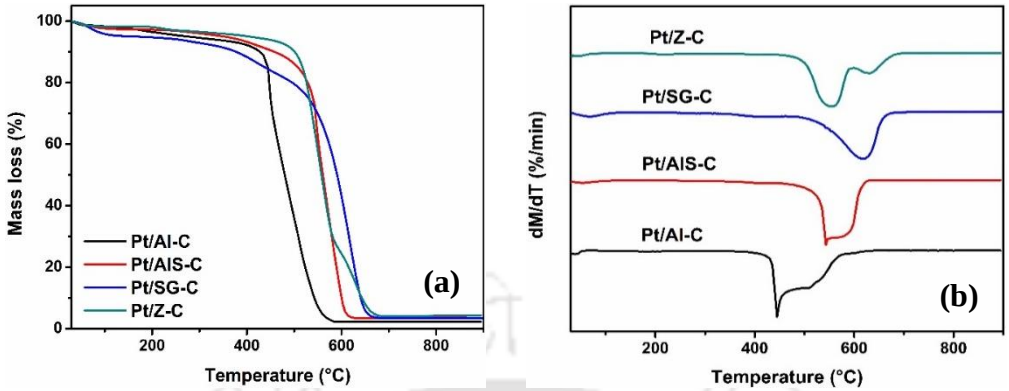

Figure 4.19: Thermal analysis of platinum doped templated carbons (a) TGA profiles (b) DTG profiles.

Figure 4.20 shows the FESEM morphology of platinum doped templated carbons. The alumina and alumina–SDS templated platinum doped carbons showed distinct ribbon like structure without any agglomerates. This is in variation to corresponding undoped templated carbons which showed agglomerated tubular/noodle like structure. The width of ribbon was higher than the corresponding tubular diameter of the undoped one. The ribbon width was 73 nm for alumina templated doped carbon compared to 52 nm for tubular diameter of undoped carbon. The ribbon width was 124 nm for alumina–SDS templated doped carbon compared to 86 nm tubular diameter for undoped carbon. For both silica gel and zeolite templated carbons, the presence of platinum did not affect the morphology of templated carbons compared to the respective undoped ones. The silica gel templated platinum doped carbon showed similar agglomerated morphology as observed for the corresponding undoped one. Both platinum doped and undoped zeolite templated carbons had uniform hexagonal particle structure. The average particle size of platinum doped zeolite carbon was 746 nm.

Figure 4.21 shows the TEM images of platinum doped templated carbons. Alumina based templated platinum doped carbons showed flat ribbon like morphology which was also observed in FESEM images. The dense agglomerates were observed for the silica gel platinum doped templated carbon, while, zeolite templated platinum doped carbon showed particle morphology. The average size of platinum clusters calculated from TEM images for alumina–SDS, alumina, zeolite and silica gel templated platinum doped carbons were 3.4, 3.0, 2.8 and 2.6 nm respectively (Table 4.11). The distribution of platinum on templated carbons was

further confirmed by EDX mapping and the corresponding Figures are included in Appendix C1.

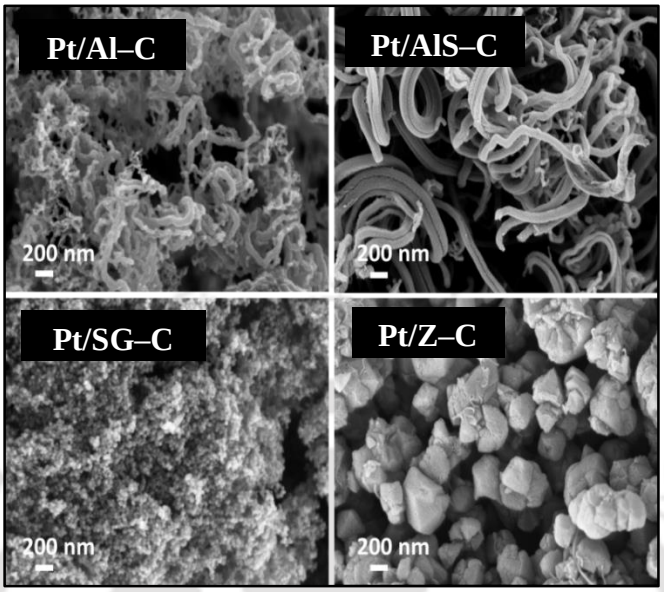

Figure 4.20: FESEM images of platinum doped templated carbons.

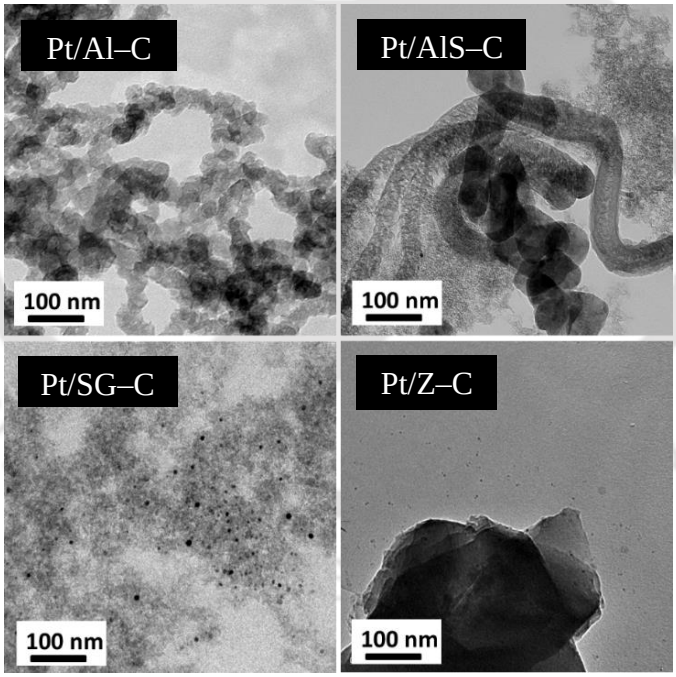

Figure 4.21: TEM images of platinum doped templated carbons.

The corresponding dispersion of platinum determined by CO–Chemisorption follows the same trend as Pt/AlS–C (28) < Pt/Al–C (30) < Pt/SG–C (33) < Pt/Z–C (35) (Table 4.11).

Table 4.11: Average metal cluster size and metal dispersion for platinum doped templated carbons.

Sample ID	Average particle size (nm)	Pt Dispersion (%)
	TEM	
Pt/Al–C	3.0	30
Pt/AlS–C	3.4	28
Pt/SG–C	2.8	33
Pt/Z–C	2.6	35

Hydrogen uptake

Figure 4.22(a) shows the hydrogen adsorption isotherms of the platinum doped templated carbons. The hydrogen uptake capacity of the samples was determined at –196 °C up to 25 bar. The hydrogen uptake capacity and density of the samples are included in Table 4.12. The effect of platinum doping on hydrogen uptake capacity of templated carbon depended on type of template used. For silica gel and zeolite templated platinum doped carbons, the hydrogen uptake capacity was enhanced. The hydrogen uptake capacity was reduced from 4.3 wt.% for undoped to 3.28 wt.% for alumina–SDS templated platinum doped carbon. In the case of alumina templated platinum doped carbon, the hydrogen uptake capacity was not affected after platinum doping.

Table 4.12: Hydrogen uptake capacity of platinum doped templated carbons at –196 °C.

Sample ID	Hydrogen uptake at 25 bar	
	wt.%	density (μmol/m^2)
Pt/Al–C	3.42	21
Pt/AlS–C	3.28	22
Pt/SG–C	2.94	26
Pt/Z–C	3.90	21

The order of hydrogen uptake (in wt.%) was Pt/Z–C (3.9) > Pt/Al–C (3.42) > Pt/AlS–C (3.28) > Pt/SG–C (2.94). Highest surface area, micropore area and dispersion of platinum for zeolite templated platinum doped carbon resulted in a positive synergistic effect giving the highest hydrogen uptake. The second highest hydrogen uptake for alumina templated platinum doped carbon was attributed to highest pore volume (1.58 cm^3/g) and second highest surface area (935 m^2/g). For alumina–SDS templated platinum doped carbon, the hydrogen uptake was decreased due to the significant blockage of pores by large platinum particles (lowest dispersion) (Figure 4.17b and Table 4.11). The blockage was also confirmed by the decrease in its average pore

size from 5.4 for undoped carbon to 4.0 nm for metal doped one (Tables 4.2 & 4.9). Figure 4.22(c) shows that the hydrogen storage increased with increase in surface area of the samples.

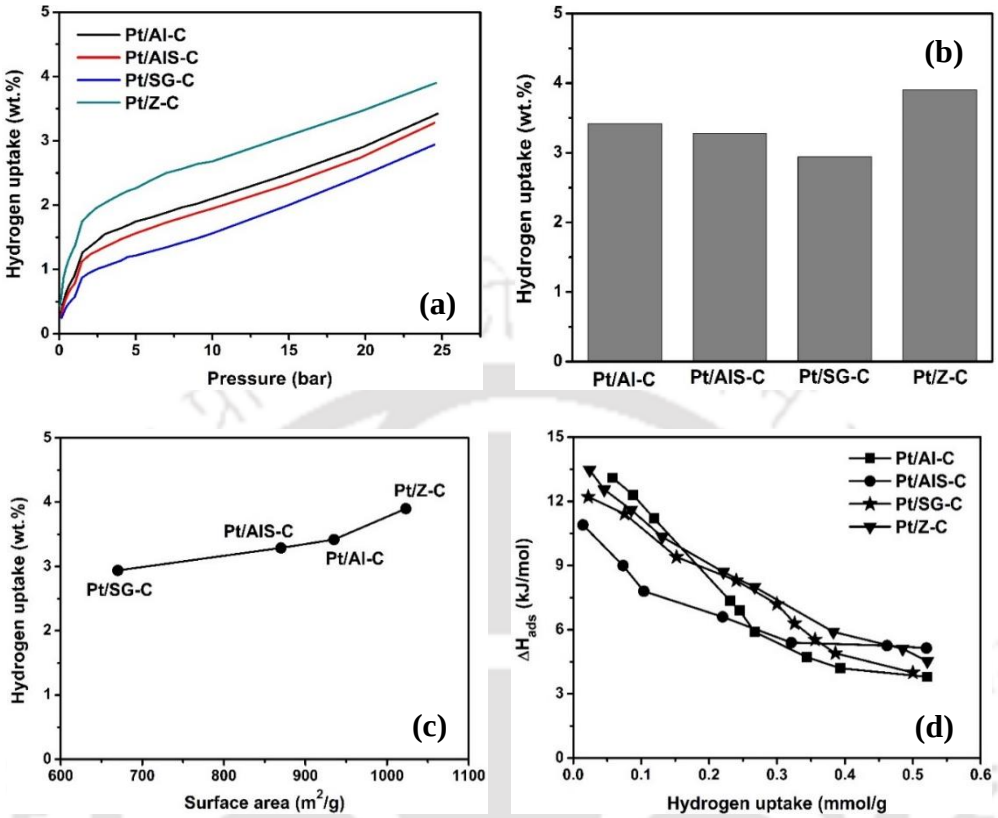

Figure 4.22: For platinum doped templated carbons (a) Hydrogen adsorption isotherms at –196 °C up to 25 bar (b) Hydrogen uptake at –196 °C and 25 bar (c) Relation between hydrogen uptake capacity and surface area (d) Isosteric heats of adsorption as a function of the amount of H_2 adsorbed.

The hydrogen uptake density of the samples was in between 21–26 µmol/m^2 as shown in Table 4.12. On platinum doping, the hydrogen uptake density enhanced as compared to that of respective undoped carbons. The mesoporous platinum doped templated carbons still gave a slightly higher density compared to microporous zeolite templated platinum doped carbon. The tendency to give similar hydrogen uptake density values suggested that the contribution of dispersed metal was more responsible for interaction with hydrogen. Similar metal loading and dispersion values resulted in lower variation in hydrogen storage properties. The results of the present study are better as compared to the reported hydrogen uptake capacity for platinum doped microporous and mesoporous carbons, as shown in Table 4.13. For microporous zeolite templated platinum doped carbon, no study was obtained at –196 °C. Hence in Table 4.13, the hydrogen uptake at room temperature is included for comparison.

Table 4.13: Comparison of physical properties and hydrogen uptake capacities for platinum doped templated carbons of present study with that reported in the literature.

Template	Nature of templated carbon	Surface area (m^2/g)	Temperature (°C)	Pressure (bar)	Hydrogen uptake (wt.%)	References
Pt/zeolite	Microporous	2755	25	100	2.2	(Lachawiec et al. 2008)
Pt/zeolite–Y	**Microporous**	**1023**	**–196**	**25**	**4.4**	**Present study**
Pt/silica	Mesoporous	882	–196	20	2.2	(Oh et al. 2013)
Pt/silica	Mesoporous	712	–196	18	1.1	(Campesi et al. 2008)
Pt/silica gel	**Mesoporous**	**620**	**–196**	**25**	**3.5**	**Present study**
Pt/alumina–SDS	**Mesoporous**	**870**	**–196**	**25**	**3.8**	**Present study**

Isosteric heat of adsorption (ΔQ_{ads}) was determined using the Clausius–Clapeyron equation and plotted as a function of hydrogen uptake. The heat of adsorption decreased with increasing hydrogen uptake for all the samples (Figure 4.22d). At lower hydrogen uptake, the heat of adsorption was in the range of 10.9–13.5 kJ/mol whereas, at higher hydrogen uptake, it was in between 3.8–5.14 kJ/mol. On doping of platinum, the heat of adsorption of the doped templated carbons was significantly increased compared to that of undoped ones except for surfactant modified alumina templated platinum doped carbon. It was enhanced from 10 to 12 kJ/mol for alumina, 7 to 12 kJ/mol for silica and 10 to 13.5 kJ/mol for zeolite templated platinum doped carbons. The highest heat of adsorption was ~13.5 kJ/mol for zeolite templated platinum doped carbon. Lowest metal dispersion for surfactant modified alumina templated platinum doped carbon might have resulted in lower interaction and lower heat of adsorption. The heat of adsorption values obtained in this study resided within the range of the reported heat of adsorption values for platinum doped carbon (9.0– 23.1 kJ/mol) (Alam et al. 2011; Li et al. 2007)

Summary

This section discussed and compared the platinum doped templated carbons prepared from mesoporous alumina, surfactant modified alumina and silica gel templates and microporous zeolite template. Equal amount of platinum was incorporated by impregnation method in all the templates before subjecting to CVD process. The drop in surface area and pore volume was observed with respect to undoped carbon after platinum doping for all the samples. The maximum surface area of 1023 m^2/g and pore volume of 1.58 cm^3/g were obtained zeolite and alumina templated for platinum doped carbons, respectively. A flat ribbon like structure was observed for platinum doped alumina and alumina–SDS templated carbons. The average metal cluster size was 2.6, 2.8, 3, 3.4 nm for zeolite, silica gel, alumina and alumina–SDS templated

carbons respectively. This order agreed with the dispersion results obtained from XRD and CO–Chemisorption analysis. The hydrogen uptake capacity of all the samples was exhibited in the range of 2.94–3.90 wt.% at –196 °C and 25 bar. The highest hydrogen uptake of 3.90 wt.% was obtained for zeolite templated platinum doped carbon. This highest uptake capacity may have resulted from the highest surface area, micropore area and dispersed platinum for zeolite templated platinum doped carbon. The platinum provided additional active sites for hydrogen adsorption. For metal doped carbons, it was observed that dispersed metal played the prominent role in hydrogen uptake and resulted in mostly similar hydrogen uptake density. Platinum doping resulted in the heat of adsorption up to ~13.5 kJ/mol for zeolite templated carbon.

4.1.6 Platinum and nitrogen co–doped templated carbons

In this section, physicochemical and hydrogen storage properties of platinum and nitrogen co–doped templated carbons, prepared using mesoporous and microporous templates, are discussed. The synergistic effect of non–metal and metal dopants on the properties of the templated carbons, is the subject of investigation here. The platinum and nitrogen co–doped templated carbons are represented as Pt/Al–N, Pt/AlS–N, Pt/SG–N, and Pt/Z–N derived from alumina, surfactant modified alumina, silica gel and zeolite templates respectively.

Table 4.14. Elemental analysis of platinum and nitrogen co–doped templated carbons using EDX.

Sample ID	Elements (wt.%)			
	Pt	C	N	O
Pt/Al–N	3.4	84.6	4.8	7.2
Pt/AlS–N	3.3	81.2	7.8	7.7
Pt/SG–N	3.0	85.7	3.1	8.3
Pt/Z–N	2.7	78.2	7.1	11.9

The EDX analysis of co–doped templated carbons are shown in Table 4.14 and the corresponding EDX spectra are shown in Appendix B2. The platinum loadings varied in the range of 2.7–3.4 wt.% and the nitrogen content in the range of 3.0 to 7.8 wt.%, depending on the type of templates. The platinum was doped first in the templates followed by incorporation of nitrogen along with carbon by vapor deposition. The comparison of nitrogen content of nitrogen doped (6–9 wt.%) and metal and nitrogen co–doped (3–8 wt.%) templated carbons suggested that the presence of impregnated metal in template did not affect the decomposition of acetonitrile precursor and extent of nitrogen doping significantly.

The nitrogen adsorption–desorption isotherms of platinum and nitrogen co–doped carbons are shown in Figure 4.23(a). The isotherms of co–doped templated carbons followed the same pattern as the corresponding nitrogen doped carbons and templates. The BET surface area, pore volume, average pore size and carbon yield of platinum and nitrogen co–doped carbons are tabulated in Table 4.15. For co–doped templated carbons, the surface area was obtained in the range of 496–1173 m^2/g and pore volume was obtained in between 0.47–1.24 cm^3/g. Both surface area and pore volume for co–doped samples decreased compared to the corresponding nitrogen doped as well as platinum doped templated carbons as can be noted from Table 4.6, 4.10 and 4.15.

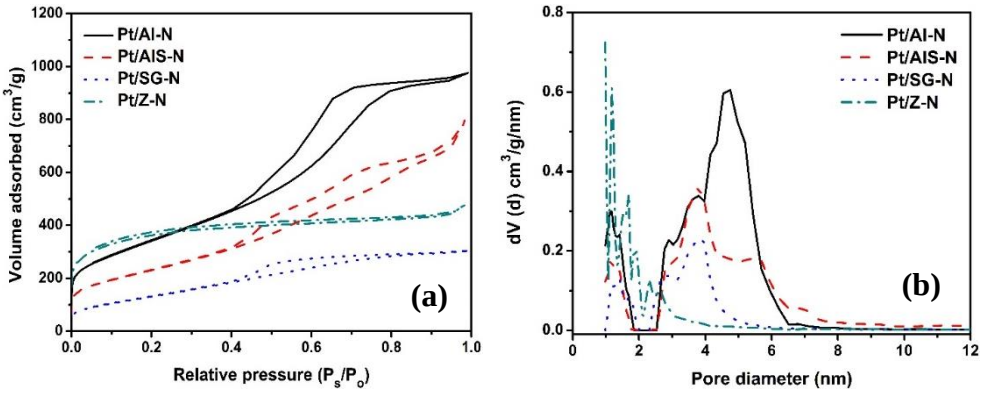

Figure 4.23: (a) N_2 adsorption–desorption isotherms (b) Pore size distributions of platinum and nitrogen co–doped templated carbons.

The drop was most significant for silica gel tenplated carbon and least for surfactant modified alumina tenplated carbon, though both were mesoporous templates with pore size distribution residing mainly in the same range. The percentage drop in surface area was highest and almost similar (~45 %) for both mesoporous silica gel and surfactant modified alumina templated carbons as observed from Table 4.15. However, the drop in pore volume was more for silica gel templated co–doped carbon compared to that of surfactant modified alumina templated co–doped carbon. The reason may be that the higher average pore diameter of the surfactant modified alumina accommodated the foreign material better. The drop in surface area and pore volume of co–doped carbons prepared from zeolite and alumina templates were comparatively lower than that of mesoporous templates.

Table 4.15: Physical properties of platinum and nitrogen co–doped templated carbons.

Sample ID	BET surface area (m^2/g)	Micropore area (m^2/g)	Total pore volume (cm^3/g)	Average pore size (nm)	I_D/I_G ratio	Carbon yield (%)
Pt/Al–N	924	41	1.15	4.7	0.97	15
Pt/AlS–N	836	30	1.24	3.8	0.96	17
Pt/SG–N	496	0	0.47	3.7	0.94	15
Pt/Z–N	1173	314	0.75	1.2	0.98	24

The most of the pores for all the co–doped templated carbons were in the range of 1–8 nm. The microporous and mesoporous natures of co–doped templated carbons were similar to corresponding nitrogen doped or platinum doped templated carbons. The co–doped zeolite templated carbon showed microporous and other samples had narrow mesoporous nature. The impregnation of platinum resulted in reducing the pore volumes as can be observed from the pore size distributions of platinum and nitrogen co–doped templated carbons shown in Figure 4.23(b) (except that for alumina templated carbon). This lowering of pore volume may have

resulted from partial blockage of the pores by the presence of platinum. The lowering was more prominent for mesoporous materials such as surfactant modified alumina and silica gel. The volume of pores above 4 nm was particularly more reduced. This was most prominent for silica gel templated carbon. Even for zeolite based co–doped carbon, the decrease in volume of pores of relatively higher sizes was observed. This suggested preferential residence of metal aggregates in corresponding sections of templates. Comparison of pore size distribution of platinum doped and co–doped templated carbons from Figure 4.17(b) and 4.23(b) shows that overall nature of plots remained same but for co–doped templated carbon, the drop in pore volume and pore range was higher which may be attributed to presence of two dopants in the carbon matrix.

Figure 4.24(a) shows the XRD profiles of co–doped templated carbons. All the co–doped templated carbons showed broad peak corresponding to graphitic carbon at 26^{o} along with sharp platinum peaks at 39.9° (111), 46.3° (200) and 67.5° (220) (Oh et al. 2013). The intensity of the graphitic peak was higher for silica gel templated platinum doped carbon compared to that of the other doped templated carbons. The sharper and intense peaks for platinum were observed for zeolite and alumina templated carbons having lower average pore size. On the other hand, mesoporous templated carbons resulted in broad and shorter peaks of platinum metal, suggesting lower size of platinum crystals. The average crystallite size of the platinum cluster was calculated to be 9, 18, 24 and 26 nm for alumina–SDS, silica gel, zeolite and alumina templated carbons respectively. This suggested higher dispersion of the metal within the matrix of mesoporous templated carbons resulting in lower crystallite size. The highest metal dispersion (lowest crystallite size) may have resulted from highest average pore size of alumina–SDS templated carbon facilitating incorporation of platinum within the templated carbon and uniform distribution.

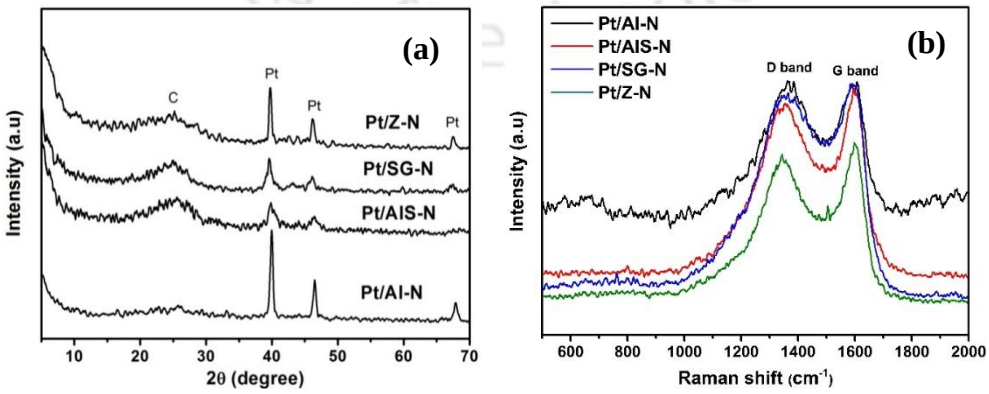

Figure 4.24: (a) XRD profiles (b) Raman spectra of platinum and nitrogen co–doped templated carbons.

Figure 4.24(b) depicts the Raman spectra of platinum and nitrogen co–doped templated carbons. The overall intensity for all co–doped samples was lower compared to nitrogen doped samples. Table 4.15 shows the intensity ratios (I_D/I_G) for the platinum co–doped samples: 0.97 for alumina, 0.95 for alumina–SDS, 0.94 for silica gel and 0.98 for zeolite co–doped templated carbons respectively. The degree of graphitization thus did not vary significantly for co–doped carbons, however, still slightly higher for silica gel co–doped templated carbon.

The FESEM images of platinum and nitrogen co–doped templated carbons are shown in Figure 4.25. The platinum and nitrogen co–doped samples showed mainly tubular noddle like structure, interspersed with agglomerates when prepared from surfactant modified alumina and silica gel templates. The tubular diameter was in the range of 12–20 nm and 35–50 nm for alumina–SDS and silica gel templated co–doped carbons respectively. The formation of tubular shape carbons was also observed for surfactant modified alumina templated platinum doped carbon and was attributed to the catalytic effect of platinum (Figure 4.20). The platinum acts as catalytic center facilitating dissolution and precipitation of carbon resulting in tubular growth. The agglomerates part of the morphology may be attributed to the presence of nitrogen as the corresponding nitrogen doped carbon showed an agglomerated structure (Figure 4.13). However, the formation of tubular structure was not observed for silica gel templated platinum doped carbon for which it was mainly amorphous. Though the tubular forms were not observed in FESEM images of alumina and zeolite templated carbons, however, they were observed in corresponding TEM images shown in Figure 4.26. The zeolite templated co–doped carbon showed particle morphology, as observed for undoped, nitrogen doped and platinum doped templated carbons.

The TEM images of platinum and nitrogen co–doped templated carbons in Figure 4.26 showed that all the templated carbons were in agglomerated state interspersed with tubular/rod like structure. For alumina templated carbon, short rod like structures were observed, whereas tubular form was observed for the rest. This suggested that the fraction or size of tubular or rod like structure was lower for alumina and zeolite templated carbons as they were not visible in FESEM images. However, for alumina–SDS and silica, the fraction of tubular structure was quite extensive and detected both in FESEM and TEM images. This suggested that the presence of higher pore size in mesoporous alumina–SDS and silica templates facilitated the formation of tubular form in presence of metal, growing in number and size.

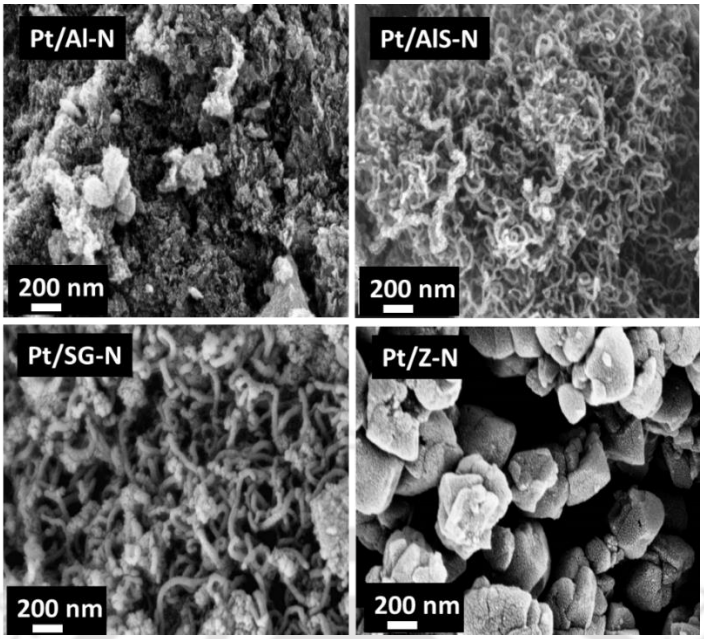

Figure 4.25: FESEM images of platinum and nitrogen co–doped templated carbons.

The particle size distribution from TEM images is shown in Figure 4.26. The average particle sizes of 4.5, 7, 12 and 14 nm were observed for alumina–SDS, silica gel, zeolite and alumina co–doped templated carbons, respectively. Though the order is in agreement with XRD results, the average values were lower than that obtained from XRD analysis. The difference may have resulted from the fact that XRD is less effective in determining the smaller crystallite size (<5 nm) (Birks et al. 1946). The particle size distribution in Figure 4.26 shows that all the samples were associated with some large particles. In XRD, mainly the larger particles were detected and contributed to the shift of average particle size to higher values. This was also observed by Nores–Pondal et al. (2009). These results suggested that platinum was more dispersed when incorporated in the mesoporous structure of alumina–SDS or silica gel. The alumina–SDS with highest average pore size facilitated the most resulting lowest average cluster size of deposited platinum.

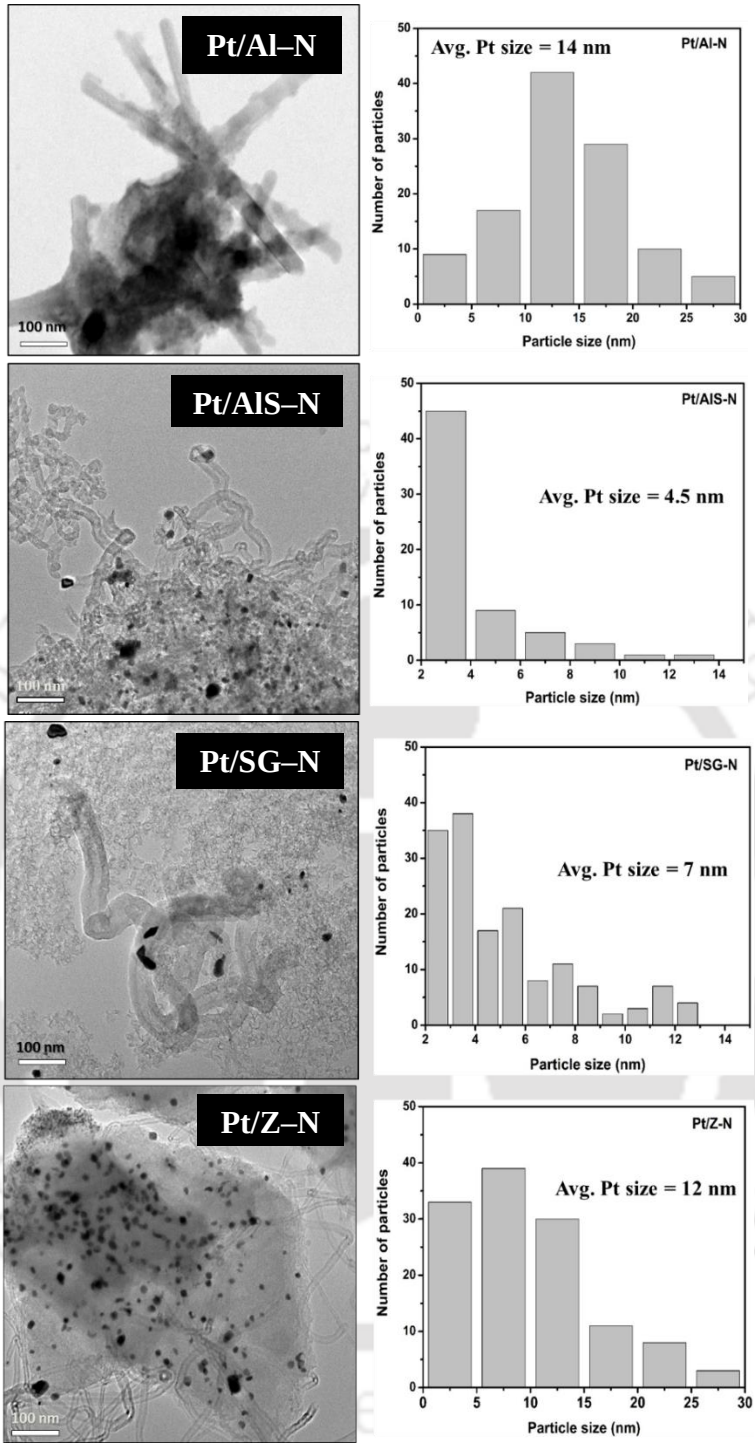

Figure 4.26: TEM images of platinum and nitrogen co–doped templated carbons and corresponding metal particle size distribution.

The TGA curves and corresponding DTG profiles of platinum and nitrogen co–doped templated carbons are shown in Figure 4.27. The residual weight of 1–6 % was observed for all the samples as earlier which may be attributed to residual platinum as well as residual templates if any. Compared to TGA profiles for all the nitrogen doped templated carbons, combustion peaks of platinum co–doped carbons were shifted to lower temperature between

300–400 °C. This can be attributed to the presence of platinum which has been reported to promote catalytic oxidation of carbon matrix at lower temperature (Su et al. 2009). After platinum addition, the combustion peak of all the carbons were more or less shifted to the same position due to the catalytic effect. However, the peak due to Pt/Z–N was associated with sharper multiple peaks compared to that of the others which were broad and single in nature. As discussed earlier presence of multiple sharp peaks is associated to the presence of different structural entity which oxidized at slightly different temperatures. The combustion temperature of the co–doped templated carbons were lower than that of nitrogen doped and platinum doped templated carbons. The co–doped templated carbons were oxidized in the temperature range of 290–610 °C whereas, platinum doped templated carbons were burned off in the temperature range of 400–675 °C.

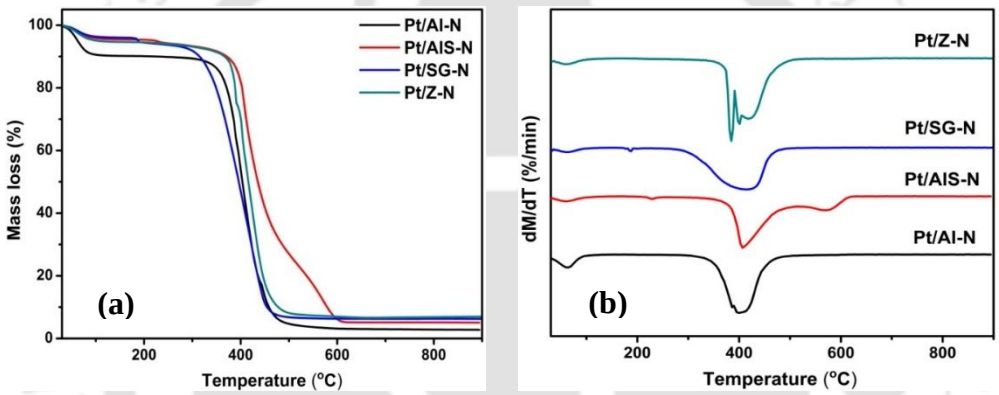

Figure 4.27: Thermal analysis of platinum and nitrogen co–doped carbons (a) TGA profiles (b) DTG profiles.

Hydrogen uptake

Hydrogen adsorption isotherms of platinum and nitrogen co–doped templated carbons were measured at –196 °C up to 25 bar and shown in Figure 4.28(a). The corresponding hydrogen uptake capacity and density are summarized in Table 4.16. The hydrogen uptake capacity was found to be in the range of 3.2–4.1 wt.% at 25 bar. For silica gel templated co–doped carbon, the lowest hydrogen uptake capacity was observed whereas, it was highest for co–doped alumina and alumina–SDS templated carbons. The plot of hydrogen storage capacity as a function of surface area is shown in Figure 4.28(c). The higher surface area in general resulted in higher hydrogen uptake. For co–doped silica gel carbon, the lowest hydrogen uptake capacity may be due to lowest surface area. This higher uptake capacity for alumina–SDS templated co–doped carbon was observed in spite of lower total surface area and absence of any micropores.

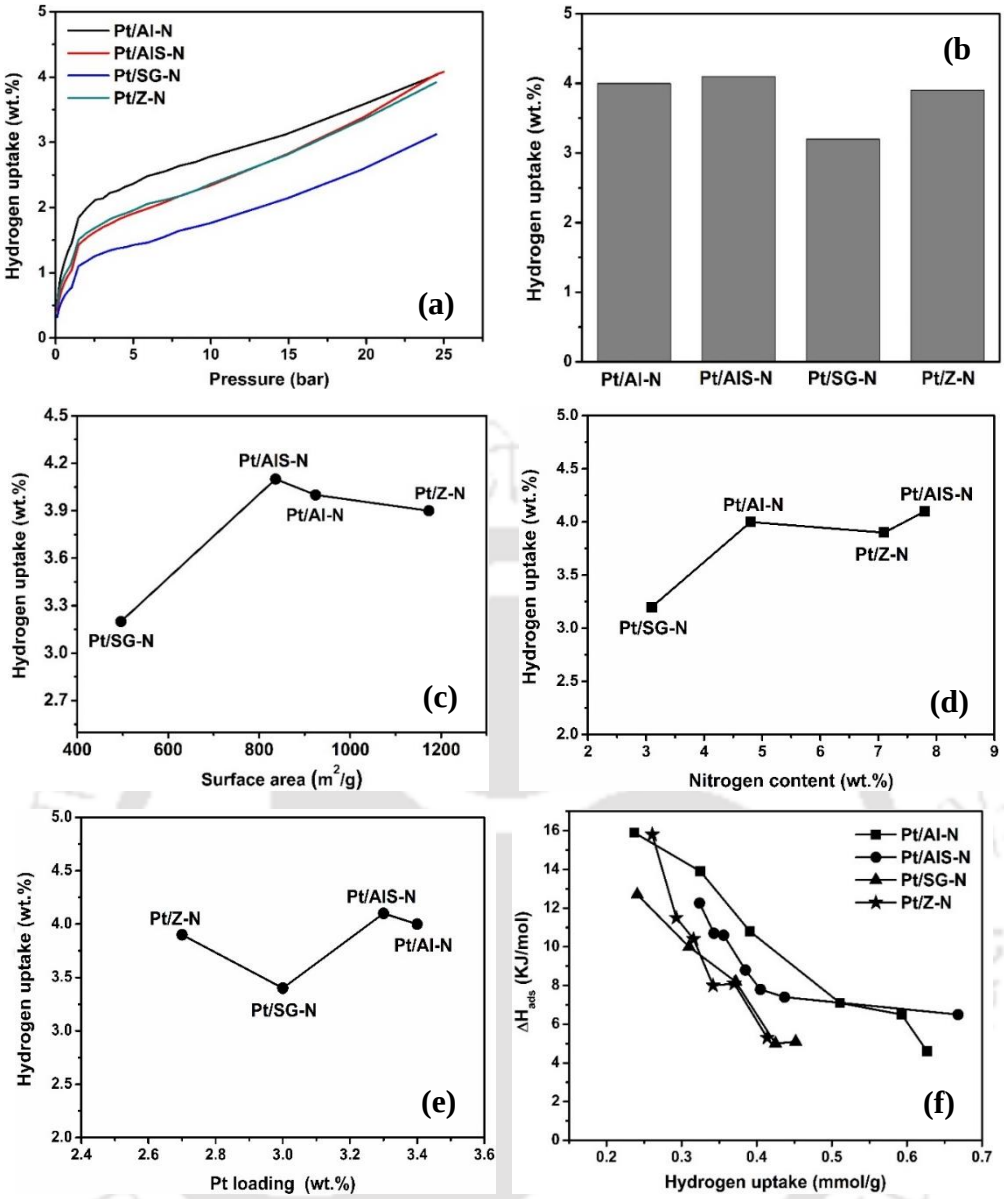

Figure 4.28: For platinum and nitrogen co–doped templated carbons (a) Hydrogen adsorption isotherms at –196 °C up to 25 bar (b) Hydrogen uptake capacity at –196 °C and 25 bar (c) Relation between hydrogen uptake capacity and surface area (d) Hydrogen uptake as a function of nitrogen content (e) Hydrogen uptake as a function of platinum content (f) Isosteric heats of adsorption as a function of the amount of H_2 adsorbed.

For doped adsorbent, in addition to surface area amount of dopants and dispersion of doped metal play a major role in providing additional active sites for adsorption of gaseous adsorbents. Figure 4.28(d) and (e) shows the variation in hydrogen uptake with nitrogen and metal content. The presence of nitrogen in carbon matrix is reported to activate dissociation of hydrogen favoring its uptake (Xia et al. 2011). The hydrogen uptake also increased with increasing nitrogen content except for zeolite templated co–doped carbon. The highest nitrogen content showed highest hydrogen uptake capacity which was for Pt/AlS–N. The increasing

order of average metal size for the co–doped templated carbons is; alumina–SDS (4.5 nm) < silica gel (7 nm) < zeolite (12 nm) < alumina (14 nm) templated co–doped carbons, respectively. Hence, dispersion decreased in the same order. Figure 4.28(d) shows that Pt/Z–N had the lowest metal content, but its hydrogen uptake was high which may be attributed to its highest surface area. In spite of having highest metal content the lower hydrogen uptake of Pt/Al–N compared to that of Pt/AlS–N may be explained on the basis of lower metal dispersion, surface area and nitrogen content of the former. Thus the higher uptake for Pt/AlS–N in spite of lower surface area can be attributed to the presence of highest amount of nitrogen, highest dispersion of metal and second highest metal content. All the parameters showed a synergistic positive effect resulting in highest hydrogen uptake for Pt/AlS–N.

Table 4.16: Hydrogen uptake capacity and density of platinum and nitrogen co–doped templated carbons at –196 °C.

Sample ID	Hydrogen uptake at 25 bar	
	wt.%	density (μmol/m^2)
Pt/Al–N	4.0	22
Pt/AlS–N	4.1	24
Pt/SG–N	3.2	31
Pt/Z–N	3.9	16

The hydrogen uptake density of the co–doped carbons exhibited in between 16–31 μmol/m^2 and maximum of 31 μmol/m^2 was obtained for silica gel co–doped carbon (Table 4.16). It was noticed that the uptake density enhanced when platinum was doped on different templated carbons.

The hydrogen uptake for platinum modified carbons obtained in this study are also better or at par compared to reported hydrogen uptake for platinum doped microporous and mesoporous carbons (Table 4.17). Alam et al. (2011) have shown that platinum doped zeolite templated carbon can store hydrogen up to 4.8 wt.% at –196 °C and 20 bar. Mesoporous carbons are particularly important for doping with metals. The mesoporous carbons are expected to accommodate the dopants more uniformly (Prasanth et al. 2010). Limited studies are reported for doped mesoporous templated carbon. Oh et al. (2013) observed hydrogen storage of 2.2 wt.% for platinum doped silica templated carbon at –196 °C and 20 bar.

Platinum is believed to provide additional active sites for the hydrogen adsorption. In addition, it facilitates spillover mechanism whereby the hydrogen is dissociated on metal sites and then diffused to carbon surface. The interaction between platinum and hydrogen is chemisorption

in nature and is much stronger than physical adsorption (Alam et al. 2011). Increase in hydrogen uptake density for platinum doped carbons suggested that even at very low temperature of –196 ^{o}C a stronger interaction compared to physisorption exists. The spillover effect for palladium co–doped templated carbons at –196 °C has been reported by the Masika et al. (2013).

Table 4.17: Comparison of physical properties and hydrogen uptake capacities at –196 °C for studied platinum and nitrogen co–doped templated carbons of present study with that reported in the literature.

Template carbon	Nature of templated carbon	Surface area (m^2/g)	Pressure (bar)	Hydrogen uptake (wt.%)	References
Pt–N/zeolite–Y	Microporous	2314	20	4.8	(Alam et al. 2011)
Pt/silica	Mesoporous	882	20	2.2	(Oh et al. 2013)
Pt–N/zeolite–Y	**Microporous**	**1173**	**25**	**3.9**	**Present study**
Pt–N/silica gel	**Mesoporous**	**496**	**25**	**3.2**	**Present study**
Pt–N/modified alumina	**Mesoporous**	**836**	**25**	**4.1**	**Present study**

N: nitrogen doped

The isosteric heat of H_2 adsorption for platinum and nitrogen co–doped templated carbons are shown in Figure 4.28(f). The highest heat of adsorption value of ~15.9 kJ/mol was obtained at lower H_2 uptake. Higher values at lower uptake may be attributed to the stronger and preferable interaction of hydrogen atoms with the platinum clusters. As coverage increased, adsorption was on comparatively weaker sites on carbon surface and consequently, the heat of adsorption decreased. In literature, the heats of adsorption for hydrogen molecules on carbons are reported for metal (Pt, Ni & Ru) doped carbons in the range of 9 to 25 kJ/mol (Alam et al. 2010; Wang et al. 2008).

It was observed that the hydrogen uptake capacity was higher for co–doped templated carbons compared to that of nitrogen doped or platinum doped carbons, when all are derived from alumina based templates. For silica gel and zeolite templated carbons, the hydrogen uptake for co–doped samples was higher compared to that of platinum doped carbons but slightly lowered compared to nitrogen doped one. This was in spite of lower surface area for co–doped carbon compared to either nitrogen doped or platinum doped one. The results suggested that the synergistic effect of presence of metal and non–metal facilitated hydrogen uptake. However, in case of metal dopant, its dispersion played a major determining role and thereby the samples with lower metal dispersion such as Pt/SG–N and Pt/Z–N gave lower hydrogen uptake than expected.

Summary

For platinum and nitrogen co–doped templated carbons, prepared from different templates, the surface areas varied in the range of 496–1173 m^2/g and pore volume between 0.47–1.24 cm^3/g. Both surface area and pore volume for co–doped samples dropped compared to corresponding nitrogen doped or platinum doped samples. Higher dispersion of the platinum metal was observed within the matrix of mesoporous templated carbons. The average size of platinum cluster was 4.5, 7, 12 and 14 nm for alumina–SDS, silica gel, zeolite and alumina templated carbons respectively. Particle morphology was observed for zeolite co–doped templated carbon. The silica gel and alumina templated co–doped carbons showed agglomerated tubular morphology. The highest hydrogen uptake of 4.1 wt.% was observed for alumina–SDS co–doped templated carbon in spite of lower surface area and may be attributed to the synergistic effect of highest amount of nitrogen, highest dispersion of metal and close second highest metal content. The effect of dopants on hydrogen uptake capacity depended on the template type. Platinum doping resulted in the heat of adsorption up to 15.9 kJ/mol.

4.1.7 Effect of different metal (Pt/Ni/Pd) modification

Results discussed in above sections showed that the surfactant modified alumina was a very effective template for preparation of mesoporous templated carbon with desirable pore properties for hydrogen storage. It was also very effective for incorporation of dopants. Hence this template was selected to prepare metal and nitrogen co–doped templated carbons using different metals such as Pt, Ni or Pd to understand the effect of different metals in the development of the structure of mesoporous templated carbon as well as the interaction of hydrogen with co–doped carbons. As before the metal precursor was first impregnated on surfactant modified alumina template and thereafter the metal–template composite was subjected to CVD process using acetonitrile as the precursor for the synthesis of the metal and nitrogen co–doped carbons. The metal and nitrogen co–doped templated carbons are represented as Pt/AlS–N, Ni/AlS–N and Pd/AlS–N prepared using platinum, nickel and palladium precursors respectively.

Table 4.18: Elemental analysis of nitrogen doped templated carbon and metal and nitrogen co–doped templated carbons using EDX.

Sample ID	Elements (wt.%)			
	Metals	C	N	O
AlS–N	–	82.8	7.6	9.6
Pt/AlS–N	3.3	81.2	7.8	7.7
Ni/AlS–N	2.0	85.3	7.0	5.7
Pd/AlS–N	2.0	74.2	21.7	2.1

The composition of the samples was determined by EDX, are summarized in Table 4.18. The corresponding EDX spectra are included in Appendix B3. Average loadings of different metals in the final co–doped templated carbons were 3.3, 2.0 and 2.0 wt.% of Pt, Ni and Pd respectively. The nitrogen content was about 7 wt.% for all the samples except that for co–doped Pd/AlS–N, which had high nitrogen loading of 21.7 wt.%. The value of nitrogen content in nitrogen doped carbon materials are reported in the range of 13.8–35.1 wt.% (Zhang et al. 2015; Jiang et al. 2010; Bagreev et al. 2004; Zackrisson et al. 1999). Non–detection of any aluminium (due to template) in the sample confirmed its effective removal from the carbon sample.

The nitrogen adsorption–desorption isotherms resembled close to type IV for all the samples (Figure 4.29a). The physical properties calculated from the isotherms are given in Table 4.19.

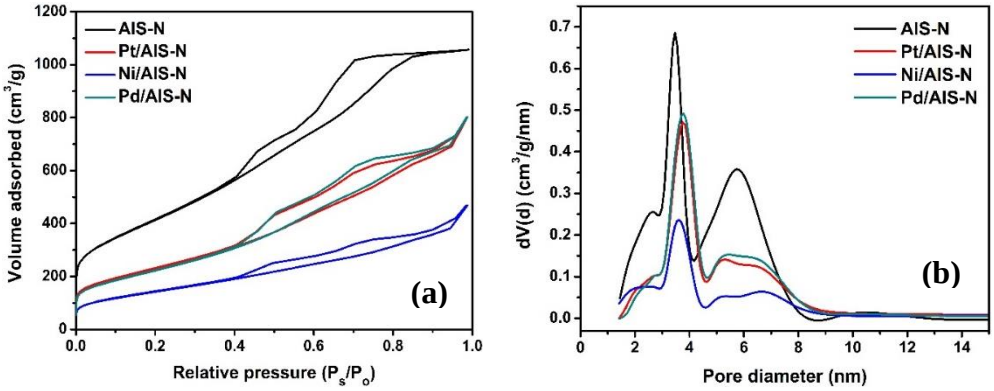

Figure 4.29: (a) N_2 adsorption–desorption isotherms (b) Pore size distributions of different metal and nitrogen co–doped templated carbons.

The BET surface area, pore volume and carbon yield of alumina–SDS templated nitrogen doped carbon was significantly higher, 1508 m^2/g and 1.64 cm^3/g respectively, compared to that of the corresponding template. The amorphous and mesoporous morphology of the template may have contributed to the development of carbon structure with enhanced surface area and pore volume.

Table 4.19: Physical properties of nitrogen doped templated carbon and metal and nitrogen co–doped templated carbons.

Sample ID	Surface area (m^2/g)	Micropore area (m^2/g)	Pore volume (cm^3/g)	Average pore diameter (nm)	I_D/I_G ratio	Metal dispersion (%)	Carbon yield (%)
AlS–N	1508	49	1.64	3.4	0.99	–	26
Pt/AlS–N	836	30	1.24	3.8	0.97	22	17
Ni/AlS–N	520	22	0.72	3.5	0.95	25	29
Pd/AlS–N	817	24	1.24	3.9	0.96	31	32

After metal doping, the surface area along with pore volume decreased. The reduction in surface area and pore volume was most significant for nickel co–doped carbon, to 520 m^2/g and 0.7 cm^3/g respectively. For platinum or palladium co–doped carbons, surface areas were in similar range, 836 and 817 m^2/g respectively. The pore volumes and average pore size were also in similar range (Table 4.19). All the samples had a bimodal pore size distribution between 2 to 8 nm (Figure 4.29b). The average pore size of doped templated carbons ranged in between 3.4 to 4 nm in the order; Pd/AlS–N (3.9 nm) > Pt/AlS–N (3.8 nm) > Ni/AlS–N (3.5 nm) > AlS–N (3.4 nm). Presence of metals in carbon matrix may have resulted in partial blockage decreasing surface area and pore volume while increasing the average pore size. The significant drop in pore volume for co–doped samples can be observed from pore size distribution given

in Figure 4.29(b). The micropore area was 49 m^2/g for AlS–N sample, which dropped to 30, 22 and 24 m^2/g for Pt/AlS–N, Ni/AlS–N and Pd/AlS–N respectively.

Figure 4.30(a) shows the X–ray diffraction profiles of the co–doped templated carbons. The AlS–N carbon showed typical peak at 2Θ = 26º due to graphitic carbon (002). For co–doped carbons, the intensity of this graphitic carbon peak was enhanced. It was most significant for nickel co–doped sample and least for platinum co–doped sample. Since the synthesis conditions were similar for all samples, the presence of nickel and palladium seems to have promoted graphitic structure. The increase in graphitic structure was also observed for platinum doped carbons in this study as discussed earlier. The catalytic effect of metal on graphitization has been reported by Campesi et al. (2008) and Ōya et al.1979. The increase in graphitic zone peak intensity with addition of palladium to mesoporous templated carbon was observed by Campesi et al. (2008). The nickel is reported to facilitate graphitization of carbon by dissolution and precipitation mechanism (Ōya et al. 1979). For Pt/AlS–N, peaks were obtained at 2Θ = 39.8° and 46.3° corresponding to Pt (111) and Pt (200) planes. The sharp peak of platinum having high intensity may be associated with the lowest dispersion. The peak relating to nickel was observed at 2Θ = 44.4° in Ni/AlS–N and can be attributed to (111) plane. The NiO peaks are reported at 37.6° (111), 43.09° (200), 63.62° (220) and 75.09° (311) (Zhang et al. 2016; Carraro et al. 2014). This nickel peak corresponded to reduced NiO or nickel in zero oxidation state, Ni° (Yadav et al. 2017; Srivastava et al. 2010). Any of the expected peaks for palladium (2Θ = 40.1°, 46.6° and 68°) were not observed in profile of Pd/AlS–N sample, which suggested higher dispersion of palladium in the carbon matrix (Cheon et al. 2009).

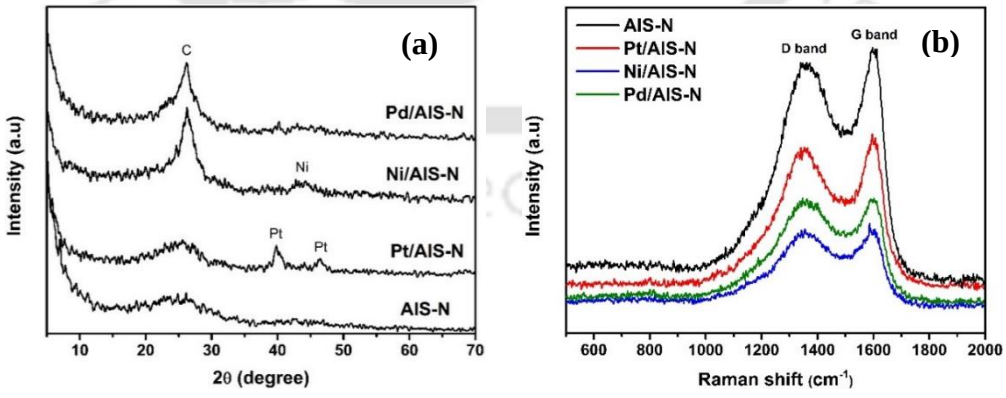

Figure 4.30: (a) XRD profiles (b) Raman spectra of different metal and nitrogen co–doped templated carbons.

The metal dispersion for co–doped carbons were determined by CO–pulse chemisorption technique at room temperature. The obtained dispersion values for Pt/AlS–N, Ni/AlS–N and

Pd/AlS–N was 22, 25 and 31 % respectively, as shown in Table 4.19. The highest dispersion of palladium doped carbon agreed with the results obtained from XRD analysis. The high dispersion which corresponds to more exposed metal site is expected to enhance the hydrogen storage capacity.

Figure 4.30(b) shows the Raman spectra for all the doped carbons. The D band and G band for all the carbons were observed in the range of 1341–1347 cm^{-1} and 1586–1600 cm^{-1} respectively. The disorder induced C–C single bond and the vibration of sp^2 hybridized carbon atoms respectively lead to the D and G bands (Oh et al. 2013). The intensity ratio of I_D/I_G is an indication of the level of graphitic ordering. The ratio of the intensity of the two bands (I_D/I_G) was calculated to be 0.99, 0.97, 0.96, and 0.95 for AlS–N, Pt/AlS–N, Pd/AlS–N and Ni/AlS–N doped carbons respectively. Hence Ni/AlS–N sample with lowest I_D/I_G ratio have the highest degree of graphitization, followed by Pd/AlS–N. This agreed with the results obtained from XRD analysis.

The TGA curves and DTG profiles of different metal and nitrogen co–doped templated carbons are shown in Figure 4.31(a) and (b) respectively. For all the samples small peak around 80–100 °C, corresponding to 3–11 % weight loss, may be assigned to the removal of moisture. For nitrogen doped carbon, the main weight loss occurred in the wide temperature range of 470–670 °C, due to combustion of carbon in the flow of air. The residue obtained was about 0.7 %, suggesting that the sample was mostly free of any residual template.

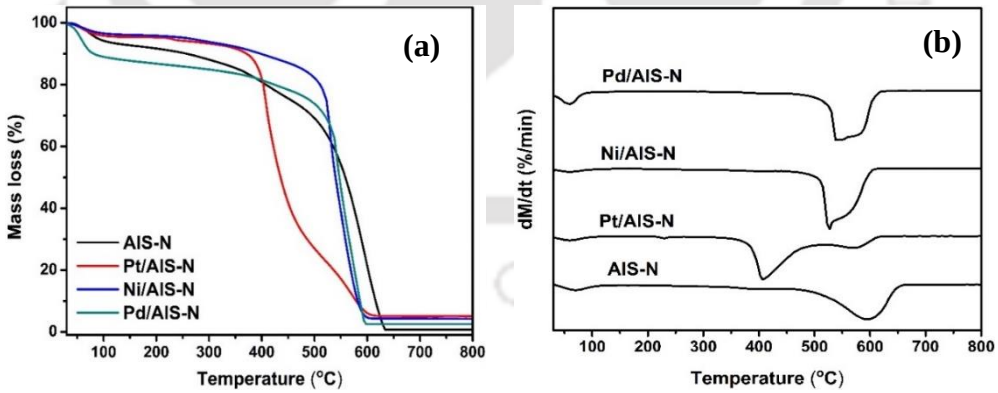

Figure 4.31: Thermal analysis of different metal and nitrogen co–doped carbons (a) TGA profiles (b) DTG profiles.

For different metal and nitrogen co–doped carbons, the combustion temperature decreased. For platinum doped carbon, the major combustion temperature was observed in the range of 360 to 470 °C, whereas Pd and Ni co–doped carbons showed combustion between 485 to 620 °C. The

residual weight of ~2.5–5.5 % might be associated with the presence of the metal oxides. The lowering of combustion temperature in the presence of metals suggests catalytic effect on the oxidation process as also discussed earlier section 4.1.5. The catalytic effect of platinum was observed to be maximum. The presence of broad multiple combustion peaks suggested presence of at least two types of carbon structures undergoing combustion at slightly different temperatures. These two structures may correspond to graphitic and non–graphitic carbons as observed from XRD and Raman analysis. Higher combustion temperatures have been reported for structured graphitic carbon compared to non–graphitic carbon; Kim et al. (2011) and Tian et al. (2014) reported 530 and 600 °C for non–graphitic and graphitic carbons respectively. Accordingly, in this study, the lower temperature peak may be assigned to the combustion of non–graphitic carbon or amorphous carbon, while the higher temperature peak to graphitic carbon or structured carbon.

Figure 4.32 shows FESEM images of doped templated carbons. Nitrogen doped carbon had agglomerated morphology. The morphologies of templated carbons totally changed when prepared in the presence of metals (Pt, Pd or Ni). Noodles like tubular tangled morphology resulted in having extensive network. The texture, extent of network as well as the diameter of tubular structure varied with type of metal present. The tubular structure was more compact and tangled for Pt/AlS–N followed by that for Pd/AlS–N carbon. The tubular structure was least dense for Ni/AlS–N with more openings in between. The more compact and tanged tubular structure of Pt and Pd doped carbons may have resulted in higher surface area and pore volume compared to that of least dense structure nickel doped carbon. The average tubular diameter of Pt, Pd or Ni doped carbons were observed for 14, 28 and 34 nm respectively.

The TEM images and corresponding metal particle size distribution of co–doped templated carbons are shown in Figure 4.33. Similar to FESEM images, the aggregated structure was observed for nitrogen doped templated carbon. For all the metal doped carbons, aggregates were observed to be interspersed with tubular structure. Platinum doped carbon had more intricate tubular structure compared to that of palladium and nickel doped carbons. Palladium co–doped carbons showed least tubular entities and presence of larger pores as can be observed from Figure 4.33.

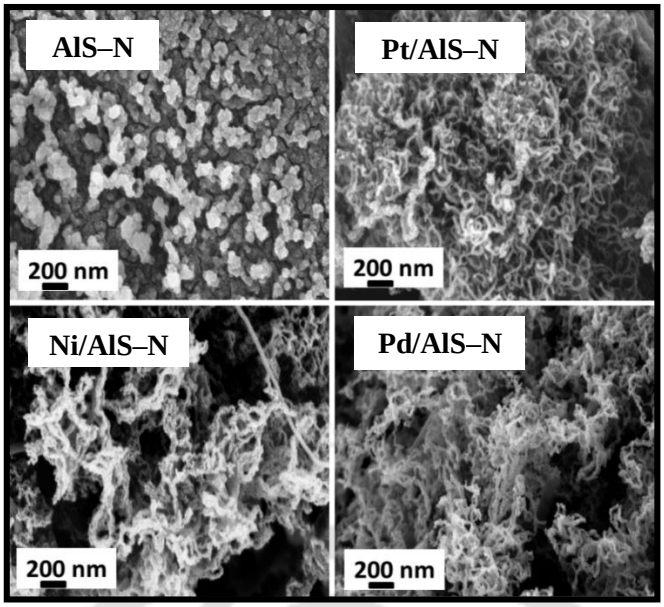

Figure 4.32: FESEM images of different metal and nitrogen co–doped templated carbons.

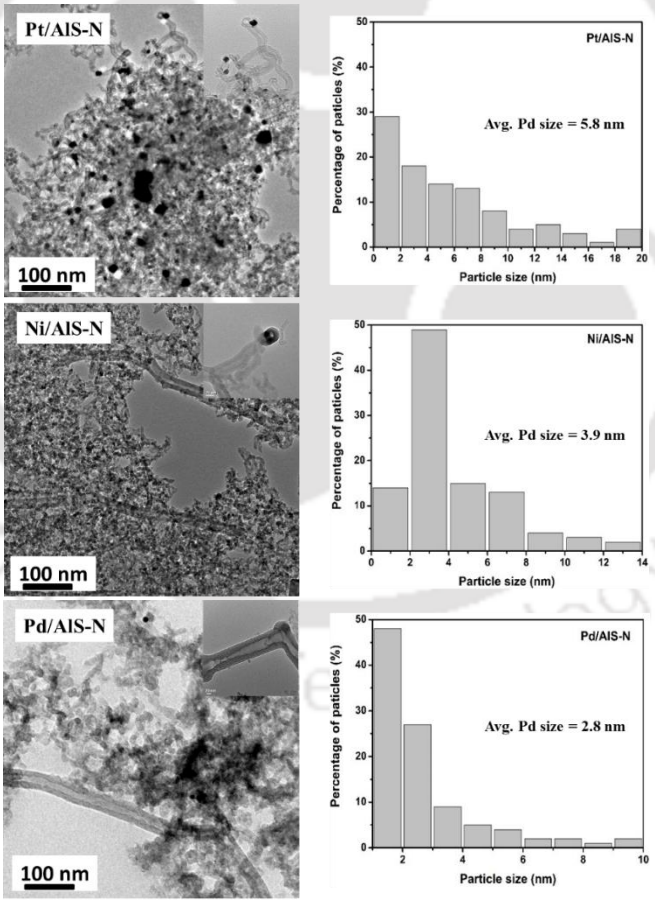

4.33: TEM images and corresponding metal particle size distribution for different metal and nitrogen co–doped templated carbons.

The magnified images (inserted) of tubular structure shows multi–wall tubes for all the samples. The metal particle size distributions (Figure 4.33) from TEM images gave the average metal cluster size as 5.8, 3.9 and 2.8 nm for Pt, Ni and Pd co–doped carbons respectively. The lowest cluster size of the palladium particles suggests highest dispersed condition compared to that of platinum and nickel particles. Similar dispersion results were obtained from XRD and Chemisorption studies.

Hydrogen uptake

Hydrogen adsorption isotherms for the nitrogen doped and metal and nitrogen co–doped templated carbons are shown in Figure 4.34(a). The hydrogen uptake isotherms were measured till 25 bar pressure at –196 °C temperature for all carbons.

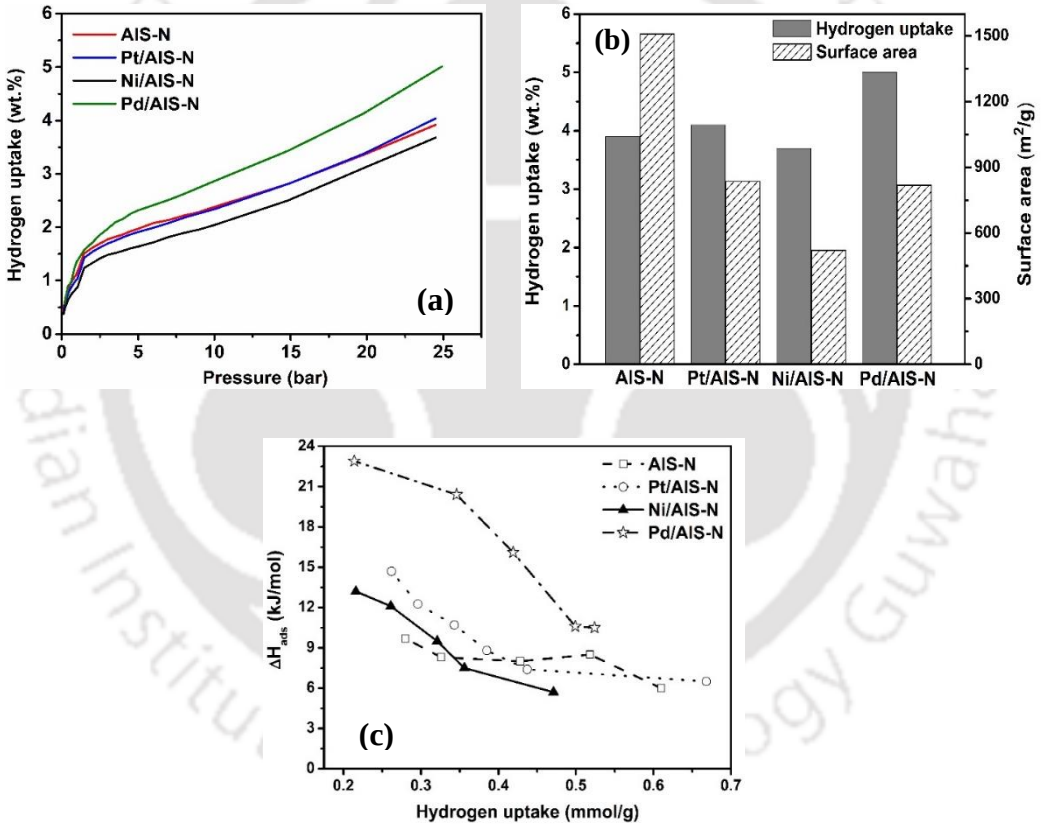

Figure 4.34: For different metal and nitrogen co–doped templated carbons (a) Hydrogen adsorption isotherms at –196 °C up to 25 bar (b) Hydrogen uptake at 25 bar and –196 °C (c) Isosteric heats of adsorption as a function of hydrogen uptake.

The nitrogen doped carbon had hydrogen uptake capacity about 3.9 wt.% at 25 bar having surface area of 1508 m^2/g. The surface area drastically decreased with metal doping and corresponding hydrogen storage capacity also varied depending on metal type as can be observed from Figure 4.34(b). Hydrogen uptake capacity of the metal doped carbons at 25 bar

was in the range of 3.7 to 5.0 wt.% (Table 4.20).

Table 4.20: Hydrogen uptake capacity of metal and nitrogen co–doped templated carbons at –196 °C.

Sample ID	Hydrogen uptake (wt.%) at 25 bar
AlS–N	3.9
Pt/AlS–N	4.1
Ni/AlS–N	3.7
Pd/AlS–N	5.0

With respect to undoped templated carbon, the hydrogen uptake was enhanced with co–doping of palladium and nitrogen but no positive effect was observed for co-doping of platinum or nickel. The decrease in hydrogen uptake may be explained by significant drop in surface area on co-doping with the additional dopant sites unable to compensate for the loss. Though for palladium it seems that presence of well dispersed metal sites and significantly higher amount of nitrogen were not only able to make up the loss in hydrogen uptake due to decrease in surface area but also enhance it further. The Pd or Pt co–doping however, increased the hydrogen uptake capacity of nitrogen doped carbons, while hydrogen uptake capacity decreased on nickel co–doping. The enhancement of hydrogen uptake for Pt or Pd co–doped carbons in spite of lower surface with respect to nitrogen doped carbon area may be again attributed to the presence of well–dispersed metal sites, which acted as additional adsorption sites for hydrogen. The higher uptake capacity of palladium co–doped carbon compared to that of platinum co–doped carbon may be attributed to the higher interaction of palladium with hydrogen (Adams et al. 2010) as well as higher dispersion of palladium particles as observed by XRD, CO–Chemisorption and TEM analysis. With respect to only platinum doped carbon, the platinum and nitrogen co-doped carbon showed enhanced hydrogen uptake. The uptake increased from 3.28 to 4.1 wt.%. The additional uptake may be accounted by the presence of second dopant as the surface area was only slightly lower for the latter.

The higher dispersion of palladium resulted in its lower average particle size (2.8 nm) compared to that of platinum (5.8 nm) and contributed to more interacting sites and increased hydrogen uptake capacity for the former. The presence of nitrogen also had a positive effect on hydrogen uptake. The hydrogen uptake was facilitated for palladium doped carbon with higher nitrogen content. As discussed in earlier section 4.1.4, nitrogen can act as activation center for hydrogen and the hydrogen uptake was observed to increase with nitrogen content (Figure 4.16d).

The slight decrease in hydrogen uptake capacity for nickel co–doped carbon compared to that of AlS–N may have resulted from various reasons. Foremost was drop in the surface area and pore volume. This may have resulted from sintering of the sample, which resulted in less dense structure and larger metal cluster as observed from microscopic images. Larger metal cluster further contributed to more effective blocking of pores lowering both the surface area and pore volume. The formation of the larger cluster also reduced the metal dispersion lowering the direct interaction of hydrogen with the metal sites. All the factors contributed to diminishing the effect of the addition of metal sites on hydrogen uptake. However, the presence of nickel did have a positive effect on hydrogen uptake. Presence of nickel seemed to have compensated the significant drop in surface area and the overall difference of hydrogen uptake of Ni/AlS–N compared to that of AlS–N was only 5 %. Here nitrogen content was same in both the Ni/AlS–N and AlS–N samples.

In Table 4.21, the hydrogen uptake of the samples prepared in this study is compared with that of reported ones. Comparing with the limited studies available for metal co–doped mesoporous carbons, the hydrogen uptake capacity of the sample reported in this study is better. Particularly the Pd–N co–doped carbon investigated in this study have high potential as the hydrogen storage material.

Figure 4.34(d) shows isosteric heat of adsorption as function of hydrogen uptake for doped carbons. The isosteric heat of adsorption for nitrogen doped carbon was 9.7 kJ/mol at lower hydrogen uptake, which was enhanced up to 22.9 kJ/mol on palladium doping. The highest heat of adsorption indicated a significant interaction between hydrogen and palladium particles. These values agree with reported heat of adsorption for metal (Pt/Pd) doped carbons (9–24 kJ/mol) (Wang et al. 2008).

Summary

Mesoporous co–doped templated carbons having nickel, platinum or palladium with nitrogen, had surface area in the range of 520–836 m^2/g and pore volume in range of 0.72–1.24 cm^3/g. The surface area decreased with respect to undoped and mono doped carbons. The platinum and nitrogen co–doped carbon gave higher surface area of 836 m^2/g followed closely by palladium and nitrogen co–doped templated carbon. The nickel and nitrogen co–doped carbon gave the lowest surface area among the co–doped samples. The highest dispersion of metal was observed for palladium and nitrogen co–doped carbon. The average metal size of Pt, Ni or Pd co–doped carbons was 5.8, 3.9 and 2.8 nm, respectively.

Table 4.21: Comparison of physical properties and hydrogen uptake capacities at –196 °C for nitrogen and metal co–doped mesoporous templated carbons of present study with that reported in the literature.

Sample	Template	Surface area (m^2/g)	Pore volume (cm^3/g)	Pressure (bar)	Hydrogen uptake (wt.%)	References
N/MTC	SBA–15	1173	0.75	20	3.4	(Xia et al. 2007)
N/MTC	SBA–15	942	1.06	30	2.8	(Giraudet et al. 2011)
N/MTC	SBA–15	334	0.36	20	1.49	(Zheng et al. 2010)
N/MTC	SBA–15	1335	–	30	2.8	(Giraudet et al. 2010)
AlS–N	**Alumina–SDS**	**1508**	**1.64**	**25**	**3.9**	**Present study**
Ni/MTC	SBA–15	948	0.99	10	1.8	(Carraro et al. 2019)
Ni/Carbon aerogel	–	968	–	40	2.3	(Kabbour et al. 2006)
Ni/MTC	MCM–41	910	0.56	10	1.2	(Carraro et al. 2014)
Ni–N/MTC	SBA–15	984	1.18	30	2.3	(Giraudet et al. 2011)
Ni/AlS–N	**Alumina–SDS**	**520**	**0.72**	**25**	**3.7**	**Present study**
Pt/silica	Silica	882	0.60	20	2.2	(Oh et al. 2013)
Pt/AlS–N	**Alumina–SDS**	**836**	**1.24**	**25**	**4.1**	**Present study**
Pd/MTC	SBA–15	712	0.84	18	1.1	(Campesi et al. 2008)
Pd/Carbon	–	617	3.14	10	1.1	(Zhong et al. 2015)
Pd/AlS–N	**Alumina–SDS**	**817**	**1.24**	**25**	**5.0**	**Present study**

N: Nitrogen; MTC : Mesoporous Templated Carbon

The FESEM images showed noddle or tubular like structure on co–doping of metals with nitrogen. The agglomerated structure interspersed with tubular/rod–like shapes was also observed from the TEM images of co–doped carbons. Palladium and nitrogen co–doped carbon with 2 wt.% Pd showed the highest hydrogen uptake of 5.0 wt.%. at –196 °C and 25 bar. This may be attributed to its highest number of active sites corresponding to the highest metal dispersion and amount of nitrogen present. Also, the highest heat of adsorption of 22.9 kJ/mol was obtained for the same sample. The study established that the surfactant–modified alumina was an effective template for the synthesis of mesoporous carbon. It facilitated incorporation of metal atom and at the same time had a significant surface area and pore volume.

4.1.8 Effect of metal (palladium) loading in co–doped carbon

In this section, the effect of variation in metal loading on physical and hydrogen uptake properties of surfactant modified alumina templated palladium and nitrogen co–doped carbon are discussed. The samples with different metal loadings were denoted as Pd_x/AlS–N where X denoted the metal loading and x= 0.6, 1, 2 and 3 wt.% of metal.

Table 4.22: Elemental analysis of nitrogen doped templated carbon and palladium and nitrogen co–doped templated carbons with different palladium loadings using EDX.

Sample ID	Elements (wt.%)			
	Metals	C	N	O
AlS–N	–	82.8	7.6	9.6
$Pd_{0.6}$/AlS–N	0.6	77.3	21.5	0.6
Pd_1/AlS–N	1.0	78.2	19.8	1.0
Pd_2/AlS–N	2.0	74.2	21.7	2.1
Pd_3/AlS–N	3.0	71.2	19.8	6.0

The EDX analysis (Table 4.22) showed variation in metal concentration in palladium and nitrogen co–doped samples. The metal was varied from 0.6 to 3 wt.%. The nitrogen content was high (19.8–21.7 wt.%) for all the palladium co–doped samples (Table 4.22). It was also observed in above section that nitrogen content of the palladium pre–deposited samples was much higher compared to when no metal was there as in AlS–N sample or metal such as Pt or Ni was pre–deposited. The high amount of deposition of nitrogen in presence of Pd was confirmed by similar results for all the four palladium containing samples. This suggested that presence of palladium during CVD promoted decomposition of acetonitrile precursor. This was also confirmed by the relatively higher yield for palladium containing carbons (Table 4.19). However, no effect of variation of palladium loading was observed on nitrogen content.

The effect of palladium loading on nitrogen adsorption–desorption isotherm and pore size distribution are presented in Figure 4.35(a) and (b). The nature of nitrogen sorption isotherms did not change with palladium loadings. However, the nitrogen adsorption reduced with increase in palladium loading from 0.6 to 3 wt.% suggesting lowering in surface area with increase in palladium loading. The physical properties of the palladium co–doped templated carbons are tabulated in Table 4.23. The surface area of palladium and nitrogen co–doped carbons dropped from 1159 to 415 m^2/g and pore volume from 1.42 to 0.74 cm^3/g with increase in palladium loading from 0.6 to 3 wt.%. This may have resulted from increased blocking of pores caused by greater palladium presence. The pore size distribution of co–doped templated

carbons (Figure 4.35b) also showed significant decrease in pore volume with increase in palladium loadings.

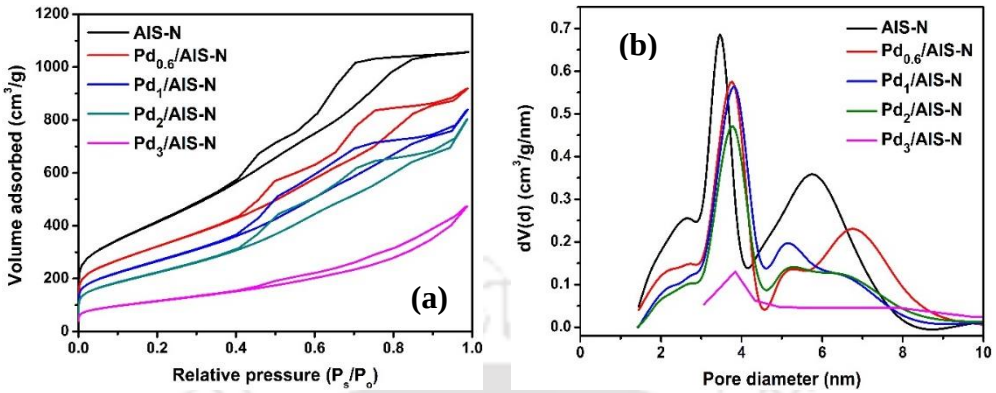

Figure 4.35: (a) N_2 adsorption–desorption isotherms (b) Pore size distributions of palladium and nitrogen co–doped templated carbons with different palladium loadings.

All the samples showed bimodal pore size distribution in the range of 2.5–10 nm. Pores in both the ranges, 2.5 to 4 nm and 4 to 8 nm, were reduced, suggesting blockage of both types by the accommodation of the dopants. At highest loading of 3 wt.% palladium, the pores were extensively blocked as can be observed from Figure 4.35(b), resulting in lowest surface area and pore volume.

Table 4.23: Physical properties of palladium and nitrogen co–doped templated carbons with different palladium loadings.

Sample ID	Pd (wt.%)	Surface area (m^2/g)	Micropore area (m^2/g)	Pore volume (cm^3/g)	Average pore size (nm)	I_D/I_G ratio	Metal dispersion (%)	Carbon yield (%)
$Pd_{0.6}$/AlS–N	0.6	1159	44	1.42	3.7	1.00	48	38
Pd_1/AlS–N	1.0	967	28	1.30	3.8	0.98	43	34
Pd_2/AlS–N	2.0	817	24	1.24	3.9	0.97	31	32
Pd_3/AlS–N	3.0	415	17	0.74	4.0	0.93	24	24

There was no significant change in micropore area for $Pd_{0.6}$/AlS–N compared to that of AlS–N sample suggesting the foreign metal resided in the mesopores, mainly 4–10 nm range. This decreased the corresponding pore volumes significantly, as discussed above. However, at higher loadings, all the other pores were also inaccessible to the adsorbent nitrogen molecules used in the characterization technique due to extensive blockage and resulted in more severe drop in all the pore volume values.

The XRD patterns of palladium and nitrogen co–doped templated carbons with different palladium loadings are shown in Figure 4.36(a). Only the 3 wt.% of palladium doped carbon showed peaks at 2Θ = 40.1°, 46.6° and 68° for diffraction planes of (111), (200) and (220) respectively corresponding to Pd° state (Giasafaki et al. 2012). The peaks due to PdO are reported in the literature at 33.9° (101), 42° (110), 54.5° (112), 60.69° (200) and 71.28° (202) (Lin et al. 2014; Ganji et al. 2013). These peaks were not detected for the present sample. Hence it can be concluded that supported palladium was mostly in the metallic state. This agreed with non–oxidative condition during the preparation of the samples. No palladium peak was observed in any of the samples with lower metal loadings, suggesting that the metal was in dispersed state. The intensity and sharpness of the graphite peak of carbon at 2Θ = 25° enhanced with increase in Pd loading, confirming the earlier observation that the presence of metals during CVD promoted the formation of the graphitic domain. Higher the content of palladium higher was the graphitic content. This result was also confirmed by Raman analysis.

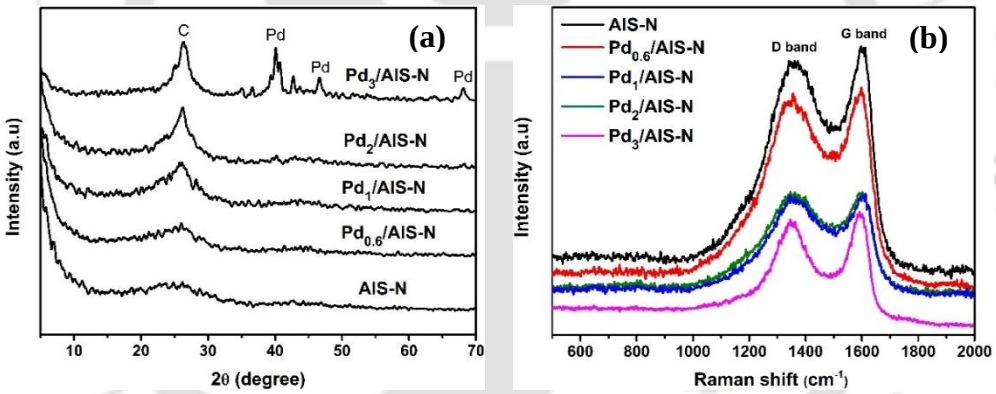

Figure 4.36: (a) XRD profiles (b) Raman spectra of palladium and nitrogen co–doped templated carbons with different palladium loadings.

The Raman patterns of doped templated carbons with different palladium loadings are shown in Figure 4.36(b). The I_G/I_D intensity ratio decreased with increased palladium loading (Table 4.23) suggesting more graphitic domain. It also agrees with the earlier observation that the presence of metals promoted the graphitic region.

The metal dispersion measured by CO–Chemisorption for palladium and nitrogen co–doped carbons was higher at lower palladium loading (Table 4.23). This phenomenon was in accordance with the formation of larger palladium clusters on the carbon surface, at higher palladium loading. Formation of larger cluster lowered the fraction of the total palladium exposed for interaction with incoming hydrogen molecules.

The TGA profiles of the palladium co–doped samples with various palladium loadings recorded in oxidized atmosphere are shown in Figure 4.37(a). All the palladium–doped samples showed major loss between 480–640 °C which corresponded to combustion of templated carbons. The gradual increase in residual mass with metal loading may be attributed to increased amount of metal oxide formed. The corresponding DTG profiles of the samples (Figure 4.37b) showed that with increase in palladium content the peak maxima shifted from 600 for AlS–N to lower temperature of 580, 554, 546 and 508 °C for 0.6, 1, 2 and 3 wt.% of palladium in the co–doped templated carbons respectively. This gradual ease of combustion confirmed the catalytic effect of metal on the oxidation reaction as was observed and discussed in the earlier section 4.1.6.

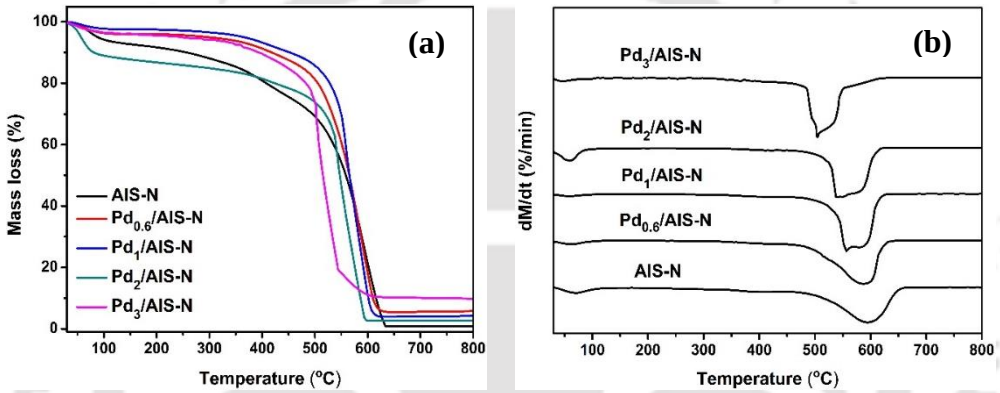

Figure 4.37: (a) TGA profiles (b) DTG profiles of palladium and nitrogen co–doped templated carbons with different Pd loadings.

The FESEM images of palladium and nitrogen co–doped carbons with different palladium loadings are shown in Figure 4.38. The overall morphologies of the samples were similar, but compactness and tangling of the tubular structures varied with palladium loading. Denser network was observed at lower palladium loading. The average tubular diameter increased with palladium content. The average tubular diameter was of 24, 26, 28 and 31 nm for 0.6, 1, 2 and 3 wt.% palladium co–doped samples, respectively.

The TEM images and corresponding particle size distribution of palladium and nitrogen co–doped carbons with different palladium loadings are shown in Figure 4.39. Mostly aggregated morphology was observed for all samples with interspersed tubular structure. The average palladium cluster size increased with palladium loading as observed from the particle size distributions (Figure 4.39) calculated using TEM images. The average metal size was 2.3, 2.6, 2.8, and 4.2 nm for palladium co–doped samples with 0.6, 1, 2 and 3 wt.% Pd, respectively. This agreed with the dispersion trend observed from CO–Chemisorption values.

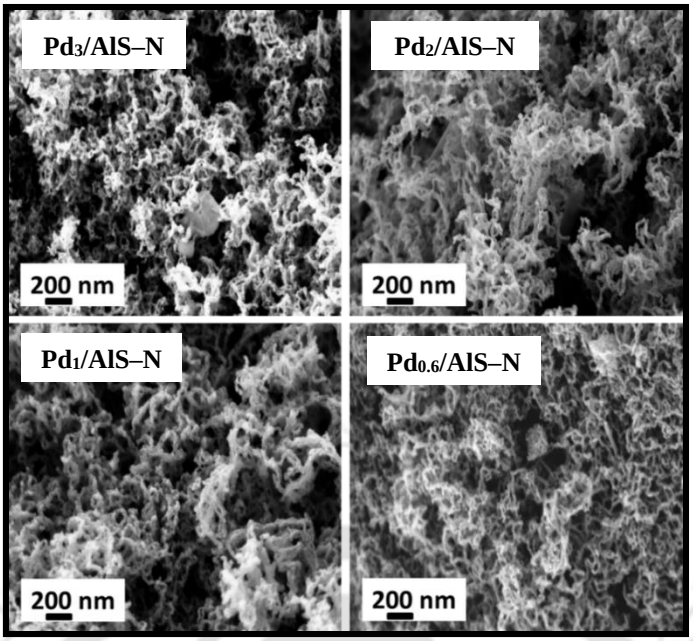

Figure 4.38: FESEM images of palladium and nitrogen co–doped templated carbons with different palladium loadings.

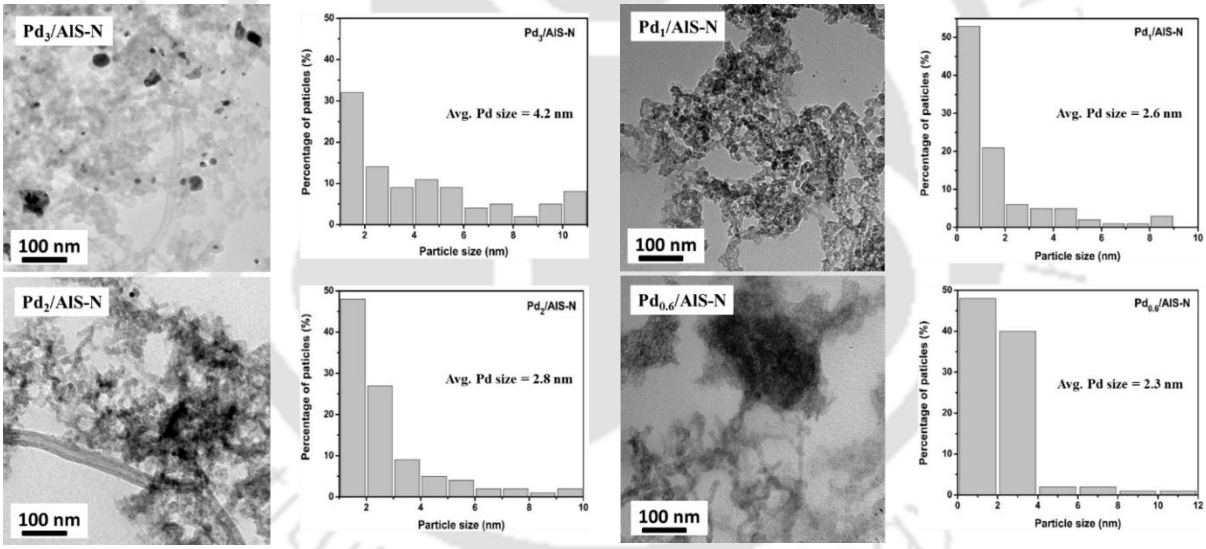

Figure 4.39: TEM images and corresponding particle size distribution for palladium and nitrogen co–doped templated carbons with different palladium loadings.

Hydrogen uptake

Hydrogen adsorption isotherms for palladium and nitrogen co–doped templated carbons with various palladium loadings at –196 °C are shown in Figure 4.40(a). The hydrogen uptake and surface area as function of palladium loadings are shown in Figure 4.40(b). The surface area steadily decreased with increasing palladium loading, but the hydrogen uptake was initially enhanced and thereafter reduced at further higher loading (Table 4.24). The maximum hydrogen uptake of 5 wt.% was observed for Pd_2/AlS–N with 2 wt.% Pd loading.

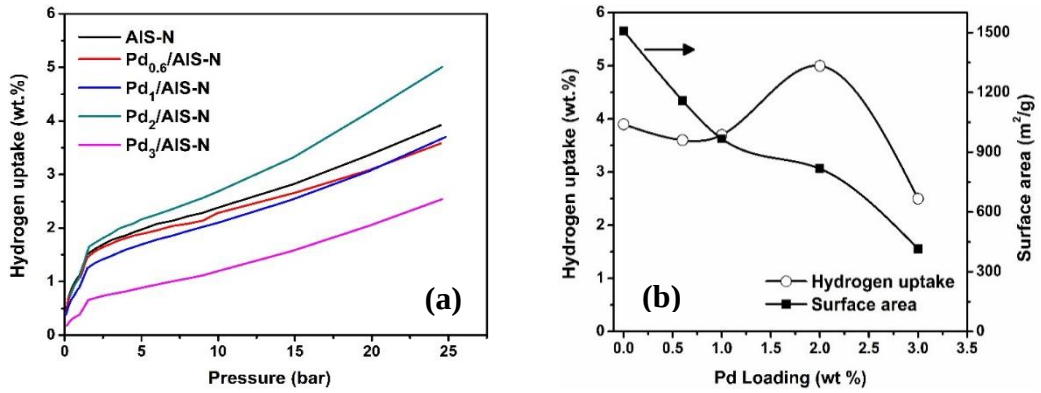

Figure 4.40: For palladium and nitrogen co–doped templated carbons with different palladium loadings (a) Hydrogen adsorption isotherms at –196 °C up to 25 bar (b) Variation of surface area and hydrogen uptake at 25 bar as a function of palladium loadings of samples.

The lower hydrogen uptake for 3 wt.% of palladium and nitrogen co–doped carbon may be attributed to various reasons including significantly lower surface area and lower metal dispersion. The increase in hydrogen uptake with palladium loading till 2 wt.% in spite of lowering of surface area may have resulted from the contribution of metal active sites towards hydrogen adsorption as discussed earlier.

Table 4.24: Hydrogen uptake capacity of palladium and nitrogen co–doped templated carbons with different palladium loadings at –196 °C.

Sample ID	Hydrogen uptake (wt.%)
	at 25 bar
Al–N	3.9
$Pd_{0.6}$/AlS–N	3.6
Pd_1/AlS–N	3.7
Pd_2/AlS–N	5.0
Pd_3/AlS–N	2.5

Summary

For palladium and nitrogen co–doped mesoporous templated carbons with various palladium loadings, the surface area and pore volume decreased with increasing palladium loading from 0.6 to 3.0 wt.%. The surface areas decreased from 1159 to 415 m^2/g and pore volumes dropped from 1.42 to 0.74 cm^3/g. The graphitic content increased with palladium loading. The overall morphologies of the samples were tubular, but compactness and tangling of the tubular structures varied with palladium loading. The average tubular diameter was of 24, 26, 28 and 31 nm for 0.6, 1, 2 and 3 wt.% palladium co–doped samples, respectively. The surface area

though steadily decreased with increasing palladium loading but the hydrogen uptake was initially enhanced till 2wt.% loading and thereafter reduced at further higher loading of 3 wt.%. The maximum hydrogen uptake of 5 wt.% was observed for Pd_2/AlS–N with 2 wt.% palladium loading. The enhancement of hydrogen uptake for 2 wt.% palladium co–doped sample in spite of lower surface area attributed to presence of additional metal active sites. The lower hydrogen uptake for 3 wt.% of palladium–doped carbon may be attributed to various reasons including significantly lower surface area and lower metal dispersion.

4.1.9 Effect of preparation methods for co–doped templated carbon

Among all the co–doped templated carbons, the 2 wt.% palladium and nitrogen co–doped alumina–SDS templated carbon (Pd_2/AlS–N) showed the highest hydrogen uptake capacity. This section discusses how the physicochemical and hydrogen uptake properties of this sample were affected when this sample was prepared by different methods. This co–doped adsorbent was originally prepared by impregnation of metal on template followed by deposition of carbon and nitrogen using CVD process (renamed as Pd/AlS–N_IMPB in this section). To see the effect of the preparation method, the same sample composition was prepared by three other methods. The second sample was prepared by first depositing the carbon and nitrogen on template using the CVD process. The resultant nitrogen doped carbon was impregnated with 2 wt.% Pd and represented as Pd/AlS–N_IMPA. In the third and fourth samples, palladium was incorporated by electroless deposition instead of impregnation in template before CVD or in nitrogen doped carbon after CVD as described for impregnated samples above. These two samples were denoted as Pd/AlS–N_EDB and Pd/AlS–N_EDA. The physical properties and hydrogen uptake capacities of these four samples were studied and compared to see the effect of preparation method.

Table 4.25: Elemental analysis of palladium and nitrogen co–doped templated carbons, prepared by different methods, using EDX.

Sample ID	Elements (wt.%)			
	Pd	C	N	O
Pd/AlS–N_IMPB	2.0	74.2	21.7	2.1
Pd/AlS–N_IMPA	2.1	69.3	24.3	4.3
Pd/AlS–N_EDB	2.2	71.9	22.8	3.1
Pd/AlS–N_EDA	2.2	70.2	23.4	4.2

IMPB & IMPA: Pd was impregnated before & after CVD process respectively, EDB & EDA: Pd incorporated by electroless deposition before & after CVD process respectively.

The elemental composition of the samples is summarized in Table 4.25. Average loadings of palladium in the final templated carbon samples were almost similar as intended, in the range of 2–2.2 wt.%. The nitrogen content varied in the range of 21.7–24.3 wt.%. The relative composition shows that the variations used in the preparation methods did not have significant effect on the decomposition of the precursors and hence on the final composition of the samples.

The nitrogen adsorption–desorption isotherms of all the co–doped carbons prepared by different methods are shown in Figure 4.41(a). The isotherms were similar in nature, type IV

with H2 hysteresis loop, for all the co–doped carbons.

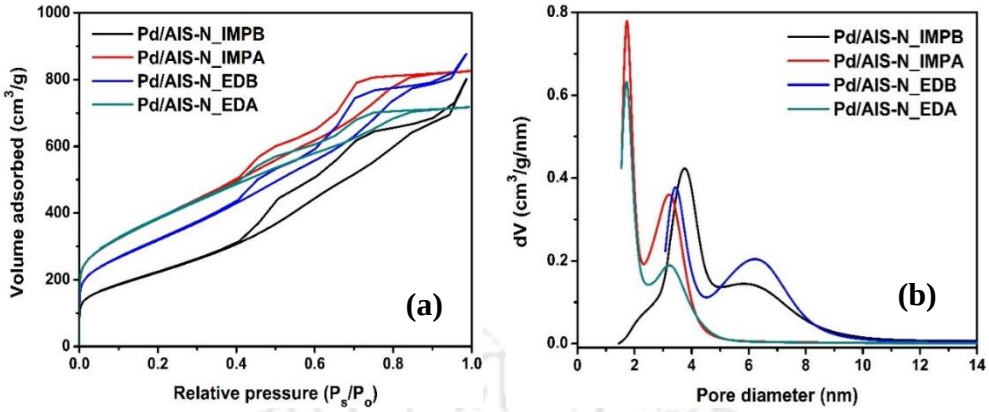

Figure 4.41: (a) N_2 adsorption–desorption isotherms (b) Pore size distributions of palladium and nitrogen co–doped templated carbons prepared by different methods.

The physical properties of the samples are included in Table 4.26. The BET surface area and pore volume of all the co–doped carbons were reduced with respect to undoped one and the extent of reduction depended on the preparation method. For the samples when palladium was incorporated before CVD, the surface area was lowered than that for the samples when metal was incorporated after CVD. This was observed for samples prepared both by impregnation and electroless deposition methods. When the metal was incorporated in nitrogen doped carbon after CVD process, irrespective of metal incorporation method, the final surface area was similar that is the surface areas of Pd/AlS–N_IMPA and Pd/AlS–N_EDA were almost similar as in 1371 and 1359 m^2/g respectively. The higher surface area of the above two samples can be explained as follows. The nitrogen doped carbon gave high surface area of 1508 m^2/g as discussed in section 4.1.4. On doping, this high surface area was reduced by around 150 m^2/g irrespective of the impregnation or electroless deposition method. It can be seen that dispersion of metal in these two samples was similar and lower than that in the samples in which metal was directly incorporated in templates before CVD. It can also be seen that incorporation of metals directly in nitrogen doped carbon reduced the pore volume in the range of 4–8 nm and simultaneously increased the micropore volume. This suggested residing of the metals in the mesopores in the range of 4–8 nm as was also observed earlier for metal doped carbon (Figure 4.29b). The micropore area was higher for samples when palladium was doped directly on the templated carbons prepared by both impregnation and electroless deposition methods. The micropore areas of the Pd/AlS–N_IMPA and Pd/AlS–N_EDA were 78 and 82 m^2/g, respectively.

When metal was incorporated in the template before CVD process, the doped metal actively influenced the vapor deposition and formation of carbon matrix. As it had been observed in earlier results of metal doped carbon, the presence of metal with in template before CVD gave better dispersion within carbon matrix, increased the graphitization level and degree of yield. The better dispersion of these two samples, for which metal was deposited before CVD, showed better dispersion (Table 4.26). All these had a combined effect of lowering the overall surface area and pore volume of co–doped carbons compared to nitrogen doped carbons. The total pore volume was comparable for all the samples (1.11–1.35 cm^3/g). Since the template was mesoporous, the samples showed very low micropores as expected.

Table 4.26: Physical properties of alumina–SDS templated palladium and nitrogen co–doped carbons prepared by different deposition methods.

Sample ID	Surface area (m^2/g)	Micropore area (m^2/g)	Pore volume (cm^3/g)	Average pore size (nm)	I_D/I_G ratio	Metal dispersion (%)
Pd/AlS–N_IMPB	817	24	1.24	3.9	0.96	31
Pd/AlS–N_IMPA	1371	78	1.28	1.7	1.00	27
Pd/AlS–N_EDB	1160	33	1.35	3.7	0.98	31
Pd/AlS–N_EDA	1359	82	1.11	1.7	1.12	25

IMPB & IMPA: Pd was impregnated before & after CVD process respectively, EDB & EDA: Pd incorporated by electroless deposition method before & after CVD process respectively.

The pore size distributions of samples as given in Figure 4.41(b) showed difference in nature of pore distribution depending on whether the metal was incorporated before or after the CVD process. The co–doped samples prepared by incorporation of metal in nitrogen doped carbon after the CVD showed presence of both micropores and mesopores. When the co–doped carbons were prepared by doping metal on template before CVD, only mesopores was observed in the final co–doped samples. These effects were observed irrespective of the metal incorporation methods. The average pore size also depended on the step of incorporation of the metal. The samples for which metal was incorporated in the template before CVD the average pore size was higher. This was observed for both the incorporation techniques of metals and interestingly the values were also similar as observed for Pd/AlS–N_IMPA and Pd/AlS–N_EDA. For the samples prepared by doping metal on nitrogen doped carbons after CVD process that is for Pd/AlS–N_IMPB and Pd/AlS–N_EDB, the values were also similar and lower.

The XRD profiles of the co–doped templated carbons synthesized using different methods are shown in Figure 4.42(a). The XRD peak for all the samples was observed at 26° which

corresponded to the graphitic plane (002). The slightly higher peak intensity was observed for co–doped templated carbons when palladium was incorporated in the template before CVD compared to that when the metal was incorporated in nitrogen doped carbon after CVD. This was observed for samples prepared both by impregnation and electroless deposition methods. The peaks related to palladium were not found in any of the samples which indicated the palladium to be in dispersed state. The metal dispersion determined by CO–Chemisorption showed higher and similar dispersion for Pd/AlS–N_IMPB and Pd/AlS–N_EDB samples. The other two samples prepared by doping metals after CVD process showed similar values but lower than that for Pd/AlS–N_IMPB and Pd/AlS–N_EDB samples.

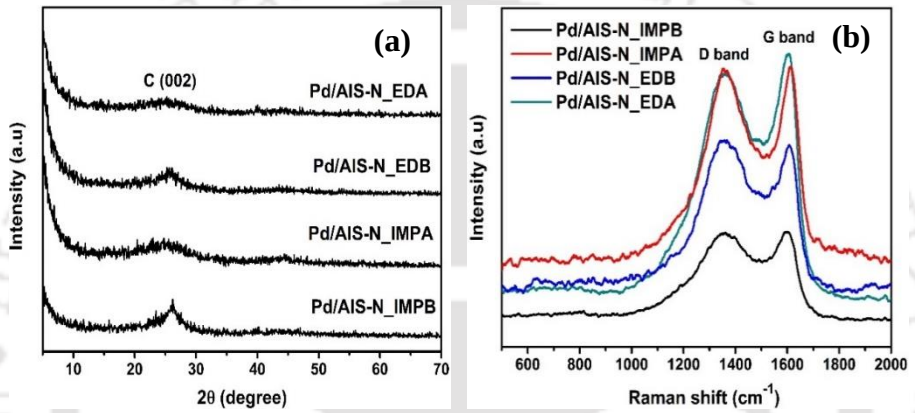

Figure 4.42: (a) XRD profiles (b) Raman spectra of palladium and nitrogen co–doped templated carbons prepared using different methods.

The Raman profiles for all the co–doped templated carbons prepared using different methods are shown in Figure 4.42(b). The D and G bands for all the samples were observed in the range of 1341–1351 cm^{-1} and 1598–1603 cm^{-1} respectively. The intensity ratio (I_D/I_G) was determined to be 0.96, 0.98, 1.0 and 1.12 for Pd/AlS–N_IMPB, Pd/AlS–N_EDB, Pd/AlS–N_IMPA and Pd/AlS–N_EDA doped carbons, respectively (Table 4.26). Lower I_D/I_G ratio was observed for samples prepared by incorporation of metal in the template before CVD process, suggesting higher degree of graphitization as was also observed from XRD results. This result agreed with the earlier observations that presence of metal during the CVD process resulted in greater graphitic domain in the samples. In this case though the samples, in which the metal was incorporated after CVD in nitrogen doped carbon, were further given a heat treatment at 400 ^oC, there was no further structural rearrangement.

Figure 4.43 shows the FESEM images of all the co–doped templated carbons prepared using different methods. The co–doped carbons for which metal was introduced in the template

before CVD process, tubular structures were observed with diameter of 28 nm for Pd/AlS–N_IMPB and 22 nm for Pd/AlS–N_EDB. No tubular structures were observed when metal was doped on the nitrogen doped carbon after CVD process, rather agglomerated structure was observed characteristics of nitrogen doped carbons (Figure 4.14). This difference in morphology because of change in metal incorporation sequence was observed for both in case when metals were incorporated by impregnation or electroless deposition methods.

The TEM morphology of all the samples is shown in Figure 4.44. The TEM images showed agglomerated form interspersed with tubular structure when palladium was introduced in the template before CVD process for Pd/AlS–N_IMPB and Pd/AlS–N_EDB samples. The TEM images agreed with that observed from FESEM images. Tubular structure was generated in Pd/AlS–N_IMPB and Pd/AlS–N_EDB due to presence of the metal during deposition by CVD, which agreed with earlier observation for metal doped carbons. When metal was incorporated in nitrogen doped carbon after CVD deposition, the agglomerated nature of nitrogen doped carbon was retained as was also observed from corresponding FESEM images of Pd/AlS–N_IMPA and Pd/AlS–N_EDA. The metal size distribution of the samples determined from TEM image analysis is plotted in Figure 4.44. It can be seen that for co–doped carbons when metal was incorporated in the nitrogen doped carbons after CVD, the larger average particle size was observed irrespective of metal incorporation technique. For Pd/AlS–N_IMPA and Pd/AlS–N_EDA, the average metal size was obtained as 3.8 and 4.0 nm respectively. When co–doped samples were prepared by metal addition in the template before CVD, lower average particle size was observed; 2.3 nm for Pd/AlS–N_EDB and 2.8 nm for Pd/AlS–N_IMPB. The particle size distribution plots also show that the most uniform and narrow distribution was obtained when metal was incorporated in template by electroless deposition method before CVD process that is for Pd/AlS–N_EDB. More broader and heterogeneous distribution of particle was observed for samples in which the metal was incorporated in nitrogen doped carbon after the CVD process. The larger average particles suggested lower metal dispersion for samples when metal was incorporated directly on carbon after CVD process. The lower dispersion values of these samples as obtained from CO–Chemisorption study (Table 4.26) corroborated the results.

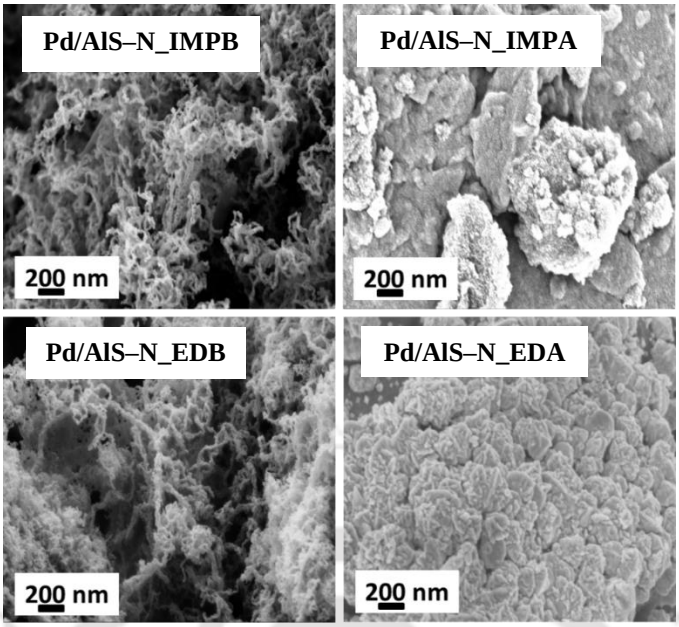

Figure 4.43: FESEM images of palladium and nitrogen co–doped templated carbons prepared using different methods.

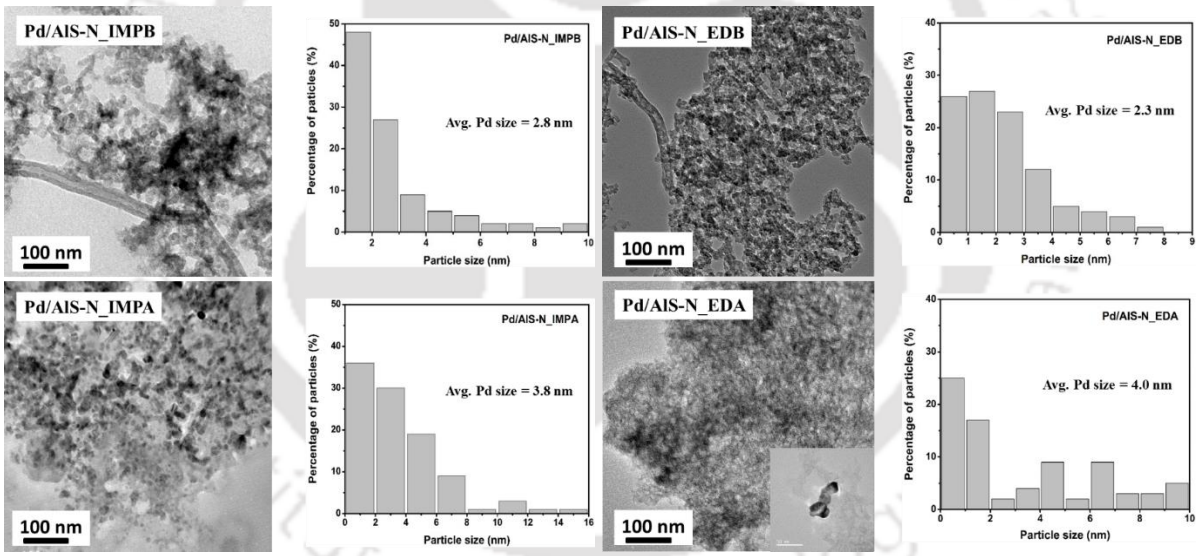

Figure 4.44: TEM images and corresponding particle size distribution of palladium and nitrogen co–doped templated carbons prepared using different methods.

Hydrogen uptake

Figure 4.45(a) shows hydrogen adsorption isotherms at –196 °C up to 25 bar for the co–doped carbons prepared by different methods. The higher hydrogen uptake capacity was achieved for co–doped templated carbons prepared by incorporation of metal into the template before CVD process. This was observed for both the samples prepared by impregnation and electroless deposition methods, Pd/AlS–N_IMPB and Pd/AlS–N_EDB samples. This was observed in

spite of lower surface area of these samples compared to that of prepared by incorporation of metal after CVD. Hydrogen uptake capacity of the samples included in Table 4.27.

Table 4.27: Hydrogen uptake capacity of palladium and nitrogen co–doped templated carbons prepared by different methods at –196 °C.

Sample ID	Hydrogen uptake (wt.%) at 25 bar
Pd/AlS–N_IMPB	5.0
Pd/AlS–N_IMPA	4.38
Pd/AlS–N_EDB	4.98
Pd/AlS–N_EDA	4.44

The highest uptake capacity was shown by Pd/AlS–N_IMPB (5.0 wt.%) followed by Pd/AlS–N_EDB (4.98 wt.%). The hydrogen uptake capacity of 4.38 wt.% obtained for Pd/AlS–N_IMPA and 4.44 wt.% for Pd/AlS–N_EDA was obtained. The results suggested that for doped carbon presence of metal played more significant role than surface area. The higher metal dispersion of Pd/AlS–N_IMPB and Pd/AlS–N_EDB samples may have resulted in comparatively higher hydrogen uptake in spite of lower surface area. The smaller particle size provided more number of the active sites for hydrogen adsorption. Tubular structure of these samples may also have contributed to higher hydrogen adsorption value.

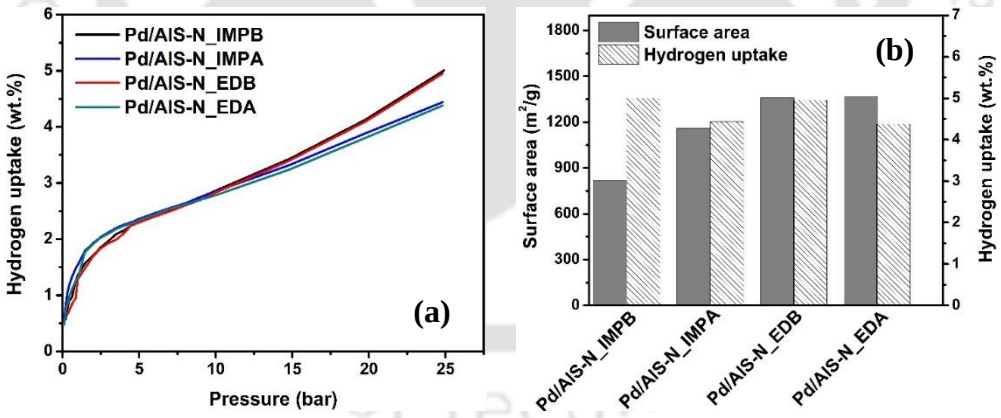

Figure 4.45: For palladium and nitrogen co–doped templated carbons prepared with different methods (a) Hydrogen adsorption isotherms at –196 °C up to 25 bar (b) Hydrogen uptake at 25 bar and –196 °C.

The results from this study suggested that the sequence of metal incorporation before or after CVD process affected the physical properties and thereby hydrogen uptake. Incorporation of metal in template before CVD resulted in more dispersed metals deep within the porous network resulting in lower metal size but also lower surface area. Also, the presence of metal

within template during CVD facilitated the formation of tubular structure. Both higher metal dispersion and tubular structure resulted in higher hydrogen uptake of the Pd/AlS–N_IMPB and Pd/AlS–N_EDB samples in spite of their lower surface areas. On comparing the two techniques of metal incorporation on substrate, impregnation or electroless deposition, it was observed that the difference was not that significant. Though, the electroless deposition method gave more uniform and narrower particle size distribution and lowest average particle size. Their surface area was also higher or comparable compared to that of samples prepared by the impregnation method.

Summary

The alumina–SDS templated 2 wt.% palladium and nitrogen co–doped carbon (Pd_2/AlS–N) was prepared by varying the sequence and method of metal incorporation. The final average loadings of palladium in the templated carbons were obtained in the range of 2–2.2 wt.%. The BET surface area and pore volume of all the co–doped carbons were reduced with respect to undoped one and the extent of reduction depended on the preparation method. The highest reduction in surface area was observed when Pd was initially doped on template followed by carbon vapour deposition as in Pd/AlS–N_IMPB. It was decreased from 1508 m^2/g for nitrogen doped to 836 m^2/g for co–doped templated carbon. The tubular structures were observed with diameter of 28 nm for Pd/AlS–N_IMPB and 22 nm for Pd/AlS–N_EDB. However, no tubular structures were observed for Pd/AlS–N_IMPA and Pd/AlS–N_EDA samples in which metal was incorporated directly in templated carbon obtained by carbon vapour deposition. The average metal size was obtained in the range of 2.3–4.0 nm for all the samples. The hydrogen uptake of 5.0 and 4.98 wt.% was observed for Pd/AlS–N_IMPB and Pd/AlS–N_EDB respectively. These values were higher than that of the Pd/AlS–N_IMPB and Pd/AlS–N_EDB. This result was obtained in spite of lower surface area of the former. The higher uptake may be attributed to higher metal dispersion, higher average pore size and presence of tubular structure for the Pd/AlS–N_IMPB and Pd/AlS–N_EDB samples.

4.2 Graphene based materials

The graphene based materials were prepared from graphite oxide by two methods; chemical reduction and thermal exfoliation. The effect of exfoliation temperature on properties of exfoliated graphene oxide (EGO) was studied by varying the temperature between 200–500 ^{o}C in a hydrogen atmosphere. The effect of exfoliation atmosphere was studied by varying the carrier gas. Reductive, inert and oxidative atmospheres were created by using hydrogen, argon and air respectively as the carrier gas. The metals were incorporated in graphene oxide before reduction or exfoliation to prepare doped graphene based materials. The physicochemical properties of the samples were determined by various characterization techniques including FTIR, UV–Vis, XPS, surface area and pore analyzer, XRD, Raman Spectroscopy, TGA, AFM, EDX, FESEM, and TEM. The hydrogen storage properties of the prepared samples were determined at –196 °C at 30 bar by volumetric adsorption analysis.

4.2.1 Analysis of graphite

Graphite was used as the starting material. The different characterization details of graphite are shown in Figure 4.46. The graphite contained 97.4 % carbon (Figure 4.46a). The TGA/DTG profile of the graphite recorded in nitrogen flow is shown in Figure 4.46 (b). The graphite was stable up to 750 °C, thereafter 4 % mass loss was observed till 900 °C. The high–intensity XRD peak at 2θ = 26.5° (Figure 4.46c), corresponded to the hexagonal graphitic plane (002) with a d–spacing of 0.337 nm (Divya et al. 2014). The high peak intensity indicated the layered crystalline structure of graphite. In the Raman spectrum of graphite, as shown in Figure 4.46(d), the sharp G band peak was observed at 1582 cm^{-1}. The 2D band appeared at 2726 cm^{-1} and this second order of D band corresponded to two–phonon lattice vibrational process (Abdelkader et al. 2015). The absence of D band suggested that defects were very low in the graphite. The type–II isotherm with H4 hysteresis loop indicated the presence of slit–shaped pores. The pores were in the broad range of 0.8 to 30 nm with very low pore volume (Figure 4.46f). The graphite had a very low surface area of 14 m^2/g and pore volume of 0.05 cm^3/g. The FESEM image of graphite showed heterogeneous layered structure, whereas the TEM image resembled dense plate like structure (Figure 4.46g and h).

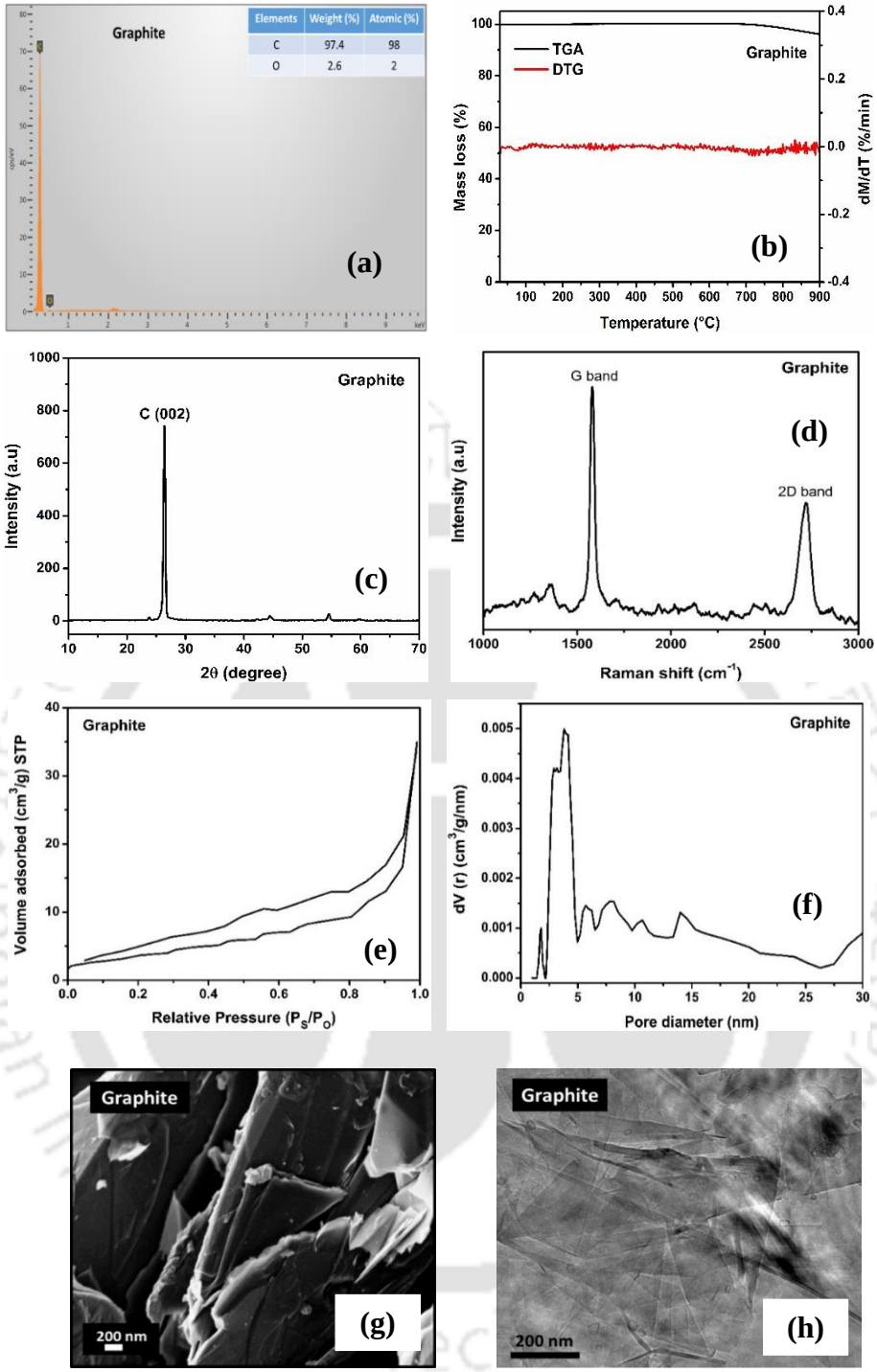

Figure 4.46: Physicochemical properties of graphite (a) EDX spectrum (b) TGA/DTG profiles (c) XRD spectrum (d) Raman spectrum (e) N_2 adsorption–desorption isotherm (f) Pore size distribution (g) FESEM image (h) TEM image.

4.2.2 Analysis of graphene oxide (GO)

The GO was prepared from graphite by modified Hummer's method. The properties of prepared GO was determined by different characterization techniques and all the results are shown in Figure 4.47. The EDX spectrum and corresponding elemental analysis of GO are shown in Figure 4.47(a) and Table 4.28, respectively. The oxygen content in GO, resulting from oxygen–containing surface functional groups, was 39.8 wt.%. The corresponding C/O ratio was 2.01. The TGA/DTG profile, recorded in flow of inert nitrogen, (Figure 4.47b) showed a weight loss of nearly 14 % as the sample was heated to the temperature of 100 °C. This loss may be attributed to moisture removal. Thereafter rapid weight loss of around 40 % was observed between 150 to 250 °C. This weight loss may be assigned to the removal of oxygen–rich functional groups in form of CO, CO_2 and/or H_2O vapor (Botas et al. 2013). This was also observed when samples were subjected to TPD analysis in different carrier gases (Appendix Figure D1). All the TPD profiles showed a peak in the range of 170–250 °C, which may be attributed to the evolution of carbon oxides and water vapour originated from the removal of the oxygen–containing surface functional group. In the TGA profile after 250 °C, the continuous and gradual mass loss of about 21 % was observed as the sample was heated up to 900 °C, suggesting gradual removal of residual surface functional groups. The GO showed an XRD peak at 10.7° (Figure 4.47c), which corresponded to the graphitic plane (002). The d–spacing was 0.849 nm. The Raman spectra (Figure 4.47d) showed the peaks at 1346 and 1589 cm^{-1} corresponding to D and G bands respectively. The I_D/I_G intensity ratio was 0.99. The nitrogen isotherm (Figure 4.47d) was of type II. The hysteresis loop was of H4 type and usually associated with slit–shaped pores. The BET surface area of GO was 41 m^2/g. The total pore volume was 0.14 cm^3/g. The GO exhibited mainly microporous character (pore range 0.5 to 3 nm) as can be observed in Figure 4.47(f). The average pore size was 1.8 nm. The FESEM and TEM images, in Figure 4.47(g) and (h) respectively, showed heterogeneous layered structures. The oxygen content increased from 2.6 wt.% in graphite to 39.8 wt.% after oxidation to graphene oxide. This may be attributed to the incorporation of oxygen–containing functional groups on the graphite surface in between layers. This increased the layer separation from 0.337 nm for graphite to 0.849 nm for GO. The surface area was enhanced from 14 for graphite to 41 m^2/g for GO and pore volume increased from 0.05 to 0.14 cm^3/g (Table 4.29). In Raman spectrum of GO, the new D–band observed after oxidation corresponded to the defects created by presence of surface functional groups (Zhou et al. 2016). The GO also showed heterogeneous layered structures but less dense compared to that of graphite.

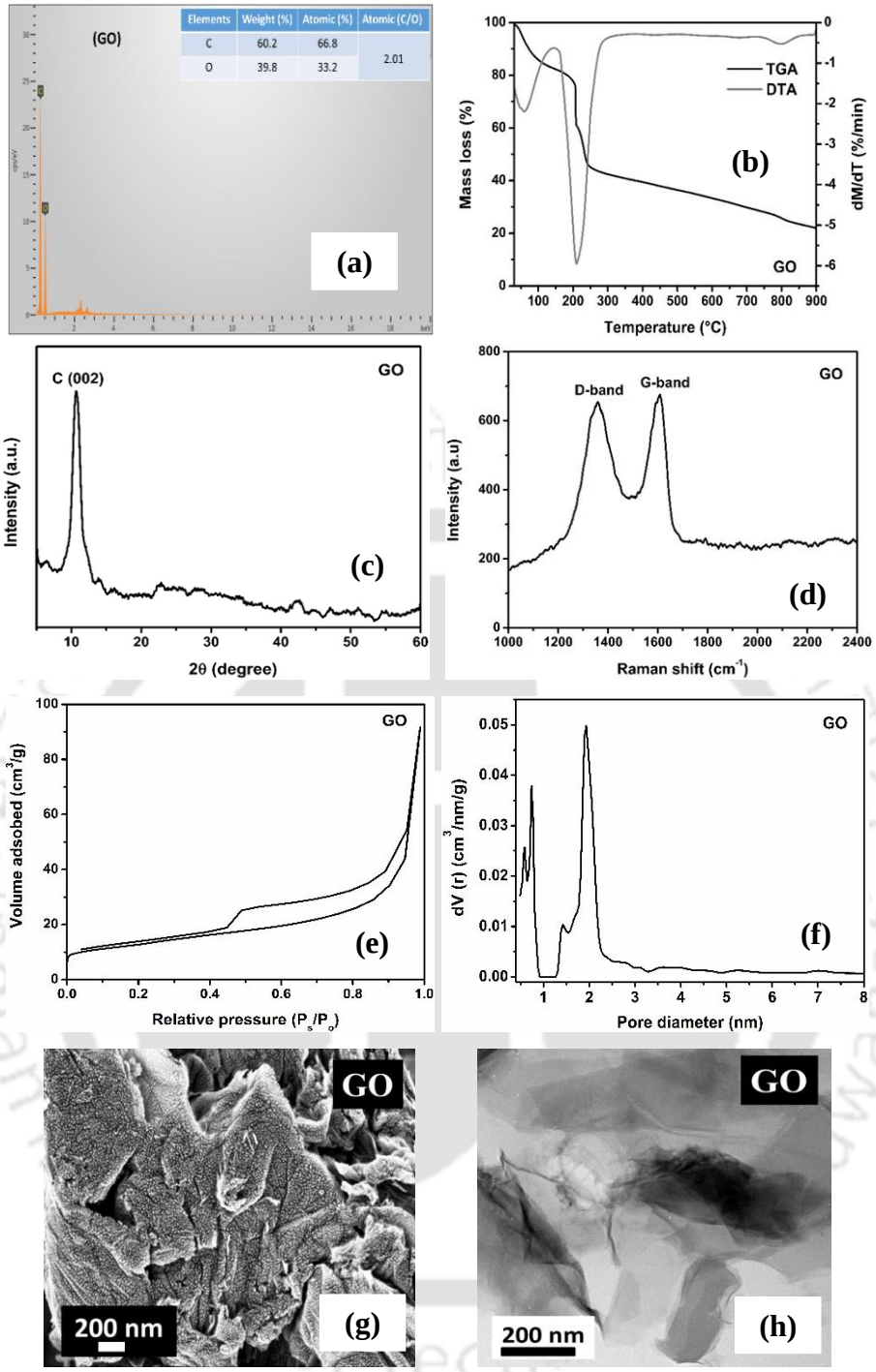

Figure 4.47: Physicochemical properties of graphene oxide (a) EDX spectrum (b) TGA/DTG profile (c) XRD spectrum (d) Raman spectrum (e) N_2 adsorption–desorption isotherm (f) pore size distribution (g) FESEM image (h) TEM image.

4.2.3 Effect of exfoliation temperature on GO

This section explores the structural changes experienced by GO as exfoliation temperature is increased from 200 to 500 °C in hydrogen atmosphere. The effect of these structural changes on hydrogen storage properties of exfoliated GO has been discussed. The hydrogen storage characteristics were measured at –196 °C up to moderate pressure of 30 bar. The exfoliated samples are represented in this section as EGO(x) where x is the corresponding exfoliation temperature.

The FTIR spectra of graphite and GO are compared in Figure 4.48. The peaks due to oxygen–containing functional groups were observed for GO sample at 1377 and 1760 cm^{-1} corresponding to the O–H deformation of the C–OH groups and C=O stretching vibration of –COOH groups respectively (Tang et al. 2012). The peak at 1760 cm^{-1} is mainly related to the ketone group (Tang et al. 2012; Das et al. 2014). The expected peaks at 1720, 1620 and 1278 cm^{-1} for carboxylic, carboxyl and epoxide groups respectively, (Das et al. 2014; Abdolmaleki et al. 2016) were not observed in the prepared GO which may be attributed to their low concentration, if present.

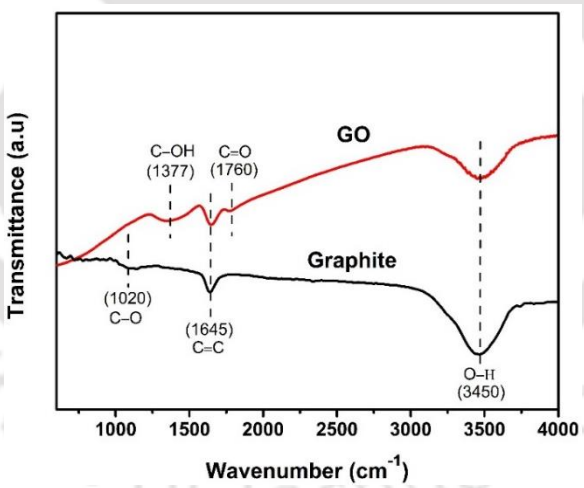

Figure 4.48: FTIR spectra of graphite and graphene oxide (GO).

The EDX composition of the GO and exfoliated GO samples are compared in Table 4.28. The oxygen content of all the exfoliated GO samples was reduced compared to that of GO. Consequently, the corresponding C/O ratio of the exfoliated GO samples increased significantly in comparison to GO. As the exfoliation temperature varied from 200 to 500 °C, the carbon content increased from 77.4 to 81.8 wt.%. The oxygen content, on the other hand, decreased from 22.6 to 18.2 wt.%. The corresponding C/O ratio of the samples increased from 4.55 to 6.0,

with exfoliation temperature. These results suggested more effective removal of oxygen–containing surface functional groups with the increase in the exfoliation temperature.

Table 4.28: Elemental analysis of GO and exfoliated GO samples using EDX.

Sample ID	Elements atomic (wt.%)		
	C	O	C/O
GO	66.8	33.2	2.01
EGO (200)	82.0	18.0	4.55
EGO (300)	83.7	16.3	5.13
EGO (400)	84.9	15.1	5.62
EGO (500)	85.7	14.3	6.00

The TGA and the corresponding DTG profiles of all the exfoliated samples recorded in nitrogen flow are shown in Figure 4.49(a) and (b). The mass loss observed below 100 °C, as discussed earlier, mainly resulted from the removal of absorbed moisture. The small peaks observed at around 280 °C are attributed to the removal of residual oxygen–containing functional groups that were present after exfoliation. The mass loss was slightly lower for samples exfoliated at higher temperatures.

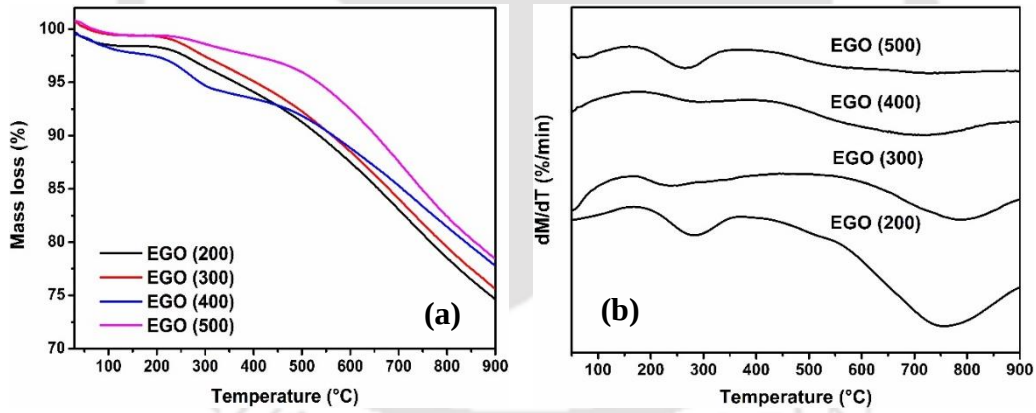

Figure 4.49: (a) TGA profiles (b) DTG profiles of exfoliated GO samples prepared at different temperatures.

The mass losses of around 23.8, 22.4, 21.7 and 20.5 % were observed for EGO(200), EGO(300), EGO(400) and EGO(500) samples, respectively. The comparatively higher mass loss observed for EGO(200) sample during TGA suggested higher content of residual surface oxygen in the sample in agreement with EDX analysis. The higher oxygen content of EGO(200) may have resulted from the least effective removal of surface functional groups during exfoliation at the lowest temperature. The lowest mass loss observed for the EGO(500) sample during TGA suggested the presence of the lowest amount of residual oxygen after exfoliation at highest

temperature. The lowest amount of oxygen was also observed from the EDX analysis for this sample. However, comparison of mass loss at 200 and 500 °C showed that the difference was not much, suggesting that most of the removal of functional groups did happen at 200 °C. This observation agreed with the TGA analysis of GO sample, where the major weight loss was observed between 150 to 250 °C (Figure 4.49b).

Figure 4.50 shows the FTIR profiles of GO and exfoliated GO samples prepared at different temperatures. The oxygen–containing functional groups were observed for GO at 1166, 1376 and 1740 cm^{-1} which corresponded to C–O, C–OH and C=O groups respectively (He et al. 2015; Tang et al. 2012). These oxygen–containing functional groups were embedded on graphene surface in–between layers during the oxidation process. Upon exfoliation of GO, the 1166 and 1376 cm^{-1} peak disappeared for EGO samples and only very low intensity peak at 1740 cm^{-1} was observed for samples exfoliated at 200 and 300 °C. As exfoliation temperature was increased further to 400 and 500 °C, the peak at 1740 cm^{-1} also disappeared. The results agreed with the observation from other characterization techniques that more effective removal of oxygen–containing functional groups occurred at higher exfoliation temperatures. All the samples showed two peaks at 1612 and 3446 cm^{-1} corresponding to C=C and O–H functional groups respectively. The intensity of the 3446 cm^{-1} also decreased at higher temperature.

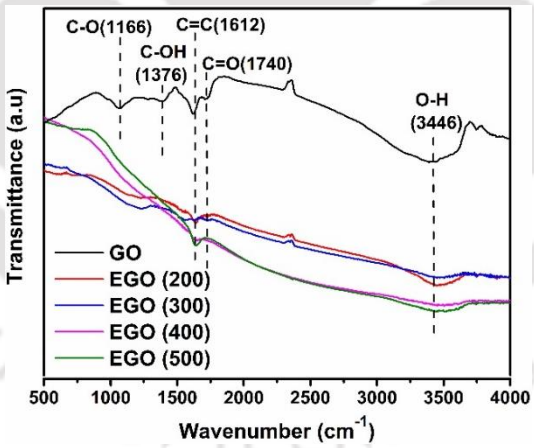

Figure 4.50: FTIR profiles of GO and exfoliated GO samples prepared at different temperatures.

Figure 4.51(a) and (b) shows the C1s and O1s XPS profiles for GO samples exfoliated at 300 and 500 °C. The surface C1s XPS spectra of the samples are further illustrated in Figure 4.51(c) and (e). The peak at 284.7 eV is designated to binding energy of C–C sp^2 bond (Hu et al. 2015; Shin et al. 2014). The deconvolution of C1s peak showed the presence of peaks for oxygen–containing functional groups at 286.4 and 287.8 eV corresponding to C–O (epoxy and hydroxyl groups) and C=O (carbonyl) respectively (Hu et al. 2015; Shin et al. 2014).

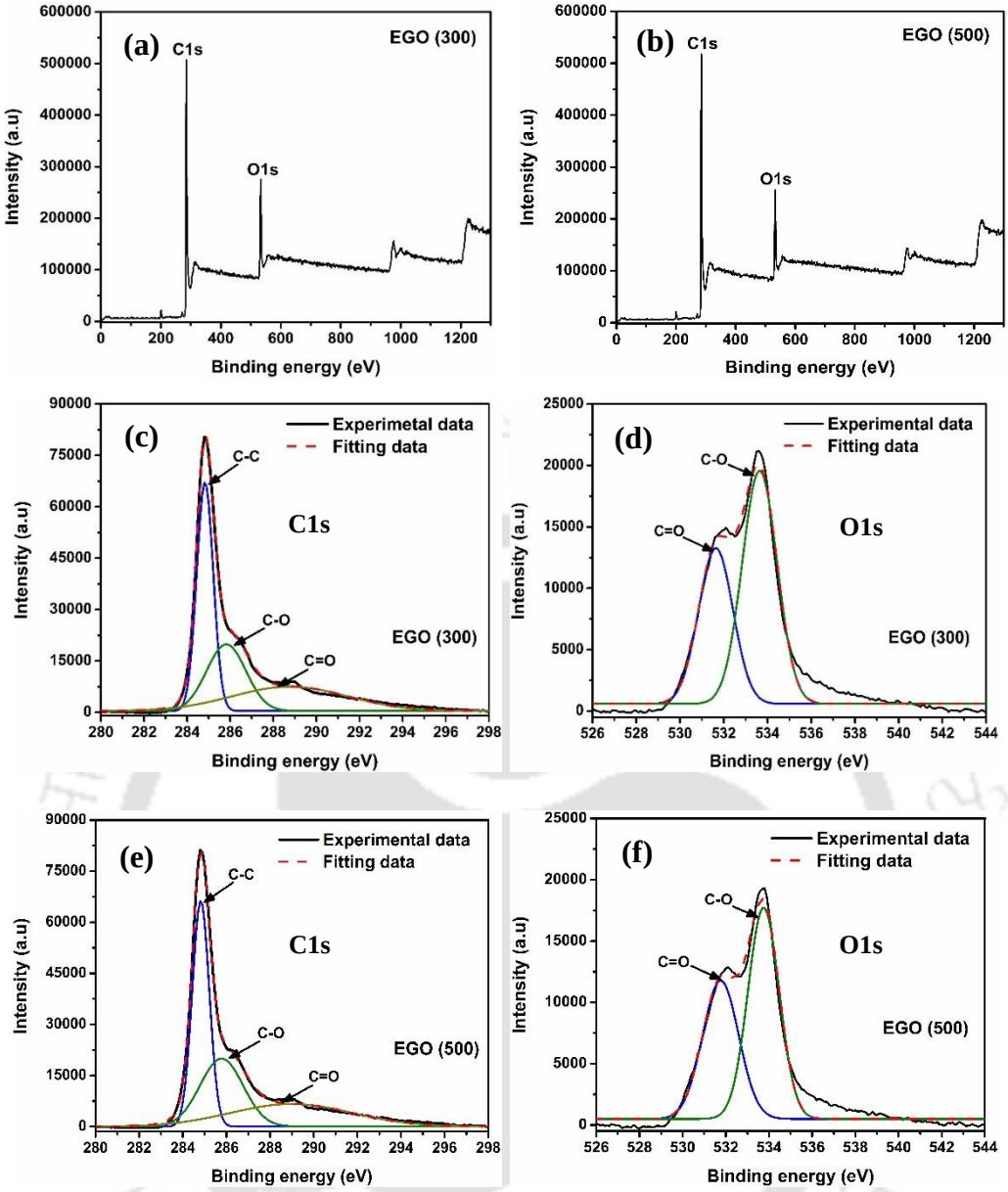

Figure 4.51: (a) Overall XPS profiles of GO exfoliated at 300 °C (b) Overall XPS profiles of GO exfoliated at 500 °C (c) C1s profile of GO exfoliated at 300 °C (d) O1s profiles of GO exfoliated at 300 °C (e) C1s profile of GO exfoliated at 500 °C (f) O1s profile of GO exfoliated at 500 °C.

These results are in a good agreement with the FTIR result shown in Figure 4.50. The presence of oxygen–containing functional groups in the EGO(300) and EGO(500) samples were also indicated by O1s peaks in Figure 4.51(d) and (f) respectively. Both the samples showed two peaks at 331.6 and 333.5 eV which are assigned to C=O and C–O respectively (Gupta et al. 2017). The comparison of the peak intensity of O1s showed a higher intensity for EGO(300) compared to that of the EGO(500) sample. In fact, the C/O ratios determined from XPS profiles were 5.10 and 5.94, respectively, for EGO(300) and EGO(500) samples. These results agreed with the of C/O ratios determined from EDX analysis which showed values of 5.13 and 6.0

respectively for EGO(300) and EGO(500). Thus the presence of higher amount of oxygen–containing functional groups in the EGO(300) sample was confirmed.

Figure 4.52(a) shows the XRD profiles of exfoliated GO samples prepared at different temperatures. Lattice spacing, crystal size and number of layers as determining from XRD profiles are tabulated in Table 4.29. All the exfoliated GO samples showed a broad peak at 24.8° corresponding to the graphitic zone plane (002). The d–spacing of the exfoliated samples were obtained in the range of 0.37 to 0.42 nm, values lower than that of GO (0.849 nm). It can be attributed to the elimination of surface functional groups intercalated between the layers.

The lowering of the d–spacing even for sample exfoliated at 200 °C confirmed the removal of surface functional groups at this temperature. However, a slight increase in d–spacing with further increase in exfoliation temperature suggested partial damage/breakage of layers at higher temperatures. This may be associated with thermal C–C bond breakage and formation of carbon oxides at higher temperature facilitated by residual surface oxygen–containing functional groups. All the samples showed a broader graphitic peak of low intensity, suggesting an overall lower graphitic zone. However, with the rise in exfoliation temperature from 200 to 500 °C, an increase in peak intensity suggested enhancement in graphitic nature (Figure 4.52b).

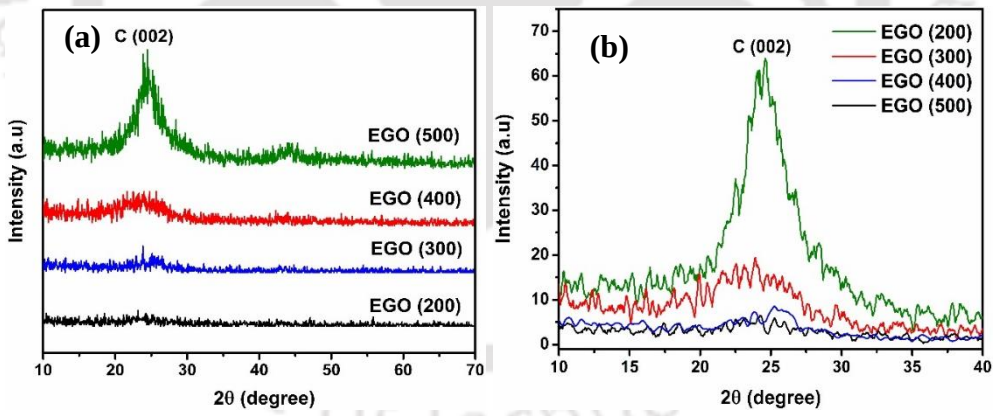

Figure 4.52: (a) XRD profiles of exfoliated GO samples prepared at different temperatures (b) Blown up XRD profiles in the range of 10°–40° for the same samples.

The number of layers in the graphitic structure was calculated from equation 2 given in the experimental section (Botas et al. 2013) $N_L = \frac{D_c}{d_{(002)}} + 1$ (2)

Here, N_L and $d_{(002)}$ represent the number of layers and spacing between the layers, respectively. D_c, the average crystal size of the graphitic zone calculated from the Debye–Scherrer equation (Appendix F).

Table 4.29: Physical and structural properties of graphite, graphene oxide (GO) and exfoliated GO (EGO) samples.

Sample ID	$d_{(002)}$ (nm)	N_{lX}	N_{lA}	A_F	S_{BET} (m^2/g)	V_T (cm^3/g)	A_P (nm)	I_D/I_G ratio
Graphite	0.337	–	–	–	14	0.05	3.8	–
GO	0.849	–	–	–	41	0.14	1.8	0.99
EGO (200)	0.372	2	5	2.2	46	0.27	2.0	0.98
EGO (300)	0.414	3	4	1.6	248	1.63	4.1	0.96
EGO (400)	0.420	5	3	1.4	218	1.40	3.9	0.94
EGO (500)	0.423	6	3	1.30	135	0.85	2.0	0.90

$d_{(002)}$: Spacing between the layers determined by XRD ; N_{lX} –: Number of layers determined by XRD ; N_{lA} – Number of layers determined by AFM ; A_F – Average thickness of layers determined by AFM ; S_{BET} : BET surface area ; V_T : Total pore volume ; A_P : Average pore size ; I_D/I_G ratio from Raman analysis.

The AFM topography images and the height profiles are included in Figure 4.53. The average thickness and number of graphene layers of exfoliated GO samples were also calculated from AFM analysis and tabulated in Table 4.29. The average thickness of samples was in the range of 1.3–2.2 nm and corresponding layers were 2–5. The calculation of number of layers was based on the reported theoretical average thickness of 0.40 nm for single–layer graphene (Pu et al. 2009; Stankovich et al. 2006). It was observed that the average thickness decreased with increase in exfoliation temperature of GO. The lower average thickness of samples prepared at higher exfoliation temperatures may be attributed to several factors including more effective removal of surface functional groups and higher separation of layers at higher temperature.

The degree of disorder and defects in the GO and exfoliated GO samples prepared at different temperatures were evaluated by Raman spectroscopy. Figure 4.54 shows the Raman spectra of samples that have been recorded between 1000 to 2400 cm^{-1}. The D–band observed between 1357–1361 cm^{-1}, resulted from defects present in the graphitic structure (Zhou et al. 2016). The appearance of D–band in exfoliated GO samples may be associated with modification during thermal treatment of GO. The G–band at 1592–1603 cm^{-1} has been assigned to in–plane stretching of symmetric sp^2 carbon atoms. The lower intensity of D and G bands for exfoliated GO samples compared to that of GO (Figure 4.54), suggested that GO had more disorder in its structure and more distortion of carbon layers. It may be attributed to the existence of the high amount of intercalated oxygen–containing functional groups in the GO.

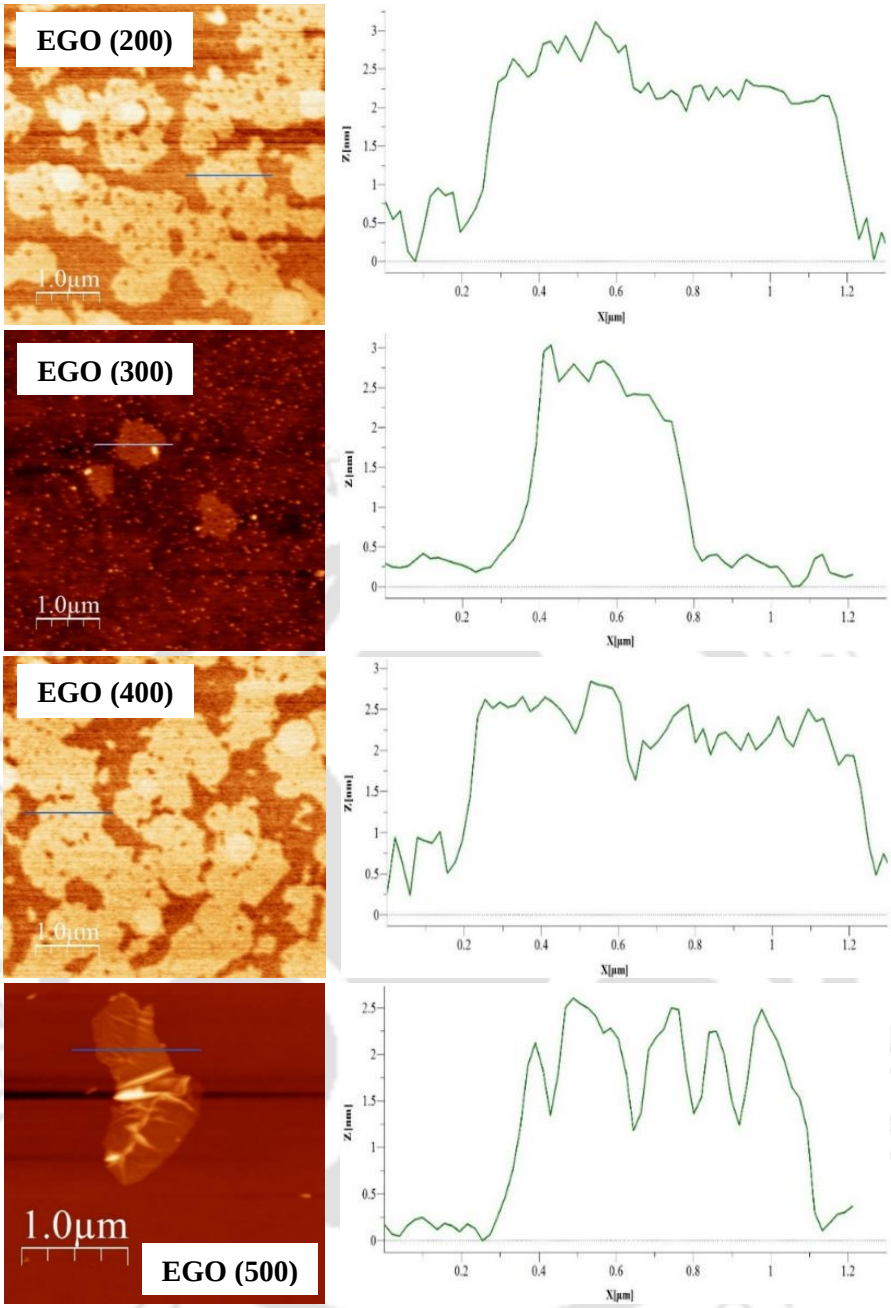

Figure 4.53: AFM topography images with corresponding height profiles of exfoliated GO samples prepared at different temperatures.

The I_D/I_G intensity ratio values corresponding to D and G bands of the samples are tabulated in Table 4.29. Higher value of intensity ratio (I_D/I_G) corresponds to lower graphitic nature and vice versa. As observed from Table 4.29, the (I_D/I_G) ratio decreased when exfoliation temperature increased. The I_D/I_G ratio for EGO(200), EGO(300), EGO(400) and EGO(500) were around 0.98, 0.96, 0.94 and 0.90 respectively. Accordingly, EGO(200), with the highest value of (I_D/I_G), had the lowest graphitization. The EGO(500) with the lowest value of I_D/I_G, had the highest level of graphitization. This result agrees with the XRD analysis.

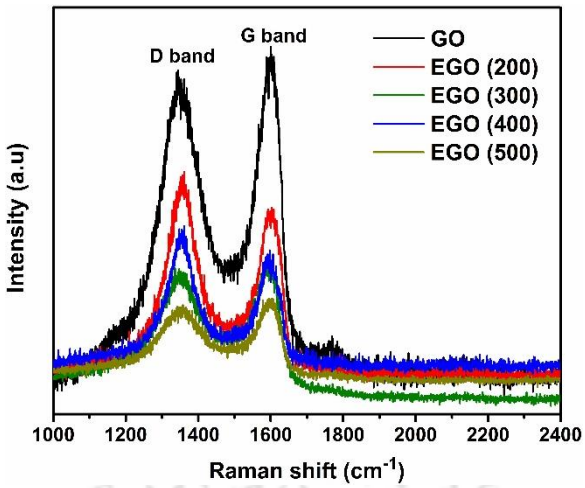

Figure 4.54: Raman spectra of graphene oxide (GO) and exfoliated GO samples prepared at different temperatures.

The nitrogen adsorption–desorption isotherms of the exfoliated samples are shown in Figure 4.55(a). All the samples showed type IV Isotherm. This was a change with respect to GO which had a type II isotherm (Figure 4.47e). The H4 hysteresis loop was observed for all samples and corresponded to the presence of narrow slit–shape pores. The presence of a large hysteresis loop in isotherms suggested wide distributions of pores. The volume of nitrogen adsorption was significantly higher for GO sample exfoliated at 300 °C compared to that of other samples.

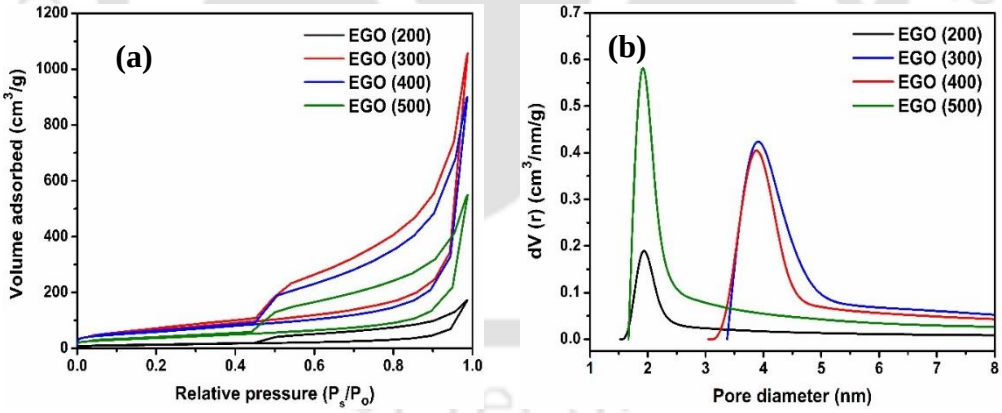

Figure 4.55: (a) N_2 adsorption–desorption isotherms (b) Pore size distribution of exfoliated GO samples prepared at different temperatures.

The physical properties calculated from the isotherm data of the samples are summarised in Table 4.29. The surface area and pore volume were not affected significantly when GO were exfoliated at 200 °C but thereafter enhancement was considerable when exfoliated at 300 °C. Both the values were highest for EGO(300); 248 m^2/g and 1.64 cm^3/g. The low surface area and pore volume for EGO(200) suggested that though the removal of surface functional groups

may have occurred at 200 °C (as suggested by TGA and XRD analysis), but layer separation was low. At 400 °C, the values decreased slightly to 218 m^2/g and 1.4 cm^3/g respectively, but thereafter the decrease was significant at 500 °C. At this temperature, higher thermal energy may have caused C–C bond breakage and partial damage of the layered structure, thereby lowering the surface area.

Pore analysis results showed that GO had very low pore volume with pores in the range of 0.5 to 3 nm (Figure 4.47f) but exfoliation at 200 °C enhanced the pore volume slightly in the same range of 1.5 to 2.5 nm. Exfoliation at 300 and 400 °C, shifted the pore size to larger values of 3 to 5 nm. The pore volume and pore size range again dropped to lower values for sample exfoliated at 500 °C. The pores of the sample exfoliated at 500 °C was in size range of 1.4 to 2.4 nm (Figure 4.55b). The results implied that at 300 °C several factors such as the removal of surface functional groups, layers separations and extent of damage to layers were balanced to result in a mesoporous pore structure. This contributed to the highest surface area and pore volume of the sample, making the 300 °C to be the optimum exfoliation temperature. At the highest temperature of 500 °C, the deep removal of surface oxygen–containing functional groups may have freed some of the spaces in–between layers creating microporous zones as observed in pore size distribution profile. However, due to the thermal damage, as discussed earlier, many of the layers got affected, lowering the pore area and pore volume.

FESEM images of GO exfoliated at different temperatures are shown in Figure 4.56. The dense, layered structure of GO (Figure 4.47g) was changed to a fluffy layered structure after exfoliation at different temperatures. However, the extent of layer separation depended on exfoliation temperature. In EGO(200) sample, the presence of a compact or dense layered structure was observed, suggesting less effective separation of layers at 200 °C. This was also observed in the XRD analysis. The layers were more separated and fluffy with increase in exfoliation temperature from 200 to 300 °C. Images showed pores and well–separated layers in GO exfoliated at 300 °C compared to that exfoliated at 200 °C. This may have been the reason for EGO(300) sample having a higher surface area as well as pore volume (Table 4.29). For EGO(400) sample, the image showed larger pores and partial damage to the continuity of layers. The extent of damage to layers seems to have increased for GO exfoliated at 500 °C. The layers were observed to be more discontinuous in EGO(500) compared to the other samples. This suggested partial breakage or damage of layers at higher temperature and may have resulted in its lowest surface area and pore volume.

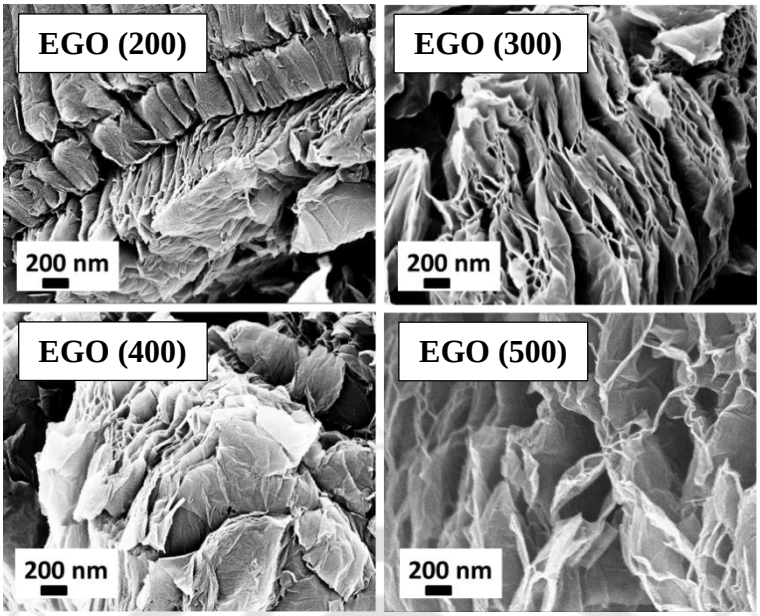

Figure 4.56: FESEM images of exfoliated GO samples prepared at different temperatures.

TEM morphology of exfoliated GO at different temperatures is shown in Figure 4.57. The TEM images of the exfoliated GO samples showed wrinkled layered structure that may have resulted during the elimination of surface functional groups by exfoliation (Mishra et al. 2011). For the EGO(200), the denser layered structure was observed as was also observed in its FESEM images. As exfoliation temperature was increased to 300 °C, the separation between the layers seemed to have increased. The effect was more prominent at higher exfoliation temperatures.

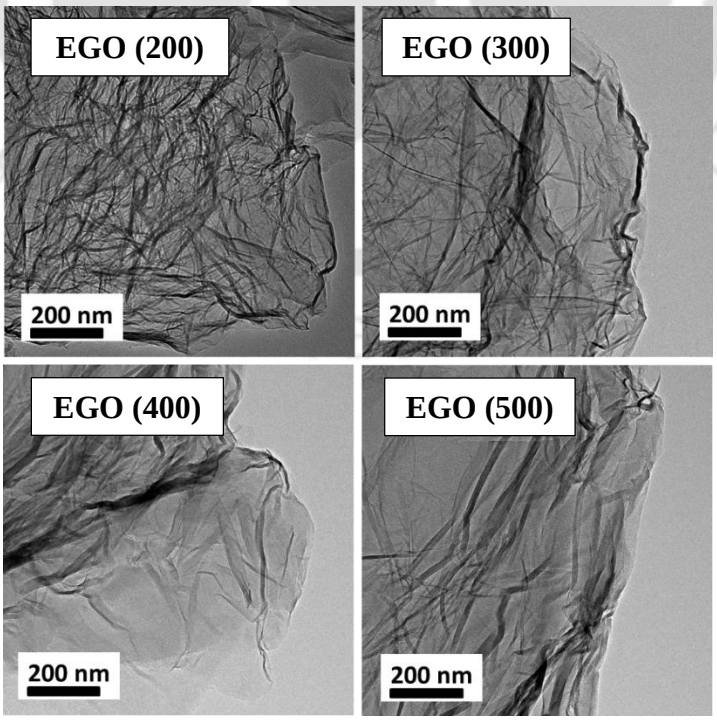

Figure 4.57: TEM images of exfoliated GO samples prepared at different temperatures.

Hydrogen storage

Figure 4.58(a) depicts the hydrogen adsorption curves of the samples at –196 °C up to 30 bar. The relative variations of hydrogen uptake, surface area and pore volume with exfoliation temperature are shown in Figure 4.58(b) and (c).

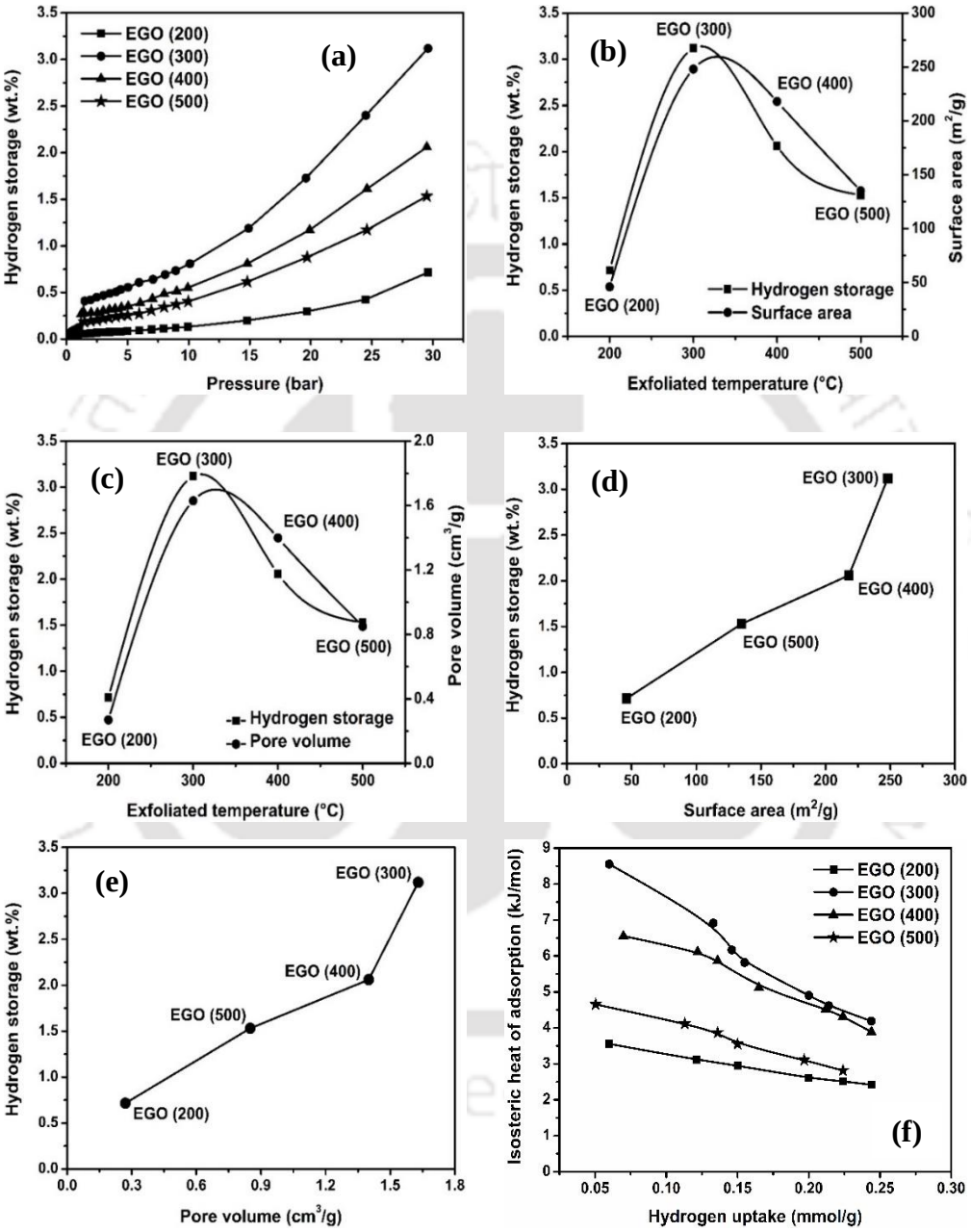

Figure 4.58: For exfoliated GO samples (a) Hydrogen adsorption isotherms at –196 °C up to 30 bar (b) Relative variation of hydrogen uptake and surface area with exfoliation temperature of samples (c) Relative variation of hydrogen uptake and pore volume with exfoliation temperature of samples (d) Hydrogen uptake as a function of surface area (e) Hydrogen uptake as a function of pore volume of samples (f) Isosteric heats of adsorption as function of hydrogen uptake of samples.

The hydrogen uptake increased with exfoliation temperature from 200 to 300 °C as the surface area and pore volume also increased. Thereafter, further increase of exfoliation temperature to 500 °C showed decrease in all the values. The hydrogen uptake capacity of exfoliated GO samples prepared at different temperatures are summarized in Table 4.30. The hydrogen uptake was highest (3.12 wt.%) for sample exfoliated at 300 °C having the highest surface area and pore volume. The plot of hydrogen uptake as a function of surface area and pore volume of the samples (Figure 4.58d and e) showed that hydrogen uptake increased with increase in both the surface area and pore volume. The results suggested that both the parameters were important and had a positive effect on the hydrogen uptake. The highest surface area provided the most number of active sites for monolayer adsorption while, higher pore volume, due to mesoporous pore structure, may have facilitated multilayer adsorption.

The hydrogen uptake of the present sample was in fact much higher with respect to its surface area as depicted by Chahine's rule of 1 wt.% H_2 per 500 m^2/g of the surface area (Poirier et al. 2001). This considerable hydrogen uptake of the present sample in spite of low surface area may be attributed to its high pore volume, mesoporous structure and fluffy layered nature. Further presence of a considerable amount of surface oxygen heteroatoms, as shown by C/O ratio, may also have facilitated hydrogen uptake. The highly electronegative oxygen sites can act as active centers for interaction with electropositive hydrogen (Agarwal et al. 1987). The oxygen can enhance the interaction with incoming hydrogen contributing positively

Several studies have also reported similar observations where hydrogen uptake was much excess to that predicted by Chahine's rule (Singh et al. 2016; Sevilla et al. 2010; Poirier et al. 2001). Limited studies are reported regarding hydrogen uptake for exfoliated GO samples. Table 4.31 compares the properties and hydrogen adsorption capacity of few exfoliated GO based materials reported in the literature with that of EGO(300) sample of the present study. The 3.12 wt.% hydrogen uptake observed for EGO(300) was higher or comparable to that reported at similar conditions.

Table 4.30: Hydrogen uptake capacity of exfoliated GO samples at –196 °C.

Sample ID	Hydrogen uptake (wt.%) at 30 bar
EGO (200)	0.71
EGO (300)	3.12
EGO (400)	2.06
EGO (500)	1.53

Figure 4.58(f) shows that the isosteric heat of adsorption (Q_{st}) decreased with hydrogen uptake. The values of Q_{st} at lower coverage were in the range of 3.5 to 8.5 kJ/mol while that at higher coverage was in the range of 2.4 to 4.1 kJ/mol under the condition of study. The highest value of Q_{st} was obtained for EGO(300) sample, which indicated higher interaction of EGO(300) surface with hydrogen molecules.

Table 4.31: Comparison of physical properties and hydrogen uptake capacity at –196 °C for exfoliated GO at 300 °C with that reported in the literature.

Graphene Type	Surface area (m^2/g)	Pressure (bar)	Hydrogen uptake (wt.%)	References
Expanded graphene	555	20	1.20	(Lueking et al. 2005)
Thermally expanded graphene sheets	300	54	1.75	(Zheng et al. 2013)
Thermally reduced graphene oxide	375	50	2.07	(Hudson et al. 2014)
Exfoliated graphene oxide	925	100	3.0	(Subrahmanyam et al. 2008)
EGO (300)	**248**	**30**	**3.12**	**Present study**

Summary

In this study, the effect of the structure of thermally exfoliated graphene oxide on hydrogen storage application was investigated. The exfoliation temperature had a significant effect on the structural properties of the samples. The graphene oxide (GO) was exfoliated at different temperatures between 200–500 °C in hydrogen flow. Reduction in oxygen content was observed on increasing the exfoliation temperature. Exfoliated GO samples had a fluffy layered structure. The separation between graphene layers increased with increasing exfoliation temperature. The GO exfoliated at 300 °C showed the highest surface area of 248 m^2/g and total pore volume (1.64 cm^3/g). The lowest exfoliation temperature of 200 °C was least effective for separations of layers. Consequently, both the surface area and pore volume were lowest for the sample. However, at higher exfoliation temperature of 500 °C, the partial damage to layers may have been responsible for lowering the surface area and pore volume. The hydrogen uptake increased with increase in surface area and pore volume. The highest hydrogen uptake of 3.12 wt.% was obtained for GO exfoliated at 300 °C (at –196 °C and 30 bar), which showed the highest surface area and pore volume. This uptake is higher compared to the reported samples in literature having similar surface area. The higher hydrogen uptake of the present sample may be a combined effect of high pore volume, mesoporous structure, fluffy layered nature and significant content of surface oxygen heteroatom.

4.2.4 Comparative effect of thermal and chemical treatment on GO

The GO was treated by chemical and thermal treatments. Their physicochemical properties and hydrogen uptakes are compared and discussed in this section. A part of the prepared GO was treated with hydrazine while the remaining part was subjected to thermal treatments under different gaseous (H_2, Ar or air) environments. The hydrogen uptake capacity was determined at –196 °C up to 30 bar. The hydrazine treated GO is represented as RGO(hyd) and the exfoliated GO samples are named as EGO(H_2), EGO(Ar) and EGO(Air) depending on the carrier gas used during exfoliation.

Table 4.32: Elemental analysis of graphene oxide (GO), reduced graphene oxide and exfoliated graphene oxide samples using EDX.

Sample ID	Elements atomic (wt.%)		
	C	O	O/C
GO	66.4	33.6	0.50
RGO (hyd)	91.6	8.4	0.09
EGO (H_2)	83.7	16.3	0.19
EGO (Ar)	84.5	15.5	0.18
EGO (Air)	83.0	17.0	0.20

The composition of the samples is given in Table 4.32. The GO showed O/C ratio of 0.50. For the RGO sample produced in the presence of hydrazine, the O/C ratio decreased drastically to 0.09. However, for EGO samples, the O/C values ranged in between 0.18–0.20 depending on exfoliation environment; the highest being that for air exfoliated sample. The removal of oxygen containing surface functional groups resulted in a lower value of O/C ratio for RGO and EGO samples compared to that of GO. The results suggested that removal was more effective in the presence of hydrazine. For exfoliated EGO samples, oxygen removal was highest for EGO(Ar) with O/C ratio 0.18 and least for EGO(Air) with O/C ratio 0.20. For EGO(H_2) the O/C was 0.19. The similar values of the O/C for the exfoliated samples suggested that the nature of the gaseous environment, inert, oxidative or reducing, during exfoliation was less determining factor. The removal of oxygen was more affected by the decomposition or oxidation reactions at higher temperature and subsequent removal by the flow of gases. This was also observed during TPD analysis, where all the samples showed TPD peaks almost in the similar temperature range of 170–250 °C corresponding to the evolution of CO/CO_2 (Appendix Figure D1). The EDX mapping (Appendix Figure C2) showed a dense oxygen distribution for GO. Compared to EGO samples, the oxygen content for RGO seemed to be less and non–

uniform. For all the exfoliated samples, the oxygen was observed to be more uniformly distributed on the sample surface, particularly for the air exfoliated GO sample.

The UV/Vis spectra (Figure 4.59) of GO had two absorption peaks. The first peak at ~230 nm is attributed to the π-π* transitions of aromatic rings. The second peak at ~300 nm is assigned to the n-π* transitions of C=O bonds (Khanra et al. 2012). The peak at 230 nm after the reduction or exfoliation was shifted to a longer wavelength region at 270 nm in RGO/EGO samples. This red shift is associated with the restoration of the electronic conjugation between graphene layers as the surface functional groups were removed during reduction or exfoliation (Zhang et al. 2014; Khanra et al. 2012).

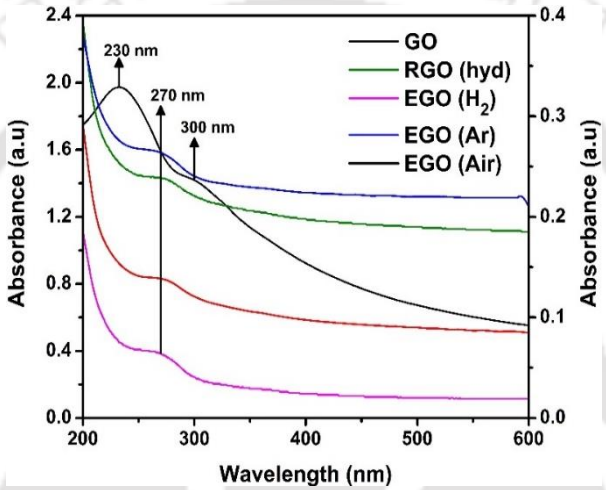

Figure 4.59: UV–Vis absorption spectra of graphene oxide (GO), reduced graphene oxide and exfoliated graphene oxide samples.

The XPS spectra of the samples prepared in the presence of hydrazine and by air exfoliation are shown in Figure 4.60(a) and (b). Presence of C1s and O1s was detected. The oxygen peaks confirmed the presence of surface functional groups. The deconvolution of C1s XPS spectra of samples are shown in Figure 4.60(c) and (e). Three peaks were obtained at 284.8, 286.4 and 287.8 eV which corresponded to C–C (sp^2 bonds), C–O (epoxy and hydroxyl groups) and C=O (carbonyl) functional groups respectively (Hu et al. 2015; Kottegoda et al. 2015). This results agreed with that obtained from FTIR analysis. The relatively higher intensity of O1s peak for EGO(Air) sample compared to that of RGO (hyd) sample suggested the presence of higher amount of oxygen–containing functional groups in the former. The presence of oxygen–containing functional groups in the RGO(hyd) and EGO(Air) samples was also confirmed by O1s peaks and the deconvolution of the peaks are shown in Figure 4.60(d) and (f). Both the samples indicated two peaks at 331.5 and 333.5 eV, which corresponded to C=O and C–O respectively (Gupta et al. 2017). The XPS elemental composition analysis gave the O/C ratios

of 0.10 and 0.20 for RGO(hyd) and EGO(Air), respectively. Similar O/C ratio values of 0.09 and 0.19, respectively, were obtained from EDX analysis of RGO(hyd) and EGO(Air).

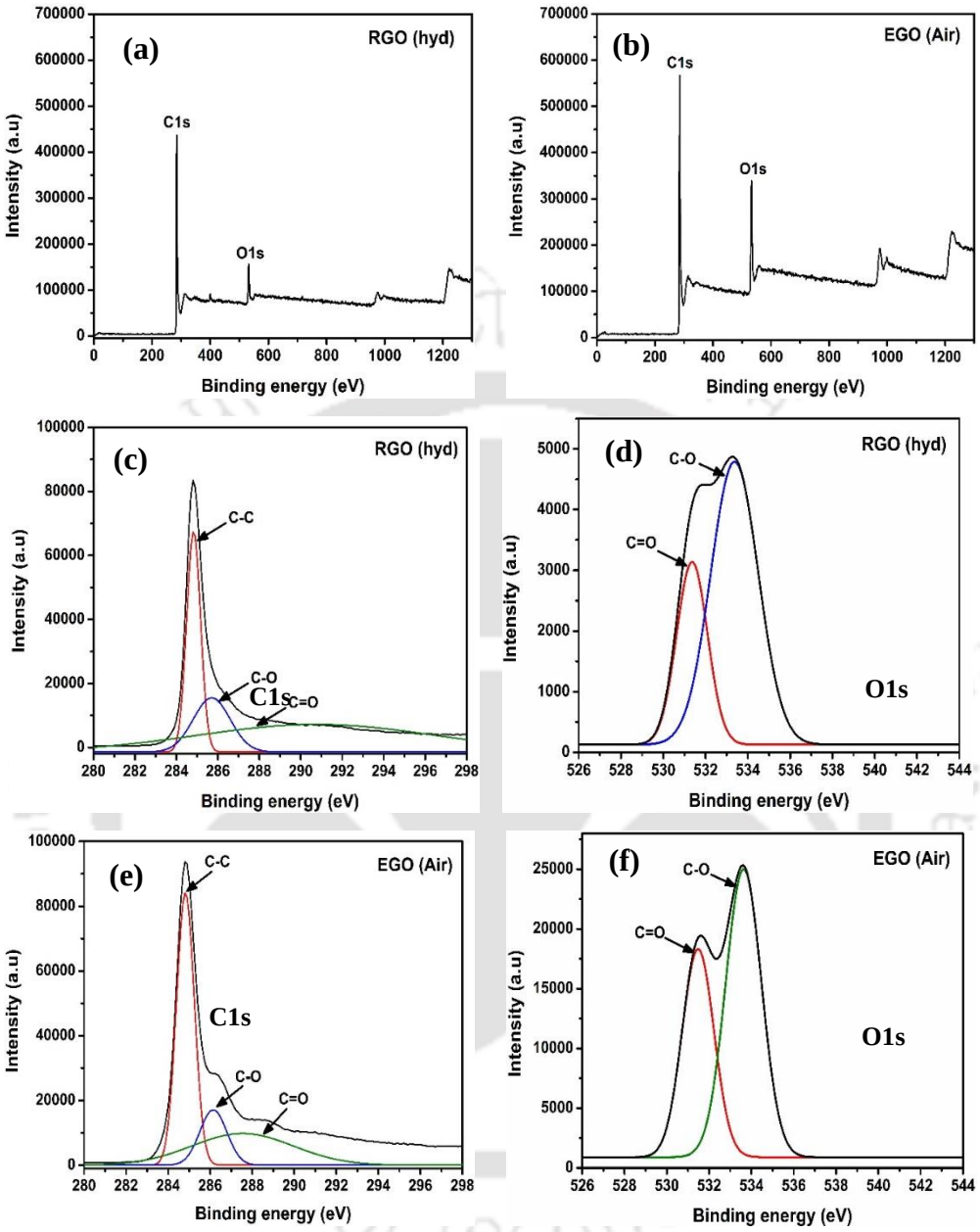

Figure 4.60: (a) Overall XPS profiles of hydrazine reduced graphene oxide RGO(hyd) (b) Overall XPS profiles of graphene oxide exfoliated in air environment EGO(Air) (c) C1s profile of RGO(hyd) (d) O1s profiles of RGO(hyd) (e) C1s profile of EGO(Air) (f) O1s profile of EGO(Air).

Figure 4.61 shows the XRD profiles of RGO and EGO samples. Lattice spacing, crystal size and number of layers as determining from XRD profiles are tabulated in Table 4.33. For RGO, the broad low–intensity peak at 2θ = 24.5° for graphitic zones C(002) planes were observed (Chowdhury et al. 2016). The d–spacing was 0.392 nm. This decrease in d–spacing from that

of GO (0.850 nm) resulted from the removal of intercalated surface functional groups as discussed earlier for EGO samples. Additionally, a low–intensity peak was also observed at 2θ = 42.8° which corresponded to (101) graphitic crystal plane (Chowdhury et al. 2016b, 2016a; Chen et al. 2013).

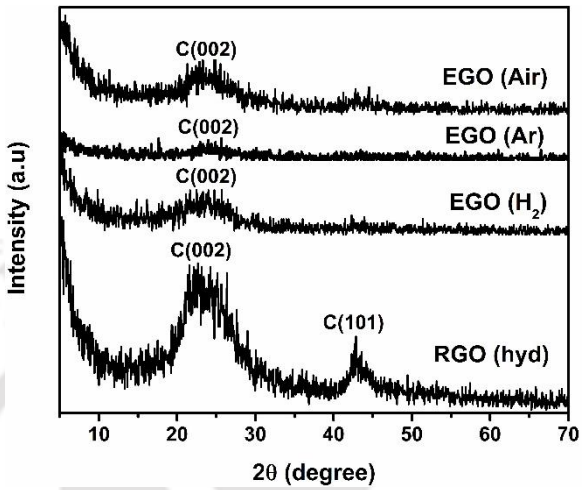

Figure 4.61: XRD profiles of reduced graphene oxide and exfoliated graphene oxide samples.

All the exfoliated samples prepared at different temperatures exhibited a broad peak at 2θ = 24.5° corresponding to graphitic C(002) plane. The d–spacings were 0.414, 0.364 and 0.381 nm for EGO(H_2), EGO(Ar) and EGO(Air) exfoliated graphene samples, respectively. This reduction in d–spacing for all the samples with respect to GO confirmed, the elimination of intercalated oxygen–containing functional groups in all the gaseous environment. The difference in d–spacing for these samples suggested difference in the extent of removal. Compared to RGO(hyd) sample, the d–spacing was higher for all the samples suggesting comparatively lower removal of oxygen–containing functional groups by exfoliation method compared to hydrazine treatment method.

Table 4.33: Structural analysis of graphene oxide (GO), reduced graphene oxide and exfoliated graphene oxide samples.

Sample ID	d–Spacing $(nm)_{(002)}$	Number of layers (XRD)	Average thickness (AFM) (nm)	Number of layers (AFM)	I_D/I_G ratio
GO	0.850	13	–	–	0.98
RGO (hyd)	0.392	2	2.8	6	0.89
EGO (H_2)	0.414	3	3.7	9	0.92
EGO (Ar)	0.364	5	3.5	8	0.94
EGO (Air)	0.381	4	3.8	9	0.90

These agreed to the very low O/C value of RGO(hyd) compared to EGO samples (Table 4.32). The broad nature and low intensity of graphite peak in RGO or EGO samples implied the loss of layered graphite and are a primary characteristic of multilayered graphene (Divya et al. 2014; Chen et al. 2013). The number of layers was determined as before from equation 2 and was in the range of 2–5. This indicated that the effective exfoliation of GO was achieved by both the hydrazine and thermal treatment.

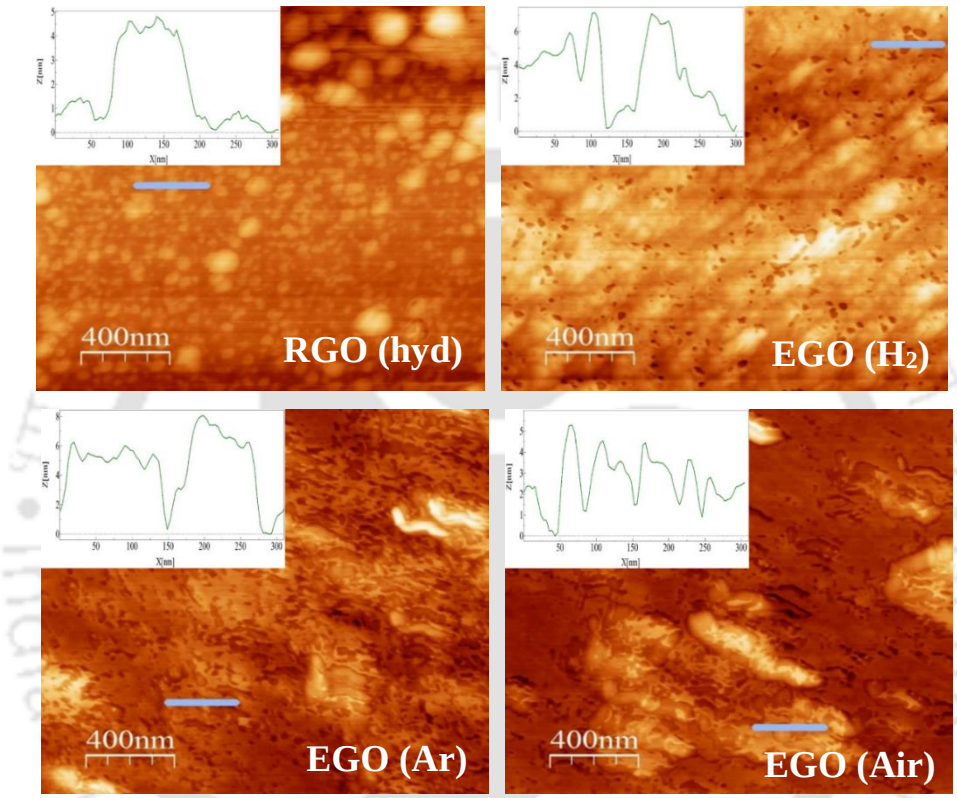

Figure 4.62: AFM images with corresponding height profiles of reduced graphene oxide and exfoliated graphene oxide samples.

Figure 4.62 shows the tapping–mode AFM topography images with height profile analysis for RGO and EGO samples. The average thickness and number of layers are summarised in Table 4.33. The average thickness of the hydrazine treated RGO was 2.8 nm and that for thermally exfoliated samples were in 3.5–3.8 nm range. The approximate number of graphene layers in a sample was calculated by dividing its average thickness with the reported theoretical thickness of 0.40 nm for single graphene layer (Pu et al. 2009; Stankovich et al. 2006). The values were obtained in the range of 6–9 for the RGO and EGO samples.

Figure 4.63 shows the Raman spectra of the samples that were recorded in the range of 500 to 3000 cm^{-1}. For all the graphene samples, the peak for D band was observed in the wave number

range of 1344 to 1356 cm^{-1} due to the defects present in the samples (Zhou et al. 2016). The appearance of D–band in graphene samples may be associated with the modifications incorporated during chemical and thermal treatment of GO. The G band appeared in the range 1589 to 1600 cm^{-1} for graphene samples. The intensity of D and G bands of graphene samples was lower than that of GO and suggested that the disorder in the structure was reduced in graphene. This may have been resulted from the removal of intercalated oxygen–containing functional groups between the layers. The lowest intensity of RGO(hyd) with respect to EGO samples also suggested lowest disorder in RGO(hyd) which may have resulted from presence of least amount of functional groups in this sample (lowest O/C ratio). The I_D/I_G intensity ratio values corresponding to D and G bands of the samples are tabulated in Table 4.33. The lowest value of I_D/I_G ratio was 0.89 for RGO(hyd) sample, which indicated the presence of the highest level of degree of graphitization. This result agreed with the XRD results.

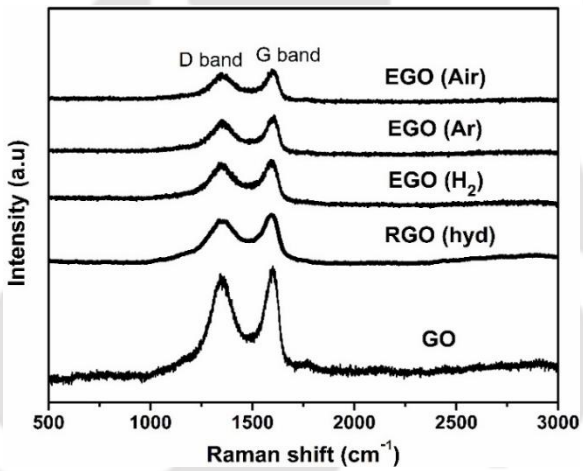

Figure 4.63: Raman spectra of graphene oxide (GO), reduced graphene oxide and exfoliated graphene oxide samples.

The nitrogen adsorption–desorption isotherms obtained at –196 °C for different graphene samples are shown in Figure 4.64(a). Type II isotherm with H4 hysteresis loop was observed for the RGO(hyd) sample same as that observed for GO (Figure 4.47e). Retainment of same type II isotherm for RGO(hyd) sample compared to that of GO suggested no major structural change during hydrazine treatment of GO sample. However, all the gas exfoliated samples showed type IV isotherm with an H4 hysteresis loop suggesting the presence of narrow slit–shaped pores (Divya et al. 2014). Change from type–II for GO to type IV isotherm after exfoliation suggested structural changes. Thus the difference in treatment of GO resulted in different structures for hydrazine and exfoliated GO samples. The nature of curves along with the presence of hysteresis loop suggested the presence of both micropores and mesopores pores

in the samples. The pore size distribution (Figure 4.64b) confirmed the presence of both types of pores in graphene samples.

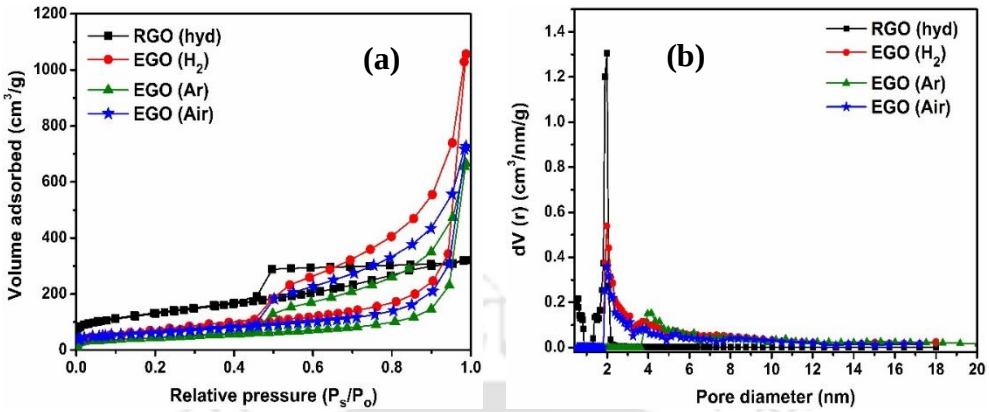

Figure 4.64: (a) N_2 adsorption–desorption isotherms (b) Pore size distribution of reduced graphene oxide and exfoliated graphene oxide samples.

The graphene prepared in the presence of hydrazine showed mainly micropores with very narrow pore size distribution in the range of 0.4 to 2.2 nm. The gas exfoliated samples were mainly mesoporous; H_2 and air exfoliated samples had pores in the range of 1.8 to 6 nm, while the Ar exfoliated sample had in 3.6 to 7 nm range. Comparison of pore size of RGO(hyd) with that of GO suggested that hydrazine treatment sharply increased the percentage of pores in the range of 1.5 to 2.2 nm. This may be associated with the removal of intercalated oxygen–containing groups between the layers, thereby increasing the available space in between the layers. For thermally exfoliated samples, though the pores in the range of 1.7–2.5 nm still existed but significant amount of pores in higher range (2.5 to 5 nm) was developed. This may have originated from the better separation of layers, assisted by the gas flow, resulting in a fluffy structure as observed from FESEM images. Partial damages of layers during thermal treatment may also have contributed to shifting of pores to meso range. The average pore size of H_2 and air exfoliated graphene were 2.8 nm. The highest average pore size of 4.1 nm observed for EGO(Ar) suggested more extensive modification in layered structure.

Table 4.34: Physical properties of reduced graphene oxide and exfoliated graphene oxide samples.

Sample ID	BET Surface area (m^2/g)	Total pore Volume (cm^3/g)	Micropore area (m^2/g)	Average pore size (nm)
RGO (hyd)	461	0.50	86	2.0
EGO (H_2)	248	1.63	0	2.8
EGO (Ar)	155	1.03	6	4.1
EGO (Air)	217	1.12	8	2.8

The BET surface area, pore volume and average pore size of samples are summarized in Table 4.34. Compared to the properties of GO (Table 4.34), the surface area drastically enhanced to 461 m^2/g on treatment with hydrazine. However, the pore volume increase was only marginal. Exfoliation in presence of different gases also increased the surface area but to a lesser extent. The surface areas of exfoliated samples were in the range of 155–248 m^2/g.

In contrast to chemical treatment, the pore volumes were significantly increased for exfoliated samples to 1.03–1.63 cm^3/g. The highest surface area of RGO(hyd) sample may correspond to the effective elimination of surface functional groups from in between layers increasing micropore area and effective surface area. The pore size distribution also established that pores in the micropore range were enhanced significantly by hydrazine treatment. The lower surface area of thermally exfoliated graphene samples may have been caused by less effective removal of the oxygen–containing functional group (as shown by the higher O/C ratio of samples). This may have been also resulted from considerable structural modification of the layers (as confirmed by FESEM images shown later in Figure 4.65). The structural modification may also be the reason for the higher pore volume observed in the thermally exfoliated samples. The highest pore volume of 1.63 cm^3/g was observed for EGO(H_2). The exfoliated graphene prepared in the presence of H_2 had both higher surface area and pore volume compared to that exfoliated in argon or air. The micropore area was very low for RGO(hyd) sample and negligible for all the EGO samples.

The morphology of the samples was studied using FESEM (Figure 4.65) and TEM (Figure 4.66). The image analysis of the graphene samples prepared by hydrazine treatment and exfoliation process showed distinctly different morphology. Thermally gas exfoliated samples had fluffier layered structure compared to that of hydrazine treated sample. For hydrazine treated sample, the presence of denser layer can be accounted for the finer pores as observed from pore analysis. More effective removal of functional groups from in–between layers may have resulted in open spaces in micropore ranges, however, the separation of layers was not significant enough and resulted in the denser structure having micropores. The fluffy structures of thermally exfoliated graphene resulted from the better separation of layers assisted by the formation of gaseous products and gas flow. For the EGO samples in addition to the elimination of oxygen–containing functional groups, the thermal treatment may have also modified the layered structure. Among thermally exfoliated graphene samples, EGO(Ar) seemed to have more spacious layered structure leading to comparatively lower surface area and pore volume

among the three EGO samples. The least detrimental effect on the layered structure was observed in the hydrogen atmosphere and resulted in the highest surface area and pore volume for EGO(H_2) among exfoliated samples.

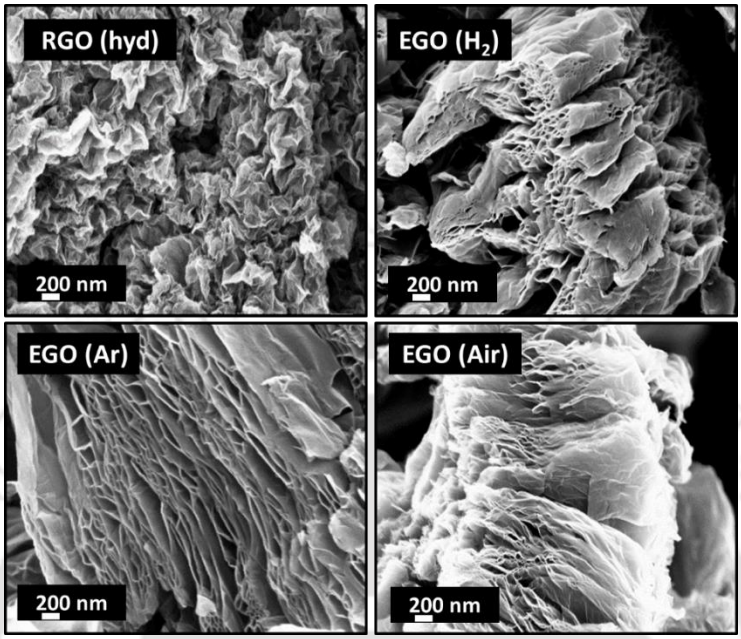

Figure 4.65: FESEM images of reduced graphene oxide and exfoliated graphene oxide samples.

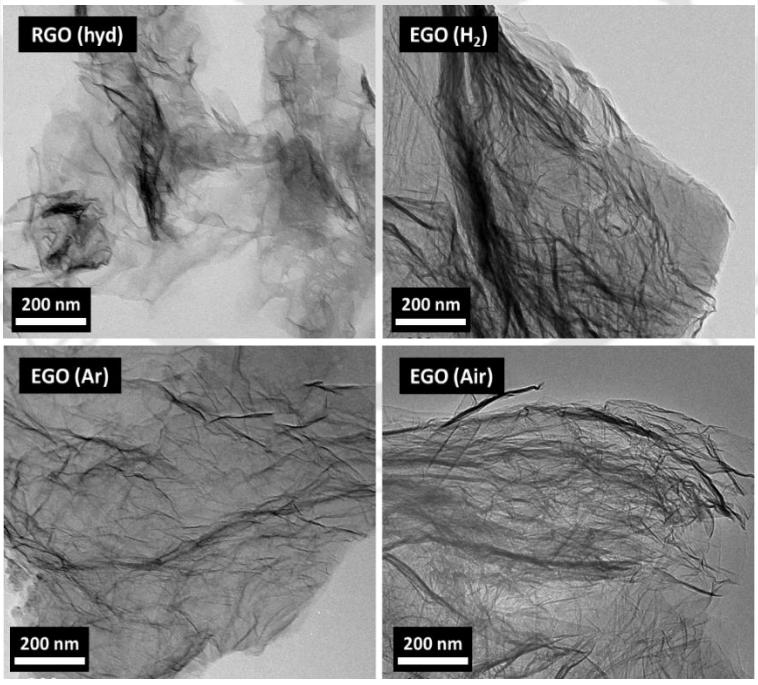

Figure 4.66: TEM images of reduced graphene oxide and exfoliated graphene oxide samples.

The TGA and DTG profiles of the samples in nitrogen flow are shown in Figure 4.67(a) and (b), respectively. All the graphene samples underwent gradual weight loss only after 500 °C

suggesting the presence of strongly bonded oxygen–containing functional groups which were retained on the surface after reduction or exfoliation and were removed only at a temperature beyond 500 °C.

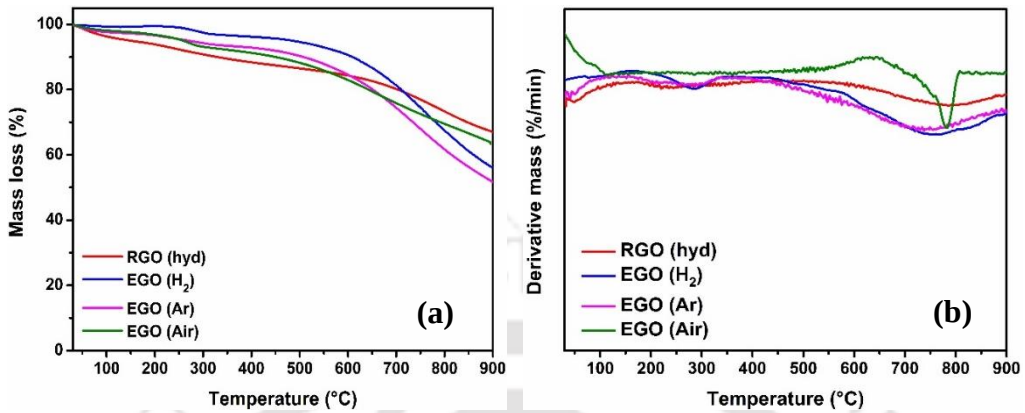

Figure 4.67: (a) TGA profiles (b) DTG profiles of reduced graphene oxide and exfoliated graphene oxide samples.

The presence of oxygen in these samples was earlier confirmed by EDX analysis. In accordance with the EDX result, the RGO(hyd) sample having the lowest O/C ratio experienced the lowest weight loss of 28 % up to 900 °C. On the other hand, EGO samples with the higher O/C ratios underwent higher weight loss. The air, H_2 and Ar exfoliated graphene samples showed mass loss of 33, 40 and 44 % respectively, up to 900 °C. The presence of a sharp peak in the range of 650–805 °C for air exfoliated graphene sample, which was not observed for any other samples, may have resulted due to removal of strongly bonded oxygen–containing functional groups retained during exfoliation in air.

Hydrogen storage

Figure 4.68(a) compares the hydrogen adsorption isotherms of the samples. The isotherms were recorded at –196 °C up to 30 bar. The GO had the lowest hydrogen uptake (1.09 wt.%). The reason may be its very low surface area and pore volume (Table 4.34). Figure 4.68(b), (c) and (d) showed the hydrogen uptake as a function of surface area, pore volume and O/C (oxygen/carbon) atomic ratio, respectively. The analysis of data suggested that the hydrogen uptake was influenced not only by the surface area and pore volume, which were defined by respective structure but also by the surface oxygen content represented by O/C ratio. Hydrogen uptake capacity of the samples at –196 °C is included in Table 4.35. The order of hydrogen uptake was EGO(Air), 3.34 wt.% > EGO(H_2), 3.12 wt.% > RGO(hyd), 2.5 wt.% > EGO(Ar), 2.2 wt.%. Thus, the RGO(hyd) showed the third highest hydrogen uptake in spite of having

significantly higher surface area compared to that of EGO(H_2) and EGO(Air) (Figure 4.68b). However, the pore volume of RGO(hyd) was comparatively very low and this could have been the reason for its lower hydrogen uptake (Figure 4.68c).

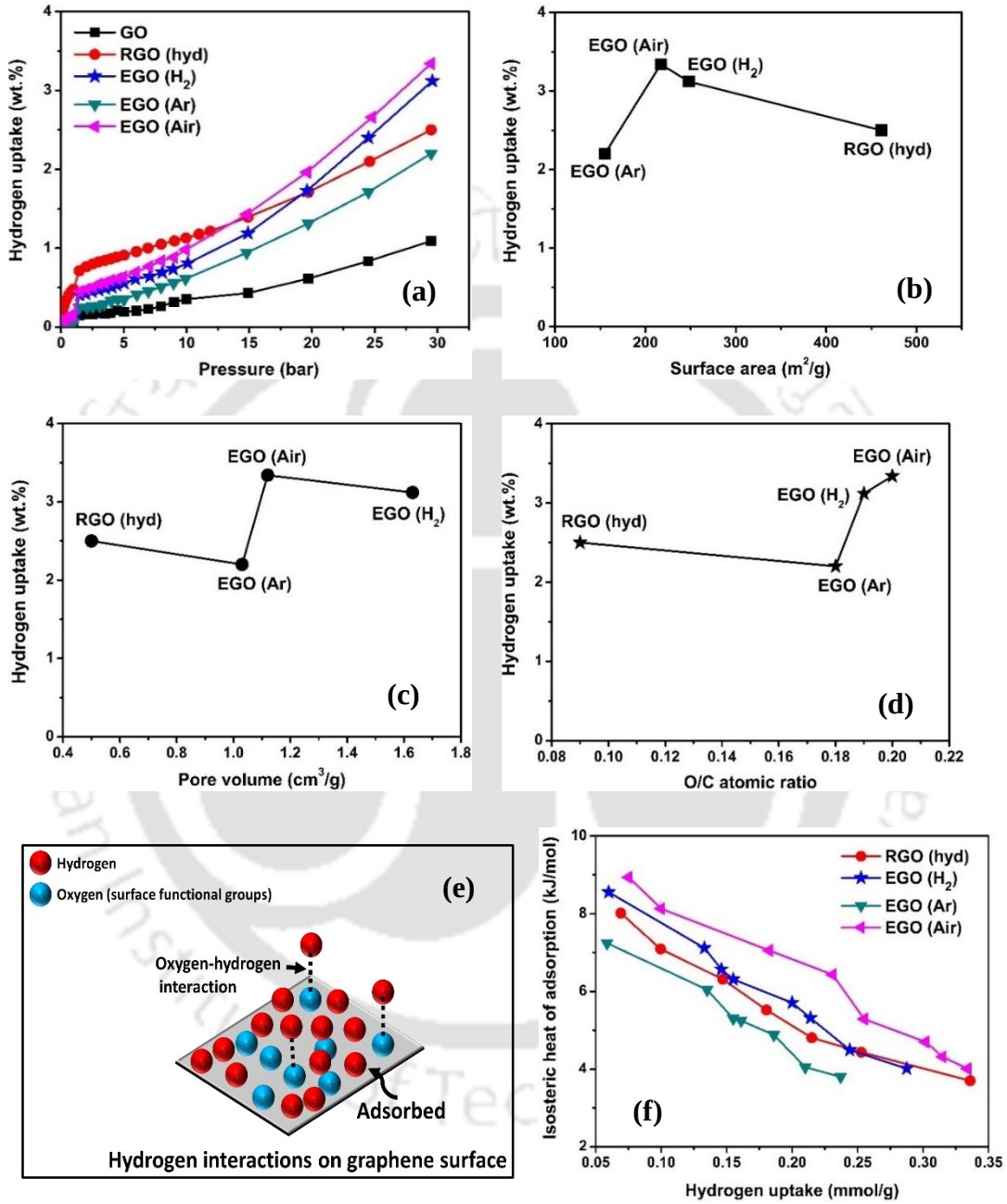

Figure 4.68: For graphene oxide (GO), reduced graphene oxide and exfoliated graphene oxide samples (a) Hydrogen adsorption isotherms of samples at –196 °C up to 30 bar (b) Relation between hydrogen uptake capacity and surface area of the samples (c) Hydrogen uptake capacity as a function of pore volume of samples (d) Hydrogen uptake capacity as a function of O/C atomic ratio of samples (e) Hydrogen interaction on graphene surface (f) Isosteric heats of adsorption as a function of the amount of H_2 adsorbed on the samples.

As was observed from microscopic images, the RGO(hyd) had a relatively dense structure consisting of mainly micropores (Figure 4.66b). This may have resulted in its higher surface area but very low total pore volume. The higher hydrogen uptake for air exfoliated sample EGO(Air) compared to that of hydrogen gas exfoliated sample EGO(H_2), though the latter had a higher surface area and pore volume, suggested that some other factor may have been playing a role. This third factor might have been the surface oxygen content originated from the surface functional groups. As also discussed in earlier section, the highly electronegative oxygen may have facilitated interaction with incoming highly electropositive hydrogen and thereby contributed to the enhancement of hydrogen uptake.

Figure 4.68(d) shows the correlation of O/C ratio with hydrogen uptake. The highest hydrogen uptake was observed for EGO(Air) sample containing the maximum O/C value. The RGO(hyd) showed the lowest O/C ratio and this may be another reason for its lower hydrogen uptake along with low pore volume. For exfoliated samples, it can be observed that with increase in O/C ratio, the hydrogen uptake capacity increased. Figure 4.68(e) represents the possible interaction between oxygen and hydrogen on the graphene surface. The highly electronegative oxygen sites may interact with the incoming hydrogen molecule facilitating its adsorption on the graphene surface. This might have also been the reason for significant hydrogen uptake of GO sample having the highest amount of oxygen–containing surface functional groups (O/C ratio= 0.50) though the surface area was very low, 41 m^2/g. Among thermally gas exfoliated samples, the lowest uptake observed for EGO(Ar) may be attributed to its lowest surface area, pore volume and O/C ratio. The results thus showed that the combined effect of surface area, pore volume and surface oxygen content contributed in enhancing interaction with hydrogen.

Table 4.35: Hydrogen uptake capacity of the reduced graphene oxide and exfoliated graphene oxide samples at –196 °C.

Sample ID	Hydrogen uptake (wt.%) at 30 bar
GO	1.09
RGO (hyd)	2.50
EGO (H_2)	3.12
EGO (Ar)	2.20
EGO (Air)	3.34

The hydrogen uptake results of this study were comparable or better than that reported for similar hydrazine reduced and exfoliated graphene samples, as shown in Table 4.36. The important characteristics for graphene–based material are that in spite of lower surface area,

they showed considerable hydrogen uptake. Appendix Table I1 summarize similar hydrogen uptake of few other carbon–based adsorbents and it can be observed that their surface areas were quite higher (Bader et al. 2016; Cai et al. 2015; Gogotsi et al. 2009; Guan et al. 2009; Jordá–Beneyto et al. 2008; Jordá–Beneyto et al. 2007; Xu et al. 2007). The higher uptake of the graphene–based adsorbents having lower surface area can be attributed to their layered mesoporous structure as well as the presence of a considerable amount of surface oxygen due to residual functional groups. In present study, the RGO(hyd) that had the highest surface area but the lowest pore volume and oxygen content showed lower hydrogen uptake.

Table 4.36: Comparison of physical properties and hydrogen uptake capacities for graphene oxide (GO), reduced graphene oxide and exfoliated graphene oxide samples prepared in this study with that reported in the literature at –196 °C.

Graphene Type	Surface area (m^2/g)	Pressure (bar)	Hydrogen uptake (wt.%)	References
Graphene oxide (GO)	–	60	0.95	(Hong et al. 2012)
Exfoliated GO	300	54	1.75	(Zheng et al. 2013)
Exfoliated GO	375	50	2.07	(Hudson et al. 2014)
Exfoliated GO	925	100	3.0	(Subrahmanyam et al. 2008)
Expanded graphene	555	20	1.20	(Lueking et al. 2005)
Reduced GO	640	10	1.17	(Srinivas et al. 2010)
Reduced GO	–	20	2.0	(Ismail et al. 2015)
Reduced GO	470	10	1.2	(Srinivas et al. 2011)
Graphene oxide (GO)	**41**	**30**	**1.09**	**Present study**
Exfoliated GO	**217**	**30**	**3.34**	**Present study**
Reduced GO	**461**	**30**	**2.50**	**Present study**

The isosteric heat of adsorption of the samples are shown in Figure 4.68(f). The heat of adsorption decreased with increasing hydrogen uptake for all the samples. At lower hydrogen adsorption, the order of heat of adsorption was EGO(Ar), 7.2 < RGO(hyd), 8.0 < EGO(H_2), 8.5 < EGO(Air), 8.9 kJ/mol, which at higher adsorption reduced to the range of 3–4 kJ/mol. The heat of adsorption being lowest for RGO(hyd) and highest for EGO(Air) may be correlated with the respective lowest and highest surface oxygen content. The less variation of the heat of adsorption for samples at higher uptake suggested that the residual weaker sites were similar nature in all the graphene oxide samples prepared in different ways. The heat of adsorption (4–9 kJ/mol) obtained in this study is slightly higher to that reported in the literature (3–6 kJ/mol) (Zheng et al. 2013; Srinivas et al. 2010; Ma et al. 2009).

Summary

The present study explored and compared the effect of physicochemical properties of graphene, prepared by different preparation techniques, on hydrogen storage application. A part of the synthesized graphene oxide (GO) was subjected to hydrazine treatment and the remaining part was thermally treated in different gaseous (H_2, Ar or air) environments. The morphology of thermally exfoliated samples (EGO) was observed to be significantly different than chemically hydrazine treated samples (RGO). Structurally RGO was similar to parent GO but O/C value was almost five–times lower. On the other hand, the EGO samples showed O/C ratios almost two–times higher compared to that of RGO sample suggesting higher retainment of oxygen–containing functional groups in former. The pore size distribution revealed the microporous nature for RGO and mesoporous for EGO samples. The RGO has an average pore size of 2.0 nm, whereas EGO samples have an average pore size between 2.8–4.1 nm. The FESEM and TEM analyses showed fluffier and distinct multi–layered structure for thermally exfoliated graphene compared to that of hydrazine reduced graphene oxide. The BET surface area was highest for RGO (461 m^2/g). The EGO(H_2) showed the highest pore volume (1.63 cm^3/g), while O/C value was highest for EGO(Air). The maximum hydrogen uptake of 3.34 wt.% was obtained for EGO(Air) at –196 °C and 30 bar followed by that of RGO. The results suggested that the combined effect of surface area, pore volume, nature of layered structure and oxygen content contributed to hydrogen uptake characteristics. In this paper, the obtained hydrogen uptake capacity for exfoliated GO prepared in the presence of air was higher compared to that of reported values of hydrogen uptake for graphene materials under similar condition. The higher uptake can be attributed to the unique layered structure and higher surface oxygen content.

4.2.5 Effect of different metal doping

In this section, effect of platinum, nickel or palladium doping on the hydrogen storage capacity of RGO has been discussed. All the metals were doped on RGO using the impregnation method. The samples are represented as M/RGO where M represents the respective metal. The samples were tested for hydrogen storage up to pressure of 30 bar at –196 °C.

Table 4.37: Elemental analysis of different metal doped RGO samples using EDX.

Sample ID	Elements (wt.%)			
	metals	C	O	O/C
RGO	–	89.6	10.4	0.116
Ni/RGO	2.2	86.6	11.2	0.129
Pt/RGO	2.0	86.1	11.9	0.138
Pd/RGO	2.0	85.2	12.8	0.150

The elemental composition of the samples was determined by EDX and summarized in Table 4.37. The final average loading of metals was about 2 wt.% for all the samples. RGO showed oxygen content of 10.4 which slightly increased with the addition of metals. The highest oxygen content of 12.8 wt.% was determined for the Pd/RGO sample. The oxygen–carbon ratio (O/C) of RGO was 0.116. With addition of metals, it increased in order of 0.129 (Ni/RGO) < 0.138 (Pt/RGO) < 0.150 (Pd/RGO). This suggested retainment of more oxygen for metal doped sample, highest being for Pd/RGO sample.

XRD profiles of different metal doped RGO samples are compared in Figure 4.69(a). The lower intensity peak observed for Ni/RGO at $2\Theta = 44.4°$ is attributed to (111) plane of metallic nickel Ni° (Yadav et al. 2017). The NiO peaks as reported in the literature at 37.6° (111), 43.09° (200), 63.62° (220) and 75.09° (311) were not observed for the sample (Carraro et al. 2014). For Pt/RGO, the three peaks at $2\Theta = 39.85°$, 46.3° and 67.1° corresponding to Pt^0 (111), Pt^0 (200) and Pt^0 (220) planes. In the case of Pd/RGO, the peaks at $2\Theta = 39.8°$ and 46.5°, resulted from the planes Pd^0 (111) and Pd^0 (200) respectively. The PdO peaks are reported at 33.9° (101), 42° (110), 54.5° (112), 60.69° (200) and 71.28° (202) (Lin et al. 2014; Ganji et al. 2013). The XRD peaks confirmed that all the metals were present in zero oxidation state or metallic state in the samples. This agreed with the reductive conditions during their preparation due to presence of hydrazine. The average crystal size of the metals (Ni, Pt or Pd) was estimated by the Debye–Scherrer formula using the prominent peak of the respective metal. The average crystallite size of nickel, palladium and platinum cluster was calculated to be 7.5, 11 and 14

nm respectively. The broad peak in the range of 23°–24.95° observed for all the samples may be attributed to the graphitic plane (002). These graphitic peaks for all the samples are compared in Figure 4.69(b). The comparative study of the peaks shows that the higher peak intensity was observed for nickel doped RGO sample compared to that of other samples. The higher peak intensity corresponded to higher graphitic zone. Platinum and palladium seemed to have negative effect on the formation of graphitic zone with respect to RGO. The decrease in graphitic plane (002) peak intensity was also observed by Vinayan et al. (2011) and Chen et al. (2011) after addition of palladium and platinum, respectively to graphene. This is in contrast to what was observed for doped templated carbons in which these metals were observed to favour the formation of graphitic zone by their presence.

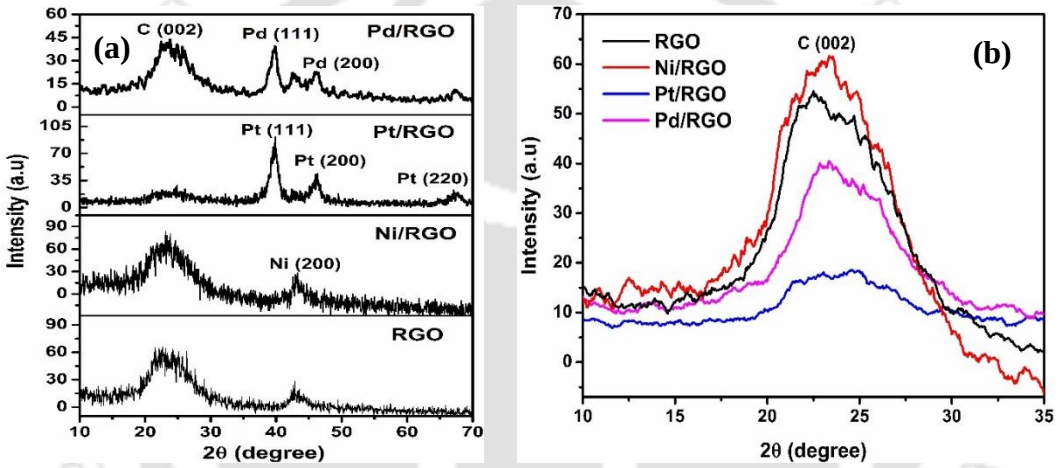

Figure 4.69: (a) XRD profiles of RGO and metal doped RGO samples (b) Blown up XRD profiles in the range of 10°–35° for the same samples.

The crystallographic properties of the samples, including d–spacing, average crystal size and numbers of layers, determined from XRD profiles, are tabulated in Table 4.38. The RGO had d–spacing of 0.392 nm. The decrease in d–spacing was observed on doping of different metals in order of 0.387 nm (RGO) > 0.358 (Pt/RGO) > 0.355 nm (Pd/RGO) > 0.353 (Ni/RGO). Most significant decrease in d–spacing was observed for nickel doped RGO sample. This decrease in separation between layers for all the doped samples may be attributed to metal particles deposited between the layers of the RGO.

The number of layers determined from XRD peak using equation 2 in the experimental section and was obtained in the range of 2–6, confirming the synthesis of few layers containing graphene.

Table 4.38: Lattice spacing, number of layers and average crystal size of the metal doped RGO samples.

Sample ID	d–Spacing $(nm)_{(002)}$	Number of layers	Average crystal size (nm)	I_D/I_G ratio
RGO	0.387	2	–	0.89
Ni/RGO	0.353	5	7.5	1.08
Pt/RGO	0.358	2	14	1.26
Pd/RGO	0.355	6	11	1.10

The Raman spectra of the samples are shown in Figure 4.70. The D–band detected in range of 1346–1350 cm^{-1} and G–band around 1591–1597 cm^{-1}. RGO had an intensity ratio (I_D/I_G) value of 0.89. With the incorporation of metals to RGO, the value of I_D/I_G was enhanced from 0.89 for RGO to 1.08 for nickel, 1.10 for palladium and 1.26 for platinum doped RGO samples. On comparison between metal doped RGO samples, the lower value of (I_D/I_G) ratio was observed for nickel doped RGO compared to that of platinum and palladium doped RGO samples, which attributed to higher level of graphitization as was also observed from XRD analysis.

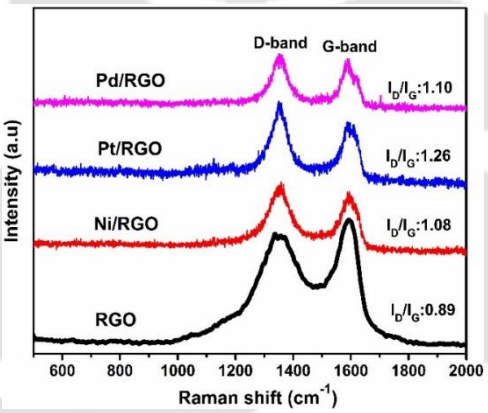

Figure 4.70: Raman spectra of RGO and metal doped RGO samples.

The nitrogen adsorption–desorption isotherms of all the samples (Figure 4.71a) were of type–II with wide H4 type hysteresis loop, signifying slit–shaped pores. As can be observed, the impregnation of metal did not affect the overall pore structure, however, the volume of nitrogen adsorption significantly decreased. This decrease may be associated with blockage of openings between the layers due to the presence of the metal clusters. The most significant decrease in volume adsorbed was for the nickel doped RGO sample. Accordingly, the lowest surface area and pore volume were observed for Ni/RGO sample (Table 4.39). The BET surface area and total pore volume of all the metal doped RGO samples reduced compared to that of undoped RGO (461 m^2/g, 0.50 cm^3/g). This decrease may have happened from blockage of the pores of RGO by the metal particles. Micropore area of 86 m^2/g was observed for RGO. With addition

of metals to RGO, micropore area was dropped from 86 to 16 m^2/g. The most significant drop in micropore area was observed for nickel doped RGO sample.

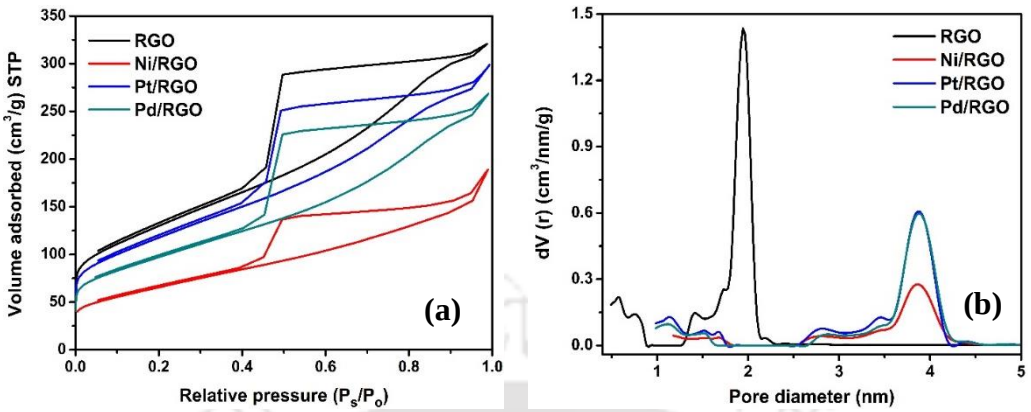

Figure 4.71: (a) N_2 adsorption–desorption isotherms (b) Pore size distribution of RGO and different metal doped RGO samples.

The pore size distributions of the samples are shown in Figure 4.71(b). The RGO seemed to have pores in very narrow range of 0.4 to 2.2 nm, showing mainly microporous nature. When impregnated with different metals, the distribution was shifted towards the larger pores. Pores were observed in the range of 2.6 to 4.4 nm for all the metal doped RGO samples. Thus, in the metal doped RGO samples, available openings were mainly mesoporous in nature with the average pore size of 3.8 nm. This suggested partial blockage of smaller pores by presence of metal clusters.

Table 4.39: Physical properties of the RGO and different metal doped RGO samples.

Sample ID	BET surface area (m^2/g)	Total pore volume (cm^3/g)	Micropore area (m^2/g)	Average pore size (nm)
RGO	461	0.50	86	1.80
Ni/RGO	234	0.29	16	3.88
Pt/RGO	417	0.46	39	3.87
Pd/RGO	345	0.41	40	3.83

The FESEM images of RGO and various metal doped RGO samples are shown in Figure 4.72. Presence of dense layer with very fine pores was observed for the RGO sample. Morphology significantly changed with the incorporation of metals into RGO. The change in morphology depended on the type of metal. Fluffy and layers structures appeared for nickel and palladium doped RGO. The palladium doped RGO had more uniform structure compared to that of nickel doped RGO.

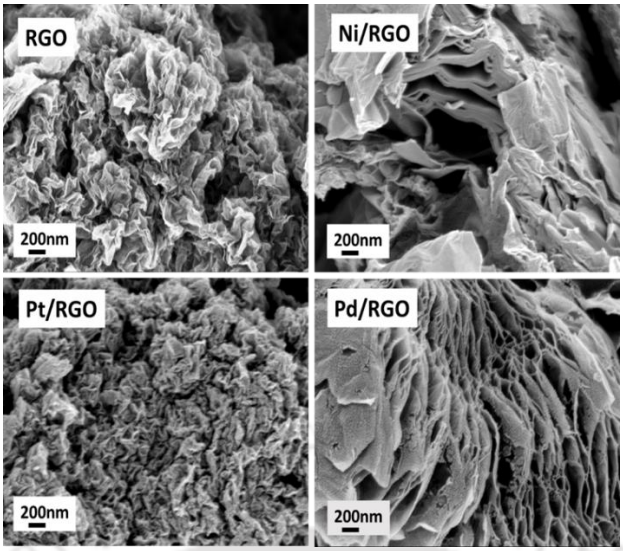

Figure 4.72: FESEM images of RGO and different metal doped RGO samples.

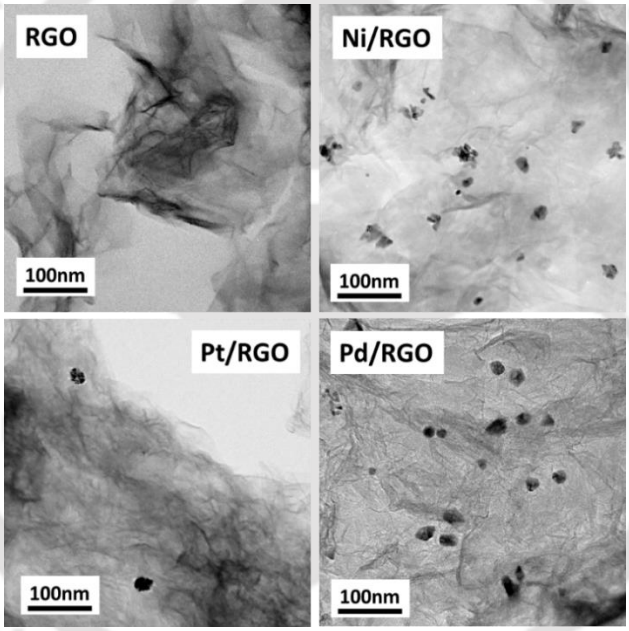

Figure 4.73: TEM images of RGO and different metal doped RGO samples.

The nickel doped RGO showed non–homogenous and less separated layers with large blank spaces in between. This may be the reason for the comparatively low surface area and pore volume of Ni/RGO as observed earlier. The platinum doped RGO showed similar structure as that of undoped RGO but bit more densed, resulting in slightly lower surface area and pore volume (Table 4.39).

TEM images of the samples are shown in Figure 4.73. The corresponding metal size distribution is shown in Figure 4.74. The average metal sizes were obtained as 2.6 nm for Pd/RGO, 2.8 nm for Ni/RGO and 3.4 nm for Pt/RGO. Thus the palladium metal particles

showed the highest dispersion. It was observed that the particle size calculated from TEM images lower than that of calculated by XRD analysis. The reason is discussed earlier in section 4.1.6 page no. 91.

The results showed that the interaction between platinum and RGO was minimum as the RGO structure was least affected by the presence of platinum as shown by FESEM images. This was also suggested by less reduction in surface area and pore volume. This lower interaction between platinum metal and RGO was also the reason for the lower dispersion of metal. This behavior of platinum was also observed by Baca et al. (2018). The TEM images also showed higher dispersion of palladium metal within the RGO matrix compared to that of nickel and platinum doped RGO.

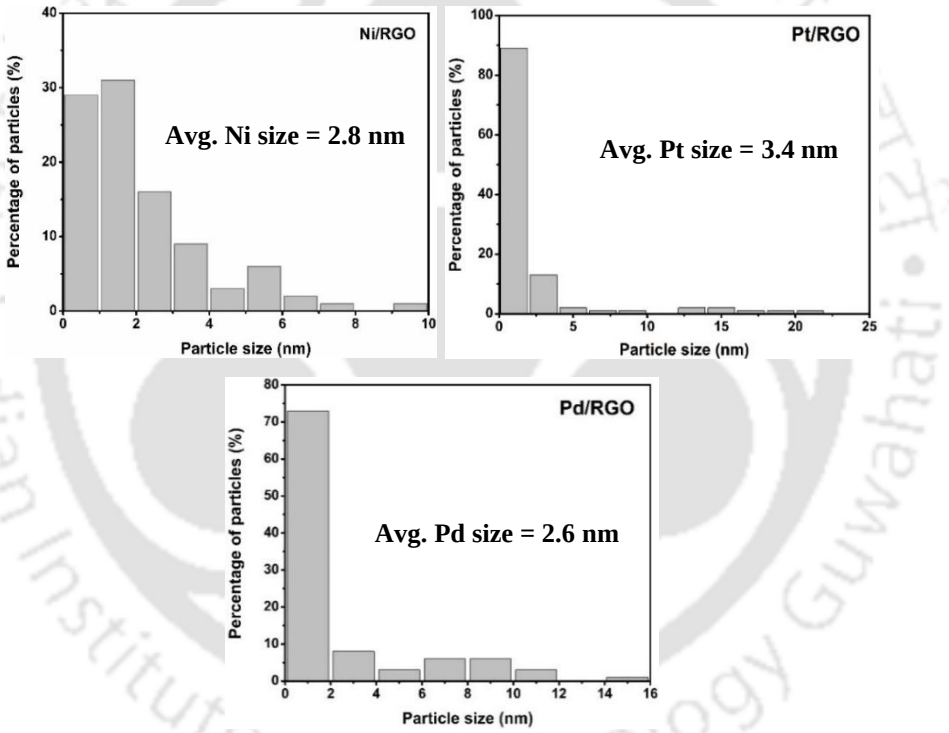

Figure 4.74: Particle size distribution of nickel, platinum and palladium doped RGO samples.

Hydrogen uptake

Hydrogen adsorption isotherms of RGO and all the metal doped RGO samples are shown in Figure 4.75(a). Hydrogen uptake was investigated at –196 °C and 30 bar. Hydrogen uptake values of the samples are included in Table 4.40. The RGO sample had hydrogen uptake capacity of 2.50 wt.%. With the addition of metals in RGO, a positive effect on hydrogen

uptake was observed for all the samples. The uptake capacity enhanced to 2.64 (Ni/RGO), 2.8 (Pt/RGO) and 3.22 (Pd/RGO) wt.%.

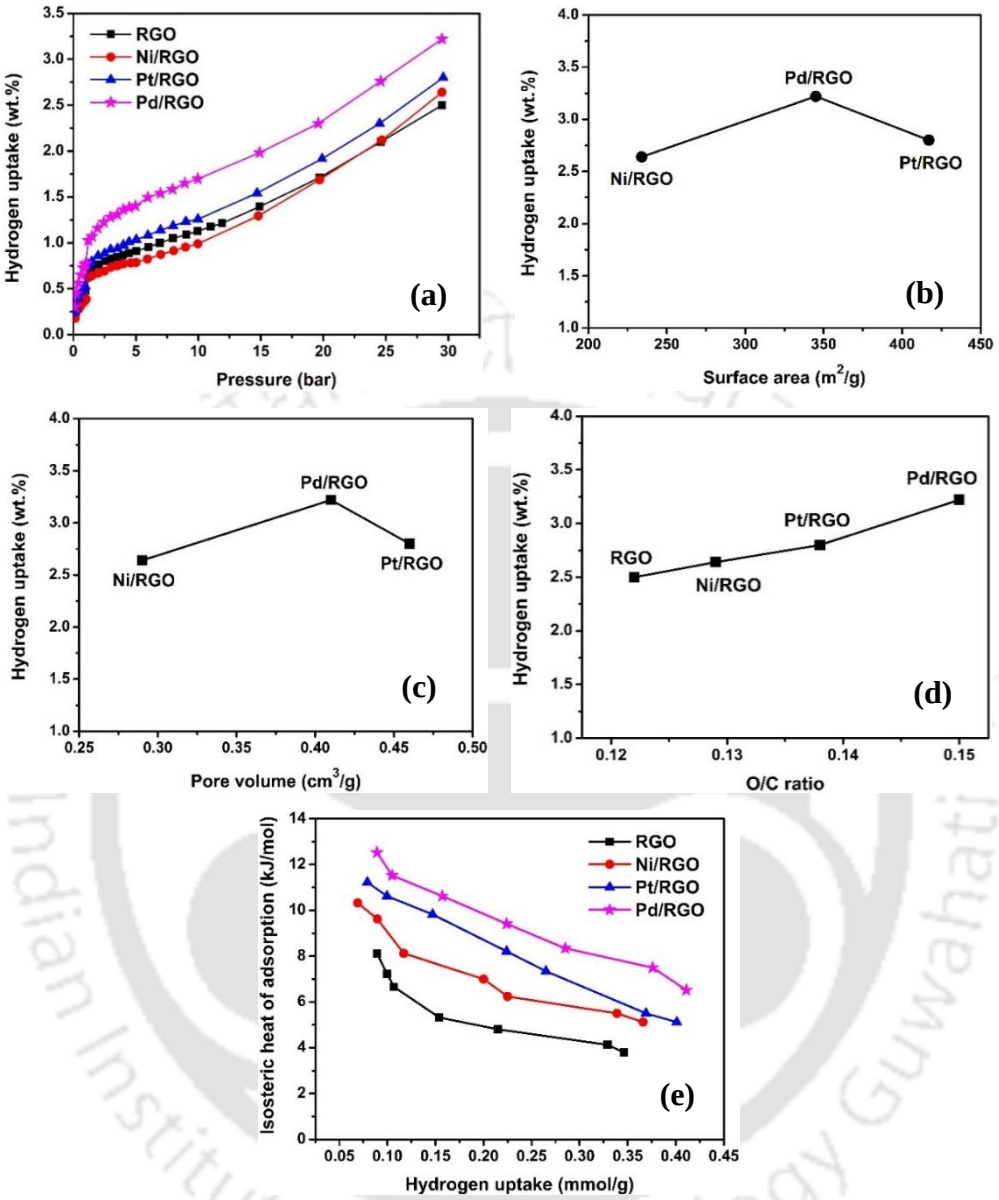

Figure 4.75: (a) Hydrogen adsorption isotherms at –196 °C up to 30 bar (b) Hydrogen uptake capacity as a function of surface area of samples (c) Hydrogen uptake capacity as a function of pore volume of samples (d) Hydrogen uptake capacity as a function of oxygen to carbon (O/C) ratio of samples (e) Isosteric heats of adsorption as a function of the amount of H_2 adsorbed on samples.

The hydrogen uptake as a function surface area and pore volume are shown in Figure 4.75(b) and (c), respectively. In general, the increase in surface area and pore volume resulted increase in hydrogen uptake. However, the highest hydrogen uptake of 3.22 wt.% was obtained for palladium doped RGO sample in spite of its lower surface area and pore volume than that of Pt/RGO. The higher hydrogen uptake capacity of palladium doped RGO may have resulted

from higher dispersion of palladium particles (Figure 4.74). The higher dispersion resulted in additional active sites for hydrogen adsorption on Pd/RGO.

Table 4.40: Hydrogen uptake capacity of RGO and different metal doped RGO samples at –196 °C.

Sample ID	Hydrogen uptake (wt.%) at 30 bar
RGO	2.50
Ni/RGO	2.64
Pt/RGO	2.80
Pd/RGO	3.22

In this study, the oxygen content seemed to have also played a significant role in hydrogen uptake enhancement. Figure 4.75(d) shows increase of the hydrogen uptake capacity with increase of oxygen content. This increase as explained earlier may be attributed to the stronger contribution of highly electronegative oxygen towards interaction with incoming highly electropositive hydrogen. The enhancement of hydrogen uptake for palladium doped RGO may also be attributed to the greater interaction of hydrogen with palladium. The hydrogen is reported to interact more strongly with palladium compared to that with nickel and platinum (Adams et al. 2010; Baca et al. 2018). The results thus suggested that the hydrogen uptake depended not only on the surface area and pore volume but also on other parameters such as the dispersion of metal, structure of layers and oxygen content.

The isosteric heat of adsorption (Q_{ads}) was calculated from the adsorption isotherms. The variation in calculated isosteric heat of adsorption with hydrogen uptake is shown in Figure 4.75(e). The isosteric heat of adsorption for RGO was 8.1 kJ/mol at lower hydrogen uptake, which was enhanced in the range 10.3–12.5 kJ/mol on doping of different metals. The increasing order of heat of adsorption for doped RGO (in kJ/mol) was Ni/RGO (10.3) < Pt/RGO (11.2) < Pd/RGO (12.5). The most significant increase was observed for Pd/RGO sample. The higher heat of adsorption indicated a significant interaction between hydrogen and metal particles. At higher hydrogen uptake, the heat of adsorption was exhibited in between 5.12–6.5 kJ/mol. The highest was obtained for the Pd/RGO sample (6.5 kJ/mol). These values agreed with the reported heat of adsorption values for RGO (2.5–6 kJ/mol) and metal (Pt & Pd) doped graphene (8.2–16.8 kJ/mol) (Gadipelli et al. 2015).

Summary

This study investigated the potential of platinum, nickel and palladium doped RGO samples as a hydrogen storage adsorbent. The metals were incorporated into RGO by impregnation method. With addition of metals to RGO, O/C ratio increased in order of 0.116 (RGO) < 0.129 (Ni/RGO) < 0.138 (Pt/RGO) < 0.150 (Pd/RGO). Significant decrease in d–spacing was observed on addition of different metals to RGO. This decrease may be attributed to metal particles deposited between the layers of RGO. With addition of different metals, the pore distributions were shifted towards the larger values with average pore size in the range of (3.83–3.88 nm). The surface area and total pore volume of all metal doped RGO reduced compared to that of undoped RGO. This reduction may have happened from blockage of the pores of RGO by the metal particles. All the metal doped RGO samples showed mesoporous nature, whereas, RGO showed microporous nature. The average metal particle size of nickel, platinum and palladium doped RGO samples were 2.8, 3.4 and 2.6 nm, respectively. The highest dispersion of metal was observed for Pd/RGO. The morphology of RGO was not affected with the addition of platinum but both nickel and palladium doped RGO samples showed layered structures. The nickel doped RGO showed non–homogenous and less separated layers with large blank spaces in between. The highest hydrogen uptake of 3.22 wt.% was obtained for palladium doped RGO sample in spite of having the lower surface area and pore volume than the Pt/RGO. The higher hydrogen uptake capacity of palladium doped RGO may have resulted from higher dispersion of metal particles, higher oxygen content and layered structure.

4.2.5.1 Effect of preparation methods and sequence of metal incorporation

The palladium doped RGO (Pd/RGO) showed the best metal dispersion and hydrogen uptake capacity. In this section, the effects of the different preparation methods and sequence of metal incorporation into RGO and EGO were investigated. The palladium was incorporated into GO exfoliated in flow of air at 300 ^{o}C. The physicochemical properties and hydrogen uptake of corresponding sample, named as Pd/EGO(Air), was compared with that of Pd/RGO. The metal was incorporated in two ways in the graphene sample as discussed in experimental section 3.2.5. Palladium was first impregnated on GO and then it was treated with hydrazine to obtain Pd/RGO or exfoliated to have Pd/EGO. In second pathway, first RGO or EGO sample was formed and then the palladium precursor was incorporated by impregnation method. These samples were denoted as Pd/RGO_A and Pd/EGO_A. The hydrogen uptake was measured at –196 °C and 30 bar for all the samples.

Table 4.41: Elemental analysis of palladium doped RGO and EGO samples prepared by different methods using EDX.

Sample ID	Elements (wt.%)			
	Pd	C	O	O/C
RGO	–	89.6	10.4	0.116
Pd/RGO	2.0	85.2	12.8	0.150
Pd/RGO_A*	2.2	84.8	13.0	0.153
EGO	–	79.1	20.9	0.264
Pd/EGO	1.8	79.6	18.6	0.233
Pd/EGO_A*	2.2	82.3	15.5	0.188

* Pd was impregnated on prepared RGO and EGO.

.

The composition of the samples prepared using different protocols are shown in Table 4.41. The final palladium loading was varied in the range of 1.8–2.2 wt.% (Table 4.41). It was observed that the oxygen content slightly increased on palladium doping for RGO samples. The increase was more when the metal was incorporated directly in RGO. The order of oxygen content in wt.% was RGO (10.4) < Pd/RGO (12.8) < Pd/RGO_A (13). The corresponding O/C ratios were 0.116, 0.15 and 0.153, respectively. This increase in O/C ratio may be explained by less effective removal of oxygen in presence metal. The metal was also reduced simultaneously by hydrazine, consuming the reducing agent and thereby limiting the hydrazine available for reduction of GO. In contrast for Pd/EGO, the oxygen content was reduced compared to that of undoped EGO sample and it was further lowered for Pd/EGO_A. The oxygen content of 20.9 wt.% for EGO was reduced to 18.6 wt.% for Pd/EGO and 15.5 wt.%

for Pd/EGO_A. The corresponding O/C ratios were 0.264, 0.233 and 0.188, respectively. Here the decrease in oxygen content with palladium doping may have resulted from the enhancement of combustion of carbon matrix by catalytic effects of the metal. This effect was less severe for Pd/EGO, for which exfoliation was carried out in flow of air after palladium was incorporated in GO. However, for Pd/EGO_A for which the palladium was incorporated in final EGO sample and thereafter, heated at 300 ^{o}C (same as the exfoliation temperature) but under static condition, more of the surface oxygen may have been used up in the catalytic combustion of matrix carbon due to limited supply of air. Consequently, the oxygen content got comparatively more reduced. All the EGO based samples had higher oxygen content than that the RGO samples and the reason have been already discussed in earlier section in page 20–21.

Figure 4.76(a) and (b) depict the XRD patterns of all the samples. The peak corresponding to graphitic carbon was observed in the range of 23.8–25.9° for the samples. The graphitic peak intensity was reduced when palladium was incorporated in RGO in the order RGO > Pd/RGO > Pd/RGO_A. This was also observed for platinum doped RGO sample, discussed in earlier section when addition of metal reduced the graphitic zone. With addition of Pd to EGO on other hand, the graphitic zone increased in the order EGO < Pd/EGO_A < Pd/EGO. This increase may be accounted by catalytic effect of metal on the formation on graphitic zone as was also observed earlier for doped templated carbons (section 4.1.4). This catalytic effect was more prominent for Pd/EGO as palladium was present during exfoliation at high temperature of 300 ^{o}C. But for Pd/EGO_A sample palladium was incorporated after exfoliation. Hence, though the final sample after metal doping was again treated at 300 ^{o}C but the effect was less.

Three XRD peaks attributed to Pd^{o} were observed at 2θ = 39.9°, 46.6° and 67.85° in both the palladium doped EGO samples. The peaks due to PdO are reported in the literature at 33.9° (101), 42° (110), 54.5° (112), 60.69° (200), and 71.28° (202) (Lin et al. 2014; Ganji et al. 2013). No peaks for oxide form was observed in present samples. For the samples prepared by metal incorporation directly on RGO and EGO samples, no peaks related to palladium were observed, indicating higher dispersion of metal on carbon surface during the impregnation process. The appearance of prominent peaks of palladium for Pd/RGO and Pd/EGO samples in which the metal was incorporated in GO and thereafter the Pd–GO composite was further treated with hydrazine at 90 ^{o}C or thermally exfoliated at 300 ^{o}C to give Pd/RGO and Pd/EGO respectively suggested agglomeration or sintering of the metal under the process conditions. The agglomeration was more for Pd/EGO because of higher treatment temperature. This was later confirmed by higher metal cluster size for Pd/EGO determined from TEM images.

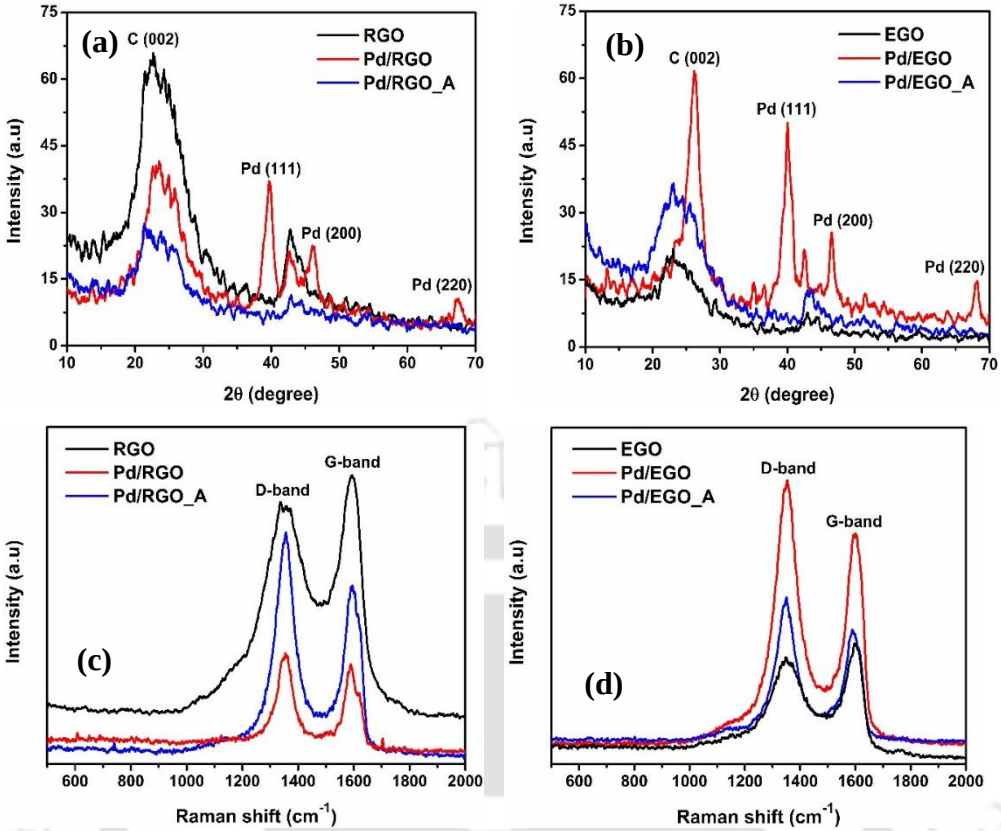

Figure 4.76: (a) XRD profiles of palladium doped RGO (b) XRD profiles of palladium doped EGO samples (c) Raman spectra of palladium doped RGO (d) Raman spectra of palladium doped EGO samples.

The lattice spacing, crystal size, number of layers and I_D/I_G ratio of samples are included in Table 4.42. The d–spacing between the layers was observed to decrease with addition of palladium to both RGO and EGO samples. It was decreased from 0.392 to 0.355 nm for Pd/RGO and from 0.381 to 0.344 nm for Pd/EGO. The decrease in d–spacing can be attributed to the presence of palladium clusters between the layers. For palladium doped on prepared RGO and EGO that is for Pd/RGO_A and Pd/EGO_A, the decrease in d–spacing was comparatively small, suggesting metal to be in well dispersed state which agreed with the XRD results. The more significant drop in d–spacing for Pd/RGO or Pd/EGO samples agreed with the XRD results that suggested formation of higher metal cluster in these samples and might be the reason for higher blockage between the layers.

The average crystal size of the metal cluster was 11 and 13 nm for Pd/RGO and Pd/EGO, respectively. This phenomenon may be explained based on the different temperature treatment that these two samples underwent. The Pd/RGO was subjected to a lower temperature (90 ^oC) compared to that of Pd/EGO (300 ^oC). Hence, the formation of cluster or agglomeration was lower in the Pd/RGO. The number of graphene layers varied in the range of 2–6. The most

significant increase in number of layers was observed for Pd/RGO (Table 4.42). This suggested that in presence of metal more graphitic zone or layer was obtained, as was also observed in previous results for metal doped carbon.

Table 4.42: Lattice spacing, crystal size, number of layers and I_D/I_G ratio of palladium doped RGO and EGO samples prepared by different methods.

Sample ID	d–Spacing $(nm)_{(002)}$	Number of layers	Average crystal size (nm)	I_D/I_G ratio
RGO	0.392	2	–	0.89
Pd/RGO	0.355	6	11	1.10
Pd/RGO_A*	0.366	3	–	1.38
EGO	0.381	4	–	0.90
Pd/EGO	0.344	3	13	1.05
Pd/EGO_A*	0.385	4	–	1.26

* Pd was impregnated on prepared RGO and EGO.

Figure 4.76(c) and (d) show the Raman spectra of RGO, EGO, palladium doped RGO and EGO samples prepared by different methods. The RGO and EGO samples have intensity ratio (I_D/I_G) of 0.89 and 0.90, respectively. The highest degree of graphitization was observed for RGO as discussed earlier. When palladium was doped on RGO and EGO, the intensity ratio (I_D/I_G) value was obtained in the range of 1.05–1.38. Intensity ratio (I_D/I_G) value was lower for palladium doped EGO (1.05) compared to that of other doped samples. This is indicating that the palladium doped EGO sample has a higher level of graphitization. In case of palladium doped directly on prepared RGO and EGO samples, the lower value of intensity ratio was obtained for Pd/EGO sample compared to that of Pd/RGO.

The nitrogen adsorption–desorption isotherms of the RGO, EGO, palladium doped RGO and EGO samples are shown in Figure 4.77(a). The nature of isotherms of Pd/RGO approached type II with H4 type hysteresis loop, signifying slit–shaped pores. However, type IV with H4 type hysteresis loop was observed for palladium doped exfoliated GO sample. No change in respective nature of isotherm and hysteresis loop was observed for when RGO or EGO samples were doped with palladium. A very wide hysteresis loop clearly observed for EGO and both the palladium doped EGO samples (Pd/EGO & Pd/EGO_A) at a higher relative pressure (P_s/P_o) of above 0.4. This suggested presence of higher amount of mesopores in these samples as compared to that in palladium doped RGO samples. Also, the volume of nitrogen adsorbed was significantly higher for palladium doped exfoliated GO samples.

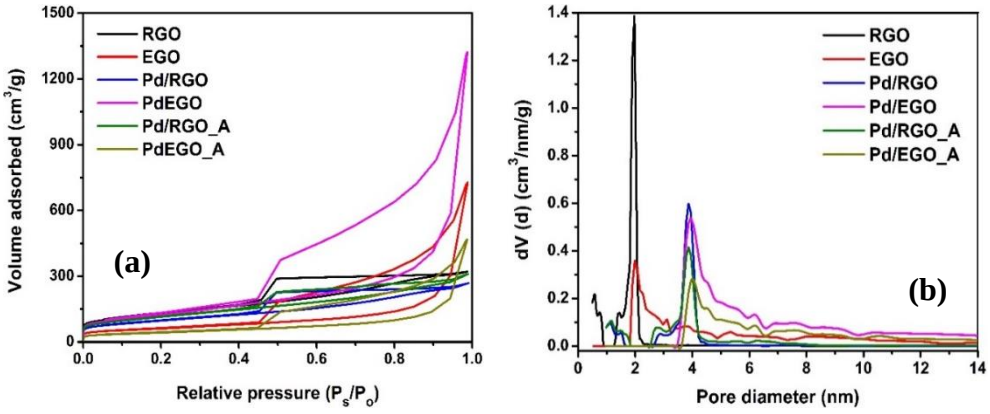

Figure 4.77: (a) Nitrogen adsorption–desorption isotherms (b) Pore size distribution of RGO, EGO, palladium doped RGO and EGO samples.

The physical properties of the samples are included in Table 4.43. For RGO (461 m^2/g; 0.50 cm^3/g), when metal was added to the GO before hydrazine treatment, the decrease in surface area and pore volume was more significant than when palladium was added directly in RGO. In first case, surface area was dropped from 461 to 345 m^2/g, while pore volume decreased from 0.50 to 0.41 cm^3/g. For the second case, surface area and pore volume dropped to 408 m^2/g and 0.47 cm^3/g, respectively. The results suggested that incorporation of metal in GO followed by hydrazine treatment may have resulted in more agglomeration of metal and thereby blocking the space in between the layers more effectively.

Table 4.43: Physical properties of RGO, EGO and palladium doped RGO and EGO samples prepared by different methods.

Sample ID	BET surface area (m^2/g)	Total pore volume (cm^3/g)	Micropore area (m^2/g)	Average pore size (nm)
RGO	461	0.50	86	1.80
Pd/RGO	345	0.41	40	3.83
Pd/RGO_A	408	0.47	24	3.81
EGO	217	1.12	8	2.81
Pd/EGO	449	2.04	4	4.78
Pd/EGO_A	152	0.75	23	4.75

* Pd was impregnated on prepared RGO and EGO.

Formation of larger cluster in Pd/RGO and well dispersion for Pd/RGO_A is established in XRD results. For EGO based samples, the effect on surface area and pore volume depended on the sequence of metal addition. When metal was added to GO and metal–GO composite was subjected to exfoliation temperature of 300 °C, there was considerable increase in surface area and pore volume. Surface area (217 m^2/g) and pore volume (1.12 cm^3/g) of EGO increased to

almost double values of 449 m^2/g and 2.04 cm^3/g respectively. The significant enhancement may be attributed to better separation of layers. As has been observed from TGA analysis, the metal had a significant catalytic effect in the combustion of carbon and thereby facilitated combustion and better separation of layers. Similar observation is also reported by Li et al. (2013). But when palladium was incorporated in prepared EGO, having lower surface area, the metal seemed to have particularly blocked the space between the separated layers resulting in further significant drop in surface area and pore volume. The surface area and pore volume dropped to 152 m^2/g and 0.75 cm^3/g for Pd/EGO_A sample. Thus the effect of preparation on the structure for palladium doped graphene was different for RGO or EGO based samples.

The pore size distributions of the samples are shown in Figure 4.77(b). The pores in the range of 2–5 nm were observed for the EGO sample, while RGO had very narrow pores in the range of 0.4–2.2 nm. The pore size was shifted to higher size range on addition of palladium to RGO and EGO, implicating blockage of small pores by the presence of metals and thereby increasing average pore size. For Pd/RGO, the pores were exhibited 2.5–4.5 nm, whereas, the Pd/EGO showed wide mesopores range of 3.4–10 nm with average pore size of 3.83 and 4.78 nm respectively. The similar effect on pore size was observed when palladium was doped directly on prepared RGO and EGO samples.

The FESEM images of samples are compared and shown in Figure 4.78. The RGO showed a dense layer with very fine pores and EGO appeared fluffy with better separation of layers. With addition of palladium to RGO, the structure was changed from dense layers to fluffy layers. Whereas, the separation of layers increased for palladium doped EGO and may be the reason for increase in surface area and pore volume of this sample. When palladium metal precursor solution was added directly to already prepared RGO and EGO sample and calcined at 300 °C for 4 h, a distorted layered structure was obtained for both the samples.

The TEM images of the sample (Figure 4.79) also showed increase in the fluffiness of structure as metal was introduced in GO and treated with hydrazine at 90 °C or exfoliated at 300 °C. The metal particles were observed having the average pore size of 9.8 and 10.4 nm for Pd/RGO and Pd/EGO, respectively. Slightly higher metal size for Pd/EGO compared to that of Pd/RGO agreed with corresponding XRD results. When palladium precursor solution was added directly on already prepared RGO and EGO samples as for Pd/RGO_A and Pd/EGO_A samples respectively, the resulting dispersion of metal increased with average metal size dropping to 7.1 and 4.8 nm respectively for Pd/RGO_A and Pd/EGO_A. The layers structure seemed to be

more distorted in these two samples as was also observed from FESEM images of these two samples.

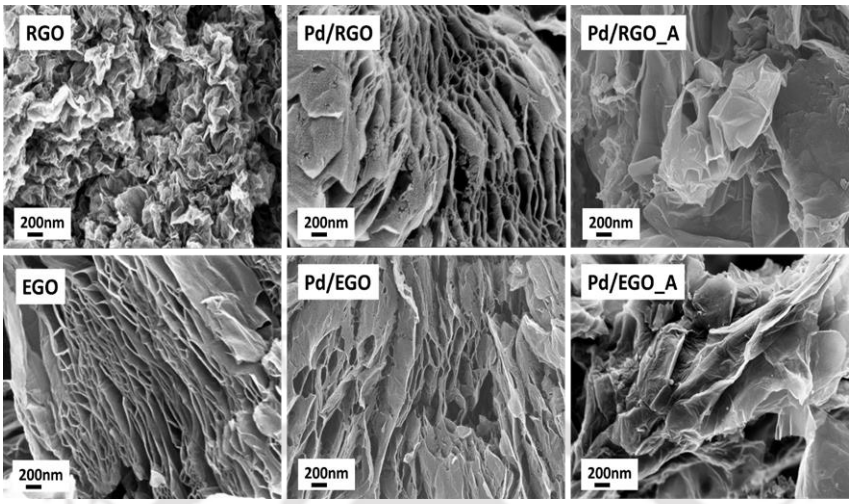

Figure 4.78: FESESM images of RGO, EGO, palladium doped RGO and EGO samples.

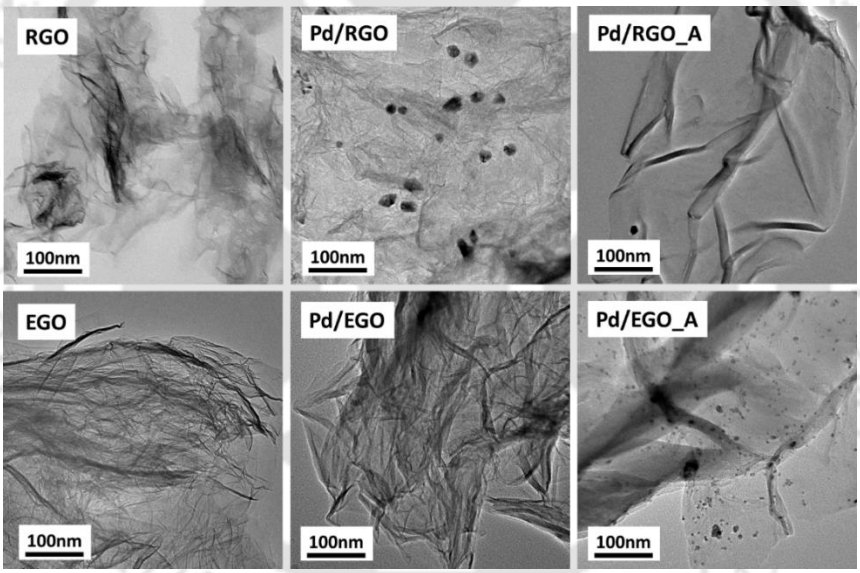

Figure 4.79: TEM images of RGO, EGO, palladium doped RGO and EGO samples.

Hydrogen uptake

Figure 4.80(a) shows hydrogen adsorption isotherms of the samples prepared following different protocols. Hydrogen storage was measured at –196 °C and up to 30 bar. The hydrogen storage capacity was exhibited in the range of 2.36–3.52 wt.% (Table 4.44). Figure 4.80(c) shows the variation of hydrogen uptake with surface area. The hydrogen uptake capacity increased almost linearly with increasing surface area of palladium doped samples. The Pd/EGO_A sample showed the lowest hydrogen uptake of 2.36 wt.% which may be attributed

to the lowest surface area and Pd/EGO showed the highest of 3.52 wt.% having the highest surface area.

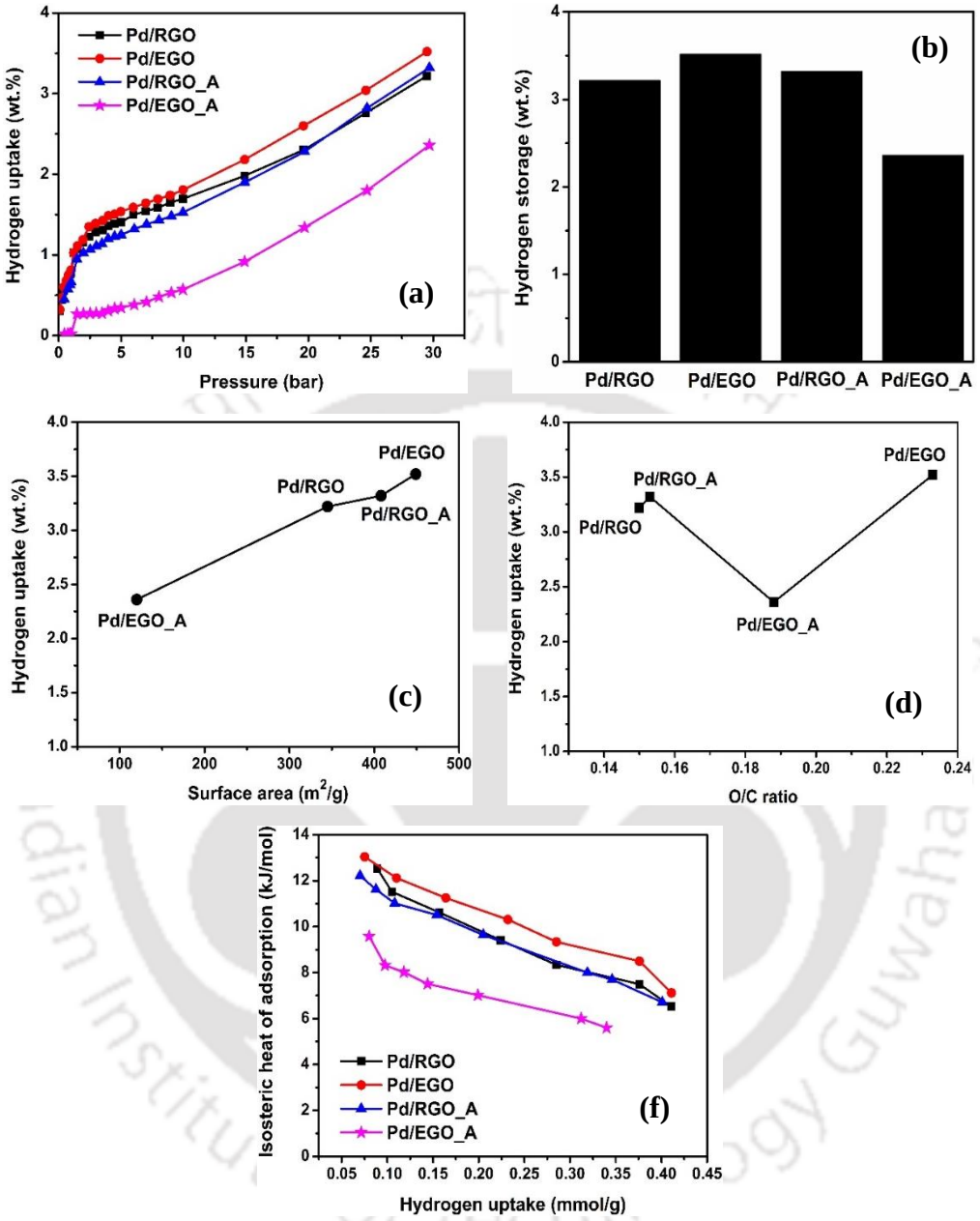

Figure 4.80: For palladium doped RGO and EGO samples (a) Hydrogen adsorption isotherms at –196 °C up to 30 bar (b) Hydrogen uptake capacity at –196 °C and 30 bar (c) Hydrogen uptake capacity as a function surface area of samples (d) Hydrogen uptake capacity as a function of O/C ratio of samples (e) Isosteric heats of adsorption as a function of the amount of H_2 adsorbed on samples.

The highest uptake of Pd/EGO can also be attributed to highest O/C ratio (Figure 7.80d). In spite of having second highest O/C ratio, lower hydrogen uptake of Pd/EGO_A may have resulted from very low surface area. Both the RGO base samples had low O/C ratio but their

high surface area contributed to high hydrogen uptake. The Pd/RGO_A having the second hydrogen uptake had second highest surface area. It also had slightly higher O/C ratio compared to Pd/RGO sample. Thus the highest uptake of Pd/EGO may be attributed to the highest surface area, pore volume, O/C ratio and dispersion of palladium particles.

Table 4.44: Hydrogen uptake capacity of the palladium doped RGO and EGO samples prepared by different methods at –196 °C.

Sample ID	Hydrogen uptake (wt.%)
	at 30 bar
Pd/RGO	3.22
Pd/EGO	3.52
Pd/RGO_A	3.32
Pd/EGO_A	2.36

The isosteric heat of adsorption (Q_{ads}) was calculated based on adsorption at –10 and 25 °C and shown in Figure 4.80(f). At lower surface coverage, the isosteric heat of adsorption for all the samples was in the range of 9.6–13 kJ/mol. After that, the heat of adsorption decreased with hydrogen uptake and obtained in the range of 7.1–5.6 kJ/mol at higher surface coverage. The heat of adsorption on Pd/EGO sample (13 kJ/mol) was highest indicating strongest interaction between hydrogen and highly dispersed palladium particles. The obtained heat of adsorption values is within the reported range for RGO (2.5–6 kJ/mol) and metal (Pt & Pd) doped graphene (8.2–16.8 kJ/mol) (Gadipelli and Guo 2015; Divya et al. 2014; Parambhath et al. 2011).

Summary

The effect of the preparation methods and sequence of palladium metal incorporation into RGO and EGO samples were investigated. The decrease in d–spacing was observed when palladium was doped in GO for the formation of Pd/RGO and Pd/EGO samples. This can be attributed to the presence of palladium clusters between the layers. The Pd/RGO showed the highest level of the graphitic zone compared to that of doped samples prepared by other methods. The effect on surface area and pore volume depended on the sequence of metal addition. The surface area (217 m^2/g) and pore volume (1.12 cm^3/g) of EGO increase to almost double values of 449 m^2/g and 2.04 cm^3/g, respectively when metal was added to GO and metal–GO composite was subjected to exfoliation temperature of 300 °C. With addition of palladium to RGO, its dense structure was changed to fluffy layers. For EGO which already had fluffy structures, the separation of layers further increased on palladium doping. When palladium metal precursor solution was added directly to prepared RGO and EGO sample, a distorted layered structure

was observed for both the samples. The highest hydrogen uptake of 3.52 wt.% was obtained for palladium doped EGO sample (Pd/RGO) at –196 °C and 30 bar. The highest uptake of Pd/EGO may be attributed to the highest surface area, pore volume, O/C ratio and dispersion of palladium particles. The overall isosteric heat of adsorption of hydrogen in Pd/EGO varied in the range of 7.1–13 kJ/mol depending on hydrogen uptake.

4.3 Hydrogen uptake at room temperature

The hydrogen uptake at room temperature (25 °C) for selected templated carbon and graphene samples were carried out and is discussed in this section.

4.3.1 Templated carbon based materials

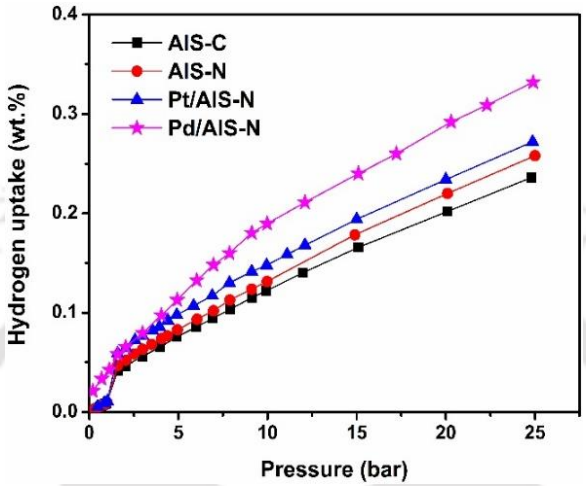

Figure 4.81: Hydrogen uptake isotherms of the selected templated carbons at 25 °C up to 25 bar.

The hydrogen uptake at room temperature was measured for the undoped (AlS–C), nitrogen doped (AlS–N), platinum and nitrogen codoped (Pt/AlS–N) as well as for palladium and nitrogen (Pd/AlS–N) co–doped templated carbons prepared from surfactant modified alumina template. The hydrogen uptake was measured up to 25 bar and adsorption isotherms are shown in Figure 4.81. The hydrogen uptake values of the samples are tabulated in Table 4.45.

Table 4.45: Hydrogen uptake capacity of undoped templated carbon, nitrogen doped templated carbon, metal and nitrogen co–doped templated carbons at 25 °C and 25 bar.

Sample ID	Hydrogen uptake (wt.%)
AlS–C	0.23
AlS–N	0.26
Pt/AlS–N	0.27
Pd/AlS–N	0.33

The hydrogen uptake of all the samples was obtained in the range of 0.23–0.33 wt.%. The undoped templated carbon (AlS–C) had hydrogen uptake of 0.23 wt.% which was slightly enhanced up to 0.26 wt.% on nitrogen doping (AlS–N).

Table 4.46: Comparison of physical properties and hydrogen uptake capacities at room temperature (25 °C) for mesoporous templated carbons of present study to that reported in the literature.

Template	Nature of templated carbon	Surface area (m^2/g)	Pressure (bar)	Hydrogen uptake (wt.%)	References
Zeolite–Y	Microporous	2136	50	0.8	(Guan et al. 2009)
Silica	Mesoporous	847	5	0.01	(Campesi et al. 2008)
Silica	Mesoporous	877	22	0.29	(Oh et al. 2013)
Silica	Mesoporous	1995	80	0.35	(Zinhua et al. 2010)
AlS–N	**Mesoporous**	**1508**	**25**	**0.26**	**Present study**
Pd/silica	Mesoporous	712	5	0.08	(Campesi et al. 2008)
Pt/silica	Mesoporous	882	22	0.30	(Oh et al. 2013)
Pt/AlS–N	**Mesoporous**	**836**	**25**	**0.27**	**Present study**
Pd/AlS–N	**Mesoporous**	**817**	**25**	**0.33**	**Present study**

This enhancement is similar to that shown at liquid nitrogen temperature (–196 ºC) as discussed in earlier section 4.1.4. With addition of platinum or palladium into nitrogen doped templated carbon, the improvement in hydrogen uptake was observed. Again the trend was same as that observed at –196 ºC. The most significant improvement was observed for palladium co–doped templated carbon (Pd/AlS–N) for which hydrogen uptake increased from 0.26 to 0.33 wt.%. In addition to the factors already mentioned earlier, the spillover mechanism attributed to metal cluster deposited on surface may have contributed in the enhancement of hydrogen uptake. The spillover mechanism has already been discussed in the Introduction and Literature Review Chapters. The hydrogen uptake studies at room temperature reported in the literature for different microporous zeolite templated carbon and mesoporous silica gel templated carbons are compared with the results of present study (Table 4.46).

4.3.2 Graphene based materials

The hydrazine reduced graphene oxide RGO(hyd), exfoliated graphene oxide in hydrogen EGO(H_2) and exfoliated graphene oxide in air EGO(Air) and palladium doped air exfoliated graphene oxide Pd/EGO, were selected for hydrogen uptake at 25 °C up to 25 bar. The hydrogen adsorption isotherms are shown in Figure 4.82 and the corresponding hydrogen uptakes are summarized in Table 4.47. The hydrogen uptake capacity was in the range of 0.18–0.24 wt.%. At this room temperature, the highest uptake capacity of 0.22 wt.% was observed for RGO(hyd), having surface area of 461 m^2/g.

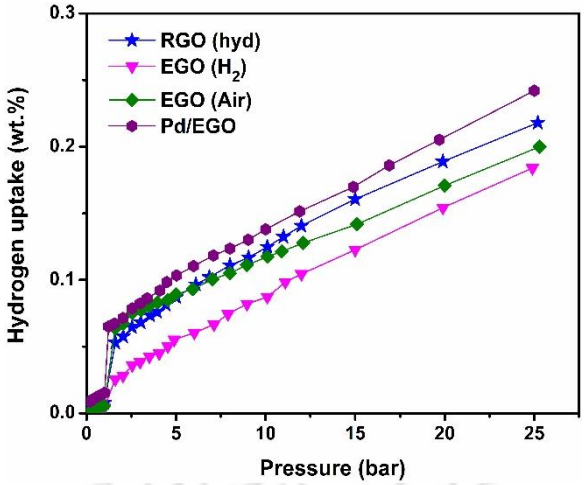

Figure 4.82: Hydrogen uptake isotherms of the selected graphene samples at 25 °C up to 25 bar.

The second highest hydrogen uptake capacity of 0.20 wt.% was obtained for EGO (Air), having surface area of 248 m^2/g. The higher uptake capacity may be attributed to highest surface area of RGO(hyd) sample.

Table 4.47: Hydrogen uptake capacity of reduced graphene oxide, exfoliated garphene oxide and palladium doped exfoliated garphene oxide samples at 25 °C and 25 bar.

Sample ID	Hydrogen uptake (wt.%)
RGO (hyd)	0.22
EGO (H_2)	0.18
EGO (Air)	0.20
Pd/EGO	0.24

When palladium was doped on air exfoliated graphene oxide, the enhancement in hydrogen uptake capacity was observed. The uptake was increased from 0.20 to 0.24 wt.%. This observation is similar to that observed at –196 ^oC. In this case also the spillover mechanism may have contributed to the hydrogen uptake capacity. The obtained hydrogen uptake capacity at room temperature is comparable with that reported in the literature, as shown in Table 4.48.

The hydrogen uptake at room temperature was much lower in comparison to hydrogen uptake measure at liquid nitrogen temperature for both templated carbon and graphene based materials. Even for metal doped carbons, the room temperature uptake values were low. However, similar hydrogen uptake trends were observed on doping the carbon matrix as was observed at –196 ^oC.

Table 4.48: Comparison of physical properties and hydrogen uptake capacities for graphene samples with that reported in the literature at room temperature.

Graphene type	Surface area (m^2/g)	Pressure (bar)	Hydrogen uptake (wt.%) (25–30 °C)	References
Expanded graphite	555	20	0.29	(Lueking et al. 2005)
Thermally expanded graphene sheets	300	54	0.10[a]	(Zheng et al. 2013)
Thermally reduced graphene oxide	375	50	0.32	(Hudson et al. 2014)
Hydrazine reduced graphene oxide	640	10	0.095	(Srinivas et al. 2010)
Hydrazine reduced graphene oxide	-	20	0.25	(Ismail et al. 2015)
RGO(hyd)	**461**	**30**	**0.22**	**Present study**
EGO(Air)	**217**	**30**	**0.20**	**Present study**
Pt/5GO/HKUST–1 composite	848	80	0.77	(Hu et al. 2014)
ZIF–8/5GO composite	1247	10	0.07[b]	(Hu et al. 2015)
Pt/graphene	478	30	0.15	(Chen et al. 2011)
Pd/graphene	544	57	0.16	(Chen et al. 2011)
Pd/EGO	**449**	**30**	**0.24**	**Present study**

Note. a) at 40 bar; b) hydrogen uptake of 0.367 mmol/g converted to wt.%

4.4 Reversibility and Cyclic stability

In this section, the hydrogen adsorption–desorption reversibility and cyclic stability of the selected samples have been discussed. The reversibility and cyclic stability of the templated carbon and graphene based samples were checked at –196 °C. The hydrogen uptake stability up to 10 cycles was tested at 25 bar for the metal and nitrogen co–doped carbon derived from surfactant modified alumina template. The hydrogen uptake stability of GO exfoliated in air at 300 °C was measured up to 5 cycles at 30 bar. The adsorbents obtained at the end of cyclic stability study was characterized by surface area analysis, pore analysis and morphology study to see the effects, if any, of the cyclic adsorption–desorption processes on the physicochemical property of the adsorbents.

4.4.1 Reversibility

Hydrogen adsorption–desorption isotherms for the nitrogen–doped and metal and nitrogen co–doped templated carbons and air exfoliated graphene oxide are shown in Figure 4.83(a) and (b). The hydrogen uptake isotherms were measured till 25 bar pressure at –196 °C temperature for all metal and nitrogen co–doped samples. For air exfoliated graphene oxide, the hydrogen uptake isotherms were measured at –196 °C up to 30 bar. Desorption curve followed back mostly the same path as adsorption curve without any hysteresis loop for all the samples. The results suggested that adsorbed hydrogen was released reversibly for all the samples. These data prove that studied carbon based hydrogen storage materials are able to function reversibly.

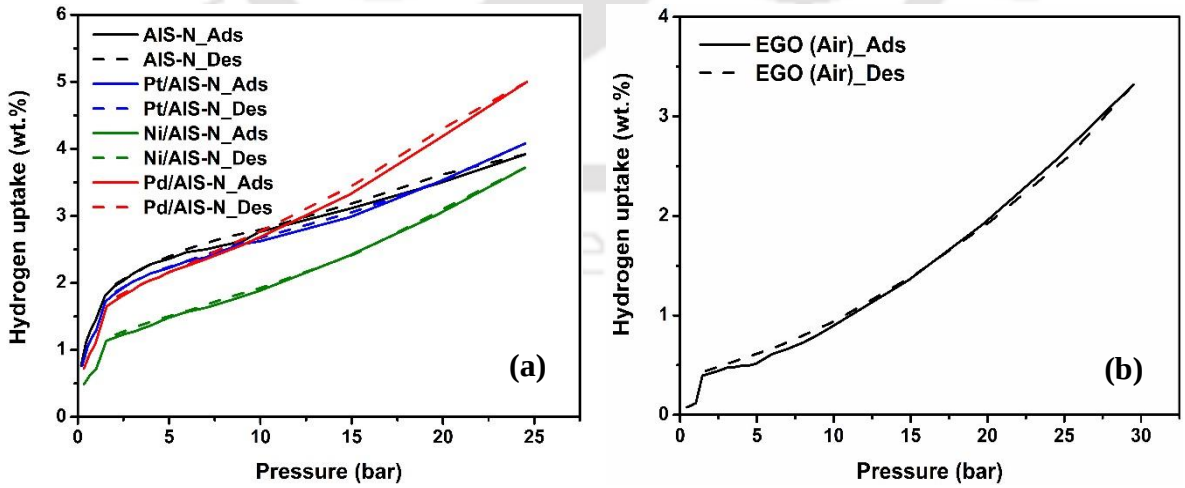

Figure 4.83: Hydrogen adsorption–desorption isotherms at –196 °C (a) Different metal and nitrogen co–doped templated carbons (b) Air exfoliated graphene oxide.

4.4.2 Cyclic stability

Templated carbon

Hydrogen adsorption–desorption cycles of all the metal and nitrogen co–doped templated carbons at –196 °C up to 25 bar are shown in Figure 4.84(a–d). The comparison of the 1st, 5th and 10th cycles showed negligible variation. Figure 4.84(e) shows the plot of hydrogen uptake as a function of the number of cycles.

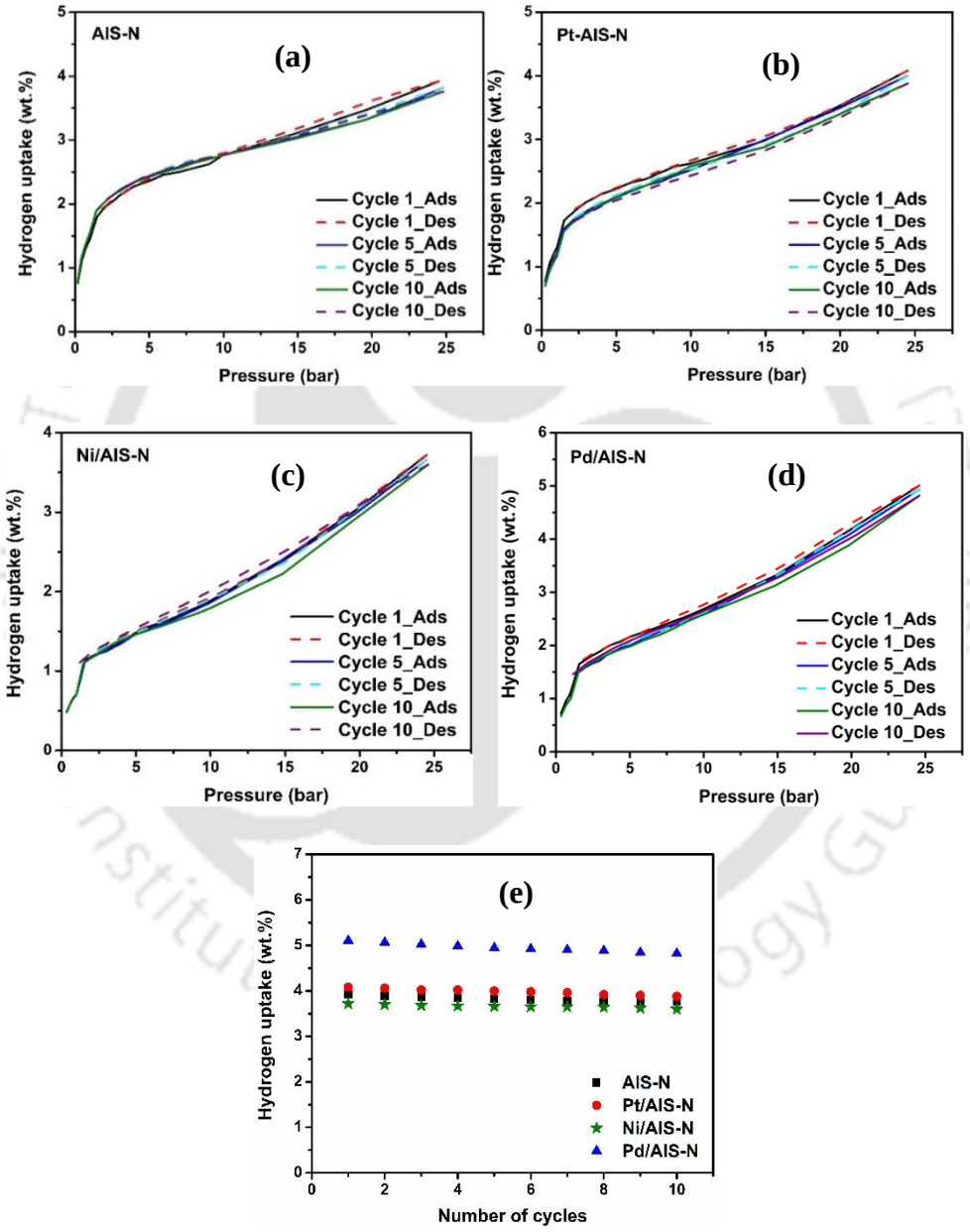

Figure 4.84: Hydrogen adsorption–desorption isotherms of 1st, 5th and 10th cycles for (a) AlS–N (b) Pt/AlS–N (c) Ni/AlS–N (d) Pd/AlS–N. (e) Hydrogen uptake as a function of number of adsorption–desorption cycles for metal and nitrogen co–doped templated carbons at –196 °C and 25 bar.

Slight reduction in hydrogen uptake capacity was observed for all samples with increase in number of cycles. The reduction in hydrogen uptake capacity at 10th cycle was about 4.1, 4.9, 3.2 and 5.5 % for AlS–N, Pt/AlS–N, Ni/AlS–N and Pd/AlS–N samples respectively compared to that of the respective first cycle.

To understand the effect of repeated adsorption–desorption cycles on properties of adsorbents, the adsorbents obtained after 10 cycles were characterized using surface area and pore analysis as well as microscopic analysis. The nitrogen adsorption–desorption of fresh and used (after 10 cycles) adsorbents are compared in Figure 4.85(a). For all the samples, there was a drop in nitrogen adsorption volume corresponding to original value as shown in Figure 4.85(a).

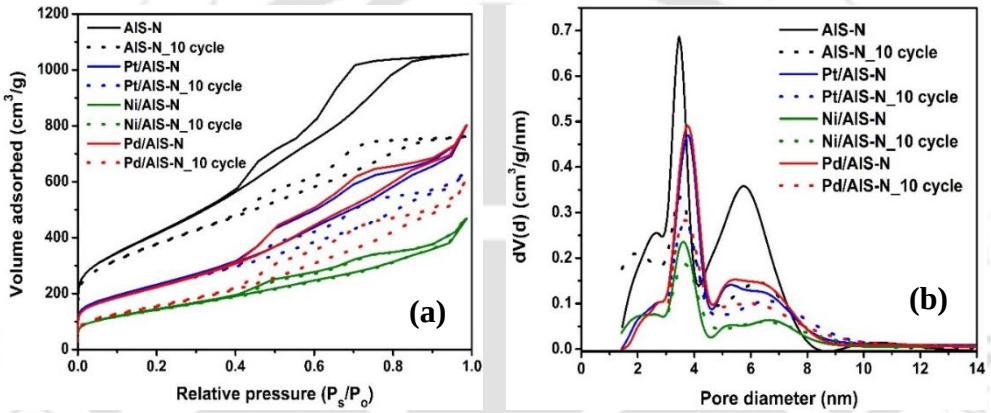

Figure 4.85: (a) N_2 adsorption–desorption isotherms (b) Pore size distributions of fresh and used (after 10 cycles) of metal and nitrogen co–doped templated carbons.

Table 4.49 showing the physical properties of fresh and used adsorbents suggested decrease of surface area as well as pore volume. The higher reduction in surface area and pore volume was observed for palladium co–doped templated carbon compared to that of platinum and nitrogen co–doped templated carbons.

Table 4.49: Physical properties of fresh and used (after 10 cycles) metal and nitrogen co–doped templated carbons.

Sample ID	BET surface area (m^2/g)	Micropore area (m^2/g)	Total pore volume (cm^3/g)	Average pore size (nm)
AlS–N	1328 (1508)	86 (49)	1.32 (1.64)	3.1 (3.4)
Pt/AlS–N	810 (836)	38 (30)	0.99 (1.24)	3.6 (3.8)
Ni/AlS–N	511 (520)	27 (22)	0.71 (0.72)	3.4 (3.5)
Pd/AlS–N	572 (817)	45 (24)	0.93 (1.27)	3.7 (3.9)

Note: Values in first bracket corresponded to that of fresh templated carbons before being subjected to cycles of adsorption and desorption

The decrease in area and pore volumes suggested collapse of inner pore walls after 10 cycles under high pressure adsorption. The pore size distribution (Figure 4.85b) of all the adsorbents showed that the slight reduction in pore volume was observed. The average pore size was also decreased after 10 cycles.

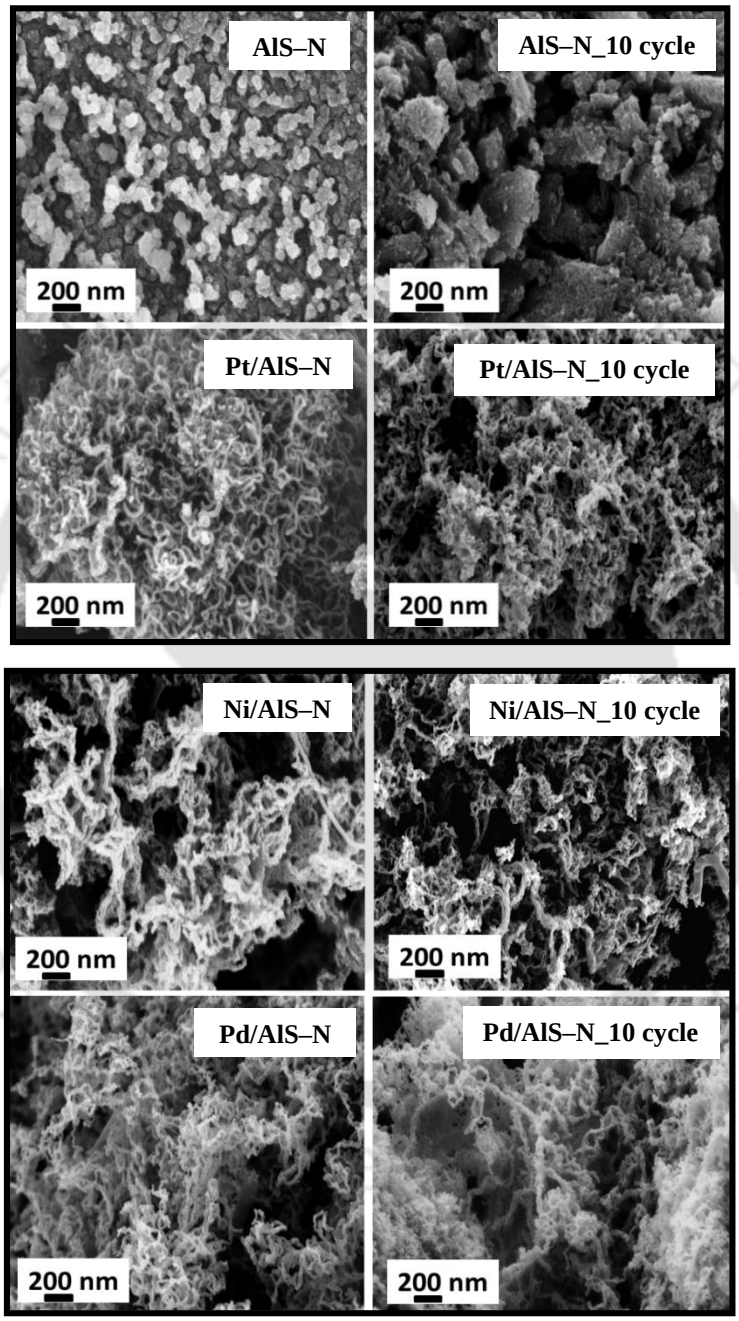

Figure 4.86. FESEM images of fresh and used (after 10 cycles) different metal and nitrogen co–doped templated carbons.

On comparison of the microscopic images of the samples before and after 10 cycles of adsorption–desorption shows (Figure 4.86) that high pressure treatment had caused slight modification of the physical structure. The agglomeration and collapse of the tubular structure

may have resulted in the lowering of surface area and total pore volume resulting in slight decrease in hydrogen uptake at 10th cycle for the present sample it decreases the adsorption sites. The partial collapse of the porous structure of templated carbons at higher pressure may have caused this. However, the present result is much better compared to the reported stability values. Mehrabi et al. (2017) reported about 17 % reduction in hydrogen uptake capacity after 6 cycles for 12 wt.% palladium doped mesoporous MWCNT while, 33 % loss in uptake capacity was reported by Campesi et al. (2008) after 3 cycles for 10 wt.% palladium doped mesoporous templated carbon.

Air exfoliated graphene

The EGO (Air) showing the highest hydrogen uptake was further subjected to cyclic stability test at –196 °C and 30 bar. The hydrogen adsorption and desorption cycle were repeated 5 times for the same sample and the corresponding profiles are shown in Figure 4.87(a) and (b). The desorption curve followed the same path as the adsorption curve for all the cycles indicating a completely reversible hydrogen adsorption process. The hydrogen uptake capacity reduced only slightly with the number of cycles. After 5 cycles, the hydrogen uptake reduced from an initial value of 3.34 to 3.02 wt.% corresponding to about 9 % reduction from the original value. This indicated a good cyclic stability of the EGO (Air) sample as a hydrogen uptake material.

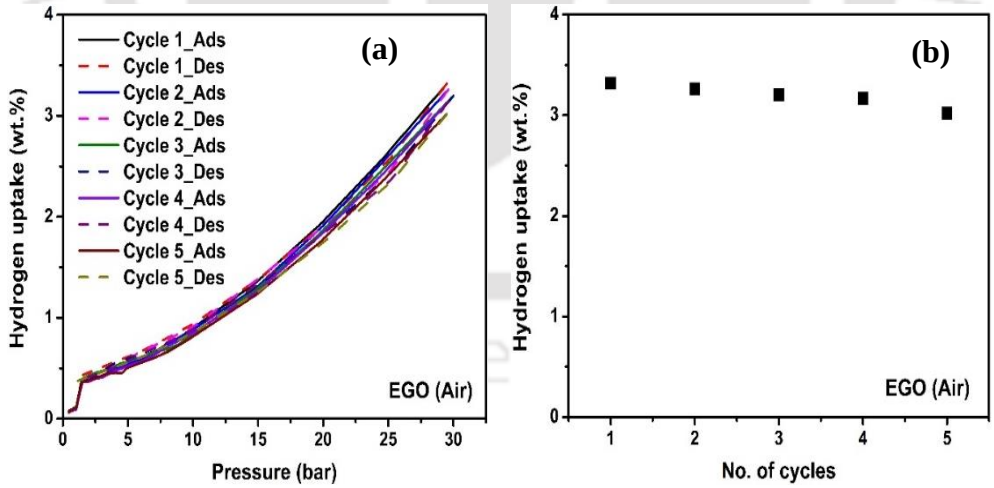

Figure 4.87: (a) Hydrogen adsorption–desorption isotherms of EGO(Air) at –196 °C up to 30 bar for 5 cycles (b) Cycling stability for hydrogen uptake of EGO(Air) sample.

The slight decrease in hydrogen uptake capacity after 5 cycles may be attributed to mainly to lowering of surface area and pore volume (Table 4.50). This was observed from Table 4.50. The surface area and pore volume were reduced from 217 to 157 m^2/g and 1.12 to 0.75 cm^3/g

respectively. The lowering of these values, in turn, may have been due to the partial damage of layers or collapse of porous structure (Figure 4.88c) due to cyclic exposure at higher pressure as was also observed for templated carbon based materials.

Table 4.50: Physical properties of fresh and used (after 5 cycles) air exfoliated GO.

Sample ID	Surface area (m^2/g)	Micropore area (m^2/g)	Pore volume (cm^3/g)	Average pore size (nm)
EGO (Air)_fresh	217	8	1.12	2.8
EGO (Air)_used	157	12	0.75	4.8

The pore size distribution of the EGO(Air) after 5 cycles (Figure 4.88b) showed that the pore size was shifted towards higher size compared to that of fresh EGO(Air) sample. The average pore size also increased. In spite of slight modification of the porous structure of the sample, the hydrogen uptake stability was observed to be good for the present sample. Few studies have been reported for hydrogen uptake cyclic stability of graphene based sample. Gadipelli et al. (2015) reported 44 % drop in hydrogen uptake for palladium doped RGO after 4 cycles. But the same group reported only 2.5 % reduction after 5 cycles for KOH activated graphene (Klechikov et al. 2015).

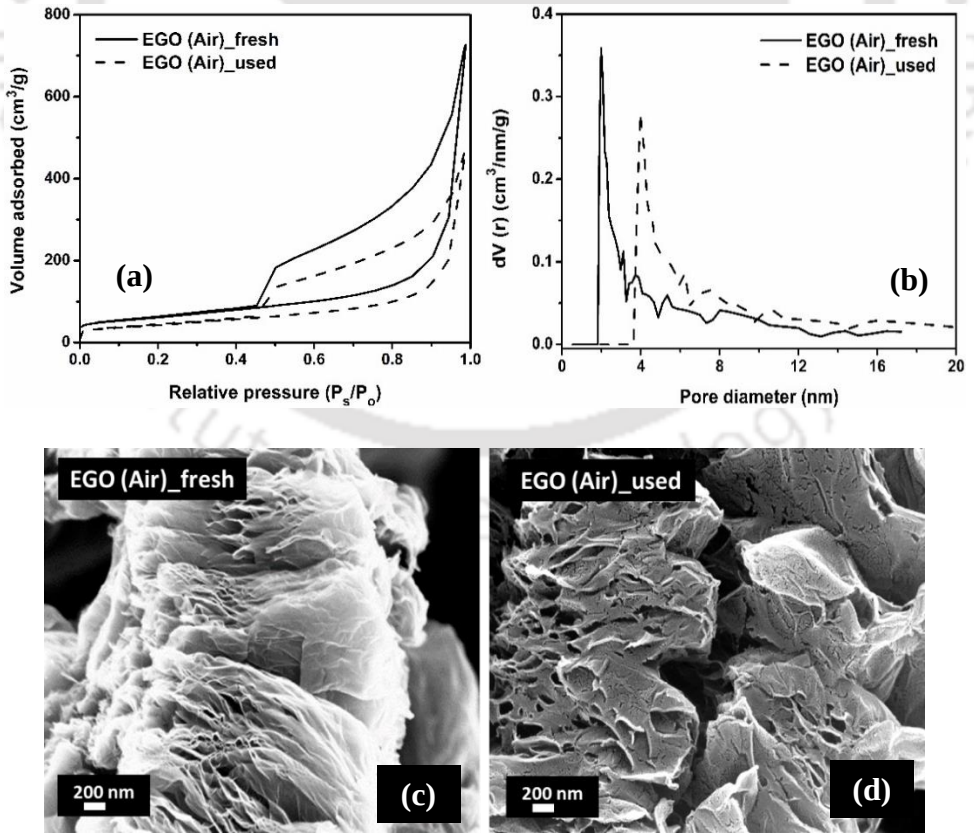

Figure 4.88: Comparison of physical properties of fresh and used (after 5 cycles) EGO(Air) (a) N_2 adsorption–desorption isotherm (b) Pore size distribution (c) FESEM image of fresh EGO(Air) (d) FESEM image of used EGO(Air).

The adsorption–desorption properties of the templated carbon and graphene materials was excellent. The desorption curve followed the same path as the adsorption curve for all the cycles indicating a completely reversible hydrogen adsorption process. The adsorption and desorption cycles were observed to have effect on the structure of both the templated carbon and graphene samples. The surface area and pore volume were reduced for both the samples after the cyclic performance. However, this modification was observed to have minimal effects on the hydrogen storage properties. The cyclic stability of the templated carbons was good with only 3–5 % loss in storage capacity up to 10 cycles. For EGO (Air) sample, the hydrogen uptake reduced from an initial value of 3.34 to 3.02 wt.% corresponding to about 9 % reduction from the original value after 5 cycles. Thus the cyclic stability of templated carbons compared to that of graphene as a hydrogen uptake material was observed to be higher for this study.

Summary

In this section, the hydrogen uptake reversibility and cyclic stability of the selected templated carbon and graphene samples were studied. The absence of any hysteresis loop in the isotherms for both the templated carbon and graphene samples suggested that the hydrogen uptake was reversible. For templated carbon samples, after 10 cycles of adsorption and desorption, the hydrogen uptake capacity was decreased by 4.1, 4.9, 3.2 and 5.5 % for AlS–N, Pt/AlS–N, Ni/AlS–N and Pd/AlS–N respectively compared to the corresponding first cycle. In case of EGO(Air) sample, the hydrogen uptake reduced from an initial value of 3.34 to 3.02 wt.% corresponding to about 9 % reduction from the original value after 5 cycles. These slight reductions in hydrogen uptake may have resulted from the lowering of surface area as well as pore volume and thereby decreasing the number of available adsorption sites. These results indicated that good reversibility and cyclic stability for both the templated carbon and exfoliated graphene samples as hydrogen uptake materials.

4.5 Mechanism of hydrogen adsorption

For carbon based hydrogen storage materials, the mechanism of adsorption depends on the nature of adsorption sites, as discussed in the introduction section. For only undoped carbon, the hydrogen mainly interacts with the carbon matrix by physisorption or physical adsorption. However, for doped carbon when additional adsorption or activation sites are present in the form of metal or non–metal atoms, they interact with the incoming adsorbate molecules, thereby positively contributing in uptake.

In this study, the matrix of the mesoporous templated carbons was having amorphous, agglomerated or tubular structure. The hydrogen molecules are expected to undergo mostly molecular adsorption on these surfaces. The tubular forms by virtue of its structure are expected to provide higher surface area for adsorption due to the availability of both internal and external wall surfaces. In fact, the templated carbons with more tubular structure did show higher uptake. The pore size of these tubes usually being in mesopore regions, 20–30 nm, can accommodate multilayer adsorption. The multilayer adsorption was also expected in all the other available mesopores in the carbon matrix which usually obtained in the range of 2–10 nm. This is shown by schematic diagram in Figure 4.89.

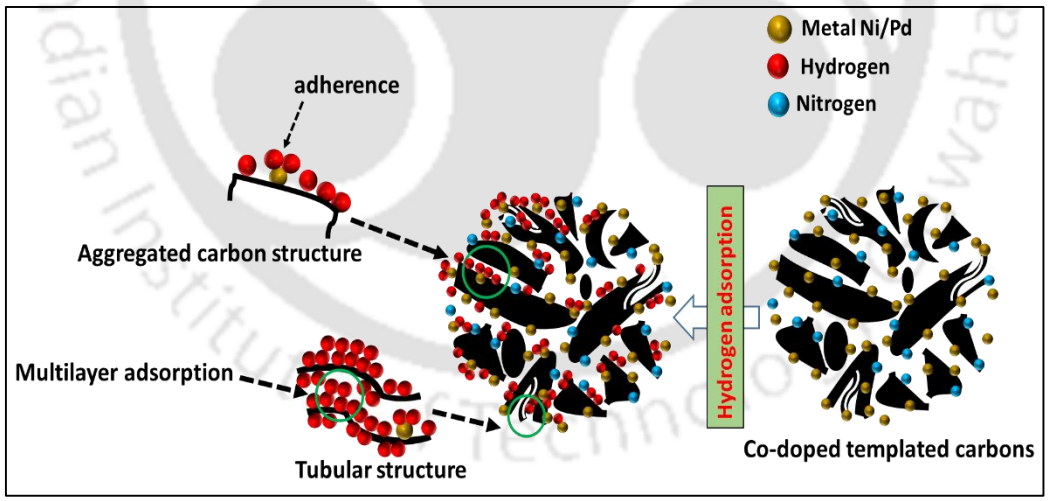

Figure 4.89: Schematic diagram of possible steps of hydrogen adsorption process over metal and nitrogen co–doped templated carbon.

For co–doped templated carbon the hydrogen can be adsorbed on the carbon surface as well as on the metal sites. The metal sites may act as catalytic sites resulting in dissociation to hydrogen atom. This step has been reported as spontaneous without any activation energy barrier (Juarez–Mosqueda et al. 2015; Psofogiannakis et al. 2009). However subsequent spillover of

dissociated hydrogen atoms to the carbon surface, being energy intensive process, may depend upon adsorption condition. The noble metals are reported to contribute towards spillover mechanism mostly at room temperature and above (Pyle et al. 2016; Geng et al. 2014; Reyhani et al. 2011; Li et al. 2011; Liu et al. 2007). However few papers reported this kind of interactions even at lower temperature from –240 to 0 °C, though needed further confirmation (Masika et al. 2013; Cheon and Suh 2009; Wang and Yang 2008b).

The enhancement shown by presence of nitrogen has been attributed mainly to nitrogen acting as activation center. The presence of nitrogen in the carbon framework strongly activates the absorbent surface towards hydrogen promoting its adsorption (Xia et al. 2011). May be the basic nature of nitrogen with presence of lone pair contributes toward interaction with highly electropositive hydrogen. The higher reduction potential of nitrogen (0.057 V) compared to that of carbon (–0.132 V) may have also facilitated activation of hydrogen molecules on the nitrogen doped surface resulting in higher uptake (Konwar et al. 2016; Viswanathan et al. 2003).

For the exfoliated graphene oxide fluffy layers kind of structure was obtained and can be considered as main contributors to the positive uptake of hydrogen. In addition, the considerable presence of surface oxygen in terms of functional groups was also found to enhance the hydrogen uptake. Figure 4.90 represents the possible interaction between oxygen and hydrogen on the graphene surface. The highly electronegative oxygen sites may enhance interaction with the incoming highly electropositive hydrogen molecule facilitating its adsorption on the graphene surface. The oxygen can interact directly or contribute toward the enhancement of pi electron cloud which in turn has more positive interaction with the hydrogen. However, more detailed study will be required to understand the molecular level interaction. The role of metal on graphene surface is expected to be the same as in templated carbon. The multilayers hydrogen adsorption may also be possible within the exfoliated graphene oxide matrix because the presence of pores in the mesoporous range of 2–6 nm. The schematic diagram of possible steps of hydrogen adsorption for exfoliated graphene oxide shown in Figure 4.90.

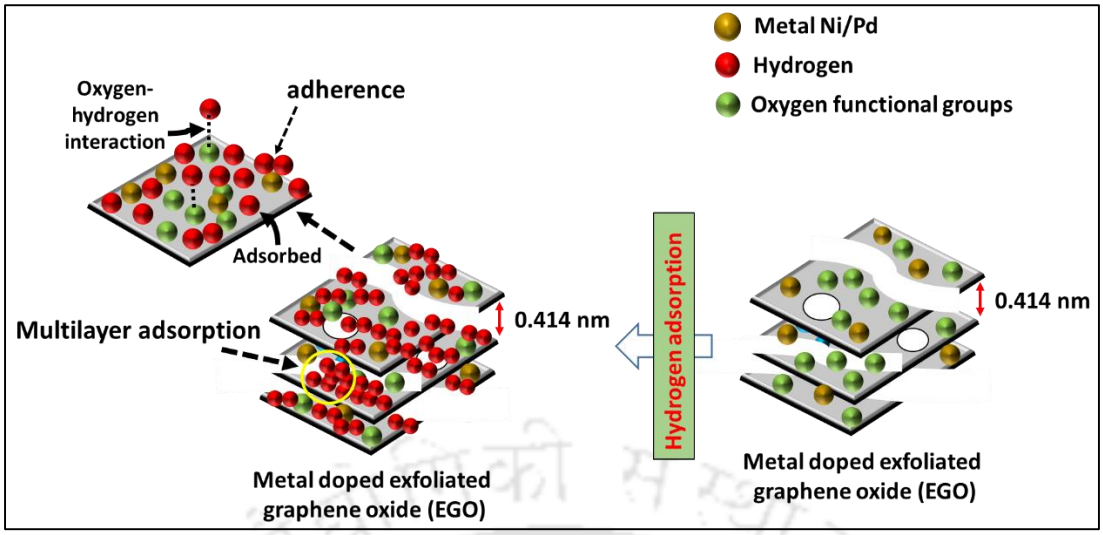

Figure 4.90: Schematic diagram of possible steps of hydrogen adsorption process over metal exfoliated graphene oxide.

4.6 Comparison between templated carbon and graphene based materials

Among templated carbons the palladium and nitrogen co–doped carbon derived from surfactant modified template showed the highest hydrogen uptake while palladium doped GO exfoliated at 300 ^{o}C in flow of air was observed to have the highest uptake among graphene based materials. Though these two carbon based adsorbents are of different genre but basic properties responsible for hydrogen uptake capacity are expected to be same and it may be worthwhile to look into and compare the physical properties responsible for their respective hydrogen uptake capacities. The properties and hydrogen uptake capacity of the samples are compared in Table 4.51.

Table 4.51: Comparison of physical properties of palladium and nitrogen co–doped templated carbon with that of palladium doped air exfoliated graphene oxide.

Sample ID	Pd (wt.%	Surface area (m^2/g)	Micropore area (m^2/g)	Pore volume	Average pore diameter (nm)	I_D/I_G ratio	Hydrogen uptake (wt.%)
Pd/AlS–N	2.0	817	24	1.24	3.9	0.96	5.0 (at 25 bar)
Pd/EGO	1.8	449	0	2.04	4.7	1.05	3.52 (at 30 bar)

The palladium and nitrogen co–doped templated carbon had a higher surface area compared to that of palladium doped EGO, whereas pore volume was higher for palladium doped EGO sample. The (Figure 4.91) showed broader pore distribution (3.5–20 nm) for Pd/EGO(Air) compared to that of Pd/AlS–N (2–9 nm). Both the samples were mainly mesoporous with the average pore size of 4.7 nm for Pd/EGO and that for Pd/AlS–N was 3.9 nm. Based on I_D/I_G ratio values, the larger level of degree of graphitization was observed in Pd/AlS–N as compared to that of Pd/EGO.

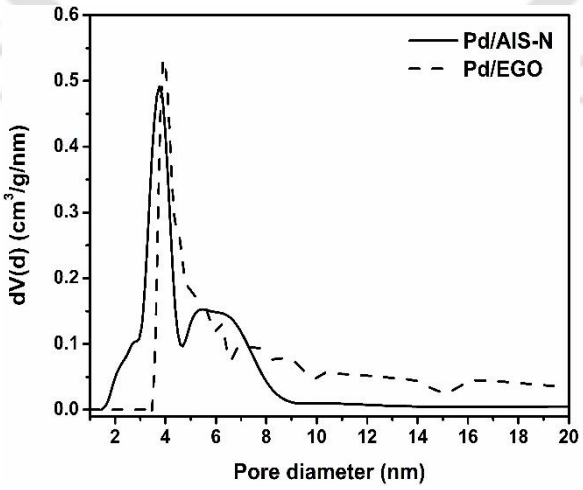

Figure 4.91: Comparison of pore size distribution of palladium and nitrogen co–doped templated carbon (Pd/AlS–N) and palladium doped air exfoliated graphene oxide (Pd/EGO).

The FESEM and TEM images of the Pd/EGO and Pd/AlS–N samples are compared in Figure 4.92. The agglomerated tubular structure was observed for co–doped templated carbons, whereas doped graphene samples showed fluffy layer structure. The dispersion of metal was lower in doped graphene sample compared to doped templated carbon. The average particle size of palladium was 2.8 and 10.4 nm for Pd/AlS–N and Pd/EGO, respectively. Much lower surface area of the doped graphene may be the reason for its lower dispersion of the metal. The lower surface area and lower metal dispersion may be the reason for lower hydrogen uptake of doped graphene oxide (3.5 wt.%) compared to that of doped templated carbon (5.0 wt.%.) The presence of nitrogen may also have enhanced the uptake for co–doped templated carbon. However, for doped GO the presence of oxygen in surface in form of different functional groups, retained from graphite oxide, played a major role in hydrogen uptake. At lower adsorption, the heat of adsorption for the co–doped templated carbon was determined as 22.9 kJ/mol and that for doped graphene oxide was 13 kJ/mol. The hydrogen storage cyclic stability of the templated carbons was also better than that graphene oxide based adsorbent. The former showed only 3–5 % loss up to 10 cycles, whereas exfoliated graphene oxide has about 9 % loss in hydrogen uptake after only 5 cycles.

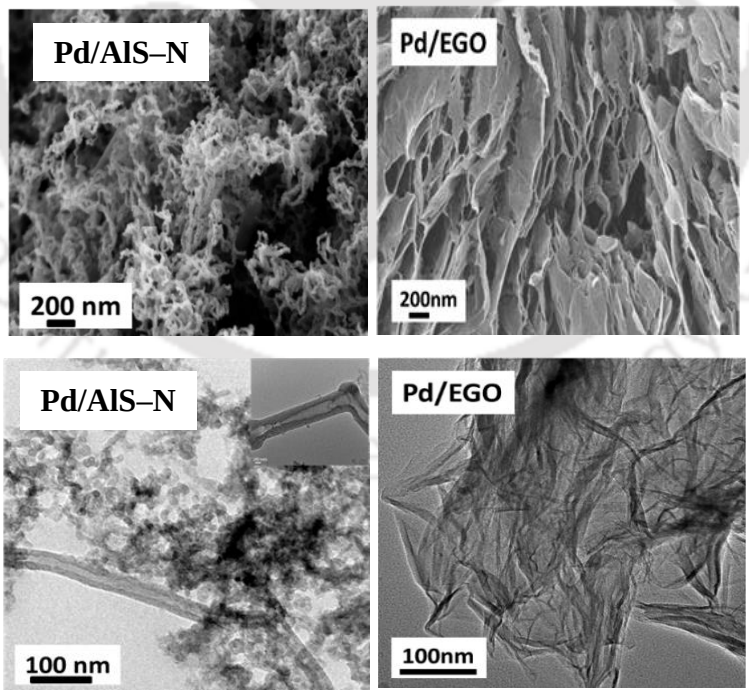

Figure 4.92: Comparison of FESEM and TEM images of palladium and nitrogen co–doped templated carbon and palladium doped exfoliated graphene oxide.

Chapter 5

Conclusions and Recommendation

भारतीय प्रौद्योगिकी संस्थान गुवाहाटी
Indian Institute of Technology Guwahati

The study was able to successfully synthesize high surface area mesoporous templated carbons from alumina based templates which was prepared by simple steps in laboratory from low cost precursors. The pore structure of the alumina template was modified using surfactant by a simplistic approach. Co-doping of nitrogen and palladium was observed to have a positive effect on physicochemical properties and consequently on hydrogen uptake. The surfactant modified alumina based templated carbons for hydrogen storage has been reported for the first time. The performance of co-doped surfactant modified templated carbon was observed to be better than that of commercially available zeolite or silica gel templated carbons. The preparation of exfoliated graphene carbons in air atmosphere was observed to be highly effective for preparation of layered structure with significant amount of residual oxygen, both of which proved to be contributing for hydrogen uptake. The surfactant modified alumina templated palladium and nitrogen co–doped carbon with 2 wt.% palladium showed the highest hydrogen uptake of 5.0 wt.%. at –196 °C and 25 bar. The detailed findings of the study are summarized below.

5.1 Conclusions

The templated carbon and graphene based hydrogen storage materials were developed in this work. The effect of templates, dopants and preparation methods were investigated and studied in details. The major findings for the templated carbon are summarized below.

1. Low cost alumina based templates were developed for preparation of highly porous templated carbon. To develop narrow and well–structured mesoporous template, the pore structure was modulated by adding surfactant to alumina precursor solution in micelle form. The surfactant modified alumina evolved as an effective and economic template for synthesis of mesoporous templated carbons. Significant surface area, pore volume, narrow pore size distribution, and the tubular structure gave unique physicochemical characteristic to surfactant modified alumina based templated carbon. The alumina based templated carbons were mainly mesoporous with average pore size in the range of 4.9–5.4 nm which agreed with more voidage observed within its agglomerated tubular structure. The highest surface area of 1221 m^2/g was obtained for surfactant modified alumina templated carbon. In comparison, the mesoporous silica gel (736 m^2/g) and microporous zeolite templated carbon (1462 m^2/g) showed spherical agglomerates and particle structure, respectively. The surfactant modified alumina templated carbon gave the highest hydrogen uptake capacity of 4.3 wt.% at –196 °C and 25 bar, in spite of lower surface area than zeolite templated carbon

which may be attributed to higher pore volume, highest average pore size and presence of tubular structures for the former.

2. The surface area and pore volume were enhanced on nitrogen doping. The highest enhancement was observed for surfactant modified alumina templated nitrogen doped carbon. This sample showed the maximum surface area of 1508 m^2/g and pore volume of 1.64 cm^3/g. The morphology of the alumina based doped carbons changed from tubular for undoped to spherical agglomerate for nitrogen doped, while there was no significant effect for silica or zeolite templated carbons. The silica and both the alumina based nitrogen doped templated carbons showed spherical agglomerates. The maximum hydrogen uptake capacity of 4.0 wt.% was obtained for microporous zeolite templated carbon having both higher surface area and nitrogen content. Among mesoporous templated carbons, the alumina–SDS templated carbon had highest hydrogen uptake capacity of 3.9 wt.% having higher surface area and nitrogen content compared to other two mesoporous carbons. The hydrogen uptake capacity almost increased linearly with increase in the surface area. The hydrogen uptake also increased with increasing nitrogen content of the sample.
3. The surface area and pore volume of templated carbons reduced on platinum doping. A flat ribbon like structure was observed for alumina based templated platinum doped carbons. The average metal cluster size was 2.6, 2.8, 3.0, 3.4 nm for zeolite, silica gel, alumina, and alumina–SDS templated carbons respectively. The highest hydrogen uptake of 3.90 wt.% was obtained for platinum doped zeolite templated carbon at –196 °C and 25 bar. This highest uptake capacity corresponded to the highest surface area, micropore area and dispersed platinum for zeolite platinum co–doped templated carbon. Platinum provided additional active sites for hydrogen adsorption.
4. Co-doping of nitrogen and platinum on templated carbons decreased the surface area and pore volume further. The surface areas were observed in the range of 496–1173 m^2/g and pore volume between 0.47–1.24 cm^3/g. Higher dispersion of the platinum metal was observed within the matrix of mesoporous templated carbons compared to that of microporous zeolite templated carbon. The silica gel and alumina templated nitrogen doped carbons showed spherical agglomerates and co–doping with platinum resulted in noddle like morphology with tubular diameter in the range of 35–50 and 12–20 nm respectively. The highest hydrogen uptake of 4.1 wt.% was obatined for surfactant modified alumina co–doped templated carbon. This highest uptake capacity for surfactant modified alumina co–doped carbon may be attributed to the synergistic effect of highest amount of nitrogen,

highest dispersion of metal and close second highest metal content. Platinum doping resulted in the heat of adsorption up to 15.9 kJ/mol.

5. Mesoporous co–doped surfactant modified alumina templated carbons having nickel, platinum or palladium with nitrogen, have surface area in the range of 520–836 m^2/g and pore volume in range of 0.72–1.24 cm^3/g. The platinum and nitrogen co–doped carbon gave higher surface area of 836 m^2/g followed closely by palladium and nitrogen co–doped templated carbon. The average metal size of Pt, Ni or Pd co–doped carbons was 5.8, 3.9 and 2.8 nm respectively, with highest dispersion for palladium and nitrogen co–doped templated carbon. The agglomerated morphologies of nitrogen doped templated carbon totally changed to noodles like tubular tangled morphology when metals (Pt, Pd or Ni) was doped. Palladium and nitrogen co–doped carbon with 2 wt.% palladium showed the highest hydrogen uptake of 5.0 wt.%. at –196 °C and 25 bar. This may be attributed to its highest number of active sites corresponding to the highest metal dispersion and amount of nitrogen present. Also, the highest heat of adsorption of 22.9 kJ/mol was obtained for the same sample. The palladium loading lower or higher than 2 wt.% was found to be less efficient for hydrogen storage.

The major findings for the graphene based hydrogen storage materials are summarized below. The effect of preparation and dopant on structure of graphene and thereby on its hydrogen storage properties was studied.

1. The exfoliation temperature had a significant effect on the structural properties of the samples. Reduction in oxygen content was observed on increasing the exfoliation temperature from 200 to 500 °C. Exfoliated GO samples had a fluffy layered structure. The separation between graphene layers increased with increasing exfoliation temperature. The GO exfoliated at 300 °C showed the highest surface area of 248 m^2/g and total pore volume of 1.64 cm^3/g. The highest hydrogen uptake of 3.12 wt.% was obtained for GO exfoliated at 300 °C (at –196 °C and 30 bar), which showed the highest surface area and pore volume. The hydrogen uptake increased with increase in surface area and pore volume.
2. The morphology of thermally exfoliated samples (EGO) was observed to be significantly different than chemically hydrazine treated samples (RGO). This characteristic can be correlated with the fluffy layer structure of the exfoliated graphene oxide compared to dense wrinkled layered structure for hydrazine reduced graphene oxide. Structurally RGO was similar to parent GO but O/C value was almost five–times lower. On the other hand, the EGO samples showed O/C ratios almost two–times higher compared to that of RGO sample suggesting higher retainment of oxygen–containing functional groups in former. Among

graphene based materials, the highest surface area of 461 m^2/g was observed for hydrazine reduced graphene oxide sample but the highest pore volume of 1.63 cm^3/g was observed for exfoliated graphene oxide in air. The pore size distribution revealed the microporous nature for RGO and mesoporous for EGO samples. The air exfoliated graphene oxide displayed maximum hydrogen uptake capacity of 3.34 wt.% –196 °C and 30 bar followed by that of RGO. The results suggested that the combined effect of surface area, pore volume, nature of layered structure and oxygen content contributed to hydrogen uptake characteristics.

3. Addition of different metals (Pt, Ni and Pd) to RGO, resulted in significant decrease in d–spacing. This decrease may be attributed to metal particles deposited between the layers of RGO. With impregnation of different metals, the pores were shifted towards the larger pores with average pore size in the range of (3.83–3.88 nm). TEM and nitrogen adsorption characterization reveals that all the metal doped RGO samples showed mesoporous nature, whereas RGO showed microporous nature. The average metal particle size of nickel, platinum and palladium doped RGO samples were 2.8, 3.4 and 2.6 nm, respectively. The well and highest dispersion of metal were observed for Pd/RGO. The morphology of RGO was not affected with the addition of platinum but both nickel and palladium doped RGO showed layered structure. The highest hydrogen uptake of 3.22 wt.% was obtained for palladium doped RGO sample and may have resulted from higher dispersion of palladium particles. On incorporation of palladium metal the hydrogen to RGO and EGO, the hydrogen uptake capacity enhanced from 2.50 to 3.22 wt.% and 3.2 to 3.5 wt.% respectively.
4. The reversibility and cyclic stability of both templated carbon and graphene based materials are excellent. Also, the hydrogen uptake capacity is also impressive at room temperature and comparable with the reported results.

5.2 Recommendation for future work

The surfactant modified alumina based templated carbons and exfoliated graphene showed good potential as hydrogen storage materials. The addition of dopants such as nitrogen, oxygen or palladium further enhanced the hydrogen storage capacity. In continuation to present studies, the following areas can be explored further in future. The effect of other non-metals and metals on the physicochemical properties and hydrogen uptake of alumina templated carbon and graphene based materials can be investigated. The detailed study of the surface interactions and adsorption-desorption kinetics for the developed templated carbon and exfoliated graphenes can be carried out. Subsequently a device for hydrogen storage can be developed using these materials and the efficiency may be tested.

References

Abdelkader, A., A. Cooper, R. Dryfe, and I. Kinloch. 2015. How to get between the sheets: a review of recent works on the electrochemical exfoliation of graphene materials from bulk graphite. *Nanoscale* 7 (16):6944–6956.

Abdolmaleki, A., S. Mallakpour, and S. Borandeh. 2016. Improving interfacial interaction of l-phenylalanine-functionalized graphene nanofiller and poly (vinyl alcohol) nanocomposites for obtaining significant membrane properties: Morphology, thermal, and mechanical studies. *Polymer Composites* 37 (6):1924–1935.

Adams, B. D., C. K. Ostrom, S. Chen, and A. Chen. 2010. High–performance Pd–based hydrogen spillover catalysts for hydrogen storage. *The Journal of Physical Chemistry C* 114 (46):19875–19882.

Adeniran, B., and R. Mokaya. 2015. Compactivation: A mechanochemical approach to carbons with superior porosity and exceptional performance for hydrogen and CO2 storage. *Nano Energy* 16:173–185.

Agarwal, R., J. Noh, J. Schwarz, and P. Davini. 1987. Effect of surface acidity of activated carbon on hydrogen storage. *Carbon* 25 (2):219–226.

Ahluwalia, R., T. Hua, J.–K. Peng, S. Lasher, K. McKenney, J. Sinha, and M. Gardiner. 2010. Technical assessment of cryo–compressed hydrogen storage tank systems for automotive applications. *International Journal of Hydrogen Energy* 35 (9):4171–4184.

Alam, N., and R. Mokaya. 2010. Evolution of optimal porosity for improved hydrogen storage in templated zeolite–like carbons. *Energy & Environmental Science* 3 (11):1773–1781.

Alam, N. 2011a. Characterisation and hydrogen storage of Pt–doped carbons templated by Pt–exchanged zeolite Y. *Microporous and Mesoporous Materials* 142 (2–3):716–724.

Alam, N. 2011b. The effect of Al content of zeolite template on the properties and hydrogen storage capacity of zeolite templated carbons. *Microporous and Mesoporous Materials* 144 (1–3):140–147.

Anson, A., M. Callejas, A. Benito, W. Maser, M. Izquierdo, B. Rubio, J. Jagiello, M. Thommes, J. Parra, and M. Martınez. 2004. Hydrogen adsorption studies on single wall carbon nanotubes. *Carbon* 42 (7):1243–1248.

Anton, D., T. Semelsberger, D. Siegel, B. Hardy, and K. Brooks. 2013. Hydrogen Storage Materials Requirements to Meet the 2017 On Board Hydrogen Storage Technical Targets.

Armandi, M., B. Bonelli, C. O. Areán, and E. Garrone. 2008. Role of microporosity in hydrogen adsorption on templated nanoporous carbons. *Microporous and Mesoporous Materials* 112 (1–3):411–418.

Attia, N. F., S. M. Lee, H. J. Kim, and K. E. Geckeler. 2013. Nanoporous carbon–templated silica nanoparticles: Preparation, effect of different carbon precursors, and their hydrogen storage adsorption. *Microporous and Mesoporous Materials* 173:139–146.

Baca, M., K. Cendrowski, W. Kukulka, G. Bazarko, D. Moszyński, B. Michalkiewicz, R. Kalenczuk, and B. Zielinska. 2018. A Comparison of Hydrogen Storage in Pt, Pd and Pt/Pd Alloys Loaded Disordered Mesoporous Hollow Carbon Spheres. *Nanomaterials* 8 (9):639.

Bader, N., and A. Ouederni. 2016. Optimization of biomass–based carbon materials for hydrogen storage. *Journal of Energy Storage* 5:77–84.

Bagreev, A., J. A. Menendez, I. Dukhno, Y. Tarasenko, and T. J. Bandosz. 2004. Bituminous coal–based activated carbons modified with nitrogen as adsorbents of hydrogen sulfide. *Carbon* 42 (3):469–476.

Balahmar, N., A. M. Lowbridge, and R. Mokaya. 2016. Templating of carbon in zeolites under pressure: synthesis of pelletized zeolite templated carbons with improved porosity and packing density for superior gas (CO 2 and H 2) uptake properties. *Journal of Materials Chemistry A* 4 (37):14254–14266.

Barsukov, I. V., C. S. Johnson, J. E. Doninger, and V. Z. Barsukov. 2006. *New carbon based materials for electrochemical energy storage systems: batteries, supercapacitors and fuel cells*. Vol. 229: Springer Science & Business Media.

Beheshti, E., A. Nojeh, and P. Servati. 2011. A first–principles study of calcium–decorated, boron–doped graphene for high capacity hydrogen storage. *Carbon* 49 (5):1561–1567.

Bénard, P., and R. Chahine. 2007. Storage of hydrogen by physisorption on carbon and nanostructured materials. *Scripta Materialia* 56 (10):803–808.

Birks, L., and H. Friedman. 1946. Particle size determination from X-ray line broadening. *Journal of Applied Physics* 17 (8):687–692.

Blankenship , T. S., N. Balahmar, and R. Mokaya. 2017. Oxygen–rich microporous carbons with exceptional hydrogen storage capacity. *Nature communications* 8 (1):1545.

Blankenship, T. S., and R. Mokaya. 2017. Cigarette butt–derived carbons have ultra–high surface area and unprecedented hydrogen storage capacity. *Energy & Environmental Science* 10 (12):2552–2562.

Botas, C., P. Álvarez, C. Blanco, R. Santamaría, M. Granda, M. D. Gutiérrez, F. Rodríguez–Reinoso, and R. Menéndez. 2013. Critical temperatures in the synthesis of graphene–like materials by thermal exfoliation–reduction of graphite oxide. *Carbon* 52:476–485.

Broom, D., C. Webb, G. Fanourgakis, G. Froudakis, P. Trikalitis, and M. Hirscher. 2019. Concepts for improving hydrogen storage in nanoporous materials. *International Journal of Hydrogen Energy* 44 (15):7768–7779.

Cai, J., S. Bennici, J. Shen, and A. Auroux. 2015. The influence of metal–and N–species addition in mesoporous carbons on the hydrogen adsorption capacity. *Materials Chemistry and Physics* 161:142–152.

Campesi, R., F. Cuevas, R. Gadiou, E. Leroy, M. Hirscher, C. Vix–Guterl, and M. Latroche. 2008. Hydrogen storage properties of Pd nanoparticle/carbon template composites. *Carbon* 46 (2):206–214.

Capuano, L., Annual Energy Outlook. 2016. US Energy Information Administration: Washington. *DC, USA*.

Carraro, P., A. G. Blanco, G. Lener, D. Barrera, S. Amaya–Roncancio, C. Chanquía, H. Troiani, M. Oliva, and G. Eimer. 2019. Nanostructured carbons modified with nickel as potential novel reversible hydrogen storage materials: effects of nickel particle size. *Microporous and Mesoporous Materials* 273:50–59.

Carraro, P., V. Elías, A. G. Blanco, K. Sapag, G. Eimer, and M. Oliva. 2014. Study of hydrogen adsorption properties on MCM–41 mesoporous materials modified with nickel. *International Journal of Hydrogen Energy* 39 (16):8749–8753.

Carraro, P., K. Sapag, M. Oliva, and G. Eimer. 2018. Comparative study of hydrogen storage on metal doped mesoporous materials. *Chemical Physics Letters* 701:93–97.

Chen, C.–H., T.–Y. Chung, C.–C. Shen, M.–S. Yu, C.–S. Tsao, G.–N. Shi, C.–C. Huang, M.–D. Ger, and W.–L. Lee. 2013. Hydrogen storage performance in palladium–doped graphene/carbon composites. *international journal of hydrogen energy* 38 (9):3681–3688.

Chen, C.–H., M.–S. Yu, C.–S. Tsao, H.–Y. Chuang, H.–H. Tseng, and T.–Y. Chung. 2012. Characterization of hydrogen adsorption in platinum–doped microporous carbon with varied catalytic properties. *Microporous and Mesoporous Materials* 152:157–162.

Chen, L., R. K. Singh, and P. Webley. 2007. Synthesis, characterization and hydrogen storage properties of microporous carbons templated by cation exchanged forms of zeolite Y with propylene and butylene as carbon precursors. *Microporous and Mesoporous Materials* 102 (1–3):159–170.

Chen, N., X. Huang, and L. Qu. 2015. Heteroatom substituted and decorated graphene: preparation and applications. *Physical Chemistry Chemical Physics* 17 (48):32077–32098.

Chen, P., X. Wu, J. Lin, and K. Tan. 1999. High H2 uptake by alkali–doped carbon nanotubes under ambient pressure and moderate temperatures. *Science* 285 (5424):91–93.

Cheon, Y. E., and M. P. Suh. 2009. Enhanced hydrogen storage by palladium nanoparticles fabricated in a redox-active metal–organic framework. *Angewandte Chemie International Edition* 48 (16):2899–2903.

Chowdhury, S., and R. Balasubramanian. 2016a. Highly efficient, rapid and selective CO2 capture by thermally treated graphene nanosheets. *Journal of CO2 Utilization* 13:50–60.

Chowdhury. 2016b. Three–dimensional graphene–based porous adsorbents for postcombustion CO2 capture. *Industrial & Engineering Chemistry Research* 55 (29):7906–7916.

Chung, T. M., Y. Jeong, Q. Chen, A. Kleinhammes, and Y. Wu. 2008. Synthesis of microporous boron–substituted carbon (B/C) materials using polymeric precursors for hydrogen physisorption. *Journal of the American Chemical Society* 130 (21):6668–6669.

Çiplak, Z., N. Yildiz, and A. Çalimli. 2015. Investigation of graphene/Ag nanocomposites synthesis parameters for two different synthesis methods. *Fullerenes, Nanotubes and Carbon Nanostructures* 23 (4):361–370.

Cui, H., Z. Zhou, and D. Jia. 2017. Heteroatom–doped graphene as electrocatalysts for air cathodes. *Materials Horizons* 4 (1):7–19.

Darkrim, F. L., P. Malbrunot, and G. Tartaglia. 2002. Review of hydrogen storage by adsorption in carbon nanotubes. *International Journal of Hydrogen Energy* 27 (2):193–202.

Das, A. K., M. Srivastav, R. K. Layek, M. E. Uddin, D. Jung, N. H. Kim, and J. H. Lee. 2014. Iodide–mediated room temperature reduction of graphene oxide: a rapid chemical route for the synthesis of a bifunctional electrocatalyst. *Journal of Materials Chemistry A* 2 (5):1332–1340.

Dehouche, Z., R. Djaozandry, J. Huot, S. Boily, J. Goyette, T. Bose, and R. Schulz. 2000. Influence of cycling on the thermodynamic and structure properties of nanocrystalline magnesium based hydride. *Journal of Alloys and Compounds* 305 (1–2):264–271.

Dillon, A. C., K. Jones, T. Bekkedahl, C. Kiang, D. Bethune, and M. Heben. 1997. Storage of hydrogen in single–walled carbon nanotubes. *Nature* 386 (6623):377.

Dincer, I. 2000. Renewable energy and sustainable development: a crucial review. *Renewable and sustainable energy reviews* 4 (2):157–175.

Divya, P., and S. Ramaprabhu. 2014. Hydrogen storage in platinum decorated hydrogen exfoliated graphene sheets by spillover mechanism. *Physical Chemistry Chemical Physics* 16 (48):26725–26729.

Durbin, D., and C. Malardier–Jugroot. 2013. Review of hydrogen storage techniques for on board vehicle applications. *International Journal of Hydrogen Energy* 38 (34):14595–14617.

Gadiou, R., S.–E. Saadallah, T. Piquero, P. David, J. Parmentier, and C. Vix–Guterl. 2005. The influence of textural properties on the adsorption of hydrogen on ordered nanostructured carbons. *Microporous and Mesoporous Materials* 79 (1–3):121–128.

Gadipelli, S., and Z. X. Guo. 2015. Graphene–based materials: Synthesis and gas sorption, storage and separation. *Progress in Materials Science* 69:1–60.

Gangu, K. K., S. Maddila, S. B. Mukkamala, and S. B. Jonnalagadda. 2019. Characteristics of MOF, MWCNT and graphene containing materials for hydrogen storage: A review. *Journal of Energy Chemistry* 30:132–144.

Ganji, S., P. Bukya, V. Vakati, K. S. R. Rao, and D. R. Burri. 2013. Highly efficient and expeditious PdO/SBA–15 catalysts for allylic oxidation of cyclohexene to cyclohexenone. *Catalysis Science & Technology* 3 (2):409–414.

Gao, H., X. B. Wu, J. T. Li, G. T. Wu, J. Y. Lin, K. Wu, and D. S. Xu. 2003. Hydrogen adsorption of open–tipped insufficiently graphitized multiwalled carbon nanotubes. *Applied physics letters* 83 (16):3389–3391.

Geng, Z., D. Wang, C. Zhang, X. Zhou, H. Xin, X. Liu, and M. Cai. 2014. Spillover enhanced hydrogen uptake of Pt/Pd doped corncob–derived activated carbon with ultra–high surface area at high pressure. *International Journal of Hydrogen Energy* 39 (25):13643–13649.

Geng, Z., C. Zhang, D. Wang, X. Zhou, and M. Cai. 2015. Pore size effects of nanoporous carbons with ultra–high surface area on high–pressure hydrogen storage. *Journal of Energy Chemistry* 24 (1):1–8.

Giasafaki, D., A. Bourlinos, G. Charalambopoulou, A. Stubos, and T. Steriotis. 2012. Synthesis and characterisation of nanoporous carbon–metal composites for hydrogen storage. *Microporous and Mesoporous Materials* 154:74–81.

Gilbert, M., J. Knox, and B. Kaur. 1982. Porous glassy carbon, a new columns packing material for gas chromatography and high–performance liquid chromatography. *Chromatographia* 16 (1):138–146.

Giraudet, S., and Z. Zhu. 2011. Hydrogen adsorption in nitrogen enriched ordered mesoporous carbons doped with nickel nanoparticles. *Carbon* 49 (2):398–405.

Giraudet, S., Z. Zhu, X. Yao, and G. Lu. 2010. Ordered mesoporous carbons enriched with nitrogen: application to hydrogen storage. *The Journal of Physical Chemistry C* 114 (18):8639–8645.

Gogotsi, Y., C. Portet, S. Osswald, J. M. Simmons, T. Yildirim, G. Laudisio, and J. E. Fischer. 2009. Importance of pore size in high–pressure hydrogen storage by porous carbons. *International Journal of Hydrogen Energy* 34 (15):6314–6319.

Guan, C., X. Zhang, K. Wang, and C. Yang. 2009. Investigation of H2 storage in a templated carbon derived from zeolite Y and PFA. *Separation and Purification Technology* 66 (3):565–569.

Gupta, B., N. Kumar, K. Panda, V. Kanan, S. Joshi, and I. Visoly–Fisher. 2017. Role of oxygen functional groups in reduced graphene oxide for lubrication. *Scientific Reports* 7:45030.

Han, Y.–J., and S.–J. Park. 2017. Influence of nickel nanoparticles on hydrogen storage behaviors of MWCNTs. *Applied Surface Science* 415:85–89.

He, D., Z. Peng, W. Gong, Y. Luo, P. Zhao, and L. Kong. 2015. Mechanism of a green graphene oxide reduction with reusable potassium carbonate. *RSC Advances* 5 (16):11966–11972.

Hirscher, M., and B. Panella. 2005. Nanostructures with high surface area for hydrogen storage. *Journal of Alloys and Compounds* 404:399–401.

Hong, W. G., B. H. Kim, S. M. Lee, H. Y. Yu, Y. J. Yun, Y. Jun, J. B. Lee, and H. J. Kim. 2012. Agent–free synthesis of graphene oxide/transition metal oxide composites and its application for hydrogen storage. *International Journal of Hydrogen Energy* 37 (9):7594–7599.

Hu, Q., Y. Lu, and G. P. Meisner. 2008. Preparation of nanoporous carbon particles and their cryogenic hydrogen storage capacities. *The Journal of Physical Chemistry C* 112 (5):1516–1523.

Hu, X., Y. Yu, Y. Wang, J. Zhou, and L. Song. 2015. Separating nano graphene oxide from the residual strong–acid filtrate of the modified Hummers method with alkaline solution. *Applied Surface Science* 329:83–86.

Huang, C. C., H.–M. Chen, C.–H. Chen, and J.–C. Huang. 2010. Effect of surface oxides on hydrogen storage of activated carbon. *Separation and Purification Technology* 70 (3):291–295.

Hudson, M. S. L., H. Raghubanshi, S. Awasthi, T. Sadhasivam, A. Bhatnager, S. Simizu, S. Sankar, and O. Srivastava. 2014. Hydrogen uptake of reduced graphene oxide and graphene sheets decorated with Fe nanoclusters. *International Journal of Hydrogen Energy* 39 (16):8311–8320.

Iijima, S. 1991. Helical microtubules of graphitic carbon. *Nature* 354 (6348):56–58.

Inagaki, M., M. Toyoda, Y. Soneda, S. Tsujimura, and T. Morishita. 2016. Templated mesoporous carbons: Synthesis and applications. *Carbon* 107:448–473.

Ioannidou, O., and A. Zabaniotou. 2007. Agricultural residues as precursors for activated carbon production—a review. *Renewable and Sustainable Energy Reviews* 11 (9):1966–2005.

Ismail, N., M. Madian, and M. S. El–Shall. 2015. Reduced graphene oxide doped with Ni/Pd nanoparticles for hydrogen storage application. *Journal of Industrial and Engineering Chemistry* 30:328–335.

Jacobson, M. Z., and M. A. Delucchi. 2011. Providing all global energy with wind, water, and solar power, Part I: Technologies, energy resources, quantities and areas of infrastructure, and materials. *Energy Policy* 39 (3):1154–1169.

Jiang, J., Q. Gao, Z. Zheng, K. Xia, and J. Hu. 2010. Enhanced room temperature hydrogen storage capacity of hollow nitrogen–containing carbon spheres. *International Journal of Hydrogen Energy* 35 (1):210–216.

Jiang, Z., Q. Pan, J. Xu, and T. Fang. 2014. Current situation and prospect of hydrogen storage technology with new organic liquid. *International Journal of Hydrogen Energy* 39 (30):17442–17451.

Jordá–Beneyto, M., D. Lozano–Castelló, F. Suárez–García, D. Cazorla–Amorós, and Á. Linares–Solano. 2008. Advanced activated carbon monoliths and activated carbons for hydrogen storage. *Microporous and Mesoporous Materials* 112 (1–3):235–242.

Jordá–Beneyto, M., F. Suárez–García, D. Lozano–Castelló, D. Cazorla–Amorós, and A. Linares–Solano. 2007. Hydrogen storage on chemically activated carbons and carbon nanomaterials at high pressures. *Carbon* 45 (2):293–303.

Juarez–Mosqueda, R., A. Mavrandonakis, A. B. Kuc, L. G. Pettersson, and T. Heine. 2015. Theoretical analysis of hydrogen spillover mechanism on carbon nanotubes. *Frontiers in Chemistry* 3:2.

Juárez, J. M., B. C. Ledesma, M. G. Costa, A. R. Beltramone, and O. A. Anunziata. 2017. Novel preparation of CMK–3 nanostructured material modified with titania applied in hydrogen uptake and storage. *Microporous and Mesoporous Materials* 254:146–152.

Jun, S., S. H. Joo, R. Ryoo, M. Kruk, M. Jaroniec, Z. Liu, T. Ohsuna, and O. Terasaki. 2000. Synthesis of new, nanoporous carbon with hexagonally ordered mesostructure. *Journal of the American Chemical Society* 122 (43):10712–10713.

Jung, H., K. T. Park, M. N. Gueye, S. H. So, and C. R. Park. 2016. Bio–inspired graphene foam decorated with Pt nanoparticles for hydrogen storage at room temperature. *International Journal of Hydrogen Energy* 41 (9):5019–5027.

Kabbour, H., T. F. Baumann, J. H. Satcher, A. Saulnier, and C. C. Ahn. 2006. Toward new candidates for hydrogen storage: high–surface–area carbon aerogels. *Chemistry of materials* 18 (26):6085–6087.

Khanra, P., T. Kuila, N. H. Kim, S. H. Bae, D.–s. Yu, and J. H. Lee. 2012. Simultaneous bio–functionalization and reduction of graphene oxide by baker's yeast. *Chemical Engineering Journal* 183:526–533.

Khanra, P., C.–N. Lee, T. Kuila, N. H. Kim, M. J. Park, and J. H. Lee. 2014. 7, 7, 8, 8–Tetracyanoquinodimethane–assisted one–step electrochemical exfoliation of graphite and its performance as an electrode material. *Nanoscale* 6 (9):4864–4873.

Kichambare, P., J. Kumar, S. Rodrigues, and B. Kumar. 2011. Electrochemical performance of highly mesoporous nitrogen doped carbon cathode in lithium–oxygen batteries. *Journal of Power Sources* 196 (6):3310–3316.

Kim, K.–S., I.–Y. Jeon, S.–N. Ahn, Y.–D. Kwon, and J.–B. Baek. 2011. Edge–functionalized graphene–like platelets as a co–curing agent and a nanoscale additive to epoxy resin. *Journal of Materials Chemistry* 21 (20):7337–7342.

Klechikov, A., G. Mercier, T. Sharifi, I. A. Baburin, G. Seifert, and A. V. Talyzin. 2015. Hydrogen storage in high surface area graphene scaffolds. *Chemical communications* 51 (83):15280–15283.

Kojima, Y., Y. Kawai, A. Koiwai, N. Suzuki, T. Haga, T. Hioki, and K. Tange. 2006. Hydrogen adsorption and desorption by carbon materials. *Journal of Alloys and Compounds* 421 (1–2):204–208.

Konwar, R. J., and M. De. 2014. Synthesis of high surface area silica gel templated carbon for hydrogen storage application. *Journal of Analytical and Applied Pyrolysis* 107:224–232.

Konwar, R. J. 2015. Development of templated carbon by carbonisation of sucrose–zeolite composite for hydrogen storage. *International Journal of Energy Research* 39 (2):223–233.

Konwar, R. J. 2016. Nitrogen modified templated carbons for energy application: Effect of templates and nitrogen precursors. *International Journal of Hydrogen Energy* 41 (46):21300–21309.

Kopac, T., Y. Kırca, and A. Toprak. 2017. Synthesis and characterization of KOH/boron modified activated carbons from coal and their hydrogen sorption characteristics. *International Journal of Hydrogen Energy* 42 (37):23606–23616.

Kottegoda, I. R., X. Gao, L. D. Nayanajith, C. H. Manorathne, J. Wang, J.–Z. Wang, H.–K. Liu, and Y. Gofer. 2015. Comparison of few–layer graphene prepared from natural graphite through fast synthesis approach. *Journal of Materials Science & Technology* 31 (9):907–912.

Kruk, M., M. Jaroniec, R. Ryoo, and S. H. Joo. 2000. Characterization of ordered mesoporous carbons synthesized using MCM–48 silicas as templates. *The Journal of Physical Chemistry B* 104 (33):7960–7968.

Kuila, T., A. K. Mishra, P. Khanra, N. H. Kim, and J. H. Lee. 2013. Recent advances in the efficient reduction of graphene oxide and its application as energy storage electrode materials. *Nanoscale* 5 (1):52–71.

Kyotani, T., Z. Ma, and A. Tomita. 2003. Template synthesis of novel porous carbons using various types of zeolites. *Carbon* 41 (7):1451–1459.

Kyotani, T., T. Nagai, S. Inoue, and A. Tomita. 1997. Formation of new type of porous carbon by carbonization in zeolite nanochannels. *Chemistry of Materials* 9 (2):609–615.
Lachawiec Jr, A. J., and R. T. Yang. 2008. Isotope tracer study of hydrogen spillover on carbon–based adsorbents for hydrogen storage. *Langmuir* 24 (12):6159–6165.
Lee, H., Y.–S. Kang, S.–H. Kim, and J.–Y. Lee. 2002. Hydrogen desorption properties of multiwall carbon nanotubes with closed and open structures. *Applied Physics Letters* 80 (4):577–579.
Lee, J., J. Kim, and T. Hyeon. 2006. Recent progress in the synthesis of porous carbon materials. *Advanced Materials* 18 (16):2073–2094.
Lee, S.–Y., and S.–J. Park. 2011. Effect of platinum doping of activated carbon on hydrogen storage behaviors of metal–organic frameworks–5. *International Journal of Hydrogen Energy* 36 (14):8381–8387.
Li, H., K. Wang, Y. Sun, C. T. Lollar, J. Li, and H.–C. Zhou. 2018. Recent advances in gas storage and separation using metal–organic frameworks. *Materials Today* 21 (2):108–121.
Li, Q., and A. D. Lueking. 2011. Effect of surface oxygen groups and water on hydrogen spillover in Pt–doped activated carbon. *The Journal of Physical Chemistry C* 115 (10):4273–4282.
Li, Z., Z. Zhou, G. Yun, K. Shi, X. Lv, and B. Yang. 2013. High–performance solid–state supercapacitors based on graphene–ZnO hybrid nanocomposites. *Nanoscale Research Letters* 8 (1):473.
Lin, J., T. Mei, M. Lv, C. a. Zhang, Z. Zhao, and X. Wang. 2014. Size–controlled PdO/graphene oxides and their reduction products with high catalytic activity. *RSC Advances* 4 (56):29563–29570.
Liu, C., Y. Chen, C.–Z. Wu, S.–T. Xu, and H.–M. Cheng. 2010. Hydrogen storage in carbon nanotubes revisited. *Carbon* 48 (2):452–455.
Liu, M., R. Zhang, and W. Chen. 2014. Graphene–supported nanoelectrocatalysts for fuel cells: synthesis, properties, and applications. *Chemical Reviews* 114 (10):5117–5160.
Liu, Y.–Y., J.–L. Zeng, J. Zhang, F. Xu, and L.–X. Sun. 2007. Improved hydrogen storage in the modified metal–organic frameworks by hydrogen spillover effect. *International Journal of Hydrogen Energy* 32 (16):4005–4010.
Lueking, A. D., L. Pan, D. L. Narayanan, and C. E. Clifford. 2005. Effect of expanded graphite lattice in exfoliated graphite nanofibers on hydrogen storage. *The Journal of Physical Chemistry B* 109 (26):12710–12717.
Ma, L.–P., Z.–S. Wu, J. Li, E.–D. Wu, W.–C. Ren, and H.–M. Cheng. 2009. Hydrogen adsorption behavior of graphene above critical temperature. I*nternational Journal of Hydrogen Energy* 34 (5):2329–2332.
Ma, Z., T. Kyotani, and A. Tomita. 2002. Synthesis methods for preparing microporous carbons with a structural regularity of zeolite Y. *Carbon* 40 (13):2367–2374.
Marsh, H., and F. R. Reinoso. 2006. *Activated carbon*: Elsevier.
Masika, E., R. A. Bourne, T. W. Chamberlain, and R. Mokaya. 2013. Supercritical CO2 mediated incorporation of Pd onto templated carbons: a route to optimizing the Pd particle size and hydrogen uptake density. *ACS Applied Materials & Interfaces* 5 (12):5639–5647.
Masika, E., and R. Mokaya. 2014. Exceptional gravimetric and volumetric hydrogen storage for densified zeolite templated carbons with high mechanical stability. *Energy & Environmental Science* 7 (1):427–434.
Mehra, N. K., V. Mishra, and N. Jain. 2014. A review of ligand tethered surface engineered carbon nanotubes. *Biomaterials* 35 (4):1267–1283.
Mehrabi, M., P. Parvin, A. Reyhani, and S. Mortazavi. 2017. Hydrogen storage in multi–walled carbon nanotubes decorated with palladium nanoparticles using laser ablation/chemical reduction methods. *Materials Research Express* 4 (9):095030.
Meyers, C. J., S. D. Shah, S. C. Patel, R. M. Sneeringer, C. A. Bessel, N. R. Dollahon, R. A. Leising, and E. S. Takeuchi. 2001. Templated synthesis of carbon materials from zeolites (Y, beta, and ZSM–5) and a montmorillonite clay (K10): Physical and electrochemical characterization. *The Journal of Physical Chemistry B* 105 (11):2143–2152.
Mishra, A. K., and S. Ramaprabhu. 2011. Carbon dioxide adsorption in graphene sheets. *AIP Advances* 1 (3):032152.
Mohan, M., V. K. Sharma, E. A. Kumar, and V. Gayathri. 2019. Hydrogen storage in carbon materials—A review. *Energy Storage*:e35.
Moon, I. K., J. Lee, R. S. Ruoff, and H. Lee. 2010. Reduced graphene oxide by chemical graphitization. *Nature Communications* 1:73.
Musyoka, N. M., K. M. Rambau, N. Manyala, J. Ren, H. W. Langmi, and M. K. Mathe. 2018. Utilization of waste tyres pyrolysis oil vapour in the synthesis of Zeolite Templated Carbons (ZTCs) for hydrogen storage application. *Journal of Environmental Science and Health, Part A* 53 (11):1022–1028.
Muthu, R. N., S. Rajashabala, and R. Kannan. 2016. Hexagonal boron nitride (h–BN) nanoparticles decorated multi–walled carbon nanotubes (MWCNT) for hydrogen storage. *Renewable Energy* 85:387–394.
Ni, M., M. K. Leung, and D. Y. Leung. 2008. Technological development of hydrogen production by solid oxide electrolyzer cell (SOEC). *International Journal of Hydrogen Energy* 33 (9):2337–2354.

Nicoletti, G., N. Arcuri, G. Nicoletti, and R. Bruno. 2015. A technical and environmental comparison between hydrogen and some fossil fuels. *Energy Conversion and Management* 89:205–213.

Nishihara, H., P.–X. Hou, L.–X. Li, M. Ito, M. Uchiyama, T. Kaburagi, A. Ikura, J. Katamura, T. Kawarada, and K. Mizuuchi. 2009. High–pressure hydrogen storage in zeolite–templated carbon. *The Journal of Physical Chemistry C* 113 (8):3189–3196.

Nishihara, H., and T. Kyotani. 2018. Zeolite–templated carbons–three–dimensional microporous graphene frameworks. *Chemical communications* 54 (45):5648–5673.

Nores–Pondal, F. J., I. M. J. Vilella, H. Troiani, M. Granada, S. R. de Miguel, O. A. Scelza, and H. R. Corti. 2009. Catalytic activity vs. size correlation in platinum catalysts of PEM fuel cells prepared on carbon black by different methods. *International Journal of Hydrogen Energy* 34 (19):8193–8203.

Oh, H., T. Gennett, P. Atanassov, M. Kurttepeli, S. Bals, K. E. Hurst, and M. Hirscher. 2013. Hydrogen adsorption properties of platinum decorated hierarchically structured templated carbons. *Microporous and Mesoporous Materials* 177:66–74.

Oriňáková, R., and A. Oriňák. 2011. Recent applications of carbon nanotubes in hydrogen production and storage. *Fuel* 90 (11):3123–3140.

Owusu, P. A., and S. Asumadu–Sarkodie. 2016. A review of renewable energy sources, sustainability issues and climate change mitigation. *Cogent Engineering* 3 (1):1167990.

Ōya, A., and S. Ōtani. 1979. Catalytic graphitization of carbons by various metals. *Carbon* 17 (2):131–137.

Panella, B., M. Hirscher, and S. Roth. 2005. Hydrogen adsorption in different carbon nanostructures. *Carbon* 43 (10):2209–2214.

Pang, J., J. E. Hampsey, Z. Wu, Q. Hu, and Y. Lu. 2004. Hydrogen adsorption in mesoporous carbons. *Applied Physics Letters* 85 (21):4887–4889.

Parambhath, V. B., R. Nagar, and S. Ramaprabhu. 2012. Effect of nitrogen doping on hydrogen storage capacity of palladium decorated graphene. *Langmuir* 28 (20):7826–7833.

Parambhath, V. B., R. Nagar, K. Sethupathi, and S. Ramaprabhu. 2011. Investigation of spillover mechanism in palladium decorated hydrogen exfoliated functionalized graphene. *The Journal of Physical Chemistry C* 115 (31):15679–15685.

Patel, C. K., P. J. Sarma, and M. De. 2015. Comparative parametric study on development of porous structure of aluminium oxide in presence of anionic and cationic surfactants. *Ceramics International* 41 (3):3578–3588.

Poirier, E., R. Chahine, P. Benard, D. Cossement, L. Lafi, E. Melancon, T. Bose, and S. Desilets. 2004. Storage of hydrogen on single–walled carbon nanotubes and other carbon structures. *Applied Physics A* 78 (7):961–967.

Poirier, E., R. Chahine, and T. Bose. 2001. Hydrogen adsorption in carbon nanostructures. *International Journal of Hydrogen Energy* 26 (8):831–835.

Prasanth, K., M. C. Raj, H. Bajaj, T. Kim, and R. Jasra. 2010. Hydrogen sorption in transition metal modified mesoporous materials. *International Journal of Hydrogen Energy* 35 (6):2351–2360.

Psofogiannakis, G. M., and G. E. Froudakis. 2009. DFT study of hydrogen storage by spillover on graphite with oxygen surface groups. *Journal of the American Chemical Society* 131 (42):15133–15135.

Pu, N.–W., C.–A. Wang, Y. Sung, Y.–M. Liu, and M.–D. Ger. 2009. Production of few–layer graphene by supercritical CO2 exfoliation of graphite. *Materials Letters* 63 (23):1987–1989.

Pyle, D. S., E. M. Gray, and C. Webb. 2016. Hydrogen storage in carbon nanostructures via spillover. *International Journal of Hydrogen Energy* 41 (42):19098–19113.

Radushkevich, L., and V. á. Lukyanovich. 1952. On the structure of carbon formed during the thermal decomposition of carbon monoxide on an iron contact. *Zurn Fisic Chim* 26 (1):88–95.

Reddy, A. L. M., and S. Ramaprabhu. 2007. Hydrogen storage properties of nanocrystalline Pt dispersed multi–walled carbon nanotubes. *International Journal of Hydrogen Energy* 32 (16):3998–4004.

Resch, G., A. Held, T. Faber, C. Panzer, F. Toro, and R. Haas. 2008. Potentials and prospects for renewable energies at global scale. *Energy policy* 36 (11):4048–4056.

Reyhani, A., S. Mortazavi, S. Mirershadi, A. Moshfegh, P. Parvin, and A. N. Golikand. 2011. Hydrogen storage in decorated multiwalled carbon nanotubes by Ca, Co, Fe, Ni, and Pd nanoparticles under ambient conditions. *The Journal of Physical Chemistry C* 115 (14):6994–7001.

Rouquerol, J., F. Rouquerol, P. Llewellyn, G. Maurin, and K. S. Sing. 2013. *Adsorption by powders and porous solids: principles, methodology and applications*: Academic press.

Ryoo, R., S. H. Joo, and S. Jun. 1999. Synthesis of highly ordered carbon molecular sieves via template–mediated structural transformation. *The Journal of Physical Chemistry B* 103 (37):7743–7746.

Sakintuna, B., F. Lamari–Darkrim, and M. Hirscher. 2007. Metal hydride materials for solid hydrogen storage: a review. *International Journal of Hydrogen Energy* 32 (9):1121–1140.

Sangchoom, W., and R. Mokaya. 2015. Valorization of lignin waste: carbons from hydrothermal carbonization of renewable lignin as superior sorbents for CO2 and hydrogen storage. *ACS Sustainable Chemistry & Engineering* 3 (7):1658–1667.

Sankaran, M., and B. Viswanathan. 2006. The role of heteroatoms in carbon nanotubes for hydrogen storage. *Carbon* 44 (13):2816–2821.

Sankaran, M. 2007. Hydrogen storage in boron substituted carbon nanotubes. *Carbon* 45 (8):1628–1635.

Selvakumar, N., A. Biswas, S. Krupanidhi, and H. Barshilia. 2018. Enhanced optical absorption of graphene–based heat mirror with tunable spectral selectivity. *Solar Energy Materials and Solar Cells* 186:149–153.

Sevilla, M., R. Foulston, and R. Mokaya. 2010. Superactivated carbide–derived carbons with high hydrogen storage capacity. *Energy & Environmental Science* 3 (2):223–227.

Shin, Y.–E., Y. J. Sa, S. Park, J. Lee, K.–H. Shin, S. H. Joo, and H. Ko. 2014. An ice–templated, pH–tunable self–assembly route to hierarchically porous graphene nanoscroll networks. *Nanoscale* 6 (16):9734–9741.

Singh, S., A. Bhatnagar, V. Dixit, V. Shukla, M. Shaz, A. Sinha, O. Srivastava, and V. Sekkar. 2016. Synthesis, characterization and hydrogen storage characteristics of ambient pressure dried carbon aerogel. *International Journal of Hydrogen Energy* 41 (5):3561–3570.

Srinivas, G., J. W. Burress, J. Ford, and T. Yildirim. 2011. Porous graphene oxide frameworks: synthesis and gas sorption properties. *Journal of Materials Chemistry* 21 (30):11323–11329.

Srinivas, G., Y. Zhu, R. Piner, N. Skipper, M. Ellerby, and R. Ruoff. 2010. Synthesis of graphene–like nanosheets and their hydrogen adsorption capacity. *Carbon* 48 (3):630–635.

Stadie, N. P., J. J. Vajo, R. W. Cumberland, A. A. Wilson, C. C. Ahn, and B. Fultz. 2012. Zeolite–templated carbon materials for high–pressure hydrogen storage. *Langmuir* 28 (26):10057–10063.

Stankovich, S., D. A. Dikin, G. H. Dommett, K. M. Kohlhaas, E. J. Zimney, E. A. Stach, R. D. Piner, S. T. Nguyen, and R. S. Ruoff. 2006. Graphene–based composite materials. *nature* 442 (7100):282.

Su, F., L. Lv, T. M. Hui, and X. Zhao. 2005. Phenol adsorption on zeolite–templated carbons with different structural and surface properties. *Carbon* 43 (6):1156–1164.

Su, F., Z. Tian, C. K. Poh, Z. Wang, S. H. Lim, Z. Liu, and J. Lin. 2009. Pt nanoparticles supported on nitrogen–doped porous carbon nanospheres as an electrocatalyst for fuel cells. *Chemistry of Materials* 22 (3):832–839.

Su, F., X. Zhao, L. Lv, and Z. Zhou. 2004. Synthesis and characterization of microporous carbons templated by ammonium–form zeolite Y. *Carbon* 42 (14):2821–2831.

Subrahmanyam, K., S. Vivekchand, A. Govindaraj, and C. Rao. 2008. A study of graphenes prepared by different methods: characterization, properties and solubilization. *Journal of Materials Chemistry* 18 (13):1517–1523.

Suh, M. P., H. J. Park, T. K. Prasad, and D.–W. Lim. 2011. Hydrogen storage in metal–organic frameworks. *Chemical reviews* 112 (2):782–835.

Takagi, H., H. Hatori, Y. Soneda, N. Yoshizawa, and Y. Yamada. 2004. Adsorptive hydrogen storage in carbon and porous materials. *Materials Science and Engineering: B* 108 (1–2):143–147.

Takeichi, N., H. Senoh, T. Yokota, H. Tsuruta, K. Hamada, H. T. Takeshita, H. Tanaka, T. Kiyobayashi, T. Takano, and N. Kuriyama. 2003. "Hybrid hydrogen storage vessel", a novel high–pressure hydrogen storage vessel combined with hydrogen storage material. *International Journal of Hydrogen Energy* 28 (10):1121–1129.

Tang, J., T. Wang, X. Sun, Y. Guo, H. Xue, H. Guo, M. Liu, X. Zhang, and J. He. 2013. Effect of transition metal on catalytic graphitization of ordered mesoporous carbon and Pt/metal oxide synergistic electrocatalytic performance. *Microporous and Mesoporous Materials* 177:105–112.

Tang, P., G. Hu, Y. Gao, W. Li, S. Yao, Z. Liu, and D. Ma. 2014. The microwave adsorption behavior and microwave–assisted heteroatoms doping of graphene–based nano–carbon materials. *Scientific Reports* 4:5901.

Tang, Z., L. Zhang, C. Zeng, T. Lin, and B. Guo. 2012. General route to graphene with liquid–like behavior by non–covalent modification. *Soft Matter* 8 (35):9214–9220.

Thomas, J. M., and W. J. Thomas. 2014. *Principles and practice of heterogeneous catalysis*: John Wiley & Sons.

Thomas, K. M. 2007. Hydrogen adsorption and storage on porous materials. *Catalysis today* 120 (3–4):389–398.

Tian, X., G. Hong, Y. Liu, B. Jiang, and Y. Yang. 2014. Catalytic performance of Au III supported on SiO 2 modified activated carbon. *RSC Advances* 4 (68):36316–36324.

Tibbetts, G. G., G. P. Meisner, and C. H. Olk. 2001. Hydrogen storage capacity of carbon nanotubes, filaments, and vapor–grown fibers. *Carbon* 39 (15):2291–2301.

Valero, A., A. Valero, G. Calvo, A. Ortego, S. Ascaso, and J.–L. Palacios. 2018. Global material requirements for the energy transition. An exergy flow analysis of decarbonisation pathways. *Energy* 159:1175–1184.

Vaqueiro–Contreras, M., C. Bartlam, R. Bonilla, V. Markevich, M. Halsall, A. Vijayaraghavan, and A. Peaker. 2018. Graphene oxide films for field effect surface passivation of silicon for solar cells. *Solar Energy Materials and Solar Cells* 187:189–193.

Vinayan, B., R. Nagar, and S. Ramaprabhu. 2013. Solar light assisted green synthesis of palladium nanoparticle decorated nitrogen doped graphene for hydrogen storage application. *Journal of Materials Chemistry A* 1 (37):11192–11199.

Viswanathan, B., M. Sankaran, and M. A. Scibioh. 2003. Carbon nanomaterials: are they appropriate candidates for hydrogen storage? *Bulletin of Catalysis Society of India* 2:12–32.

Wang, H., Q. Gao, and J. Hu. 2009. High hydrogen storage capacity of porous carbons prepared by using activated carbon. *Journal of the American Chemical Society* 131 (20):7016–7022.

Wang, L., and R. T. Yang. 2008a. Hydrogen storage properties of carbons doped with ruthenium, platinum, and nickel nanoparticles. *The Journal of Physical Chemistry C* 112 (32):12486–12494.

Wang, L. 2008b. New sorbents for hydrogen storage by hydrogen spillover–a review. *Energy & Environmental Science* 1 (2):268–279.

Wang, L. 2009. Hydrogen storage properties of N–doped microporous carbon. *The Journal of Physical Chemistry C* 113 (52):21883–21888.

Wang, Y., C. X. Guo, X. Wang, C. Guan, H. Yang, K. Wang, and C. M. Li. 2011a. Hydrogen storage in a Ni–B nanoalloy–doped three–dimensional graphene material. *Energy & Environmental Science* 4 (1):195–200.

Wang, Y., J. Liu, K. Wang, T. Chen, X. Tan, and C. M. Li. 2011b. Hydrogen storage in Ni–B nanoalloy–doped 2D graphene. *International Journal of Hydrogen Energy* 36 (20):12950–12954.

Wang, Y., K. Wang, C. Guan, Z. He, Z. Lu, T. Chen, J. Liu, X. Tan, T. T. Y. Tan, and C. M. Li. 2011c. Surface functionalization–enhanced spillover effect on hydrogen storage of Ni–B nanoalloy–doped activated carbon. *International Journal of Hydrogen Energy* 36 (21):13663–13668.

Wang, Z., L. Sun, F. Xu, H. Zhou, X. Peng, D. Sun, J. Wang, and Y. Du. 2016. Nitrogen–doped porous carbons with high performance for hydrogen storage. *International Journal of Hydrogen Energy* 41 (20):8489–8497.

Wei, L., and Y. Mao. 2016. Enhanced hydrogen storage performance of reduced graphene oxide hybrids with nickel or its metallic mixtures based on spillover mechanism. *International Journal of Hydrogen Energy* 41 (27):11692–11699.

Wu, C. G., and T. Bein. 1994. Conducting polyaniline filaments in a mesoporous channel host. *Science* 264 (5166):1757–1759.

Wu, Z. S., W. Ren, L. Gao, B. Liu, C. Jiang, and H.–M. Cheng. 2009. Synthesis of high–quality graphene with a pre–determined number of layers. *Carbon* 47 (2):493–499.

Xia, Y., and R. Mokaya. 2007. Ordered mesoporous carbon monoliths: CVD nanocasting and hydrogen storage properties. *The Journal of Physical Chemistry C* 111 (27):10035–10039.

Xia, Y., R. Mokaya, D. M. Grant, and G. S. Walker. 2011. A simplified synthesis of N–doped zeolite–templated carbons, the control of the level of zeolite–like ordering and its effect on hydrogen storage properties. *Carbon* 49 (3):844–853.

Xia, Y., G. S. Walker, D. M. Grant, and R. Mokaya. 2009. Hydrogen storage in high surface area carbons: experimental demonstration of the effects of nitrogen doping. *Journal of the American Chemical Society* 131 (45):16493–16499.

Xia, Y., Z. Yang, and Y. Zhu. 2013. Porous carbon–based materials for hydrogen storage: advancement and challenges. *Journal of Materials Chemistry A* 1 (33):9365–9381.

Xu, W. C., K. Takahashi, Y. Matsuo, Y. Hattori, M. Kumagai, S. Ishiyama, K. Kaneko, and S. Iijima. 2007. Investigation of hydrogen storage capacity of various carbon materials. *International Journal of Hydrogen Energy* 32 (13):2504–2512.

Yadav, A., M. Faisal, A. Subramaniam, and N. Verma. 2017. Nickel nanoparticle–doped and steam–modified multiscale structure of carbon micro–nanofibers for hydrogen storage: Effects of metal, surface texture and operating conditions. *International Journal of Hydrogen Energy* 42 (9):6104–6117.

Yang, Z., Y. Xia, and R. Mokaya. 2007. Enhanced hydrogen storage capacity of high surface area zeolite–like carbon materials. *Journal of the American Chemical Society* 129 (6):1673–1679.

Yang, Z., Y. Xia, X. Sun, and R. Mokaya. 2006. Preparation and hydrogen storage properties of zeolite–templated carbon materials nanocast via chemical vapor deposition: effect of the zeolite template and nitrogen doping. *The Journal of Physical Chemistry B* 110 (37):18424–18431.

Yürüm, Y., A. Taralp, and T. N. Veziroglu. 2009. Storage of hydrogen in nanostructured carbon materials. *International Journal of Hydrogen Energy* 34 (9):3784–3798.

Zacharia, R., K. Y. Kim, A. F. Kibria, and K. S. Nahm. 2005. Enhancement of hydrogen storage capacity of carbon nanotubes via spill–over from vanadium and palladium nanoparticles. *Chemical Physics Letters* 412 (4–6):369–375.

Zackrisson, J., and H.–O. Andrén. 1999. Effect of carbon content on the microstructure and mechanical properties of (Ti, W, Ta, Mo)(C, N)–(Co, Ni) cermets. *International Journal of Refractory Metals and Hard Materials* 17 (4):265–273.

Zaluska, A., L. Zaluski, and J. Ström–Olsen. 2000. Sodium alanates for reversible hydrogen storage. *Journal of Alloys and Compounds* 298 (1–2):125–134.

Zhang, C., M. Chen, X. Xu, L. Zhang, L. Zhang, F. Xia, X. Li, Y. Liu, W. Hu, and J. Gao. 2014. Graphene oxide reduced and modified by environmentally friendly glycylglycine and its excellent catalytic performance. *Nanotechnology* 25 (13):135707.

Zhang, S., S. Tsuzuki, K. Ueno, K. Dokko, and M. Watanabe. 2015. Upper limit of nitrogen content in carbon materials. *Angewandte Chemie International Edition* 54 (4):1302–1306.

Zhao, T., X. Ji, W. Jin, W. Yang, and T. Li. 2017a. Hydrogen storage capacity of single–walled carbon nanotube prepared by a modified arc discharge. *Fullerenes, Nanotubes and Carbon Nanostructures* 25 (6):355–358.

Zhao, W., V. Fierro, C. Zlotea, M. Izquierdo, C. Chevalier–César, M. Latroche, and A. Celzard. 2012. Activated carbons doped with Pd nanoparticles for hydrogen storage. *International Journal of Hydrogen Energy* 37 (6):5072–5080.

Zhao, W., L. Luo, T. Chen, Z. Li, Z. Zhang, H. Wang, J. Rao, L. Feo, and M. Fan. 2019. Synthesis and characterization of Pt–N–doped activated biocarbon composites for hydrogen storage. *Composites Part B: Engineering* 161:464–472.

Zhao, W., L. Luo, H. Wang, and M. Fan. 2017b. Synthesis of bamboo–based activated carbons with super–high specific surface area for hydrogen storage. *BioResources* 12 (1):1246–1262.

Zheng, Q., X. Ji, S. Gao, and X. Wang. 2013. Analysis of adsorption equilibrium of hydrogen on graphene sheets. *International Journal of Hydrogen Energy* 38 (25):10896–10902.

Zheng, Z., Q. Gao, and J. Jiang. 2010. High hydrogen uptake capacity of mesoporous nitrogen–doped carbons activated using potassium hydroxide. *Carbon* 48 (10):2968–2973.

Zhong, M., Z. Fu, L. Yuan, H. Zhao, J. Zhu, Y. He, C. Wang, and Y. Tang. 2015. A solution–phase synthesis method to prepare Pd–doped carbon aerogels for hydrogen storage. *RSC Advances* 5 (27):20966–20971.

Zhou, C., J. A. Szpunar, and X. Cui. 2016. Synthesis of Ni/graphene nanocomposite for hydrogen storage. *ACS applied materials & interfaces* 8 (24):15232–15241.

Zieliński, M., R. Wojcieszak, S. Monteverdi, M. Mercy, and M. Bettahar. 2007. Hydrogen storage in nickel catalysts supported on activated carbon. *International Journal of Hydrogen Energy* 32 (8):1024–1032.

Züttel, A. 2004. Hydrogen storage methods. *Naturwissenschaften* 91 (4):157–172.

Züttel, A., A. Remhof, A. Borgschulte, and O. Friedrichs. 2010. Hydrogen: the future energy carrier. *Philosophical Transactions of the Royal Society A: Mathematical, Physical and Engineering Sciences* 368 (1923):3329–3342.

Züttel, A., S. Rentsch, P. Fischer, P. Wenger, P. Sudan, P. Mauron, and C. Emmenegger. 2003. Hydrogen storage properties of LiBH4. *Journal of Alloys and Compounds* 356:515–520.

Appendices

Appendix A: Interaction between aluminum hydroxide and SDS surfactant micelles in solution

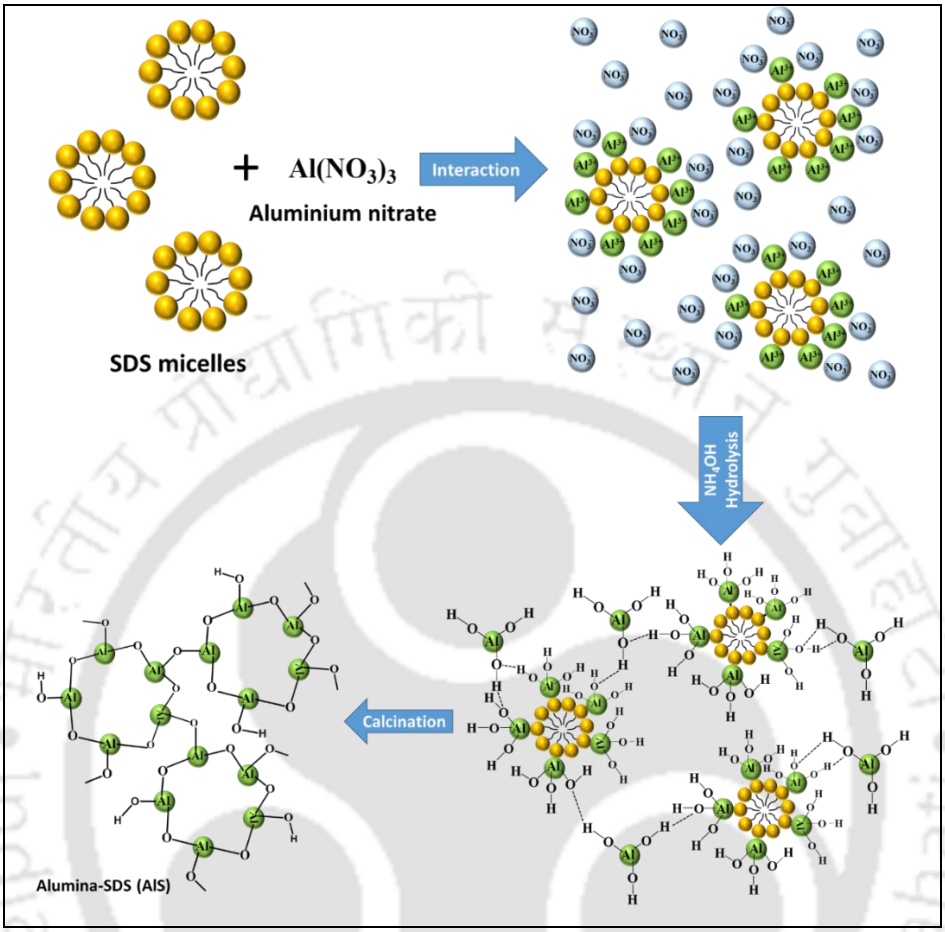

Figure A1: Schematic representation of the interaction between aluminum hydroxide and SDS surfactant micelles in solution.

Appendix B: EDX spectra of different doped templated carbons

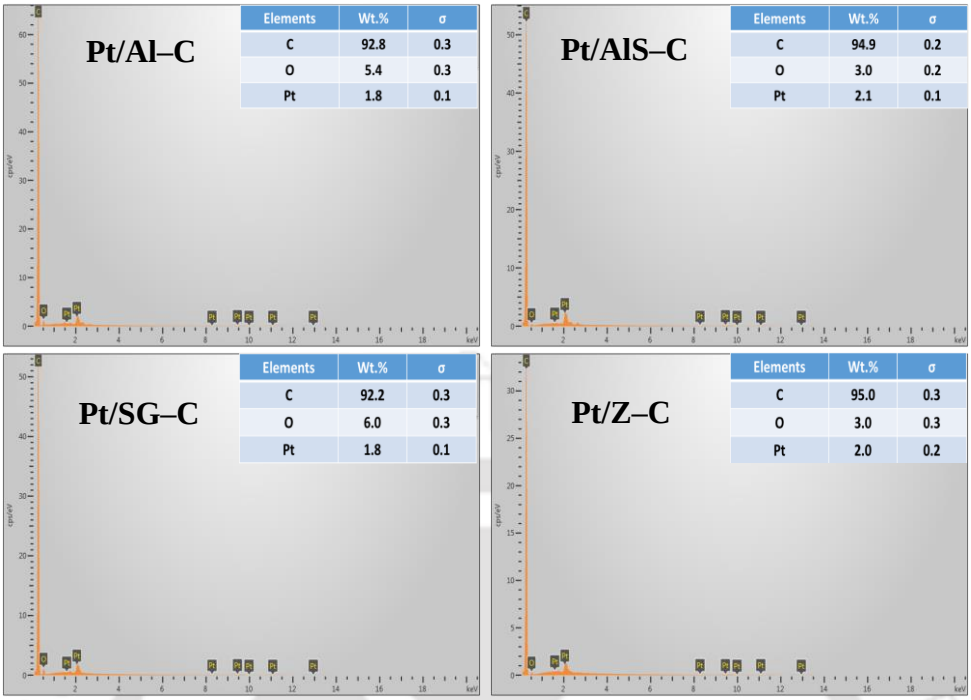

Figure B1: EDX spectra of platinum doped templated carbons derived from different templates.

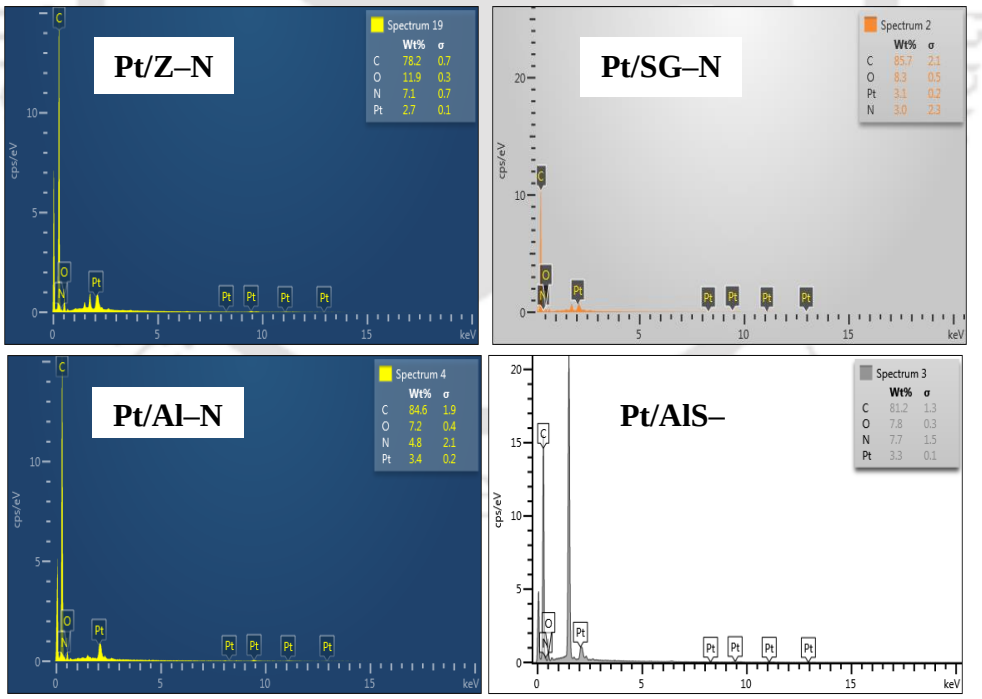

Figure B2: EDX spectra of platinum and nitrogen co–doped templated carbons derived from templates.

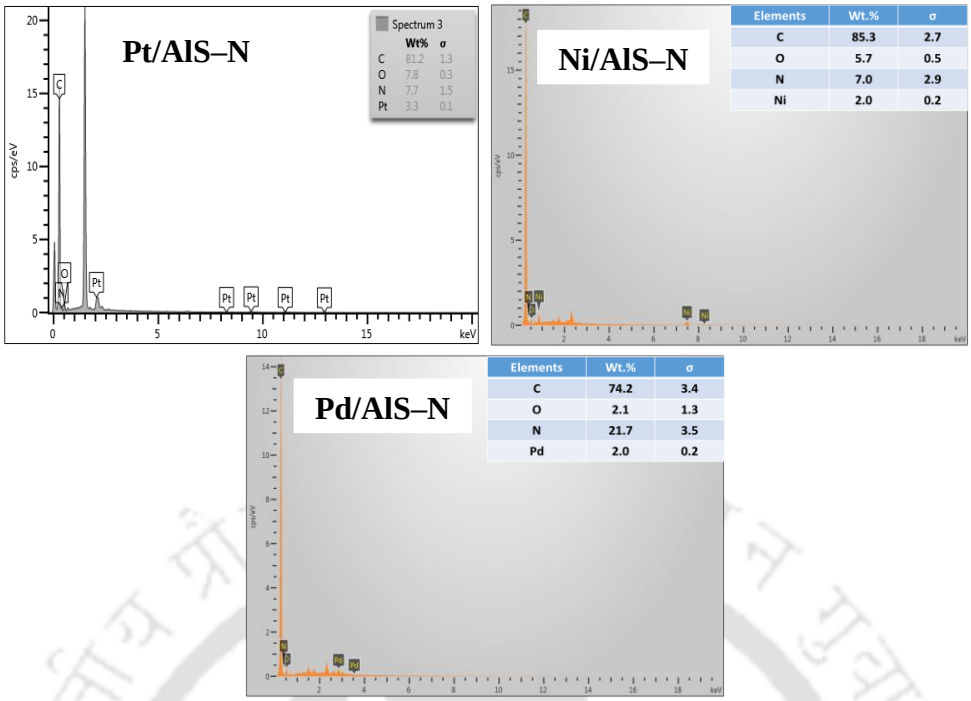

Figure B3: EDX spectra of different metal and nitrogen co–doped templated carbons.

Appendix C: EDX mapping of templated carbon and graphene based materials

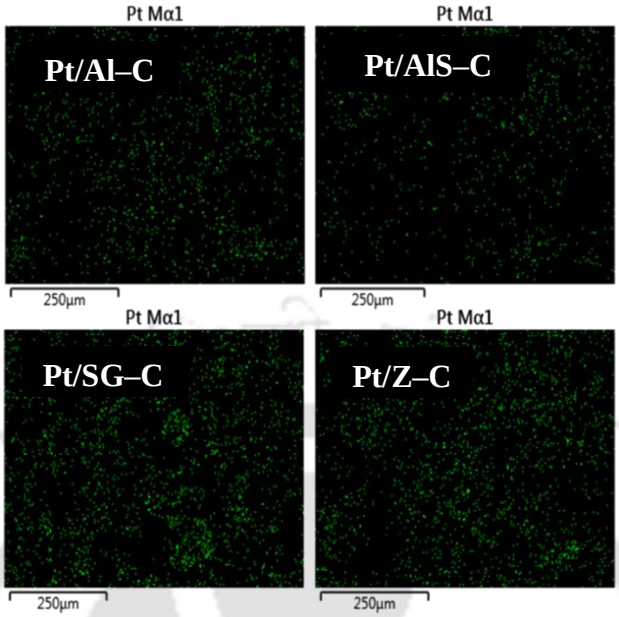

Figure C1: EDX mapping images of platinum doped templated carbons.

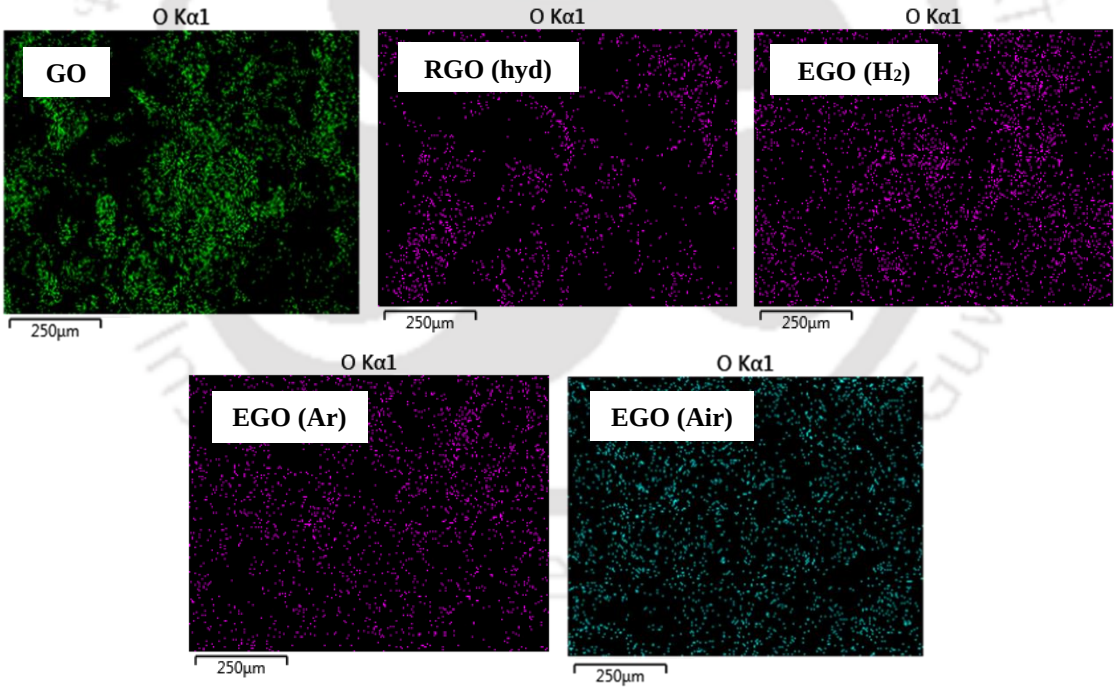

Figure C2: EDX mapping images of graphene oxide (GO), reduced graphene oxide and exfoliated graphene oxide samples.

Appendix D: TPD profiles of graphene oxide (GO) in different carrier gas of H_2, Ar and air

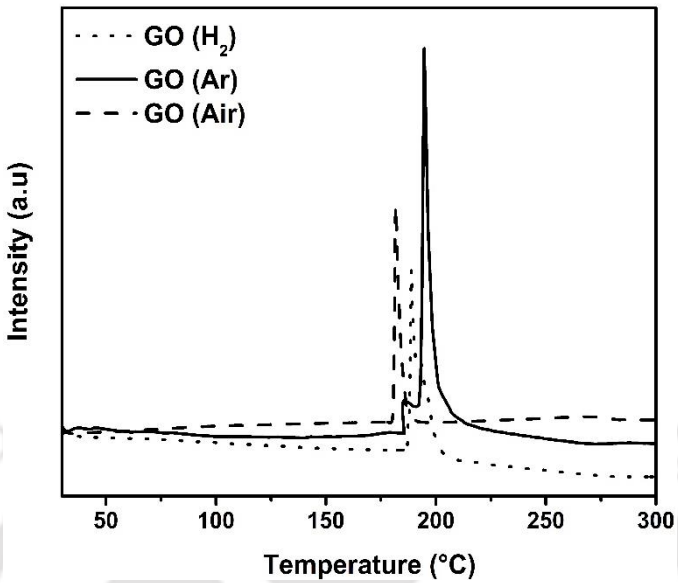

Figure D1: TPD profiles of graphene oxide (GO) in different carrier gases of H_2, Ar or air.

TPD was carried out in Chemisorb 2720 (Micromeritics). In this method, the required amount of GO was taken in U–shape quartz tube and degassed at 40 °C for 1 h in the flow of He gas. Then the GO was heated in desired carrier gas from room temperature to 300 °C at a heating rate of 10 °C/min.

Appendix E: Calculations for metal dispersion by Carbon monoxide Chemisorption

The 2 wt.% Pd doped AlS–N (2Pd/AlS–N) sample calculation for metal dispersion is shown below (section 4.1.7). Sample amount: 0.0604 g; Active gas: 10 % Co/He; Carrier gas: He; Sample temperature: 27 ^{o}C; Each pulse volume: 0.1 cm^3. The sample was given 5 (five) pulses; each pulse was of 0.1 cm^3 volume. Five peaks were obtained and area for each peak is given in Table E1. The area differences corresponded to volume of CO chemisorbed on the metal.

Table E1: Peak areas for five pulses of CO injected to the sample.

Pulse no.	Peak area	Area difference (Ai–Aj)
1	0.00489	0.00056
2	0.00498	0.00047
3	0.00510	0.00035
4	0.00545	0
5	0.00545	0
	Total area	0.00138

A_j = area under each peak; A_i= area for 0.1 cm^3 peak = 0.005453
At STP, volume of active gas injected = V_{inj}

$$V_{inj} = V_{syr} \times \frac{T_{std}}{T_{amb}} \times \frac{P_{amb}}{P_{std}} \times \frac{A}{100} \qquad (A1)$$

Where, V_{syr} = injected syringe volume = 0.1 cm^3; T_{std} = standard temperature= 273 K ; T_{amb} = ambient temperature =27 ^{o}C = 300 K; P_{amb} = ambient pressure = 743 mmHg; P_{std} = standard pressure = 760 mmHg; A = % active gas = 10 %

From equation 1, $V_{inj} = 0.1 \times \frac{273}{300} \times \frac{743}{760} \times \frac{10}{100}$ V_{inj} = 0.018 cm^3

Hence, 0.005453 area corresponding to 0.1 cm^3 of mixture actually represented volume of 0.018 cm^3 at STP.
For sample amount of 0.0604 g, the total area of adsorption = 0.00138

Hence adsorbed $CO = \frac{Volume\ of\ active\ gas\ \text{injected}\ (V_{inj})}{Area\ corresponding\ to\ 0.1\ \text{cm}^3\ \text{injection}} \times \text{Total area of the adsorption}$

$$CO = \frac{0.018}{0.00545} \times 0.00138 = 0.00455 \text{ ml/0.0604 g}$$

Or Volume of CO adsorbed = $\frac{0.00455\ ml}{0.060\ g\ of\ sample}$ = 0.0758 ml/g = $\frac{0.0758}{22414}$ = 3.38 × 10^{-6} moles/g

Metal dispersion (d_m) is defined as

$$d_m = \frac{Total\ no.\ of\ \text{exposed surface atoms}\ (N_S)}{Total\ no.\ of\ \text{metal atoms present in sample}\ (N_T)} \qquad (A2)$$

For 2 wt. % Pd/AlS–N on 1 g basis, the total moles of palladium atom present in sample (N_T) =

$$N_T = 60 \times \frac{1.9}{100} = 1.20\ mg\ of\ Pd = \frac{1.20}{106.42} = 0.01127\ mmoles of\ Pd\ /\ g\ of\ samples$$
$$= 11.27 \times 10^{-6}\ moles of\ Pd\ /\ g\ of\ samples$$

Where 106.42 is the molecular weight of Pd

From the equation (A2), $d_m(\%) = \frac{3.38 \times 10^{-6}}{10.71 \times 10^{-6}} \times 100 = 30\%$

Appendix F: Calculation for crystallite size of metal from XRD profile

The sample calculation for platinum crystallite size is determined for the Pt/AlS–N sample (section 4.1.6).
Maximum intensity peak at 2θ = 39.9 correspondings to Pt (111) plane was selected for crystal size calculation (Figure 4.24). The average crystallite size was evaluated using Scherrer's formula as describle in experimental section 3.3.6:–

$$D_C = \frac{K\lambda}{\beta \cos\theta} \qquad (1)$$

Where,

D = crystallite size in nm; K = Shape factor = 0.9; λ = wavelength of radiation = 0.154 nm; θ = 39.9/2 = 19.95; cosθ = 0.9399; β = Full width of half–maximum intensity = 0.01574

Hence, from the equation (1), the average crystal size is given as

$$D_C = \frac{0.9 \times 0.154}{0.01574 \times 0.9399} = 9.36\, nm$$

Appendix G: Calculation of number of layers in graphene samples from XRD profiles

The sample calculation for platinum crystallite size is determined for EGO (Air) sample. The graphitic peak at 2θ = 24.5 corresponding to C (002) plane was selected for crystal size calculation. The number of graphene layers was determined by the equation :

$$N_L = \frac{D_c}{d_{(002)}} + 1 \qquad \text{(A3)}$$

Where, N_L = numbser of layers; $d_{(002)}$ = spacing between the layers = 0.381 nm; respectively. D_c = average crystal size of the graphitic zone = 1.35 nm

Hence, from the equation (A3), the number of layers is

$$N_L = \frac{1.35}{0.381} + 1 = 4.54$$

The average crystallite size of graphitic zone (002) for different graphene samples used for number of layers in respective sample is given below.

Table G1: Average crystallite size of A) exfoliated GO (EGO) samples. B) chemically and thermally treated GO samples C) metal doped RGO samples D) Pd–doped RGO and EGO samples

A)

Sample ID	Average crystallite size $(nm)_{(002)}$
EGO (200)	1.01
EGO (300)	1.19
EGO (400)	1.88
EGO (500)	2.52

B)

Sample ID	Average crystallite size $(nm)_{(002)}$
GO	11
RGO (hyd)	1.01
EGO (H_2)	1.19
EGO (Ar)	1.89
EGO (Air)	1.35

C)

Sample ID	Average crystallite size $(nm)_{(002)}$
GO	1.01
Ni/RGO	1.49
Pt/RGO	1.02
Pd/RGO	1.65

D)

Sample ID	Average crystallite size $(nm)_{(002)}$
RGO	1.01
Pd/RGO	1.65
Pd/RGO_A*	1.15
EGO	1.31
Pd/EGO	1.24
Pd/EGO_A*	1.10

Appendix H: Calculation for isosteric heat of adsorption

Isosteric heat of adsorption (ΔH_{ads}) was determined as a function of hydrogen uptake using the Clausius–Clapeyron equation from the uptake data collected at –10, 0 and 25 °C. The Clausius–Clapeyron equation is given below:

$$\Delta H_{ads} = R\left[\frac{d(\ln P)}{d(1/T)}\right]_q \qquad \text{(A4)}$$

Where q is the giving uptake, R is the universal gas constant, P is pressure and T is adsorption temperature.

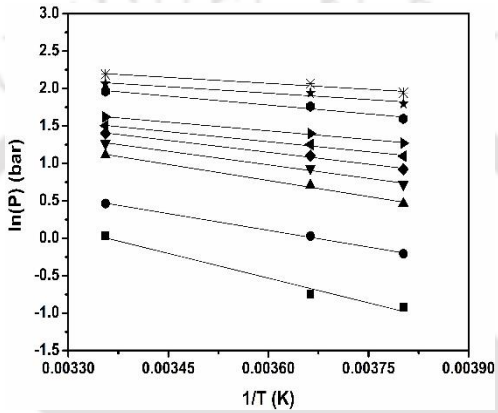

Figure H1: Typical plot of ln(P) versus (1/T) of 2Pd/AlS–N sample (section 4.1.7) for evaluation of isosteric heat of adsorption.

Figure H1 shows the graph between ln (P) and (1/T) for hydrogen adsorption capacities at different constant equilibrium hydrogen uptakes. The value of ΔH_{ads} was obtained from the slope ($\Delta H_{ads}/R$) of the plot of ln (P) versus (1/T) at a constant adsorbed amount of H_2. The calculated heat of adsorption values for Pd/AlS–N sample is shown in Figure H2.

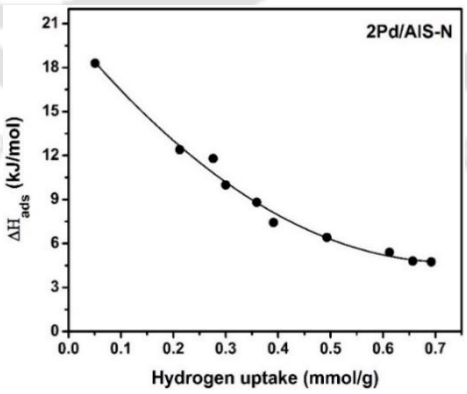

Figure H2: Variation of the isosteric heat of adsorption with the amount of hydrogen adsorption for Pd/AlS–N sample.

Appendix I: Comparison of physical properties and hydrogen uptake capacities of graphene samples of present study with other carbon based materials that reported in literature

Table I1: Comparison of physical properties and hydrogen uptake capacities for samples prepared in this study with other carbon based materials that reported in the literature at –196 °C.

Graphene Type	Surface area (m^2/g)	Pressure (bar)	Hydrogen uptake (wt.%)	References
Biomass based carbon	760	25	1.8	(Bader et al. 2016)
SWCNT	~325	50	2.9	(Xu et al. 2007)
MWCNT	1220	40	2.2	(Jordá–Beneyto et al. 2007)
Templated carbon	2090	36	3.07	(Cai et al. 2015)
Templated carbon	2545	10	2.4	(Guan et al. 2009)
Activated carbon	1594	40	3.2	(Jordá–Beneyto et al. 2008)
Graphene oxide (GO)	**41**	**30**	**1.09**	**Present study**
Exfoliated GO	**217**	**30**	**3.34**	**Present study**
Reduced GO	**461**	**30**	**2.5**	**Present study**

Appendix J: Hydrogen adsorption-desorption device description

The iSorb–HP1–XKRLSPN100 (Make: Quantachrome) is a volumetric gas sorption system capable for performing gas sorption analyses and generating full high-pressure isotherms. The volumetric adsorption system has a manifold section of known volume connected to other areas of the system through pneumatic valves. By using high sensitivity pressure sensors, the exact amount of gas enclosed in these areas is known at any given time. The Figure J1 shows a basic process and instrumentation diagram of a general volumetric system.

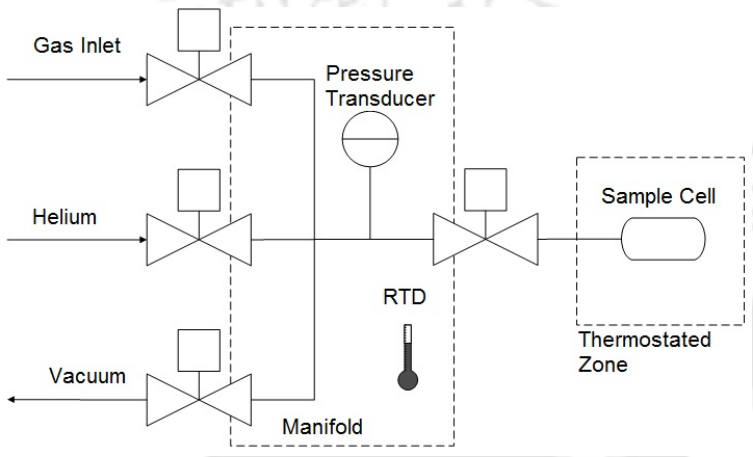

Figure J1: General volumetric system diagram (High pressure gas sorption system Operating Manual, Version 2.1.0, Quantachrome Instruments, USA, 2012-2013)

The system is initially fully evacuated. Then, the gas inlet valve is opened allowing the nitrogen gas to fill the manifold until a certain pressure is reached. As the pressure, temperature, and volume of the system are known, the amount of gas present in the system is calculated. Next the manifold's valve to the sample cell is opened allowing the gas to flow to the sample in the sample cell. The system is allowed to reach a state of equilibrium pressure. From known volume of the cell via a helium expansion calibration step, the final pressure of the system is obtained. However, the actual remaining pressure differs from that previously calculated pressure due to some of the gas being adsorbed onto the sample. The difference between the actual and calculated pressure of the system represents the amount of gas adsorbed onto the sample.

The manifold is connected via pneumatic valves to up to three gas reservoirs (gas tanks, etc.), a helium gas reservoir, a vacuum pump, a calibration cell, a vent, and a connection for the sample cell itself. The manifold and sample cell are equipped with high pressure transducers

capable of measuring up to 100 bar. The standard pressure transducers are accurate to ±0.05% of full scale. The manifold was maintained at 36 ºC. The sample cell temperature was controlled at –196 ºC (77K) using liquid nitrogen. For the range of –20 to 100 ºC, a recirculating bath with a suitable fluid such as ethylene glycol or water was used.

Before each analysis, buoyancy correction is performed using helium till 20 bar and void volume was calculated using helium gas at analysis temperature. In a typical experiment about 100 mg of sample is taken into the sample holder and then the sample holder is tightly fitted with adsorption apparatus. During analysis, hydrogen is inserted in the sample chamber at the desired pressure and the system is kept on hold for 20 minutes till equilibrium is reached. The changes in weight, pressure and temperature are measured continuously for every pressure point and the hydrogen adsorption capacity is evaluated at different temeratures.